# Brillouin cavity optomechanics with whispering-gallery microresonators

Thesis by

Georg P. A. Enzian

Keble College, Oxford

Submitted in partial fulfilment of the requirements
for the degree of
Doctor of Philosophy at the University of Oxford

Hilary Term, 2020

Academic advisors:
Prof. Ian A. Walmsley and Dr. Michael R. Vanner

Clarendon Laboratory
University of Oxford
United Kingdom

**Abstract**

Cavity quantum optomechanics is a field of investigation which studies the interaction between optical and mechanical degrees of freedom applying the powerful methods of quantum optics. These theoretical methods and experimental techniques have been developed through the second half of the 20th century and gained significant momentum following the invention of the laser. Upon the realisation that coherent manipulation of the motion of mesoscopic, or even macroscopic, mechanical systems was feasible using laser light, interest in cavity quantum optomechanics grew and groups across the globe began working towards the preparation of non-classical mechanical states. The field is now well established, but the preparation of non-classical states of the motion via interaction with optical fields remains challenging to explore, which is believed will open the door to studies of fundamental physics regarding decoherence, the quantum-to-classical transition or may even shed light on the interface between quantum mechanics and gravity.

This thesis explores Brillouin scattering in whispering-gallery-mode microresonators. The parametric coupling between high frequency (11 GHz) elastic waves and infrared (1550 nm) light via electrostriction is used to demonstrate several interesting cavity optomechanical phenomena. This thesis contributes to developing this new approach to optomechanics in four key ways.

By use of a pair of optical resonances of different transverse structure spaced by the material's Brillouin shift, reaching the cavity optomechanical strong coupling regime was experimentally demonstrated with a fused silica microrod resonator. Operation in this regime is crucial for many optomechanical protocols, importantly optomechanical state-swap between the optical and mechanical modes.

A similar resonator was employed to demonstrate measurement-enhanced optomechanical sideband cooling. Here the measurement record of the continuously monitored heterodyne measurement of Brillouin anti-Stokes scattered light is used to reduce the phase-space uncertainty of the mechanical state, effectively cooling the mode beyond the sideband-cooling limit. For this purpose the conservation of Gaussianity of the state (initially a thermal state) under linear measurement (heterodyne detection) is used within a stochastic master equation approach.

In another experiment, single-phonon addition and subtraction to a mechanical thermal state was demonstrated, showing a characteristic doubling of the mean phonon number of the mechanical mode. For this experiment a crystalline microresonator of barium fluoride was used, a material which allows reaching superb optical quality factors combined with highest elastic isotropy for a crystalline substance. The non-Gaussianity of the single-quantum subtracted state is demonstrated.

Finally, the platform of Brillouin cavity optomechanics with high-frequency phonons in crystalline (barium fluoride) whispering-gallery resonators at cryogenic temperatures is discussed.

# Contents


**1 Introduction** **1**

1.1 Quantum mechanics - basic theory . . . 2
1.1.1 Closed quantum systems . . . 2
1.1.2 Modes, quantisation, and the quantum harmonic oscillator . . . 5
1.1.3 Open quantum systems . . . 7
1.2 Cavity quantum optomechanics . . . 11
1.2.1 Radiation pressure coupling in a Fabry-Perot resonator . . . 12
1.2.2 Resolved sideband regime . . . 14
1.2.3 Unresolved sideband regime . . . 15
1.2.4 Thermodynamic picture of cavity optomechanics . . . 15
1.3 Whispering-gallery waves . . . 16
1.3.1 Elastic waves . . . 17
1.3.2 Electromagnetic whispering-gallery waves . . . 22
1.4 Brillouin scattering . . . 25
1.4.1 Classical equations of motion for stimulated Brillouin scattering . . . 28
1.4.2 Electrostriction and Brillouin gain . . . 30
1.5 Brillouin optomechanics in microresonators . . . 34
1.5.1 Brillouin phase matching . . . 35
1.5.2 Optomechanical coupling rate . . . 40
1.5.3 Brillouin lasing . . . 44
1.5.4 Beam splitter and two-mode-squeezing type Hamiltonians . . . 45
1.5.5 Other nonlinear effects . . . 48

**2 Experimental setup** **52**

2.1 Setup overview . . . 52
2.2 Tapered fiber evanescent coupling to optical whispering-gallery modes . . . 54
2.2.1 Resonator and taper mounts . . . 56
2.2.2 Polarisation control . . . 57
2.3 Microresonators . . . 58
2.3.1 Silica microrod resonators . . . 59
2.3.2 Silica microspheres . . . 60
2.3.3 Barium fluoride crystalline microresonators . . . 61
2.4 Lasers, modulation, locking . . . 63
2.4.1 Laser locking . . . 63
2.5 Optical measurement devices . . . 66

2.5.1 Photodetectors . . . 66
2.5.2 Optical spectrum analyser . . . 66
2.5.3 Optical balanced homodyne and heterodyne detection . . . 67
2.5.4 Single photon avalanche diode (SPAD) photodetectors . . . 69
2.6 Optical filtering . . . 69

**3 Brillouin optomechanical strong coupling 72**
3.1 Introduction . . . 73
3.2 Experimental setup . . . 74
3.3 Model . . . 77
3.3.1 System Hamiltonian . . . 78
3.3.2 Quantum Langevin equations of motion . . . 85
3.3.3 Heterodyne power spectrum . . . 87
3.4 Observation of normal-mode splitting and avoided crossing . . . 89
3.4.1 Normal mode splitting and strong coupling condition in the model . . . 94
3.5 Practical aspects . . . 96
3.5.1 Identifying cavity-mode pairs . . . 98
3.5.2 Detuning dependence . . . 98
3.5.3 Kerr frequency comb as nonlinear loss channel . . . 100
3.5.4 Determining the intracavity power . . . 101
3.6 Conclusions . . . 102

**4 Single-phonon addition and subtraction to a thermal state 104**
4.1 Introduction . . . 105
4.2 Experimental scheme . . . 107
4.3 Setup . . . 108
4.4 Measurement results . . . 110
4.5 Theoretical model . . . 113
4.5.1 Single-phonon addition and subtraction to a thermal state . . . 114
4.5.2 Dynamics . . . 115
4.5.3 Quantum Langevin equations . . . 116
4.5.4 Detection . . . 122
4.5.5 Effect of multi-modeness . . . 128
4.6 Non-Gaussian nature of the prepared state . . . 133
4.6.1 Toy model and lossy read-out of non-Gaussian quadrature distribution 135
4.6.2 Experimental results . . . 139
4.7 Outlook . . . 140

**5 Heterodyne-measurement-enhanced optomechanical sideband cooling 144**
5.1 Introduction . . . 145
5.2 Theory . . . 147
5.3 Experimental setup . . . 155
5.3.1 Measured heterodyne current and its appropriate normalisation . . . 157
5.4 Experimental results . . . 160
5.5 Summary . . . 163

**6 Outlook** **165**
6.1 Crystalline Brillouin cavity optomechanics with barium fluoride whispering-gallery microresonators . . . 165
6.1.1 Material choice and elastic isotropy . . . 166
6.1.2 Temperature dependence of the Brillouin shift . . . 170
6.1.3 Possible diffraction contribution to the acoustic linewidth . . . 170
6.1.4 Optomechanically induced transparency as a tool to measure mechanical detunings and linewidths . . . 172
6.1.5 Use of fused silica microresonators at cryogenic temperatures and saturation of two-level system damping . . . 173
6.1.6 Physics . . . 174
6.2 Transition from thermal Brillouin scattering to Brillouin lasing and the degree of second-order coherence . . . 177
6.3 Narrowband heralded single-photon source using spontaneous four-wave mixing in a whispering-gallery microresonator . . . 180
6.3.1 Phase matching . . . 184
6.3.2 Pair generation rate . . . 186
6.3.3 Setup and filtering scheme . . . 187
6.3.4 Measurements . . . 189

**A Optical ring resonator compendium** **192**

**Bibliography** **204**

# List of Figures


1.1 Quantum harmonic oscillator. . . . . 6
1.2 Canonical optomechanical system. . . . . 13
1.3 Simplified thermodynamic picture of cavity optomechanics. . . . . 16
1.4 Bulk phonon dispersion relation. . . . . 20
1.5 Phase velocity increase due to transverse guiding. . . . . 21
1.6 Displacement field of pseudo-longitudinal acoustic whispering-gallery mode of a sphere. . . . . 21
1.7 Optical whispering-gallery mode profiles. . . . . 24
1.8 Brillouin scattering schematically. . . . . 26
1.9 Stimulated Brillouin scattering scheme. . . . . 33
1.10 Brillouin phase matching in a waveguide. . . . . 36
1.11 Brillouin phase matching in a microresonator. . . . . 39
1.12 Optical and acoustic density of states scheme. . . . . 40
1.13 Optical density of states. . . . . 46
1.14 Kerr frequency comb. . . . . 50

2.1 Setup overview. . . . . 53
2.2 Tapered fiber with microrod resonator. . . . . 55
2.3 Resonator and tapered fiber mounts. . . . . 56
2.4 Cryogenic coupling setup. . . . . 57
2.5 Optical microscope image of a fused silica microrod resonator. . . . . 60
2.6 Example of an optical spectrum of a microresonator. . . . . 60
2.7 Fused silica microsphere. . . . . 61
2.8 Barium fluoride microrod resonators. . . . . 62
2.9 Thermal triangle with crossing of Brillouin lasing threshold. . . . . 64
2.10 Pound-Drever-Hall error signal. . . . . 66
2.11 Optical spectrum analyser recording of Brillouin lasing. . . . . 67
2.12 Optical balanced homodyne detection. . . . . 68

3.1 Optical and acoustic wave vectors and energy in microresonator Brillouin scattering. . . . . 74
3.2 Experimental setup for observation of strong coupling. . . . . 75
3.3 Optical power dependence of the detuning. . . . . 76
3.4 Heterodyne spectra of optomechanical strong coupling via Brillouin scattering. 90
3.5 Brillouin optomechanical coupling rate vs damping rates. . . . . 92
3.6 Heterodyne spectra with varying pump power. . . . . 93

3.7 Contour plots of optical spectra for different forms of the power dependence of the detuning and optomechanical coupling strength. . . . . 97

4.1 Scheme and setup used in the single-phonon addition/subtraction experiment. 108
4.2 Mean quadrature variance around the time of single-phonon addition and subtraction to a mechanical thermal state. . . . . 111
4.3 Simplified schematic of setup to implement single-phonon addition and subtraction to a mechanical thermal state. . . . . 118
4.4 Thermodynamic picture of multiple mechanical modes and reservoirs. . . . . 130
4.5 Correlation function for a multi-mode field. . . . . 133
4.6 Theory plot of quadrature distribution of phonon subtracted thermal state. . 136
4.7 Toy model of single-phonon subtraction from a thermal state. . . . . 137
4.8 Toy model of quadrature distribution measurement including optical loss. . . 138
4.9 Non-Gaussian quadrature distribution of phonon subtracted thermal state. . 141
4.10 Time evolution of non-Gaussian quadrature distribution. . . . . 142
4.11 Toy model fit to measured non-Gaussian quadrature distribution. . . . . 143

5.1 Illustration of the heterodyne measurement cooling protocol. . . . . 148
5.2 Oscillating variance due to finite heterodyne frequency. . . . . 154
5.3 Experimental setup for heterodyne-measurement-enhanced cooling. . . . . 157
5.4 Quantum trajectory of the mechanical mode obtained with simulated data for unfiltered and filtered shot noise at the detector. . . . . 160
5.5 Heterodyne-measurement enhanced cooling results. . . . . 161
5.6 Heterodyne-measurement-enhanced optomechanical cooling advantage compared to plain sideband cooling. . . . . 163

6.1 Dependence of acoustic phase velocity on propagation direction in a barium fluoride crystal. . . . . 167
6.2 Acoustic phase velocity over a whispering-gallery round-trip. . . . . 169
6.3 Sideband cooling to the ground state via Brillouin scattering. . . . . 175
6.4 Transition from thermal Brillouin scattering ("spontaneous") to Brillouin lasing in terms of the degree of second order coherence $g^{(2)}(0)$. . . . . 178
6.5 Optical heterodyne spectra below, just below, and above the Brillouin lasing threshold. . . . . 179
6.6 Heterodyne time trace of Stokes scattered light at the Brillouin lasing threshold. 181
6.7 Principle of spontaneous four-wave mixing. . . . . 182
6.8 Photon number distribution of the two-mode squeezed vacuum state for squeezing parameters $r = 0.05$ and $r = 0.5$. . . . . 184
6.9 Phase matching of four-wave mixing in a resonator. . . . . 185
6.10 Setup for the four-wave-mixing-based single photon source experiment. . . . 188

A.1 Scheme of the coupling between a side channel and a microresonator modelled through a lossless beam splitter. . . . . 193
A.2 Undercoupling, critical coupling and overcoupling to an optical resonator. . . 195

# List of Tables

3.1 Parameters achieving Brillouin optomechanical strong coupling. . . . . 94

4.1 Parameters for single-phonon addition/subtraction to a mechanical thermal state. . . . . 110

# Chapter 1

# Introduction

In this chapter the key concepts are introduced and described which serve to provide a foundation for the later results chapters.

This thesis explores the nonlinear optical phenomenon of Brillouin scattering in the context of cavity optomechanics. Experiments were carried out with whispering-gallery microresoantors to demonstrate some interesting cavity-optomechanical phenomena, mediated by the electrostrictive coupling associated with Brillouin scattering.

Brillouin scattering is a widely-studied phenomenon in the non-linear optics community, in particular in non-linear fiber optics, however was only fairly recently demonstrated in whispering-gallery-mode optical microresonators, when Brillouin lasing was observed by two groups in 2009 [TC09; GMM09]. Most studies in this area are younger than 10 years.

This thesis work continues this line of research and shall make a contribution to establishing Brillouin cavity optomechanics with high-frequency phonons in whispering-gallery resonators as a platform for experimental quantum science. Here I present some useful theoretical background, although to an expert in the field the results should be understandable as self-contained.

## 1.1 Quantum mechanics - basic theory

### 1.1.1 Closed quantum systems

As of 2019 quantum mechanics in all its facets represents the backbone of our fundamental theory of nature, and as of today there are no known experimental observations at odds with its predictions. In the non-relativistic regime, the fundamental equation of quantum mechanics is the Schrödinger equation, the equation of motion for the quantum wave function $\psi$.

$$i\hbar\frac{\partial}{\partial t}\psi = \hat{H}\psi \tag{1.1}$$

where $\hat{H}$ is the Hamiltonian operator, i.e. the quantized version of the total energy function of the system at hand. The Hamiltonian operator thus governs the complete time evolution of a system and this time evolution is deterministic. This assumes that all parts and degrees of freedom comprising the system are described and represented in the Hamiltonian, i.e. the quantum system is isolated from its environment. While for some quantum systems this closed quantum system description is a good one, in many scenarios and especially in the context of cavity quantum optomechanics the coupling of the system's degrees of freedom to the environment can't be neglected. The term "the environment" is used to describe the many degrees-of-freedom that couple to and "surround" the system of interest for which we have no control over, and only statements about averages can be made. A quantum system, in which the coupling to the environment (in this context also often called "heat bath" or "reservoir") can't be neglected, we call *open*.

Alternatively to the above description in terms of a wave function in the so-called Schrödinger picture, a different approach to quantum dynamics has been formulated by Heisenberg, in which the time evolution of a quantum system is carried by the observables, represented through Hermitian operators, while the quantum state is constant. Dirac showed that these approaches are, in fact, equivalent, as in that they make the same predictions about outcomes of experiments. The equation of motion in the Heisenberg picture is

the Heisenberg equation for time evolution of the observable $\hat{O}$

$$\frac{d}{dt}\hat{O} = \frac{i}{\hbar}[\hat{H}, \hat{O}] + \frac{\partial}{\partial t}\hat{O} \ . \tag{1.2}$$

where [ , ] stands for the commutator of operators.

While there is no doubt that the results obtained through application of the mathematical formalism of quantum mechanics is in excellent agreement with observations of nature (e.g. different flavours of quantum field theories regularly get praised for being the best theory ever invented by humans), there is vast disagreement among experts about what the theory means and what it actually says about the nature of the world[1]. Many working physicists have therefore adopted the standpoint to not worry too much about the meaning as long as the formalism makes correct predictions. Nevertheless it is important to keep the various interpretations in mind, as some might turn out more fruitful than others for advancing our understanding in the face of new evidence.

At risk of falling down a rabbit hole of mumbo-jumbo, very pictorially one could say: At the fundamental level the natural world seems to possess both discrete (particle-like) and continuous (wave-like) aspects, united. Associated with this is a scale at which the acquisition of what one would classically call "full information" about the state of a system (or the so-called reality) is principally impossible. Or alternatively: One can't find out anything about the state of the world without profoundly disturbing it in the process of acquiring the information. This comes for example with far-reaching consequences like: The future is impossible to predict, since we can't determine the present.

### Measurements in quantum mechanics

Quantum mechanics as a mathematical theory was rigorously developed in the second half of the 1920's and there are some axioms at the core of the mathematical formulation, which were introduced by Dirac [Dir30] and von Neumann [vNeu32], working closely with many

[1] see e.g. [SKZ13]

others. Here, only a short overview will be given.

The quantum state: the (pure) state of a physical system is represented by a vector in a complex Hilbert space. When working in the position representation this space can be thought of as the space of square integrable functions, in which all possible wave functions solving Schrödinger's equation 1.1 live. Cases of finite, infinite-countable and infinite-uncountable dimensions of Hilbert spaces are all frequently found in quantum physics.

The usual way of describing the process of measurement, known as the measurement postulate, is as follows. While Schrödinger's equation 1.1 is deterministic in governing the time evolution of a quantum system in a pure state, a very different time evolution is encountered upon measurement of a system. This is thought of when a microscopic system in a quantum state interacts with a (classical) measurement apparatus, such that the large classical measurement apparatus records a measurement outcome readable for the experimenter. Of course this separation into some parts of the natural world being described by quantum mechanics and others by classical mechanics is, some have argued, arbitrary and artificial. As a matter of fact, the experimenter will always measure only eigenvalues of the operator representing the observable quantity he/she is measuring, independent of the input state. Which eigenvalue is found, is as of current understanding purely random, and the probabilities are given by the squares of the amplitude overlap between the state prior to measurement $\psi$ and the eigenstate associated with the obtainable eigenvalues $\phi_n$, i.e. the probability to find eigenvalue $n$ is given through $p_n = |\langle\psi|\phi_n\rangle|^2$. This is called Born's rule, after physicist Max Born, who suggested the statistical interpretation of the wave function [Bor26].

One crucial aspect of quantum physics lies in the fact that its governing equation of motion, the Schrödinger equation, is linear, and therefore allows for superpositions of solutions to also represent solutions. This describes the observation that, prior to a measurement, a system can indeed be found in a superposition of different eigenstates of that observable.

### 1.1.2 Modes, quantisation, and the quantum harmonic oscillator

In this work the notion of a mode will be of utmost importance. It is a term with many aspects and uses in physics and we will give a working definition here. A mode is a self-consistent field (also displacement field) configuration solving a linear wave equation. Its excitation can be mathematically treated as a harmonic oscillator.

Its significance stems from the fact that any physical system that is in a stable equilibrium around a minimum of the potential energy, responds harmonically (i.e. like a harmonic oscillator) when displaced from equilibrium, in the limit of small displacements. This can simply be seen from doing a Taylor expansion of the potential function around a local minimum, where the lowest order terms will be a constant plus a parabola. As a constant in the potential energy doesn't affect the dynamics (the force is given by the derivative of the potential energy), the parabolic (harmonic) potential is the lowest order term that needs to be considered.

When treated quantum mechanically, a quantisation procedure leads to a description of the modes formally equivalent to a collection of quantum harmonic oscillators. This holds true for both the electromagnetic field (see e.g. [GL91; MW95; GW96; Lou00; WM08; DH14]), as well as for acoustic/elastic waves (see e.g. [Fre32; Yar65; SS16; ZH16]).

The Hamiltonian of the harmonic oscillator is

$$\hat{H} = \frac{\hat{p}^2}{2m} + \frac{1}{2}m\omega^2\hat{x}^2 \tag{1.3}$$

where $\hat{p}$ is the momentum operator, $m$ the mass, $\omega$ the oscillator's eigenfrequency and $\hat{x}$ the position operator.

It can be shown that the spectrum of this Hamiltonian is a ladder of equidistant energy levels, starting at the lowest energy state $E_0 = \frac{1}{2}\hbar\omega$ (the ground state) which possesses a finite energy. The next energy levels have increasing energy in steps of $\hbar\omega$.

One can define raising and lowering operators which can be expressed in terms of the

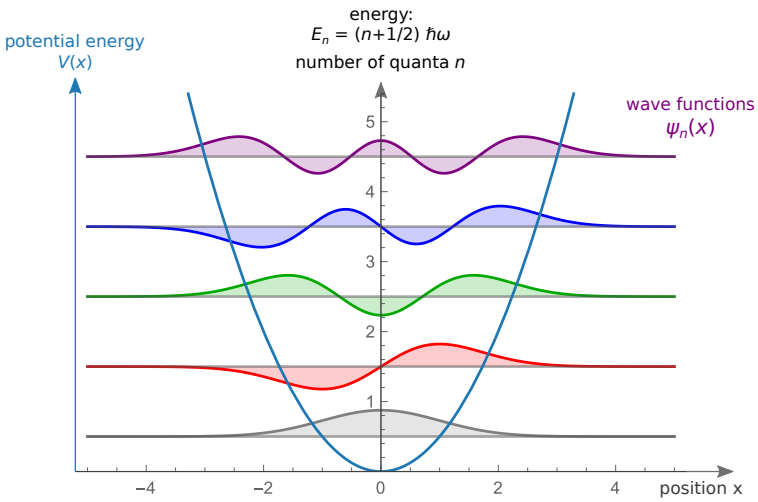


Figure 1.1: Potential energy function, and energy eigenfunctions (Fock state wave functions) of the first few states starting from the ground state of the quantum harmonic oscillator. The spectrum is an equidistant ladder with the ground state possessing a finite energy of half a quantum. Bosonic modes (as those of light and sound) are described by the quantum harmonic oscillator, and their quanta are called photons and phonons, respectively.

position and momentum operators, and take one from an energy eigenstate to the next higher/lower one. They are given through

$$a = \frac{1}{\sqrt{2}}\,(X + iP) \tag{1.4}$$

$$a^\dagger = \frac{1}{\sqrt{2}}\,(X - iP)\ , \tag{1.5}$$

where $X$ and $P$ are the dimensionless position and momentum operators of the oscillator, which are linked to the position and momentum operators $x$ and $p$ via $x = \sqrt{\hbar/(m\omega)}X$ and $p = \sqrt{\hbar m\omega}P$. So $X$ describes the displacement of the oscillator in the natural units of the zero-point fluctuation.

Using these, the Hamiltonian can be rewritten as

$$\hat{H} = \hbar\omega(\hat{a}^\dagger\hat{a} + 1/2)\ . \tag{1.6}$$

Its eigenvalues are the energies $E_n = n\hbar\omega + 1/2$.

A mode in the state with eigenvalue $E_n$ in quantum field theory is then said to be excited

with $n$ quanta, and is labelled by $n$ which is the eigenvalue of the number operator $n = a^\dagger a$, and we call it a number state (or Fock state) represented by the ket $|n\rangle$, with $\hat{n}|n\rangle = n|n\rangle$.[2]

### 1.1.3 Open quantum systems

We now come to the common scenario where the presence of an environment interacting with the system of interest can't be neglected. In general it can be said that we have little or no control over the degrees of freedom of the reservoir and that the number of degrees of freedom is very large. The uncontrollable interaction with the reservoir has the tendency of (from the experimenter's perspective) reducing the "quantum coherence" in the system, such that its quantum features decay with time. This disappearance of quantum coherence is, according to decoherence theory, only apparent. The coherences persist between the enormous number of degrees of freedom of the uncontrollable bath, and the degrees of freedom of the system under study. In line with the fluctuation-dissipation theorem, the bath will both excite and attenuate the system in an unpredictable way, only obeying stochastic laws [CW51]. In cavity quantum optomechanics, the mechanical mode couples to its surrounding environment, which causes rethermalization and decoherence of the mechanical motion.

We can divide the approaches to open quantum systems into two categories, one starting from the Schrödinger picture, and the other starting from the Heisenberg picture of quantum mechanics. The first route builds on the concept of the so-called density operator (or statistical operator) $\rho$, which unites the framework of statistics theory with the quantum state of Schrödinger's equation (classical probabilities are assigned to each pure quantum state of the system). This approach is very powerful and general. The density operator's time evolution is then described in terms of a master equation, which is a first order differential equation over time.

The second route starts from the Heisenberg picture and introduces randomness/noise into the equations of motion by randomly fluctuating operators, the Langevin operators

[2]Hats to distinguish between operators and conventional variables will not be used unless strictly necessary for clarity.

[BR97]. The Langevin equations have a simple intuitive interpretation akin to classical equations of motion.

Both approaches to open quantum systems will be drawn from in this thesis.

### Quantum Langevin equations

The extension of the Heisenberg picture to describe the open quantum systems leads to quantum Langevin equations. For an optical cavity mode coupled to a (heat) bath the field operator dynamics are governed by

$$\dot{\hat{a}} = -\kappa\hat{a} + \frac{i}{\hbar}[\hat{H}, \hat{a}] + \sqrt{2\kappa}\hat{a}_{\text{in}} \tag{1.7}$$

where $\hat{a}$ is the cavity mode operator, $\kappa$ its amplitude damping rate, $\hat{H} = \hbar\omega(\hat{a}^\dagger\hat{a} + 1/2)$ the system Hamiltonian, and $\hat{a}_{\text{in}}$ the input noise (or Langevin) operator. This equation closely resembles a classical equation of motion for the amplitude of an oscillator under dissipative conditions, with the added element of quantum noise. More generally than optics, often it can be assumed that the bath has a certain temperature, and is $\delta$-correlated, i.e. fulfilling

$$\langle\hat{a}^\dagger_{\text{in}}(t)\hat{a}_{\text{in}}(t')\rangle = \bar{n}\delta(t - t') \tag{1.8}$$

$$\langle\hat{a}_{\text{in}}(t)\hat{a}^\dagger_{\text{in}}(t')\rangle = (\bar{n} + 1)\delta(t - t') \ , \tag{1.9}$$

where $\bar{n}$ is the mean number of quanta per degree of freedom in the thermal reservoir.

### The density operator

The concept of the density (or statistical) operator $\hat{\rho}$ to describe the quantum state of a system unites the frameworks of statistical mechanics and that of the dynamics of pure quantum states as governed by the Schrödinger equation 1.1. The density operator can be defined by writing

$$\hat{\rho} = \sum_i p_i|\psi_i\rangle\langle\psi_i| \ \ , \tag{1.10}$$

where $p_i$ is the (classical) probability that the experimenter assigns to finding the system in the pure quantum state $|\psi_i\rangle$. The statistical operator thus holds the information at any moment in time about a statistical mixture of quantum states. The density operator contains all the information available to the experimenter about the state of the system at a particular instance in time. Different observers, observing the same quantum system, will in general have different records and different density operators associated with the state of the system, as they both have incomplete information. The density operator therefore doesn't represent some fundamental truth about the universe, but rather incorporates all information an observer has about the state of a system.

### von Neumann equation

The von Neumann (or Liouville-von Neumann) equation derives directly from the Schroedinger equation and describes how the density operator evolves in time. By combining equations 1.1 and 1.10 one finds

$$\frac{\partial \hat{\rho}}{\partial t} = -\frac{i}{\hbar}\left[\hat{H}, \hat{\rho}\right] \tag{1.11}$$

which applies to a closed quantum system in a mixed state. Although formally very similar except for a different sign, this equation should not be confused with the Heisenberg equation 1.2, which describes the time evolution of observable quantities.

### Master equations

In order to incorporate open system dynamics in the density operator formalism, quantum master equations were developed. They include dissipation or decoherence terms, typically obtained via an approximation of the many degrees of freedom a system couples to. The effect of this coupling to the inaccessible environment is often the disappearance over time of any quantum coherence that the system might originally possess. This effect manifests itself typically as a reduction in the off-diagonal elements in the matrix representation of the density operator. Compared to classical master equations the quantum master equations

also include the time evolution of off-diagonal elements of the density operator (the system's "coherences"). Master equations are discussed in detail for example in references [Car93; BP02; GZ04].

A simple master equation approximating dynamics fulfilling the Markov property (memoryless stochastic process) is given by the master equation in Lindblad form

$$\frac{d\rho(t)}{dt} = -\frac{i}{\hbar}[H, \rho(t)] + \frac{1}{2\hbar}\sum_j \left([V_j\rho(t), V_j^\dagger] + [V_j, \rho(t)V_j^\dagger]\right) \quad , \tag{1.12}$$

where $V_j$ describe the coupling between the system and the environment.

An introduction to the use of master equations in the context of cavity quantum optomechanics can be found in [MW11].

### Stochastic master equations

Master equations can also be generalised to include a continuous measurement made on the quantum system. In this thesis, such stochastic master equations are used to describe dynamics of a continuously monitored optomechanical system.

The theory draws from stochastic calculus, in particular Itô calculus. The foundations of this approach are discussed e.g. in [JS06; WM09]. At the core of Itô calculus is a new chain rule, Itô's lemma. Essentially, there is a new differential element $dW$ introduced, representing white noise. For this differential and the conventional time differential $dt$ the following pedestrian rules apply: $dW^2 = dt$ and $dt^2 = 0$, and $dtdW = 0$. We can apply this such that we count $dW$ as if it was $dt^{1/2}$ when deciding which terms to keep in expansions of functions of the differentials.

A generic stochastic master equation can be written in the form

$$d\hat{\rho} = \frac{1}{i\hbar}[\hat{H}, \hat{\rho}]dt + \mathcal{L}_{\text{env}}\{\hat{\rho}\}dt + \sqrt{\eta}\mathcal{H}[\hat{c}]\{\hat{\rho}\}dW \ , \tag{1.13}$$

where $\rho(t)$ describes a "quantum trajectory" that the system follows in one particular ex-

perimental iteration. $\mathcal{L}_{\text{env}}$ is the Liouville superoperator, describing the system-environment interaction, $\mathcal{H}[\hat{c}]$ is the measurement superoperator, and $dW$ the Itô differential, which incorporates the stochasticity into the mathematical description.

The stochastic master equation will be used in chapter 5 and more details will be given there.

## 1.2 Cavity quantum optomechanics

Generally speaking, cavity quantum optomechanics deals with the parametric coupling between mechanical degrees of freedom and an optical field. Under commonly found conditions, the light field's quantum character is readily observable, while the mechanical degrees of freedom's quantum properties are somewhat hidden because of the hot environment (hot in a quantum sense). As early as 1967 Braginsky and Manukin [BM67] realised the effects of the momentum carried by photons in an optical interferometer, thus being one of the first works in the direction of optomechanics. Here we are going to give a general introduction of some important concepts. A nice introduction to the field of cavity optomechanics can be found in the review article by Aspelmeyer, Marquardt and Kippenberg [AKM14].

Some of the main goals of the quantum optomechanics community include non-classical mechanical state generation, and studies of quantum decoherence with massive objects, on the fundamental side, as well as a large number of applied research directions which fit into the quantum technology realm, e.g. microwave-to-optical conversion and high-precision force sensing.

In these endeavours heating due to optical absorption and surface effects [Eic+09], e.g. in silicon nanodevices, has presented a major challenge. A good figure of merit when evaluating how well a mechanical oscillator performs with respect to reaching the quantum domain is obtained by comparing its frequency to the decoherence rate, corresponding to the rate at which quanta "flow in" from the thermal environment. This gives the number of coherent oscillations, and it is proportional to the so-called $Q \times f$ product:

$$\frac{\omega}{2\bar{n}_{\mathrm{th}}\gamma} \underset{\bar{n}_{\mathrm{th}}>1}{\approx} \frac{\omega}{2\frac{k_{\mathrm{B}}T}{\hbar\omega}\gamma} = \frac{\hbar}{k_{\mathrm{B}}} \cdot \frac{1}{T} \cdot \frac{\omega^2}{2\gamma} \propto Q_{\mathrm{m}} \cdot \omega \ . \tag{1.14}$$

Here $\omega$ is the angular eigenfrequency, $\bar{n}_{\mathrm{th}}$ is the thermal mean phonon number, $\gamma$ is the amplitude decay rate in angular frequency units, and $Q_{\mathrm{m}}$ is the mechanical quality factor.

So from this perspective, the quantum prospects of a mechanical oscillator, at a given environment temperature $T$, are well measured by the $Q \times f$ product, and it is highly desirable to improve mechanical $Q \times f$ products.

This thesis introduces a new experimental platform and makes significant advances towards these highly sought goals. For the platform presented here, at room temperature $Q \times f$ is already of the same order of magnitude as $k_{\mathrm{B}}T/h \approx 6 \cdot 10^{12}$, thus offering comparable performance at room temperature in this regards as the system presented, for example, in [NMG16]. Towards cryogenic temperatures of $\approx 4$ K, as both $T$ decreases and $Q_{\mathrm{m}}$ is expected to increase, the system presented here will lie deep within the low decoherence regime. Additionally, the backscattering geometry and high mechanical frequency have the big advantage that the signal can be separated more easily from the pump light than in systems where pump and signal fields are co-propagating or scattered light is spectrally closely adjacent to the pump fields. While the mechanical $Q \times f$ product in Brillouin scattering at a particular temperature is frequency independent (i.e. the same for all light colours and for forward and backward Brillouin scattering), the aforementioned comparison applies between backward and forward Brillouin scattering platforms [Bah+12; Don+15].

### 1.2.1 Radiation pressure coupling in a Fabry-Perot resonator

The canonical example system in cavity optomechanics consists of the Fabry-Perot resonator where one of the cavity mirror's center of mass is considered harmonically bound (see figure 1.2).

For the following discussion of the Hamiltonian that the system comprises, we will consider only a single optical mode and a single mechanical mode. In this configuration, the

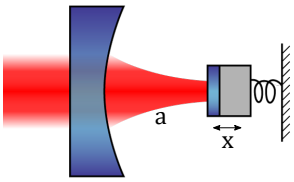


Figure 1.2: Canonical optomechanical system. An optical field within a Fabry-Perot cavity is coupled parametrically via radiation pressure to the center-of-mass motion of one of its mechanically compliant end mirrors. [Image adapted from CC Schmoele.]

eigenfrequency of the optical cavity mode will depend on the cavity length $L$, and thus any displacement of the suspended mirror from the equilibrium length of the cavity $L_0$ will give rise to a frequency shift of the optical frequency. This gives rise to an optomechanical coupling as we will see in the following pedestrian-level derivation:

Let's start with the free Hamiltonian $H = \hbar\omega_\mathrm{l} a^\dagger a + \hbar\omega_\mathrm{m} b^\dagger b$, where $a$ and $b$ represent the optical and mechanical field operators, respectively, and $\omega_\mathrm{l}$ and $\omega_\mathrm{m}$ are the optical cavity and mechanical mode's eigenfrequencies. Then the eigenfrequency of the $N$th longitudinal optical mode is given through $\omega_\mathrm{l} = 2\pi N \cdot \frac{c}{2L} = \frac{\pi N c}{L_0 + x}$, which we can expand in a Taylor series for small $x/L_0 \ll 1$, giving

$$\omega_\mathrm{l} = \omega_0 - \omega_0 \cdot \frac{x}{L_0} + \mathcal{O}((x/L_0)^2) \ , \tag{1.15}$$

where $\omega_0 = \pi N c/L_0$ is the undisturbed optical eigenfrequency.

Then, using $x = x_\mathrm{zpf}(b + b^\dagger)/\sqrt{2}$, with the mechanical zero-point fluctuation $x_\mathrm{zpf} = \sqrt{\hbar/(2m\omega_\mathrm{m})}$, we obtain a Hamiltonian containing an optomechanical coupling term

$$H = \hbar\omega_0 a^\dagger a + \hbar\omega_\mathrm{m} b^\dagger b + \hbar g_0 a^\dagger a (b + b^\dagger) \ , \tag{1.16}$$

where $g_0 = \frac{\omega_0}{2L_0}\sqrt{\frac{\hbar}{m\omega_\mathrm{m}}}$ is the optomechanical coupling rate.

While this coupling mechanism and derivation is frequently found in optomechanics, we will later discuss a different kind of coupling, which is found in Brillouin optomechanics.

In addition to the (coherent) optomechanical coupling rate, and the mechanical frequency, other important quantities in cavity optomechanics are the damping (or decay) rates of the optical and mechanical modes, associated with the (incoherent) coupling of these modes to their respective environments. Coupling itself is, by nature, always coherent, but the lack of control over the degrees of freedom makes it appear incoherent. The optical damping rate $\kappa$ can be attributed to loss through scattering, absorption or coupling to the side channel (tapered optical fiber) in this work. For the mechanical/acoustic damping rate, we typically write $\gamma$. It describes the loss rate of phonons from the mode of interest to the environment via absorption or scattering. We will use the convention of amplitude decay rates throughout this thesis, if not otherwise stated.

### 1.2.2 Resolved sideband regime

While the frequency of the electromagnetic field is generally (in optomechanics) much higher than the mechanical frequencies (typically 100's THz optical frequency versus typically kHz to GHz regime of the mechanical frequency) the optical cavity linewidth can be larger or smaller than the mechanical frequency, depending on the physical platform. The former case, when the optical cavity lifetime is shorter than a mechanical oscillation period, is frequently named the "unresolved sideband regime" (or "bad cavity regime"), while the latter case is called the "resolved sideband regime". In the resolved sideband regime, the condition

$$\omega_{\mathrm{m}} \gg \kappa \tag{1.17}$$

applies. A valid picture here, is to imagine the motion of the cavity mirror phase modulating the optical field leading to sidebands in the optical spectrum.

This regime is well studied for optomechanical laser cooling (also referred to as sideband cooling or back-action cooling) [Wil+07; Mar+07; Riv+11; Teu+11; Cha+11], state transfer [PK99; ZPB03; Pal+13], which can be applied in a configuration such that the optomechanical system implements a quantum memory [Nun+08], all associated with red

detuned drive fields, and the generation of correlation and entanglement [Lee+11; Rie+18] when used in combination with measurement, associated with driving blue-detuned. Also the phenomenon of optomechanically induced transparency (OMIT) [Wei+10; Don+15] is associated with this regime.

Importantly, the interaction Hamiltonian can be made to take the form of a beam-splitter or two-mode squeezer type Hamiltonian in the resolved sideband regime, which is of great importance for the results parts of the thesis, and will be further discussed in section 1.5.4.

### 1.2.3 Unresolved sideband regime

In the unresolved sideband regime, where the optical cavity lifetime is shorter than the mechanical oscillation period, or equivalently the cavity linewidth is larger than the mechanical frequency

$$\kappa \gg \omega_{\mathrm{m}} \ , \tag{1.18}$$

some physical schemes include quantum-nondemolition measurement of mechanical position via optical pulses [Van+11] or the cooling of the mechanical mode by measurement and feedback (cold damping) which recently culminated in the cooling of a membrane to the quantum ground state [Ros+18].

This thesis focuses on the resolved sideband regime, which is readily deeply reached with the very large mechanical frequencies ($\approx 10$ GHz) in Brillouin backscattering and the narrow optical linewidths ($\approx 1$ MHz) of fused silica and crystalline whispering-gallery resonators.

### 1.2.4 Thermodynamic picture of cavity optomechanics

When dealing with coupled oscillators, it can be helpful to draw pictograms of the thermodynamic arrangement of the modes and all relevant heat baths that they are coupled to, especially as the coupling to the thermal environment is a major point of concern in almost all experimental studies of quantum optomechanics. The thermodynamic picture for a single

optical and mechanical whispering-gallery mode of the microresonator (see section 1.3), as used in this work, is shown in figure 1.3.

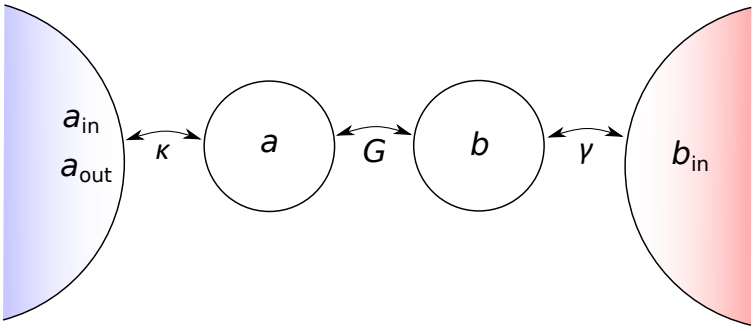


Figure 1.3: Simplified thermodynamic picture of cavity optomechanics. A single optical mode with annihilation operator $a$ and a single mechanical mode with annihilation operator $b$ are coupled to each other via an optomechanical coupling rate $G$, and to the environment via their respective damping rates $\kappa$ and $\gamma$. While the thermal occupation of the environment at the mechanical frequency may be large, that of the optical input mode is practically zero at room temperature.

## 1.3 Whispering-gallery waves

First, the phenomenon of whispering galleries was discovered for acoustic waves in air, when people realised that certain concave, curved structures would guide the sound of spoken or whispered word. The first to scientifically examine the effect (and giving it its name) was Lord Rayleigh [Str78], using the dome of St. Paul's cathedral in London. Here the pressure wave is guided along the smooth, concave wall, making the sound pressure level decay much slower than the usual inverse distance squared scaling. This makes it possible to hear the whispers of a person normally too far away, if the sound source (mouth) and detector (ear) are placed close to the wall.

The first studies on the phenomenon were done with acoustic (i.e. sound) waves. In gases there is only pressure waves (no shear waves), such that the displacement in a continuum picture is always longitudinal with the propagation direction. For the experiments presented in this work, optical whispering-gallery microresonators which at the same time support elastic whispering-gallery waves have been used. Here we shall introduce some physical

background to these wave phenomena.

### 1.3.1 Elastic waves

In the glass and crystalline resonators used in this work, there is an analogous phenomenon of the elastic wave nature[3]. In a general (elastically non-isotropic) crystalline solid, in the bulk of the material, for a particular propagation direction, there are three different stationary plane wave solutions to the elastic wave equation. A (quasi-)longitudinal wave which generally has the highest velocity, and two transverse waves (a slow and a fast one).

Generally speaking, the phase velocity of these elastic waves depends on the propagation direction. In isotropic solids there is no such directional dependence. Fused silica, as used in this work, and more generally glasses provide an example of elastically isotropic materials. Interestingly, while the cubic crystal structure is optically isotropic, it is not elastically isotropic. There is no elastically isotropic crystal structure. This is related to the symmetries of the elastic tensor, which is a fourth rank tensor, compared to those of the dielectric tensor, which is a second rank tensor.

Hooke's law of elasticity in a homogeneous, but generally anisotropic, elastic medium, which is valid in the limit of small displacements, reads

$$\sigma_{ij} = C_{ijkl}\epsilon_{kl} = C_{ijkl}\frac{\partial u_k}{\partial x_l} \ , \tag{1.19}$$

where $\sigma_{ij}$ is the stress tensor, $\epsilon_{kl}$ the strain, $C_{ijkl}$ the stiffness (or elastic constant) tensor, and $u_i$ the displacement, and we use the Einstein summation convention of summing over repeated indices.

Cauchy's elastodynamic equation, which can be obtained from Newton's second law applied in a continuum setting, for the displacement vector $\vec{u}$ (the elastic wave equation)

[3]Note on nomenclature: Within this thesis, the terms "mechanical", "elastic wave", "acoustic"/"acoustic wave", or "sonic"/"sound" are frequently used interchangeably, and it is herewith pointed out that they always refer to the wave phenomena as described in this section, i.e. pseudo-longitudinal elastic waves guided by a convex boundary, analogous to the well-known whispering-gallery waves in the acoustic and optical domains.

then reads

$$\rho \frac{\partial^2 u_i}{\partial t^2} - C_{ijkl} \frac{\partial^2 u_k}{\partial x_j \partial x_l} = 0 \ , \tag{1.20}$$

where $\rho$ is the density of the medium, and absence of external forces is assumed.

Making a plane wave ansatz for solving the elastic wave equation, in the form $u_i = U p_i \exp(i\omega(t - \vec{n} \cdot \vec{x}/v)$, where $p_i$ is a polarisation unit vector, $\vec{n}$ is a unit vector giving the propagation direction, and $v$ is the phase velocity of the wave, we obtain from equation 1.20 the Christoffel equation

$$(M_{ij} - \rho\omega^2 \delta_{ij}) p_j = 0 \ , \tag{1.21}$$

for a monochromatic plane wave with wave vector $q$, polarisation $p_j$, frequency $\omega$, through a medium with density $\rho$, where $M_{ij} = q_k C_{iklj} q_l$ is the Christoffel matrix.

In this work we are mainly interested in isotropic media (amorphous silica) or almost isotropic media (crystals with cubic lattice), whose elastic tensors have few independent components. By general symmetry considerations the $3^4 = 81$ components of the elastic tensor $C_{ijkl}$ reduce to $\frac{1}{2} \cdot 6 \cdot (6+1) = 21$ independent components. Isotropic media like fused silica have only two independent parameters , and it can be written in Voigt notation[4] as

$$C_{\alpha\beta} = \begin{pmatrix} K + \frac{4}{3}\mu & K - \frac{2}{3}\mu & K - \frac{2}{3}\mu & 0 & 0 & 0 \\ K - \frac{2}{3}\mu & K + \frac{4}{3}\mu & K - \frac{2}{3}\mu & 0 & 0 & 0 \\ K - \frac{2}{3}\mu & K - \frac{2}{3}\mu & K + \frac{4}{3}\mu & 0 & 0 & 0 \\ 0 & 0 & 0 & \mu & 0 & 0 \\ 0 & 0 & 0 & 0 & \mu & 0 \\ 0 & 0 & 0 & 0 & 0 & \mu \end{pmatrix} \ , \tag{1.22}$$

where $K$ is the bulk modulus, and $\mu$ is the shear modulus, while materials with cubic crystal

[4]Voigt notation is the mapping of indices ($ij \to \alpha$): $(11 \to 1)$, $(22 \to 2)$, $(33 \to 3)$, $(23, 32 \to 4)$, $(31, 13 \to 5)$, and $(12, 21 \to 6)$.

symmetry have three independent parameters, and their stiffness tensor can be written as

$$C_{\alpha\beta} = \begin{pmatrix} C_{11} & C_{12} & C_{12} & 0 & 0 & 0 \\ C_{12} & C_{11} & C_{12} & 0 & 0 & 0 \\ C_{12} & C_{12} & C_{11} & 0 & 0 & 0 \\ 0 & 0 & 0 & C_{44} & 0 & 0 \\ 0 & 0 & 0 & 0 & C_{44} & 0 \\ 0 & 0 & 0 & 0 & 0 & C_{44} \end{pmatrix}, \tag{1.23}$$

with $C_{44} = \mu$.

The eigenvalue problem of solving Christoffel's equation results in, for each and every distinct propagation direction, three polarisations and corresponding wave velocities, of which two are of transverse character, and one of longitudinal character. We are here only interested in the quasi-longitudinal waves. They possess the highest phase velocity, and thus highest frequency at given wave number.

**Elastic wave dispersion relation**

The dispersion relation, i.e. the connection between the angular frequency $\omega$ and wave-vector $k$ of an elastic wave, characterizes the propagation behaviour, as it contains the information about the speed of sound (phase velocity $v_{\mathrm{ph}} = \omega/k$ ) and group velocity of a pulse ($v_{\mathrm{gr}} = d\omega/dk$). It is generally obtained from solving the elastic wave equation 1.20 for a given geometry and material.

In Brillouin scattering with visible and near infrared light, the acoustic wavelength, being approximately half the optical wavelength (1550 nm used in this work), is much longer than the intermolecular spacing in the glass/crystal. This is equivalent to saying the waves fall into a part of the Brillouin zone close to the origin, where in a simple chain model of acoustic waves the dispersion relation is to a good approximation linear. It's widely agreed that in this regime (elastic wavelength much longer than the intermolecular spacing) the concept of phonons is well-defined even for disordered media like fused (vitreous) silica [TE97].

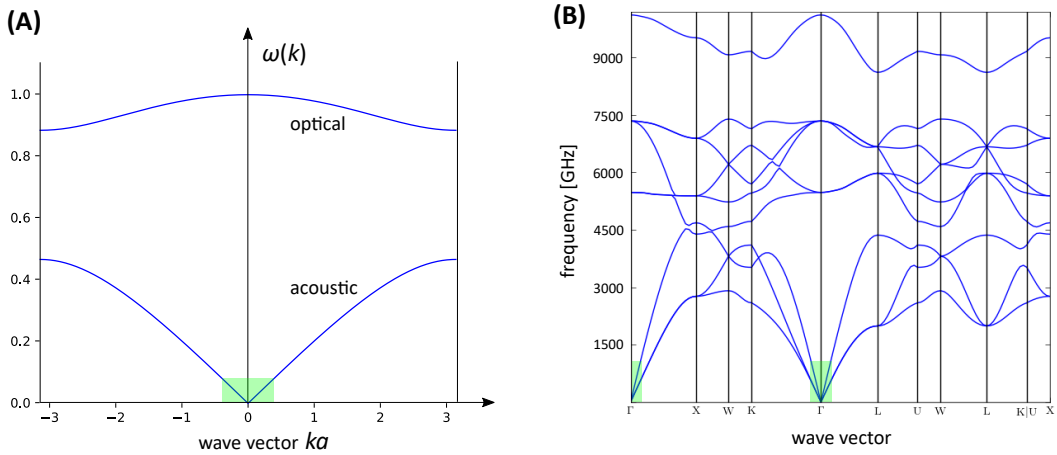


Figure 1.4: Phonon dispersion relation: Frequency $\omega(k)$ as a function of wavenumber $k$ in the first Brillouin zone. (A) Simple phonon dispersion in a 1D two-atomic chain, with mass ratio 3.6. (B) Phonon dispersion in $BaF_2$ along directions of high symmetry (adapted from [Jai+13]). Comparable calculations for fused silica have revealed phonon-like behaviour and pseudo-zone boundaries [TE97]. The dispersion relation for acoustic phonons in bulk Brillouin scattering is approximately linear. Relevant frequency and wavenumber ranges are shaded green (not to scale).

In the proximity of material boundaries, or if the elastic waves are confined in the lateral direction, the acoustic wave dispersion relation is altered from the linear bulk relation of figure 1.4 to a relation that has a low frequency (= long wavelength) cut-off. This can be intuitively understood from the fact that once the wave is laterally confined, the transverse component of its wavevector $k_\perp$ cannot take arbitrarily low values, such that the wavenumber $|k| = \sqrt{k_z^2 + k_\perp^2}$ obtains a lower bound. This then results in the phase velocity $v_{\mathrm{ph}} = \omega/k_z$ obtaining higher values than the phase velocity of a plane wave in the bulk material for the same propagation constant $k_z$ (component of the wavevector in the propagation direction), see figure 1.5. An exact dispersion relation for acoustic whispering-gallery modes within the theory of elasticity was obtained in [SB15b]

### Types of elastic whispering-gallery waves

In a whispering-gallery resonator made of an elastic solid, there exist a few types of waves of whispering-gallery character, guided by the material boundary. We can distinguish in decreasing order of their typical phase velocities: (pseudo-)longitudinal waves [SB15b], shear-

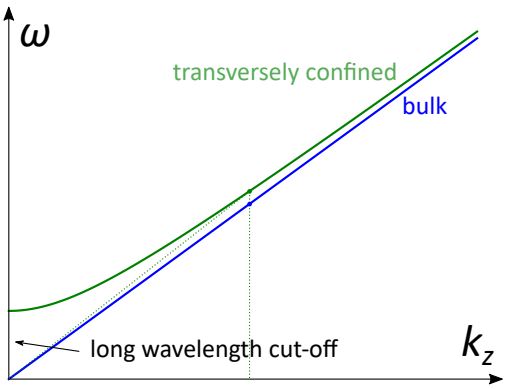


Figure 1.5: Phase velocity $\omega/k_z$ increase due to transverse guiding/confinement of sound waves. In the whispering-gallery geometry $k_z$ is replaced by $k_\phi = M/R$, the component of the wave-vector in the azimuthal direction.

polar waves, and Rayleigh-type surface acoustic waves (where the atoms at the surface follow elliptic trajectories). For the purpose of this work we focus on the highest velocity pseudo-longitudinal whispering-gallery waves, as they are believed to have the largest electrostrictive coupling to optical modes, and are responsible for stimulated Brillouin scattering in microresonators [TC09; GMM09]. Some numerical analyses were performed in [Zeh+11] for whispering-gallery waves in isotropic spheres, and a more detailed theoretical analysis was performed in [SB15b], which included the derivation of closed-form expressions for spheres and cylinders. Figure 1.6 shows a result from this study, for a sphere, which has similarity with the whispering-gallery modes used in the context of this work.

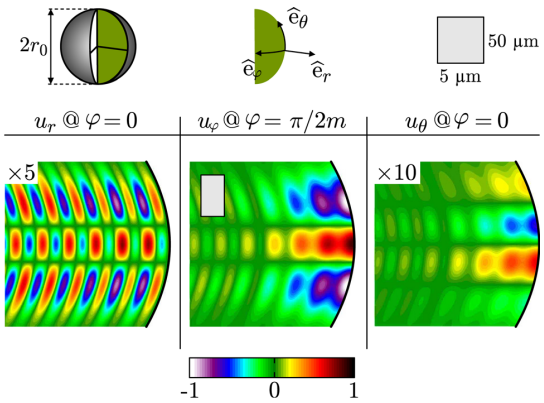


Figure 1.6: Pseudo-longitudinal acoustic whispering-gallery mode of a sphere. Plotted are the components of the displacement field $\vec{u}$. Reproduced with friendly permission from [SB15b], J. Appl. Phys. 118, 013102. Copyright 2015, AIP publishing.

### 1.3.2 Electromagnetic whispering-gallery waves

Convex surfaced dielectric objects with a polar symmetry possess electromagnetic excitations similar to the phenomenon in the acoustic wave domain. The boundary between the dielectric and the surrounding air or vacuum guides light and other types of electromagnetic waves around the perimeter of the structure. In a ray-optics picture this may be understood as a perpetual total internal reflection under glancing angles. First to theoretically examine the electromagnetic whispering-gallery modes in dielectric resonators was Richtmyer [Ric39].

A nice review of electromagnetic whispering-gallery waves is presented in [Ora02]. Precise spectroscopy of dielectric spherical resonators was done in [SB91] including identification of modes. The ultimate optical quality factors of silica microsphere resonators were examined in [GSI96], including identification of decay mechanisms and of time scales of quality factor degradation.

While an analytic solution of Maxwell's equations for a general axisymmetric dielectric resonator has not been achieved, for dielectric spheres an analytical approach was found by Debye [Deb09] using Debye potentials, which is laid out in [Ora02]. Precise analytical approximations were found for spheroidal axisymmetric bodies [GF06] with the hint that a generalisation towards arbitrary axisymmetric bodies is possible.

For a spherical resonator the solutions can be found from a scalar function $U$, the Debye potential, which fulfils

$$\frac{\partial^2 U}{\partial r^2} + \frac{1}{r^2 \sin(\theta)} \frac{\partial}{\partial \theta} \left( \sin(\theta) \frac{\partial U}{\partial \theta} \right) + \frac{1}{r^2 \sin^2(\theta)} \frac{\partial^2 U}{\partial \phi^2} + k^2 U = 0 \ , \tag{1.24}$$

where $k = k_0 \sqrt{\epsilon \mu}$ inside the sphere, $k = k_0$ outside the sphere, and $k_0 = \omega / c$.

The magnetic $H_{\{r,\theta,\phi\}}$ and electric $E_{\{r,\theta,\phi\}}$ field components can then be directly obtained from the Debye potential $U$. Making a separation of variables-ansatz for the Debye potential $U = R(r)\Theta(\theta)\Phi(\phi)$, one can find the following equations for the radial, polar and azimuthal

dependency:

$$\frac{d^2R}{dr^2} + \left(k^2 - \frac{c_1}{r^2}\right) R = 0 \ , \tag{1.25}$$

$$\frac{1}{\sin(\theta)} \frac{d}{d\theta} \left(\sin(\theta) \frac{d\Theta}{d\theta}\right) + \left(c_2 - \frac{c_3}{\sin^2(\theta)}\right) \Theta = 0 \ , \tag{1.26}$$

$$\frac{d^2\Phi}{d\phi^2} + c_3\Phi = 0 \ , \tag{1.27}$$

where $c_1, c_2, c_3$ are constants.

Then the solution inside the dielectric sphere has the form

$$U^i_{mn}(r, \theta, \phi) = C_i P^m_n(\cos\theta)(kr)^{1/2} J_\nu(kr) e^{\pm im\phi} \ , \tag{1.28}$$

and outside the sphere

$$U^e_{mn}(r, \theta, \phi) = C_e P^m_n(\cos\theta)(kr)^{1/2} H^{(1)}_\nu(k_0 r) e^{\pm im\phi} \ , \tag{1.29}$$

where $C_i$, $C_e$ are arbitrary constants, whose ratio are determined by the continuity condition at the material interface, $P^m_n(\cos\theta)$ are the adjoint Legendre polynomials, and $J_\nu(kr)$ and $H^{(1)}_\nu(kr)$ are the Bessel function and Hankel function of the first kind, respectively.

Numerically, using the finite element method, e.g. as in packages such as Comsol Multiphysics, optical whispering-gallery modes of more general axisymmetric bodies can be straightforwardly computed. In figure 1.7 typical mode field functions (electric field distribution) of two optical whispering-gallery modes are shown. They were numerically obtained via the finite element method using the Comsol Multiphysics software package. It should be noted that while such simulations can give relatively precise field distributions, the eigenfrequencies obtained are by far not precise enough to be matched with experimentally found resonances. That's due to the fact that the actual geometry of the physical resonator cannot be determined with sufficient precision at the moment, and that minute deviations in the glass mixture from a known refractive index function will have large effects on the eigenfrequency. The relative precision required in order to identify modes by their eigenfrequency

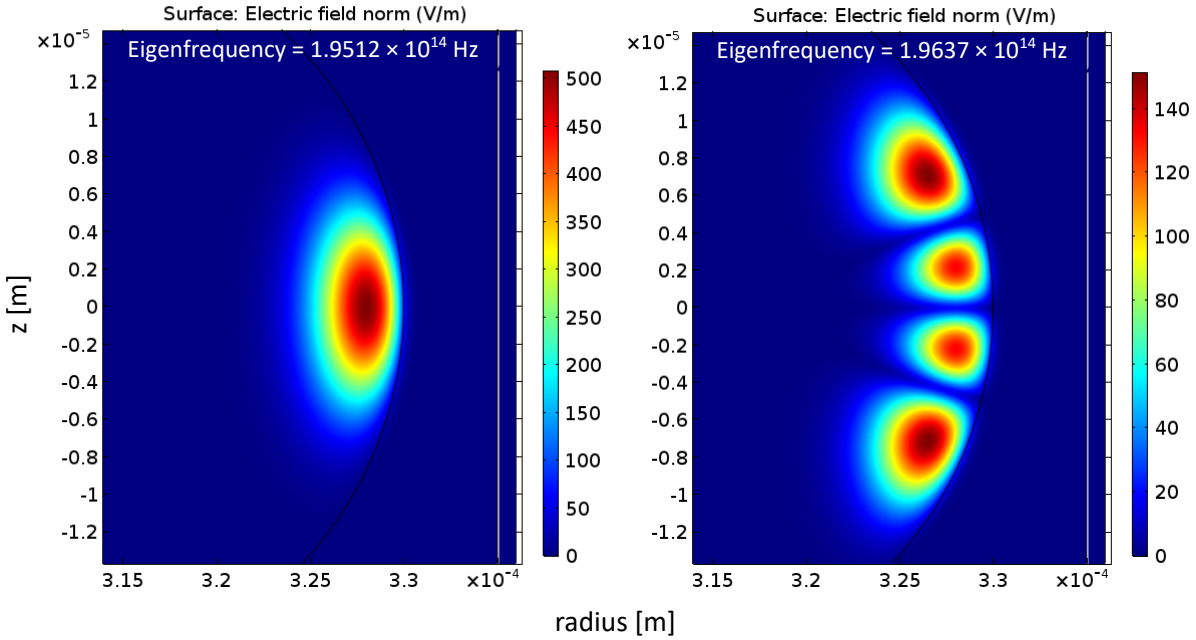


Figure 1.7: Optical whispering-gallery mode profiles, obtained with the finite element method using the Comsol Multiphysics software. Colour encodes the absolute value of the electric field. Shown are the lowest order (left) and fourth polar order mode (right) of a fused silica structure with an outer diameter of 660 µm, and a radius of curvature of 20 µm, approximating a microrod resonator with strong lateral confinement. The azimuthal mode number is $M = 2000$ for both modes.

would be of order 10 MHz/200 THz $= 5 \cdot 10^{-8}$, which is not experimentally feasible at present.

For the eigenfrequency of optical whispering-gallery modes, we can write down a simple formula (neglecting "waveguide dispersion, such that transverse mode numbers are not accounted for):

$$\nu_0 = \frac{\omega_0}{2\pi} = M \cdot \frac{c}{n(\omega)\pi D} \ , \tag{1.30}$$

where $\nu$ ($\omega$) is the optical (angular) eigenfrequency, $M$ the azimuthal (longitudinal) mode number, $c$ the (vacuum) speed of light, $n = n(\omega)$ the frequency dependent refractive index, and $D$ the resonator diameter.

## 1.4 Brillouin scattering

The inelastic scattering of light from thermally or self-excited elastic waves (at the quantum level: acoustic phonons) we call Brillouin scattering[5] (or Brillouin-Mandelstam scattering) and it is one of the most ubiquitous and extensively studied nonlinear optical phenomena [Boy08; Agr13]. It was first predicted by Brillouin in 1922 [Bri22], and Mandelstam in 1926 [Man26], and first experimentally observed by Gross in 1930 [Gro30b; Gro30a], shortly after Raman scattering was discovered two years earlier in 1928 [RK28].

In essence, it describes a particular regime of parametric coupling between light waves propagating in a dielectric medium and acoustic waves (density waves) that this same medium supports. The opto-acoustic interaction that lies at the core of Brillouin scattering can also be understood as an optomechanical kind of interaction as light couples to the local displacement of the (macroscopic) medium from its equilibrium position. Different from other types of optomechanical interaction, Brillouin scattering is a bulk effect, and characteristic for its dynamics is the ratio of wave velocities (typically $2 \cdot 10^8$ m/s light speed versus $6 \cdot 10^3$ m/s sound speed), as well as the attenuation hierarchy of the electromagnetic and acoustic excitations, where at room temperature typically spatial decay is much faster for the phonons, while temporal decay timescales of the photons and phonons can be comparable.

In its most basic configuration, we can imagine a continuous wave light beam, and a sound wave, propagating in the same direction in a dielectric bulk medium, for example, a block of glass (see figure 1.8). If the sound wave has a certain wavelength (about half the light wavelength) it can form a moving Bragg grating for the light, and become very reflective, Doppler red-shifting the incoming light beam upon reflection [Cha65]. The reflected beam overlaps with the incoming beam and reinforces the sound wave by electrostriction.

The consideration of energy and quasi-momentum conservation in the Brillouin scattering

[5]Note on terminology: More generally Brillouin scattering does not only include the scattering of photons off acoustic phonons, but also off scalar quasiparticles in a medium which carry quasimomentum associated with refractive index modulation. Other than mass displacement waves (phonons) these excitations include spin waves in magnetic materials (magnons) [CL86], and exciton-polaritons [BZB72; WU82].

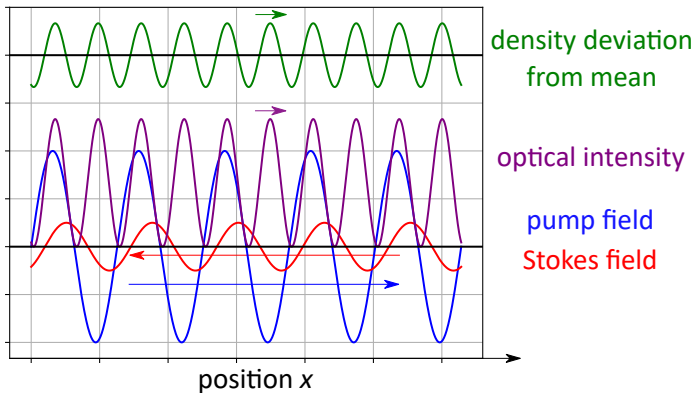


Figure 1.8: Brillouin scattering in one dimension, schematically. Arrows symbolize phase velocity. A strong pump wave (blue) is moving in the positive x-direction, while a Stokes wave of slightly bigger wavelength (difference not visible at this scale) is moving in the opposite direction (red). Their overlap leads to a almost-standing wave, whose intensity maxima are flashing at an instantaneous frequency of twice the optical frequency, while slowly moving in the positive x-direction. Via electrostriction, which is not sensitive to the sign of the electric field, the light induces density variation in the medium (green). Brillouin phase matching between pump, Stokes and sound waves is fulfilled once the intensity pattern (purple) moves at the speed of sound.

process returns what's often called "phase matching" conditions. As the pump photon is reflected, its wavelength is downshifted. The excess energy goes into the creation of a phonon. As the process is a bulk effect, the involved fields (acoustic and electromagnetic) need to maintain a fixed phase relationship over finite volumes of the dielectric medium in order to lead to observable effects, and not have the scattering contributions from different regions cancel.

Similar to other parametric processes[6] Brillouin scattering is not dependent on the presence of an initial coherent sound wave, but can also be self excited. In fact it is most commonly only then referred to as Brillouin scattering. For example, in the operation of acousto-optical modulators the same acousto-optic coupling is exploited, but a coherent ultrasonic wave is generated using non-optical means. These bulk waves are typically excited by driving a piezoelectric transducer with radio-frequency electrical signals and are used to inelastically scatter light under glancing angles, in order to achieve frequency shifting and switching of light fields.

[6]Depending on the definition, Brillouin scattering can be considered a non-parametric or parametric process. As the phononic excitation plays a role analogous to one of the optical fields in three-wave mixing or parametric fluorescence in $\chi^{(2)}$ media, we will refer to the process as parametric in this work.

In the common scenario when there is no coherent sound wave excited, light will undergo thermal Brillouin scattering[7]. We can compute the *Brillouin shift*, i.e. the frequency shift that the light undergoes when it is inelastically scattered from acoustic phonons in a bulk medium. It is the frequency shift for which the optical beat note of incoming and scattered light travels at the speed of sound (phase matching condition):

$$\Delta\nu_{\mathrm{B}} = \frac{2 \cdot \frac{v_{\mathrm{a}}}{c/n} \cdot \nu}{1 \pm \frac{v_{\mathrm{a}}}{c/n}} \approx 2 \cdot \frac{v_{\mathrm{a}}}{c/n} \cdot \nu \ , \tag{1.31}$$

where $\Delta\nu_{\mathrm{B}}$ is the Brillouin frequency shift, $v_{\mathrm{a}}$ is the phase velocity of acoustic waves, $c$ the vacuum speed of light, $n$ is the refractive index, and $\nu$ the optical frequency of the pump wave. The Brillouin down- and up-shift are slightly different, with the plus sign in the denominator holding for the Stokes process, the minus sign for the anti-Stokes process. Here the factor of 2 can be interpreted as stemming from the non-sensitivity of the acoustic wave to the sign of the electric field.

We will focus our attention here exclusively to the case of 180° backscattering, as this is the relevant case for operating with fiber and microresonator geometries, where acoustic wave propagation is only supported in the directions parallel or antiparallel with the light propagation direction. We will also not discuss the 0° forwards scattering case between different transverse optical modes which has been reported in the literature [SLB85] and used with microresonators for cooling [Bah+12] and observation of optomechanically induced transparency [Don+15], as this work is focussing on the high frequency phonons addressable via the back-scatter interaction, whose thermal occupation will be close to unity using standard cryogenic (4 K) equipment. In the forward Brillouin works the acoustic frequency was 42 MHz and 95 MHz, respectively, and the acoustic azimuthal mode number is suspected to be $|M_{\mathrm{a}}| < 10$ ([Don+15] quote 6). In the general case (e.g. in a bulk medium which supports wave propagation in all directions), when Brillouin scattering is observed under an angle $\phi$, the shift is scaled by the angle as in $2 \cdot \frac{v_{\mathrm{a}} n}{c} \nu \cdot \sin(\phi/2)$ [Bri22; Man26;

[7]Some authors have called this "spontaneous Brillouin scattering", but this nomenclature should be avoided as the majority of the effect is not due to the presence of acoustic vacuum fluctuations but the thermal hypersonic excitations present in the material due to its finite temperature.

Boy08], as already confirmed in the very first reported observation of Brillouin scattering by Gross in 1930 [Gro30a].

The red-shifting process we call Brillouin Stokes scattering, while the blue-shifting process we call Brillouin anti-Stokes scattering. The red and blue shifts can also be thought to arise from Doppler red or blue shifting from a moving index grating, which the sound wave in the dielectric medium constitutes. In the bulk case with only thermally excited sound, one can think of phase matched spatial Fourier components which contribute to the scattering, because they have the right periodicity, while most acoustic wavelength components don't contribute to the thermal Brillouin scattering. That this picture is indeed valid was, for example, shown in [Cha65].

### 1.4.1 Classical equations of motion for stimulated Brillouin scattering

Whenever the fields are large and single quantum processes or quantum noise can be neglected, we can treat Brillouin scattering (which is then synonymous with stimulated Brillouin scattering, as the thermal and spontaneous contributions are neglected) by classical equations of motion.

Following Boyd's treatment [Boy08], let's describe the classical waves in a one-dimensional Brillouin-active medium by

$$\begin{aligned} E_1(z,t) &= A_1(z,t)\cdot e^{i(k_1 z-\omega_1 t)} \ + \ \text{c.c.} \\ E_2(z,t) &= A_2(z,t)\cdot e^{i(k_2 z-\omega_2 t)} \ + \ \text{c.c.} \\ \tilde{\rho}(z,t) &= \rho_0 + \left(\rho(z,t)e^{i(qz-\Omega t)} \ + \ \text{c.c.}\right) \ , \end{aligned} \tag{1.32}$$

where $A_1(z,t),\ A_2(z,t),\ \rho(z,t)$ are slowly varying amplitudes of the optical pump and Stokes fields and acoustic fields, respectively, $\rho_0$ is the mean density of the medium, $\Omega = \omega_1 - \omega_2$ and $q = 2k_1$.

Further we will assume that the density wave fulfils the acoustic wave equation including

damping and driving terms (generalisation of equation 1.20 in the isotropic case).

$$\frac{\partial^2\tilde{\rho}}{\partial t^2} - \Gamma'\nabla^2\frac{\partial\tilde{\rho}}{\partial t} - v^2\nabla^2\tilde{\rho} = \nabla\cdot\vec{f}\,, \tag{1.33}$$

where the force density $\vec{f} = \nabla p_{\mathrm{elstr}}$ is due to the electrostrictive pressure $p_{\mathrm{elstr}} = -\frac{1}{2}\epsilon_0\gamma_e\langle E^2\rangle$.

Neglecting spatial variations of the density, one obtains the steady-state conditions

$$\rho(z,t) = \epsilon_0\gamma_e q^2\frac{A_1A_2^*}{\Omega_B^2 - \Omega^2 - i\Omega\Gamma_B}\ . \tag{1.34}$$

The spatial evolution of the optical fields is governed by the wave equation

$$\frac{\partial^2 E_i}{\partial z^2} - \frac{1}{(c/n)^2}\frac{\partial^2 E_1}{\partial t^2} = \frac{1}{\epsilon_0 c^2}\frac{\partial^2 P_i}{\partial t^2}\ ,\ i = 1,2, \tag{1.35}$$

where the source term (polarisation) is given by $P = \epsilon_0\Delta\epsilon E = \epsilon\gamma_e\frac{\rho}{\rho_0}E$.

Assuming phase matching and making the slowly-varying optical amplitude approximation, one arrives at the classical SBS equations of motion

$$\begin{aligned}\frac{\partial A_1}{\partial z} + \frac{1}{c/n}\frac{\partial A_1}{\partial t} &= \frac{i\omega\gamma_e}{2nc\rho_0}\rho A_2\ ,\\ -\frac{\partial A_2}{\partial z} + \frac{1}{c/n}\frac{\partial A_2}{\partial t} &= \frac{i\omega\gamma_e}{2nc\rho_0}\rho^* A_1\ ,\end{aligned} \tag{1.36}$$

which form a set of three coupled equations, together with equation 1.33.

Often a random acoustic noise force term $f_{\mathrm{a}}(z,t)$ is heuristically added to the right hand side of equation 1.33 in the classical treatment of Brillouin scattering, in order to describe the thermal Brillouin noise. Such a noise term is, for example, necessary to describe the initiation of SBS from thermal Brillouin scattering with a monochromatic optical pump field in an optical fiber.

### 1.4.2 Electrostriction and Brillouin gain

Electrostriction (photoelasticity), which is present in all dielectric media, is the force responsible for Brillouin scattering [Wol+15]. The potential energy per volume $u$ of a dielectric medium is changed in the presence of an electric field by the amount $u = \frac{1}{2}\epsilon\epsilon_0 E^2$ compared to the field-free case. If we now consider the situation where the density of a compressible medium changes in a small volume in response to the field present in the volume, and associated with that change will be a refractive index change, then we can write the change in potential energy as

$$\Delta u = \frac{1}{2}\epsilon_0 E^2 \Delta\epsilon = \frac{1}{2}\epsilon_0 E^2 \left(\frac{\partial\epsilon}{\partial\rho}\right)\Delta\rho \ . \tag{1.37}$$

As energy is conserved, the change in the energy per volume $\Delta u$ will correspond to the work done per volume to compress the medium $\Delta w = p_{\mathrm{elstr}}\Delta V/V = -p_{\mathrm{elstr}}\Delta\rho/\rho$, where $p_{\mathrm{elstr}}$ is the electrostrictive pressure. Combining these, we obtain

$$p_{\mathrm{elstr}} = -\frac{1}{2}\epsilon_0\rho\left(\frac{\partial\epsilon}{\partial\rho}\right)E^2 = -\frac{1}{2}\epsilon\gamma_e E^2 \ , \tag{1.38}$$

where in the last step we defined the (dimensionless) electrostrictive constant $\gamma_e = \rho(\partial\epsilon/\partial\rho)$.

For centrosymmetric materials the value of the electrostrictive constant $\gamma_e$ can be estimated from the Clausius-Mossotti relation (or the equivalent Lorenz-Lorentz relation), which relates the polarisability of a medium to its permittivity $\epsilon$ (or refractive index $n$)

$$\gamma_e = (n^2 - 1)(n^2 + 2)/3 \ , \tag{1.39}$$

which shows that it is of order unity for condensed matter. For fused silica at 1550 nm with a refractive index of 1.444 we obtain $\gamma_e = 1.48$ from this relation.

Electromagnetic radiation passing through any kind of dielectric material creates electrostriction, the slight local compression (or expansion) of the dielectric in response to the electric field applied. In the common use (and that's how we'll use it here) electrostriction stands for the effect, where the response is proportional to the square of the electric field.

It is therefore to be distinguished from the inverse piezoelectric effect, where the stress is proportional to the electric field itself. The piezoelectric effect does not occur in amorphous materials like fused silica. In the context of cavity optomechanics the electrostricition effect gives rise to a type of optomechanical coupling different from the conventional radiation pressure mechanism commonly found to occur at boundaries and related to the force that the recoil of photons produces. We will use Brillouin optomechanical interaction and electrostrictive/photoelastic coupling synonymously in this work to refer to this type of interaction.

While in conventional radiation pressure cavity optomechanics the optomechanical coupling can be obtained from the analysis of the frequency shift a mechanical displacement imparts on the optical cavity's resonance frequency, i.e. $g_0 = -\frac{\partial \omega_{\mathrm{cav}}}{\partial x_{\mathrm{m}}} \cdot x_{\mathrm{zpf}}$, where $g_0$ is the intrinsic optomechanical coupling rate, $\omega_{\mathrm{cav}}$ is the cavity eigenfrequency, $x_{\mathrm{m}}$ is the mechanical displacement from equilibrium, and $x_{\mathrm{zpf}}$ is the mechanical zero-point fluctuation (compare equation 1.15, [AKM14]), the same cannot be done in Brillouin optomechanical coupling as the cavity's resonance frequency does not depend on the mechanical amplitude.

Rather a different approach is required, starting from the change in electromagnetic energy induced by a density fluctuation via the change in the dielectric constant tensor, similar to what we discussed above for a DC electric field, see equation 1.37. Such a standpoint has been presented e.g. in [Yar65].

It should also be noted that electrostriction, aside from Brillouin scattering, also contributes to the (non-instantaneous part of the) third order susceptibility, namely by $\chi^{(3)}(\omega = \omega + \omega - \omega) = 1/3\epsilon_0 C_T \gamma_e^2$ [Boy08]. This can be seen by considering that there will be a density related effect of the electric field on the permittivity, and thus on the susceptibility proportional to $E^2$. Just, as a field is applied, this part of the third-order response of the medium will be delayed related to the elasticity and density of the medium, as opposed to the quasi-instantaneous response of the electronic shells, responsible for the $\chi^{(3)}$ nonlinearity.

Following Boyd further, let's now consider the scenario where a (strong) pump field traverses a medium over a lengh $L$ and focus on the stationary case, where we drop temporal derivatives in equation 1.36. A light field counter-propagating and red detuned by approx-

imately the Brillouin shift with respect to this pump field will then experience parametric gain (Brillouin gain) and grow exponentially in the backwards direction, as we shall see.

Inserting equation 1.34 into 1.36 we obtain

$$\begin{aligned} \frac{dA_1}{dz} &= \frac{i\epsilon_0\omega q^2\gamma_e^2}{2nc\rho_0}\frac{|A_2|^2 A_1}{\Omega_B^2-\Omega^2-i\Omega\Gamma_B} \ , \\ \frac{dA_2}{dz} &= \frac{i\epsilon_0\omega q^2\gamma_e^2}{2nc\rho_0}\frac{|A_1|^2 A_2}{\Omega_B^2-\Omega^2-i\Omega\Gamma_B} \end{aligned} \tag{1.40}$$

and after defining the intensity $I_i = 2n\epsilon_0 c|A_i|^2$ and the Brillouin gain $g$ we obtain

$$\begin{aligned} \frac{dI_1}{dz} &= -gI_2I_1 \ , \\ \frac{dI_2}{dz} &= -gI_1I_2 \ . \end{aligned} \tag{1.41}$$

Here the Brillouin gain is given through

$$g = \tilde{g}_0\frac{(\Gamma_B/2)^2}{(\Omega_B-\Omega)^2+(\Gamma_B/2)^2} \ , \tag{1.42}$$

with the peak Brillouin gain given by $\tilde{g}_0 = \frac{\gamma_e^2\omega^2}{nv_a c^3\rho_0\Gamma_B}$ with units $[\tilde{g}_0] = \mathrm{m}^{-1}\mathrm{W}^{-1}$. Note here that the peak (line-center) Brillouin gain $\tilde{g}_0$ is frequency independent, as the Brillouin linewidth $\Gamma_B$ is proportional to $\omega^2$.

This expression can also be found in reference [LC03] and it is pointed out here, that the experiment supports the observation in the respective expression that the Brillouin gain curve has a temperature invariant area. This is especially interesting towards low temperatures, where in amorphous materials the closing of the two-level-system acoustic damping mechanism leads to a significant narrowing of the Brillouin linewidth [VSH80; Phi81; LC03]. In a recent experiment [Beh+17] the authors showed how strong acoustic driving can saturate the two-level system absorbers in an amorphous sample and significantly reduce the acoustic attenuation in a "transparency window" around the drive frequency. This approach might prove valuable when minimising two-level system acoustic damping at cryogenic temperatures in amorphous microresonators. Aside from the derivation following Boyd [Boy08] there

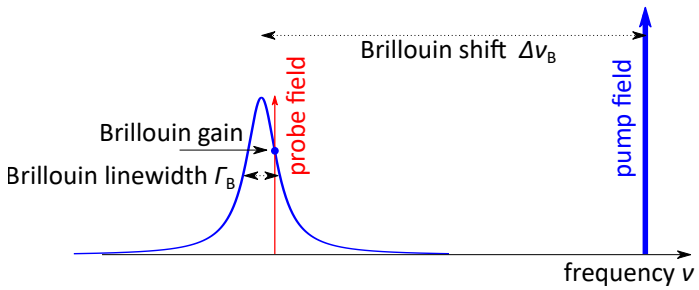


Figure 1.9: Stimulated Brillouin scattering scheme. A strong pump field (blue) sets up Brillouin gain (blue curve) for a counter-propagating red detuned probe field (red) which experiences exponential growth in the backwards direction, as long as the pump is not depleted.

are alternative routes to derive the Brillouin gain, via the photoelastic coefficient tensor $p_{ijkl}$, also called elasto-optic or Pockels coefficient tensor, which is defined via $\delta\epsilon_{\mathrm{ij}} = -\epsilon^2 p_{\mathrm{ij,kl}}\eta_{\mathrm{kl}}$, where $\eta$ is the displacement gradient tensor (strain) and $\epsilon$ is the permittivity (dielectric constant) tensor. The expression is e.g. given in [NTR97]:

$$\tilde{g}_0 = \frac{2\pi n^7 p_{12}^2}{c\lambda_{\mathrm{p}}^2 \rho_0 v_{\mathrm{a}} \Delta\nu_{\mathrm{Br}}} \ , \tag{1.43}$$

where $n$ the refractive index, $p_{12}$ a component of the photoelastic tensor of the material, $c$ the speed of light, $\lambda_{\mathrm{p}}$ the pump (vacuum) wavelength, $\rho_0$ the density of the material, $v_{\mathrm{a}}$ the velocity of sound, and $\Delta\nu_{\mathrm{Br}}$ the Brillouin linewidth (FWHM). It turns out that the connection between the electrostrictive constant and the component of the photoelastic tensor is via $\gamma_{\mathrm{e}} = p_{12}n^4$. Note that aside from the pump wavelength the Brillouin gain depends only on local properties of the material.

The photoelastic constants of fused silica have both been measured [Ved50; Sch80] and theoretically computed from first principles [DBT03]. The experimental value is $p_{12} = 0.28$ (0.27 and 0.285, respectively). Donadio et al give the defining expression $\Delta\epsilon_{\mathrm{ij}}^{-1} = p_{\mathrm{ijkl}}\eta_{\mathrm{kl}}$, and stress that the dielectric tensor is, here, to be understood as the response of the electronic shell, i.e. evaluated at frequencies much higher than the lattice vibrations, but lower than electronic transition frequencies. This range e.g. includes the visible and near infrared range of the optical spectrum for most conventional glasses. For barium fluoride, which will be discussed later in this thesis, the photoelastic constants were measured in [RN70], and

the numerical value lies very close to that of fused silica, at $p_{12} = 0.277$, in line with the expectation from their similarity of refractive indices ($BaF_2$ at 1550 nm: $n = 1.46$) and the Clausius-Mossotti relation.

## 1.5 Brillouin optomechanics in microresonators

While early work on Brillouin scattering was mostly concerned with the effects on the light field [Boy08], in the context of (cavity) optomechanics, growing interest is being devoted towards the acoustic part of the interaction and the study and manipulation of the mechanical degrees of freedom that come with it. So far we have discussed the phenomenon of Brillouin scattering in bulk samples or waveguides and how it is connected with the material properties, and that it can be thought of as giving rise to parametric gain.

In this section we will discuss how the situation changes when one considers Brillouin scattering in an optical ring resonator, particularly in whispering-gallery resonators, where the electrostrictive interaction gives rise to an optomechanical coupling. Let's imagine a waveguide or optical fiber being continuously transformed into a closed loop ring resonator [VBV16]. It becomes clear that now any light traversing the region will be recycled and will traverse the same path repeatedly. Instead of an optical loss per unit length, we will now be interested in a cavity quantity, that is the lifetime of the light in the cavity (or its inverse, the linewidth). It also becomes clear that while in a waveguide there was a flat continuous density of states, now the phase acquired on a round trip will lead to resonances, see appendix A.

The same happens to the sound waves, but in room-temperature Brillouin optomechanics with high frequency phonons (backscattering) the acoustic lifetime is much shorter than the round trip time of the acoustic waves. Thus, the acoustical finesse $\mathcal{F} = \Delta\nu_{\mathrm{FSR}}/\Delta\nu_{\mathrm{Br}}$ is smaller than unity, and the cavity is not "felt" by the sound waves. We can call this the "Brillouin regime". A very useful tutorial article on the related topic of Brillouin optomechanics in nanophotonic structures was recently provided [WDM19].

Early results that utilise of Brillouin optomechanical coupling in microresonators include the sideband cooling using Brillouin forward scattering of a 50 MHz sound wave [Bah+12], and the observation of optomechanically induced transparency via Brillouin scattering [Don+15], a cavity optomechanical phenomenon analogous to EIT in atomic systems. In these studies forward scattering with low frequency sound waves was exploited, which has the advantage of coming with much lower acoustic attenuation (acoustic attenuation in this frequency range scales as $\omega^2$, see e.g. [Boy08]), but at the price of a much higher thermal occupation.

### 1.5.1 Brillouin phase matching

A point of particular importance with Brillouin scattering in optical cavities is that of phase matching. Here by phase matching we mean that the three waves taking part in the interaction maintain a certain phase relationship through the entirety of the interaction region, such that scattering amplitudes from different regions constructively interfere. In waveguides and optical fibers which have a flat optical density of states, Brillouin phase matching is "automatically" fulfilled, as in, there will always be an optical mode present in the center of the Brillouin gain profile, which will experience the highest parametric gain, see figure 1.10. Then, during the onset of stimulated Brillouin scattering this Stokes wavelength will have the largest gain and lead to a narrow spectrum [YDT02].

Throughout physics, energy and (quasi-)momentum must be conserved, which are the central conditions to phase matching in nonlinear optics and Brillouin scattering. These requirements impose conditions on which (or alternatively how strongly certain) waves will interact via the Brillouin optomechanical coupling, which can be represented by a three-wave-mixing type Hamiltonian.

These conditions can be formulated as

$$\hbar\omega_{\mathrm{p}} = \hbar\omega_{\mathrm{s}} + \hbar\omega_{\mathrm{m}} \tag{1.44}$$

$$\hbar k_{\mathrm{p}} = \hbar k_{\mathrm{s}} + \hbar k_{\mathrm{m}} \ , \tag{1.45}$$

where $\omega$ is the angular frequency, $k$ the wave-vector of pump light (p), Stokes light (s) and mechanical (m) waves.

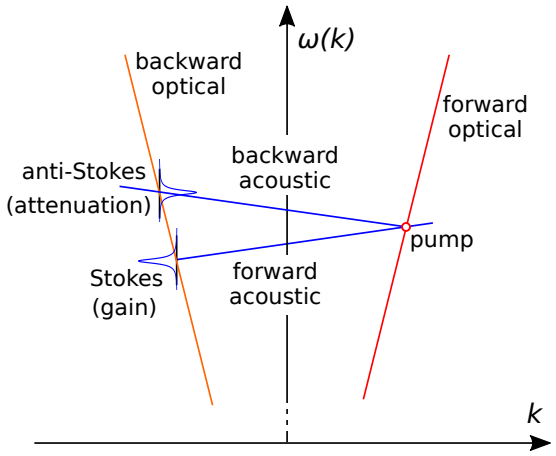


Figure 1.10: Automatic phase matching of Brillouin scattering in a waveguide (e.g. an optical fiber supporting guided acoustic waves) supporting single optical and acoustic spatial modes. The dispersion relations of the optical and acoustic waves cross at exactly two points, corresponding to Brillouin Stokes and anti-Stokes scattering.

### Brillouin phase matching in a whispering-gallery microresonator

In an optical cavity, the phase matching condition of Brillouin scattering is not anymore automatically fulfilled. The alteration of the optical density of states makes phase matching more complicated, as the optical (and also mechanical) spectra discretize in the presence of boundary conditions.

In order to understand Brillouin phase matching let's consider a forward (pump) optical resonance, a backward (anti-Stokes) optical resonance and an acoustic whispering-gallery mode with a decay width longer or shorter than the acoustic FSR. We assume that the separation of the pump and anti-Stokes resonances is approximately the Brillouin shift in

the material. The periodic boundary conditions of the cavity will create "resonances", both for the light and sound waves. While there can be a variety of transverse modes, on a particular transverse mode, changing the number of wave cycles on a round trip brings us from one mode to the next within what is sometimes called a "mode family"[8]. They are labelled by an azimuthal mode number $M$ which corresponds to the number of wave cycles on a round trip (compare section 1.3). The frequency difference between two adjacent modes of a mode family $\nu_{M+1} - \nu_M = \Delta\nu_{\mathrm{FSR}}$ is the free spectral range (compare appendix).

Superimposing the pump and anti-Stokes optical waves, which are counter-propagating with respect to each other, returns an intensity pattern that is slowly moving (it's an "almost standing wave"). Since both the pump and anti-Stokes waves are resonant by construction, they will each have integer azimuthal mode numbers $M_{\mathrm{p}}$ and $M_{\mathrm{aS}}$. As one can convince oneself the slowly moving beat note of the waves will have $M_{\mathrm{p}} + M_{\mathrm{aS}}$ intensity maxima: If we assume two optical waves $A$ and $B$, for simplicity with the same amplitude, counter-propagating and resonant with two different whispering-gallery resonances, such that their amplitudes are given by

$$\begin{aligned} A(\phi, t) &= \cos(M_A\phi - \omega_A t) = \frac{1}{2}\left(e^{i(M_A\phi-\omega_A t)} + e^{-i(M_A\phi-\omega_A t)}\right) \\ B(\phi, t) &= \cos(-M_B\phi - \omega_B t) = \frac{1}{2}\left(e^{i(M_B\phi+\omega_B t)} + e^{-i(M_B\phi+\omega_B t)}\right) \ , \end{aligned} \tag{1.46}$$

where we assumed $M_A, M_B, \omega_A, \omega_B > 0$, and manually added a minus sign in front of one of the $M$'s to represent counter-propagation, then the total intensity can be written as

$$\begin{aligned} |A+B|^2 = 1 + \frac{1}{2}\cos(2(M_A\phi - \omega_A t)) + \frac{1}{2}\cos(2(M_B\phi + \omega_B t)) + \\ \cos((M_A - M_B)\phi - (\omega_A + \omega_B)t) + \cos((M_A + M_B)\phi - (\omega_A - \omega_B)t) \ . \end{aligned} \tag{1.47}$$

In this expression all terms are oscillating at optical frequencies except the last term, which is oscillating at the difference frequency $\omega_A - \omega_B$. This is the relevant term inducing density variations via electrostriction.

[8]There seem to be different uses of the term "mode family" floating around, and they are almost orthogonal. We will use it here for the set of modes which only differ in their azimuthal mode number $M$, but have identical transverse (polar, radial) profiles.

Let's now consider the electrostrictive effect that this optical beat note will have on the acoustic wave. Only if the acoustic wave's azimuthal mode number matches the number of anti-nodes of the optical beat note, will there be a significant electrostrictive coupling, as otherwise contributions from different sites around the perimeter will cancel. This can be seen to formally correspond to the azimuthal part of the mode field function $\propto e^{i(\pm M_\mathrm{m}\phi \mp M_\mathrm{p}\phi \pm M_\mathrm{aS}\phi)}$ showing a wave number balance of the three interacting waves (compare 1.3). We can formulate this condition for Brillouin back-scattering in the form

$$|M_\mathrm{m}| = |M_\mathrm{p}| + |M_\mathrm{aS}| \ . \tag{1.48}$$

At typical resonator dimensions, with $\pi D \approx 2\,\mathrm{mm}$, and optical wavelength in the medium of $\lambda \approx 1\,\mu\mathrm{m}$ the azimuthal mode numbers for the optical resonances would typically be $|M_\mathrm{p}| \approx |M_\mathrm{aS}| \approx 2000$, and the acoustic azimuthal mode number, with $\lambda_\mathrm{m} \approx 0.5\,\mu\mathrm{m}$, typically be $|M_\mathrm{m}| \approx 2|M_\mathrm{p}| \approx 2|M_\mathrm{aS}| \approx 4000$.

In the case that the acoustic azimuthal mode number differs from the number of anti-nodes of the optical beat note (e.g. by 1) the sites of high intensity will coincide with an anti-node of the acoustic wave on one side of the cavity, acting to contract the medium, while on the opposite side sites of high optical intensity will coincide with nodes of the acoustic wave, thus having the opposite effect. The contributions cancel. In this way the optical resonance pair picks out/selects a particular acoustic azimuthal mode number, while couplings to all other azimuthal mode number modes cancel. This is an advantage of the whispering-gallery-resonator approach being pursued here.

Of course, equation 1.48 is a manifestation of wave vector conservation (equation 1.45), as the azimuthal mode number and the wave vector are connected via $k_i = \frac{M_i}{R}$, where $R$ is the resonator radius.

But what about energy conservation? We write down the phase velocity of the acoustic

wave and the velocity of the optical beat note:

$$v_{\mathrm{ph,m}} = \frac{\omega_{\mathrm{m}}}{k_{\mathrm{m}}} = \frac{\omega_{\mathrm{m}}}{M_{\mathrm{m}}} \cdot R \tag{1.49}$$

$$v_{\mathrm{beat}} = \frac{\omega_{\mathrm{aS}} - \omega_{\mathrm{p}}}{k_{\mathrm{aS}} - k_{\mathrm{p}}} = \frac{\omega_{\mathrm{aS}} - \omega_{\mathrm{p}}}{M_{\mathrm{m}}} \cdot R \ , \tag{1.50}$$

where we used in the last step that equation 1.48 is already fulfilled.

So we have shown how the condition of energy conservation in the electrostrictive interaction, $\omega_{\mathrm{aS}} - \omega_{\mathrm{p}} = \omega_{\mathrm{m}}$, is equivalent to the condition that the optical beat note of pump and anti-Stokes optical waves travels around the perimeter at the speed of sound (acoustic phase velocity). The phase matching situation in a whispering-gallery-mode microresonator is illustrated in figure 1.11, with the resulting three-mode interaction picture depicted in figure 1.12.

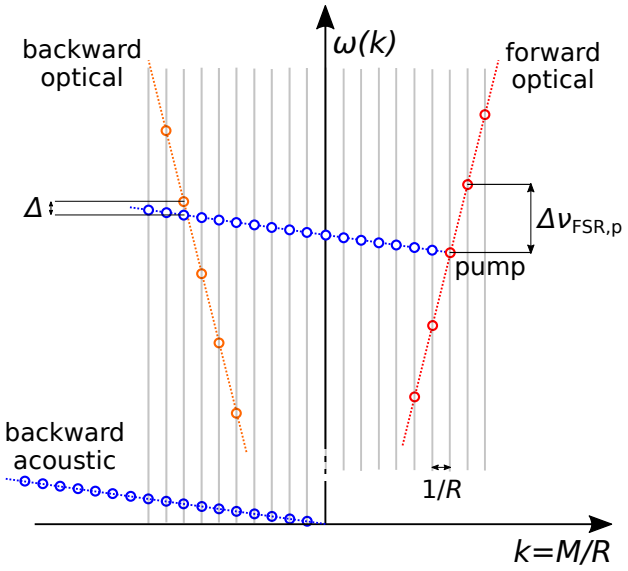


Figure 1.11: Brillouin phase matching in a microresonator. The periodic boundary conditions lead to resonances with integer azimutal mode number $M$ (grey vertical lines). Shown are only one forward and one backward optical mode family, as well as one acoustic mode family, while mode families with different transverse (polar, radial) profiles are not shown, for simplicity.

For the typical diameters of resonators used in this work (300 µm to 1.5 mm) the phonon mean free path at the frequency of 11 GHz, $l_{\mathrm{coh}} = c_{\mathrm{m}} \cdot \tau_{\mathrm{coh}} \approx 6\mathrm{km/s} \cdot 10\ \mathrm{ns} = 60\,\mu\mathrm{m}$ is shorter than the round trip length $L = \pi d \approx 2$ mm. Thus, we can speak of a quasi-

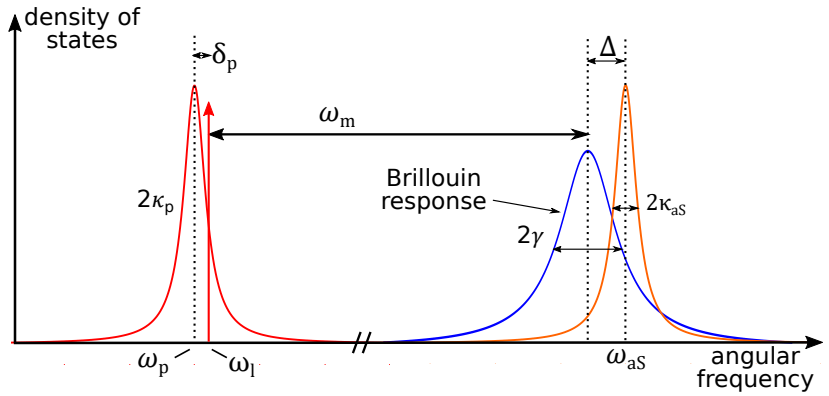


Figure 1.12: Optical and acoustic density of states for Brillouin cavity optomechanics experiments in the anti-Stokes scattering configuration (i.e. pump laser on the red resonance of the optical resonance pair). Depicted is the three oscillator model with detunings.

continuum for the acoustic waves. While this is true at room temperature, it is expected that at cryogenic temperatures because of reduced mechanical damping, the cavities will also become resonators (finesse $> 1$) for the acoustic waves. This has been called the "coherent phonon regime", as opposed to the "Brillouin regime" [Ren+18].

Independent of whether one operates in the coherent phonon or Brillouin regimes, in whispering-gallery Brillouin optomechanics the coupling will always be to a single acoustic azimuthal mode within a mode family only. Nevertheless, multi-modeness can still arise in the coupling to different transverse spatial acoustic modes with the same azimuthal mode number, although it is expected that these acoustic modes will have a frequency spread, and thus come with individual optomechanical detunings, additional to individual coupling rates (see sections 1.5.2 and 4.5.5). This can be viewed from different angles, one of which is the cancellation argument presented above (which also holds for heavily damped acoustic modes). From this perspective, the azimuthal mode number conservation (wave vector conservation) selects exactly one mode out of the quasi-continuum (see figure 1.11).

### 1.5.2 Optomechanical coupling rate

A quantity of key interest in cavity quantum optomechanics is the optomechanical coupling rate, quantifying the strength with which optical and mechanical degrees of freedom coher-

ently affect each other. The connection between the electrostriction effect, Brillouin scattering and optomechanical coupling was studied theoretically for nanophotonic and integrated waveguides in recent studies [Wol+15; SS16; ZH16]. In Brillouin cavity optomechanics the interaction Hamiltonian can be considered of three-wave-mixing type, with an interaction term of the form

$$\hbar g_0 (a_{\text{blue}} a^\dagger_{\text{red}} b^\dagger \ + \ \text{h.c.}) \tag{1.51}$$

where $g_0$ is the (bare) cavity optomechanical coupling rate, $a$, $b$ are the annihilation operators of the optical and mechanical modes, respectively.

The optomechanical coupling rate $g_0$ is intimately linked to the Brillouin gain coefficient $\tilde{g}_0$ in the cavity (equation 1.43) [VBV16] and a relation can be specified between them: $\tilde{g}_0 = 4|g_0|^2 n^2 L/(\hbar\omega c^2 \Gamma_m)$.

An approximate expression for $g_0$ was derived for forward Brillouin scattering [Tom+11], and for standing acoustic wave optomechanical coupling experiments [Ren+18].

Tomes et al [Tom+11] obtain the result $g_0 = A_{\text{opt}} L \gamma_e q u_q E_k E_{k+q}/(2\hbar)$, where $A_{\text{opt}}$ is an interaction area approximated as the optical mode area, $L$ is the round trip length, and $u_k$ and $E_k$ are the zero-point fluctuation of the acoustic and optical modes with wavenumber $k$, respectively, given through $E_k = \sqrt{\hbar\omega_k/(2A_{\text{opt}}L\epsilon)}$ for the optical, and $u_k = \sqrt{\hbar/(2A_m L\rho\omega_m k)}$ for the acoustic field. In [Tom+11] the interaction area is assumed to be approximately equal to the optical mode area in the case where the optical mode area is much smaller than the acoustic mode area. We will now leave the interaction area general and make replacements for $q$ and $\omega_{\text{m}}$ according to the acoustic dispersion relation and Brillouin phase matching condition, after which we obtain

$$g_0 = \frac{\gamma_e}{4}\sqrt{\frac{\hbar\omega^3}{c v_{\text{a}} n^3 \rho}} \cdot \frac{1}{\sqrt{L \cdot \frac{A_1 A_2 A_{\text{m}}}{A^2_{\text{int}}}}} \ . \tag{1.52}$$

Thus we see that the bare coupling rate $g_0$ is proportional to something similar to $1/\sqrt{V}$, where $V$ is a mode volume. As we shall later see, the rate of the Brillouin scattering process will be $\propto G^2 = g_0^2|\alpha|^2$, where $\alpha$ is the (classically treated) coherent amplitude of the pump

mode. With $|\alpha|^2 = n_{\mathrm{cav}} = P_{\mathrm{cav}}/(\hbar\omega) \propto 1/\kappa \propto Q$ and $g_0^2 \propto 1/V$ we see that the rate of the nonlinear process scales $\propto Q/V$.

Renninger et al [Ren+18] quote an approximate (order of magnitude) bare coupling rate of

$$g_0 = i\frac{\omega^2 n^3 p_{13}}{2c}\sqrt{\frac{\hbar}{\omega_{\mathrm{m}}\rho A L}} \tag{1.53}$$

for a $z$-cut crystal, where $A$ is the common mode area of optics and acoustics, assumed for simplicity to be a box function. This expression agrees with equation 1.52 except a factor of $\sqrt{2}$.

Let's now focus our attention to the interaction area. The coupling rate will be proportional to the triple overlap integral of mode field functions of the two optical and the acoustic whispering-gallery waves of the form

$$\int d\phi d\vec{r}_\perp E_{\mathrm{p}}(\vec{r}_\perp, \phi) E_{\mathrm{s}}(\vec{r}_\perp, \phi) u_{\mathrm{m}}(\vec{r}_\perp, \phi) \ , \tag{1.54}$$

where we assume the optical fields to have the same polarisation, and make the approximation that the gross part of the acoustic energy of the tl-modes is in the azimuthal direction (for the validity of this assumption, please refer to [SB15a]). This overlap integral also embodies the aforementioned important phase-matching condition for Brillouin scattering in a microresonator equation 1.48, namely separating the azimuthal integration leads to a term

$$\int d\phi e^{iM_{\mathrm{p}}\phi} e^{-iM_{\mathrm{s}}\phi} e^{iM_{\mathrm{m}}\phi} \ , \tag{1.55}$$

with integer $M$'s resulting in $g_0 \propto \delta_{|M_{\mathrm{p}}|+|M_{\mathrm{s}}|,|M_{\mathrm{m}}|}$ (for high frequency Brillouin optomechanics pump and Stokes are propagating in opposite directions, so the absolute values were chosen here for clarity). Assuming the azimuthal mode number matching to be fulfilled we are left with the overlap integral in the transverse plane. As in our geometry the Brillouin-active medium completely fills the cavity round-trip, this cancellation for all except one azimuthal mode is exact and an important difference compared to work done with bulk acoustic resonators [Ren+18], where coupling to a multitude of longitudinal modes occurs

and even changes depending on placement of the bulk sample within the optical cavity. This feature can therefore prove valuable in achieving single-mode optomechanical coupling.

If we define the mode field functions $E_i(\vec{r}_\perp)$ and $u_\mathrm{m}(\vec{r}_\perp)$ as normalised, such that $\int d\vec{r}_\perp |u_\mathrm{m}(\vec{r}_\perp)|^2 = A_\mathrm{m}$ and likewise for the optics, we can write down the bare coupling rate in terms of this overlap

$$g_0 = \gamma_e \sqrt{\frac{\hbar\omega^3}{8cv_\mathrm{a}n^3\rho}} \cdot \frac{1}{\sqrt{\pi D}} \cdot \int d\vec{r}_\perp E_\mathrm{p}(\vec{r}_\perp) E_\mathrm{s}(\vec{r}_\perp) u_\mathrm{m}(\vec{r}_\perp) \ , \tag{1.56}$$

where we assumed the optical fields having the same polarisation and the displacement field in the azimuthal direction. We see that, apart from the transverse mode overlap integral, the increase of the coupling rate with reducing the round trip length is only proportional to $1/\sqrt{\pi D}$. For spherical resonators, the coupling rate of equation 1.56 can be evaluated based on the analytical results for the optical [Ora02] and (pseudo-)longitudinal acoustic whispering-gallery modes [SB15b], or numerically for more general geometries. It is once again stressed here that at the current state this can merely serve as a confirmation/cross check for experimentally observed coupling rates, in the case that the participating modes can actually be identified. This is a challenge in itself, but has been accomplished for optical modes in [Sch+14]. The precision required to manufacture whispering-gallery resonators with optimized coupling rate based on achieving phase matching for a particular mode trio seems very challenging.

An important fact to point out here is, that a particular pair of optical resonances will generally couple to several acoustic eigenmodes sharing the same azimuthal mode index $M$, with individual optomechanical coupling rates $g_0^i$, which are also going to have individual detunings, based on the exact eigenfrequencies $\omega_\mathrm{m}^i$ of the acoustic modes. Here $i$ is an index labelling transverse modes. It can be assumed that the acoustic mode density decreases with stronger transverse confinement, such that the degree of mechanical multimodeness will on average be lower in such systems, and higher in e.g. a spherical geometry, which might be exploited for exploration of multi-mode physics. The typical case is trivially that one acoustic mode comes with the highest coupling rate and dominates the interaction

Hamiltonian in a hierarchy of coupling rates. The experimenter might then choose optical resonance pairs based on their degree of single-modeness or multi-modeness owing to such a coupling/detuning hierarchy. Depending on the achievable damping rates, it might be possible at cryogenic temperatures to obtain a "fingerprint" of the coupling/detuning landscape of acoustic modes by an OMIT type measurement (see outlook).

It is conceivable that the radiation pressure/moving boundary effect will slightly modify the optomechanical coupling strength, but it can be assumed that for our geometry the contribution will be negligible. An interplay of these different contributions to the optomechanical coupling in solid-state nanodevices was for example examined in [Rak+12].

### 1.5.3 Brillouin lasing

Once the round trip Brillouin gain in a resonator exceeds the round trip loss which an optical (Stokes) field experiences, thermally scattered Stokes light will be exponentially amplified via stimulated Brillouin scattering [CTS64], creating what is sometimes referred to as a Brillouin laser. Instead of relying on optical gain based on a population inversion, it is based on parametric gain. Thus it occupies somewhat of a middle ground between a conventional laser and an optical parametric oscillator [Yar65].

An approximate expression for the Brillouin lasing threshold power is given by [GMM09]

$$P_{\mathrm{thr}} = \frac{\pi^2 n^2 V \Delta\nu_{\mathrm{p}} \Delta\nu_{\mathrm{s}}}{c^2 g} \ , \tag{1.57}$$

where $V$ is the mode volume, $\Delta\nu_{\mathrm{p}}$, and $\Delta\nu_{\mathrm{s}}$ are pump and Stokes linewidths, respectively, and $g$ is the Brillouin gain. This expression should give an order of magnitude estimate of expected thresholds, where imperfect mode overlaps will increase the threshold.

Brillouin lasing was first experimentally observed in microresonators of fused silica and calcium fluoride [TC09; GMM09], and has since been observed in a variety of other geometries and materials. Sturman and Breunig showed in a detailled analysis [SB15a] how Brillouin lasing thresholds are affected by the transverse-longitudinal character of the pseudo-

longitudinal acoustic whispering-gallery modes in microresonators, especially long "tails" of the transverse component.

To the best of the author's knowledge, the role of the three-mode detuning in conjunction with the optomechanical mode overlap for Brillouin lasing in microresonators hasn't yet been fully appreciated in the literature. I think that the exact value of the detuning (as well as the optical mode overlap) will affect the Brillouin lasing thresholds. In the context of this thesis, Brillouin lasing was used from an early stage as an indicator of the presence of an optical mode pair with significant optomechanical coupling rate. Also, experiments were conducted in order to show the change in the degree of second-order coherence of the Stokes light across the Brillouin lasing threshold (see outlook). This thesis focussed on experimental advancements and does not aim to derive/advance the theoretical understanding of the Brillouin lasing threshold.

### 1.5.4 Beam splitter and two-mode-squeezing type Hamiltonians

All experiments in this work are operating in the so-called resolved sideband regime of cavity optomechanics. This means that the optical linewidth is much smaller than the mechanical frequency $\kappa \ll \omega_{\mathrm{m}}$, as discussed previously in section 1.2.2. From here onwards, by that we mean that the condition applies to both resonances of an optical mode pair (depending on their role called pump and Stokes (anti-Stokes) modes), while in conventional cavity optomechanics most of the time only one optical resonance of the cavity is considered, and the influence of other optical resonances can often be neglected [AKM14].

When exciting a particular carefully selected optical mode of the resonator with a coherent drive ("pump" laser), only either Stokes or anti-Stokes Brillouin scattering will be resonantly enhanced through the optical cavity's density of states, e.g. Stokes scattering when pumping on the second mode from the left in figure 1.13. Thus the situation is different from waveguide or bulk experiments, where the optical density of states is mostly flat and both Stokes and anti-Stokes scattering from thermal excitation is nearly equally probable.

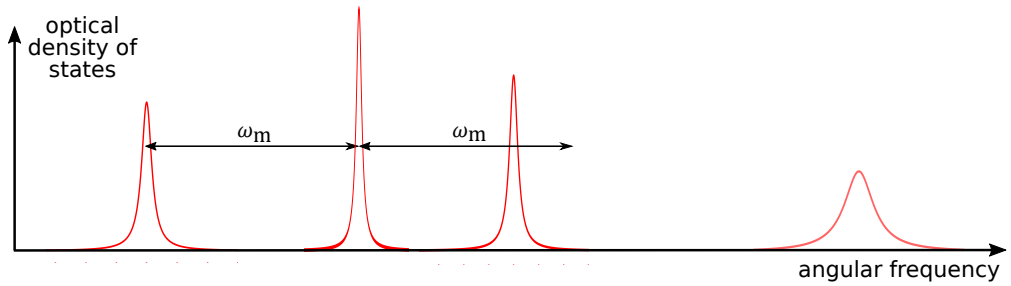


Figure 1.13: Example sketch of a cavity's optical density of states (pictorially). A particular pair of optical resonances (first and second from the left) is separated by the frequency $\omega_m$ of an acoustic eigenmode, such that Brillouin scattering occurs if the modes substantially overlap. While Stokes scattering is resonantly enhanced for photons occupying the second mode from the left, anti-Stokes scattering is suppressed by the cavity's density of states. What a spectrum can not show is the matching of azimuthal mode numbers, or a spread of the mechanical eigenmodes' frequencies, thus a frequency difference in the right range is only a necessary, but not sufficient condition for a potential significantly coupled mode trio.

Once a coherent drive is sufficiently strong, the quantum fluctuation of the drive field can be neglected, and we can approximate the interaction Hamiltonian with $a_{\mathrm{blue}} \to \alpha$ (parametric approximation) as

$$\frac{H_{\mathrm{int}}}{\hbar} = g_0(a_{\mathrm{blue}}a_{\mathrm{red}}^\dagger b^\dagger + a_{\mathrm{blue}}^\dagger a_{\mathrm{red}} b) \quad \to \quad \frac{H_{\mathrm{TMS}}}{\hbar} = G(a_{\mathrm{red}}^\dagger b^\dagger + a_{\mathrm{red}} b) \ , \tag{1.58}$$

introducing the pump-enhanced optomechanical coupling rate $G = g_0|\alpha|$. This Hamiltonian is frequently referred to as a two-mode squeezing (TMS) hamiltonian, in analogy of optical squeezing, where it was first studied [Hei+87]. It is of the same form as the Hamiltonian of parametric fluorescence in photonics, but the physics is somewhat different due to the very different speeds of light and sound waves, the substantial damping of sound waves, and the very different thermal occupations of field modes typically found in the acoustic versus the optical domain.

Analogously, we find the beam-splitter-type Hamiltonian, when driving on the red resonance of an optical mode pair

$$\frac{H_{\mathrm{BS}}}{\hbar} = G(a_{\mathrm{blue}}^\dagger b + a_{\mathrm{blue}} b^\dagger) \ . \tag{1.59}$$

This Hamiltonian resembles that of an optical beam splitter, however, here the beam splitter is between light and sound, rather than between two optical fields.

Two-mode squeezing and beam-splitter-type Hamiltonians are important as they form an operator basis for all bi-linear operators in optomechanics. In radiation pressure coupling they are only the consequence of an approximation, while fundamentally the interaction Hamiltonian is nonlinear (compare equation 1.16).

One can note that even if both the red and blue sideband were equally resonantly enhanced by the optical cavity in Brillouin optomechanics, the coupling would not be to the same acoustic mode, but to forward and backward propagating sound waves, thus a coupling to the mechanical position $X$, like in the bad cavity regime of standard radiation pressure optomechanics, cannot be easily engineered in Brillouin optomechanics with whispering-gallery resonators.

### Rotating frame and interaction picture

It is often helpful in practice to describe quantum phenomena of coupled harmonic oscillators in a "rotating frame". This corresponds to a rotation transformation being applied to the state vector, such that the time evolution of this new state vector under the free Hamiltonian (Hamiltonian excluding coupling terms) becomes simpler (or in some cases, trivial).

In order to go to a rotating frame, we apply a unitary transformation $R(t)$ to the state vector $|\Phi(t)\rangle = R(t)|\Psi(t)\rangle$, which will then obey a modified Schrödinger equation of the form

$$\begin{aligned} i\hbar\partial_t|\Phi(t)\rangle &= i\hbar\partial_t(R(t)|\Psi(t)\rangle) \\ &= (i\hbar\partial_t R(t))|\Psi(t)\rangle + R(t)i\hbar\partial_t|\Psi(t)\rangle \\ &= i\hbar\dot{R}(t)|\Psi(t)\rangle + R(t)H|\Psi(t)\rangle \\ &= i\hbar\dot{R}(t)R^\dagger(t)|\Phi(t)\rangle + R(t)HR^\dagger(t)|\Phi(t)\rangle \\ &= H'|\Phi(t)\rangle \ , \end{aligned} \tag{1.60}$$

with the Hamiltonian in the rotating frame $H' = i\hbar\dot{R}(t)R^\dagger(t) + R(t)HR^\dagger(t)$. This Hamilto-

nian can equivalently be written as $H' = R(t)(H - i\hbar\frac{d}{dt})R^\dagger(t)$.

Choosing $R(t)$ the adjoint of the free time evolution operator,

$$U_0^\dagger(t;t_0) = e^{i\omega_\mathrm{p}(a_\mathrm{p}^\dagger a_\mathrm{p}+\frac{1}{2})t+i\omega_\mathrm{aS}(a_\mathrm{aS}^\dagger a_\mathrm{aS}+\frac{1}{2})t+i\omega_\mathrm{m}(b^\dagger b+\frac{1}{2})t} \ , \tag{1.61}$$

would bring us to the interaction picture, while we are going to a rotating frame with respect to the optical pump and anti-Stokes fields, and to a detuned frame with respect to the mechanical field, so that

$$R(t) = e^{i\omega_\mathrm{p}(a_\mathrm{p}^\dagger a_\mathrm{p}+\frac{1}{2})t+i\omega_\mathrm{aS}(a_\mathrm{aS}^\dagger a_\mathrm{aS}+\frac{1}{2})t+i(\omega_\mathrm{m}+\Delta)(b^\dagger b+\frac{1}{2})t} \ , \tag{1.62}$$

with the optomechanical detuning $\Delta = \omega_\mathrm{aS} - \omega_\mathrm{p} - \omega_\mathrm{m}$, then we find that the full optomechanical Hamiltonian

$$H = \hbar\omega_\mathrm{p}\left(a_\mathrm{p}^\dagger a_\mathrm{p} + \frac{1}{2}\right) + \hbar\omega_\mathrm{aS}\left(a_\mathrm{aS}^\dagger a_\mathrm{aS} + \frac{1}{2}\right) + \hbar\omega_\mathrm{m}\left(b^\dagger b + \frac{1}{2}\right) + \hbar g_0(a_\mathrm{p}a_\mathrm{aS}^\dagger b + a_\mathrm{p}^\dagger a_\mathrm{aS} b^\dagger) \tag{1.63}$$

transforms to the Hamiltonian in the rotating frame

$$H' = \hbar g_0(a_\mathrm{p}a_\mathrm{aS}^\dagger b + a_\mathrm{p}^\dagger a_\mathrm{aS} b^\dagger) - \hbar\Delta b^\dagger b \ . \tag{1.64}$$

### 1.5.5 Other nonlinear effects

#### Thermal nonlinearity

One of the first things one notices when performing experiments with optical whispering-gallery microresonators is their thermal response. Changing the temperature of the material in the optical mode volume affects the refractive index and thus the frequency of optical resonances. Similarly the temperature affects also the linear dimensions of the cavity. Both these effects lead to a shift of optical resonance frequencies depending on the temperature.

In fused silica, probed at 1550 nm, we have $\frac{1}{n}\frac{\partial n}{\partial T} \approx 5.8 \times 10^{-6}/\mathrm{K}$ at room temperature,

and $\frac{1}{L}\frac{\partial L}{\partial T} \approx 5 \times 10^{-7}$/K [LF06]. The refractive index depends both on the temperature and probe light wavelength, and is most conveniently described empirically by Sellmeier formulae [Sel71]. For fused silica both thermal expansion and refractive index effects contribute to resonance shifts with the same sign at room temperature and the consequence is a red shift of optical resonance frequencies by approximately 10 pm/K (or 1.2 GHz/K). The thermo-optic coefficient for barium fluoride at 1550nm and room temperature is $dn/dT = -1.6 \times 10^{-5}$/K [LFK05; Web02].

The temperature dependence of the refractive index (thermo-optic coefficient) decreases as temperature decreases, both for fused silica and barium fluoride, thus that thermal effects can be assumed to play a significantly smaller role when operating around the base temperature of a 4 K cryostat.

A characteristic of the presence of thermal effects in a whispering-gallery resonator is an asymmetric non-lorentzian lineshape, which generally will depend on the sweep direction (blue to red or red to blue). In fused silica, upon sweeping blue to red, one will observe a so-called thermal triangle induced by the red shifting of the resonance during the laser scan, in which the laser becomes increasingly resonant with the line until eventually reaching zero detuning, after this point, the heating power drops leading to a rapid increase of detuning, resulting in a sharp flank observed in transmission. The exact shape of the thermal triangle depends on sweep speed, optical power and bulk mass (thermal inertia) of the resonator. For a depiction of a thermal triangle as observed in the experiments, see figure 2.9.

### Kerr ($\chi^{(3)}$) nonlinearity and four-wave mixing

Aside the optomechanical and thermal nonlinearities, the third-order nonlinear susceptibility $\chi^{(3)}$ of the optical materials studied here, also referred to as Kerr nonlinearity, gives rise to relevant physical effects. While only optical materials violating inversion symmetry possess a non-vanishing second order susceptibility $\chi^{(2)}$, which is associated with phenomena like difference and sum frequency generation or parametric fluorescence, all optical materials possess a third order susceptibility.

It can be introduced by writing down the polarisation induced in a medium by the electric field of a passing electromagnetic wave, and splitting it into a power series of the electric field

$$P = \epsilon_0 \chi^{(1)} E + \epsilon_0 \chi^{(2)} E^2 + \epsilon_0 \chi^{(3)} E^3 + \dots \,. \tag{1.65}$$

Classically, this can be thought of as arising from the anharmonicity of the potential associated with displacing the charge distribution of the medium out of equilibrium.

Most relevant in the context of this thesis, amongst Kerr-induced phenomena, is four-wave mixing. In microresonators it can lead to a type of parametric oscillation, called Kerr frequency combs, which have recently developed into an active field of investigation. Such a frequency comb is shown in figure 1.14. In this work, Kerr frequency combs arose as a

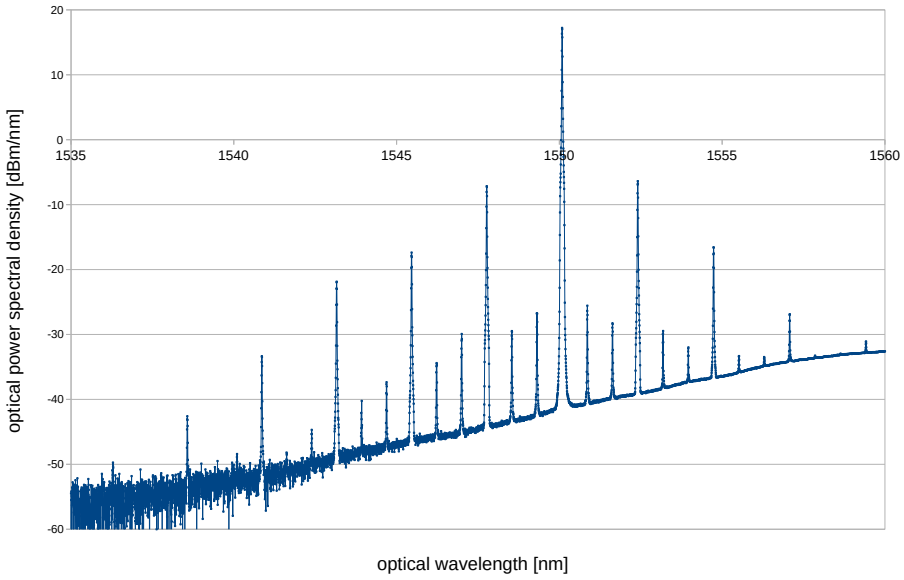


Figure 1.14: A Kerr frequency comb observed in a fused silica microrod resonator of $\approx$ 660 $\mu$m diameter with a free spectral range of 100 GHz (97.3 GHz measured). Phase matching is best three FSRs out from the pump resonance, and this is where parametric oscillation starts, then quickly the rest of the comb is populated by intercombination FWM. The background noise is most probably amplified spontaneous emission (broadband superluminescence) from the erbium doped fiber laser exciting the comb.

spurious unwanted effect during the push towards Brillouin optomechnical strong coupling, effectively opening an extra loss channel for the pump light. In degenerate four-wave mixing two pump photons are converted into a pair of photons, one redder and one bluer than the

original pump field colour. The sub-threshold phenomenon of spontaneous four-wave mixing can be exploited to engineer a heralded source of single photons (see outlook section).

Apart from the possibility of creating new colours of light, the Kerr nonlinearity in a medium also leads to a shift in the refractive index which light fields experience, proportional to the optical intensity present in the medium. This phenomenon is called the optical Kerr effect and it is quantified by the nonlinear refractive index $n_2$, which for negligible optical absorption, can be expressed as $n_2 = 3\chi^{(3)}/(4n_0^2\epsilon_0 c)$, where $n_0$ is the linear refractive index.

This effect is relevant, as it contributes to the optomechanical detuning dependence on the light power, combined with the thermal effects, which also play a significant role. It can be straightforwardly examined, by heating/cooling the structure to predefined temperatures and observing dispersion of resonance shifts, at negligible optical power, such as to controllably switch off the contribution of the optical Kerr effect. Further details about the optical Kerr effect and the role of self- and cross-phase modulation are discussed in section 3.3.1.

The effects of thermo-optic, thermal expansion and Kerr nonlinearities on the instantaneous frequency shift can be summarised as

$$\frac{\Delta\nu}{\nu} = \left( -\frac{1}{n}\frac{\partial n}{\partial T}\Delta T_{\text{mode}}(t) - \alpha\Delta T(t) - n_2\frac{P_{\text{cav}}(t)}{A_{\text{eff}}} \right) , \tag{1.66}$$

where $T_{\text{mode}}$ is the temperature of the mode volume, $T$ an effective temperature of the structure, $\alpha$ the thermal expansion coefficient of the material, and $A_{\text{eff}}$ is the effective mode area. As the precise modelling of the thermal response is non-trivial, this equation is put here rather for pedagocical purposes.

Nonlinearities, and especially the interplay of thermal and Kerr effects in whispering-gallery microresonators, have been studied since optical whispering-gallery microresonators became a focus of attention [BGI89]. The interplay has been studied in silica microsphere whispering-gallery resonators, with respect to chaotic behaviour [Fom+05], and its effect on observed lineshapes at different wavelength sweep speeds [Sch+08]. In the latter work, no clear separation of Kerr and thermal effects on the lineshape could be achieved.

# Chapter 2

# Experimental setup

## 2.1 Setup overview

In this chapter an overview of the most common experimental techniques used in this work is given. Details more specific to a certain experimental arrangement will be given in the respective results chapters.

The experimental setup for the work conducted in this thesis is centered around a fused silica (barium fluoride) microresonator mounted on a three dimensional translation stage, to which light is coupled in and out of via a tapered optical fiber. The experiment is all-fiber-based, operating at the telecommunications wavelength of 1550 nm. For the light sources, we use two erbium doped continuous wave fiber lasers, with ultranarrow linewidth (NKT Photonics Koheras Adjustik E series), which have a thermal tunability around their 1550 nm operating point of +/- 0.5 nm, as well as a piezo tuning port, which is important in order to tune to and stabilise the laser on whispering-gallery resonances of the microresonators. The thermal tuning spans a range larger than the resonator's optical free spectral range for typical resonator dimensions. The bandwidth of the thermal tuning is slow ($< 1$ Hz), while the piezo tuning bandwidth is of the order 10 kHz, with the piezo voltage span of 200 V corresponding to a laser frequency shift of $\sim 3$ GHz ($\sim 25$ pm), which is smaller than both typical optical free spectral ranges of the microresonators used ($\sim 100$ GHz), and smaller

than the Brillouin shifts of fused silica and barium fluoride (11 GHz and 8 GHz, respectively). In a typical experiment one of the lasers would take the role of pumping the optical cavity on a resonance. This laser would then be either actively stabilized ("locked") to remain in resonance, or forcing the cavity via its thermal response to stay resonant (passive/thermal lock). A schematic of the experiment is depicted in figure 2.1.

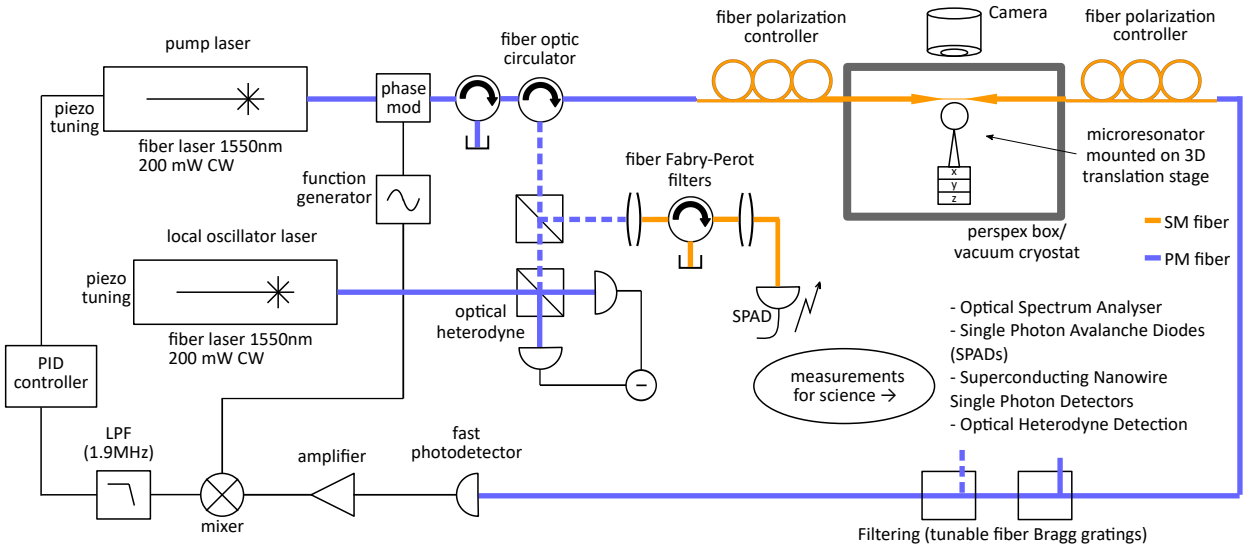


Figure 2.1: Setup overview. A whispering-gallery microresonator mounted on a 3D translation stage within a perspex box/cryostat chamber is coupled to via a tapered optical fiber. A pump laser can be scanned in frequency and the transmission is observed with a photodetector, showing optical cavity resonances. Pound-Drever-Hall locking can be applied to lock to cavity resonances. Light backscattered from the resonator is observed using different measurement aparatus. Optionally light can be filtered in the forward direction with tunable fiber Bragg gratings for Kerr four-wave mixing physics. The frequency difference of the lasers can be stabilized at the Brillouin shift frequency (∼10 GHz) by feeding back to the piezo tuning port of the local oscillator laser (not shown in scheme here).

During the course of this work, I first designed and set up a room-temperature setup, then later began to work on a cryogenic setup, which is currently ongoing and looking promising with respect to reaching the quantum regime starting from a temperature of 4 K. The results of strong optomechanical coupling and measurement-enhanced cooling were obtained using the initial room-temperature setup, all featuring fused-silica microresonators. This setup was also used to explore the Kerr-nonlinearity induced four-wave mixing physics, but following the design stage of the experiment (described in outlook), the focus was shifted towards Brillouin optomechanics. A silica microsphere resonator was also used with the room

temperature setup to observe the transition from thermal Brillouin scattering to Brillouin lasing (see outlook). The cryogenic setup was used for the measurements on single-phonon addition and subtraction to thermal states, where a barium flouride whispering-gallery microresonator was used. This experiment provides the platform for Brillouin optomechanics with crystalline (barium fluoride) whispering-gallery microresonators at cryogenic temperatures, which is currently ongoing (see outlook section).

To explore the optical mode structure, the pump laser is scanned in frequency with a ramp voltage on its piezo tuning port, while the optical cavity transmission is observed with a photodiode. Once a suitable experimental configuration, for example of optomechanical coupling, has been achieved, light backscattered from the resonator is separated from the pump via an optical circulator, to be subsequently measured by either an optical heterodyne detection scheme, or single-photon detectors.

As the optical cavity response is polarisation dependent, the setup is designed to use polarisation maintaining (PM) fiber wherever applicable in order to achieve highest possible stability of experimental conditions. The only parts of the setup which use non-polarisation maintaining single-mode fiber are the tapered fiber used to evanescently couple to the microresonator, which is connected to the PM part of the setup on both the input and output side with fiber polarisation controllers ("paddles"), and the fiber Fabry-Perot filters. Also, since for the Brillouin optomechanics experiments small signals (due to comparedly low thermal occupations at moderate temperatures) have to be measured in the back-scattering direction, it was decided to use angled connectors (FC/APC) throughout, to suppress back-reflections at interfaces.

## 2.2 Tapered fiber evanescent coupling to optical whispering-gallery modes

In the experiment, light is coupled in and out of the whispering-gallery mode resonators via a tapered optical fiber [Kni+97; CPV00]. This has proven to be a comparatively simple and

effective way of coupling. For this purpose the tapered fiber is brought into close proximity of the resonator surface (wavelength scale), such that the evanescent optical fields of the travelling tapered fiber modes spatially overlap with the optical whispering-gallery modes of the microresonator. This way, coupling between the side channel and the resonator can be achieved, which is formally equivalent to the coupling mirror in a one sided Fabry-Perot cavity [Yar00; AKM14].

Alternatives to this approach are e.g. prism coupling [BGI89] and coupling from an angle-cut optical fiber. Prism coupling is robust and has been one of the early approaches to couple to optical whispering-gallery modes, but alignment is challenging. It comes with the advantage that phase matching can be achieved by adjusting the incident angle at the total internal reflection, which can be useful when dealing with resonator materials with a large deviation of the refractive index from the tapered fiber index. Coupling with an angle-polished optical fiber has some advantages, like relative ease and robustness, and the possibility to adjust the face angle to achieve phase matching, but has the inconvenience that transmitted light is coupled to free space [Chi+10].

A tapered optical fiber, as used in the experiments, adjacent to a fused silica whispering-gallery resonator is shown in figure 2.2, and also in figure 2.8 together with a barium fluoride resonator.

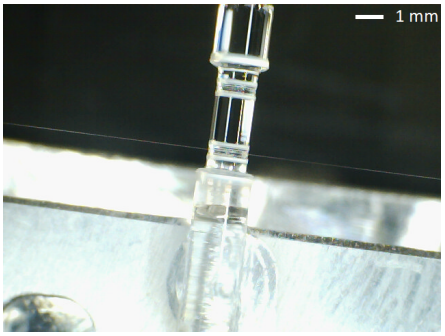


Figure 2.2: Tapered fiber with fused silica microrod resonator. The rod in the picture has two bulges supporting whispering-gallery modes, one of which is in use here being coupled to via the tapered optical fiber (faint white diagonal line).

### 2.2.1 Resonator and taper mounts

For room temperature experiments with fused silica resonators, the resonator was mounted on an aluminium plate with a V-groove, which itself was mounted on a three axis translation stage allowing for sub micrometer precision positioning in all three axes. The tapered optical fibers were glued to a U-shaped aluminium bracket, mounted with screws in an upright position. Then the resonator would be brought into proximity of the tapered fiber from beneath via adjustments of the translation stage. The approximate relative position of taper and resonator could be judged from a low magnification camera which was mounted above the arrangement and could be lowered through a circular cut-out of the perspex box enclosing the coupling setup. The adjustment knobs of the translation stage were accessible from outside the perspex box through recesses of the latter. Photos of this coupling/mounting setup are shown in figure 2.3.

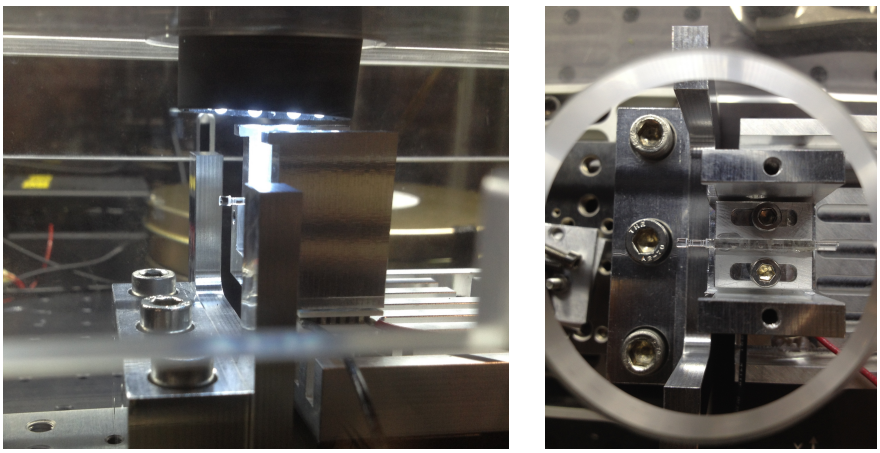

Figure 2.3: Resonator and tapered fiber mounts. Left: Side view along the taper axis. U-shaped taper holder, and resonator on aluminium mount. Right: View from the top through cut-out of the perspex box. This room-temperature setup was used for the demonstration of optomechanical strong coupling via Brillouin scattering and heterodyne-measurement-enhanced cooling of a mechanical mode of the cavity.

In preparation for cryogenic experiments a coupling setup was designed to fit inside the inner heat shroud of an attoDry800 low-vibration cryostat, which is able to cool a cold head down to 4 K and possesses vacuum feedthroughs for optical fibers. For this purpose, a taper holder in the form of an Invar steel-bracket was designed, which is connected to the cryostat base-plate by four brass posts. The low thermal expansion coefficient of the steel

ensures that the tapered fiber, which is glued to the bracket at room temperature, does not experience a significant length change of its support (the thermal expansion coefficient of fused silica is much smaller than that of, for example aluminium, which was used for room-temperature brackets). A picture of the cryogenic coupling setup is shown in figure 2.4. The vacuum is at this stage only required for the operation of the cryostat, as gas damping of the mechanical modes is expected to be negligible. The cryostat allows the sample temperature to be stabilised at any temperature between 4 K and $> 300$ K, which allows pre-cooling of a silica Brillouin optomechanical system to a thermal occupation of $\approx 8$, and the temperature stabilisation is beneficial to maintain a phase matching condition. This temperature stability was useful for the measurements presented in chapter 4.

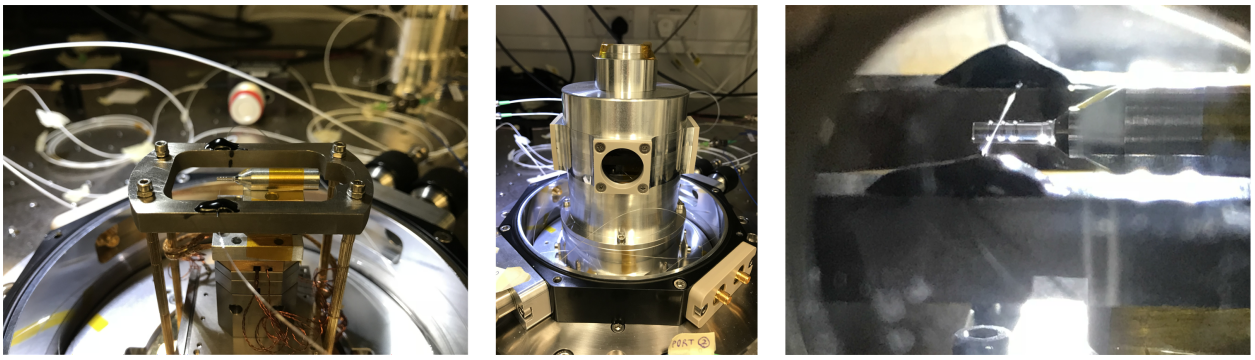

Figure 2.4: Cryogenic coupling setup. Left: Taper bracket (here aluminium, identically shaped Invar bracket used for cryogenic experiments) on brass posts and barium fluoride microrod resonator on 3D piezo translation stage, mounted within the vacuum chamber of an attocube attoDry800 cryostat. Middle: Inner heat-shroud and fiber. Right: View of barium fluoride microrod resonator with fused silica tapered fiber viewed through the windows of inner and outer heat-shrouds.

### 2.2.2 Polarisation control

The whispering-gallery modes of the microresonators are non-degenerate in polarisation, i.e. their resonance frequencies are different for different input polarisations. In fact, the natural polarisation axes of linear polarisation are given by the resonator's symmetry axis, and the axis orthogonal to it. Thus, once the linear polarisation of the light propagating through the tapered fiber is not aligned with either of these axes, a substantial portion of the light will not be resonant with respective resonances and thus be transmitted through the taper with

no extinction. On the other hand, adjusting the polarisation to couple to both polarisation resonance families of the cavity, allows one to examine both resonance families in a single measurement.

In any case, in order to be able to access a particular resonance of the microresonator, it is required to control the polarisation in the tapered fiber. The tapered fiber is made from, and is continually transforming into single mode fiber, which is connected to the polarisation maintaining fiber on both input and output sides. Due to the polar symmetry of the single mode fiber, there is no way to match the tapered fiber orientation with respect to the resonator, when splicing the connectors to the ends of the tapered fiber. Therefore polarisation controllers are required.

While in free-space optics polarisation control of light beams can be conveniently achieved using wave-plates, a standard way in fiber optics is to use "paddles", where a controlled torque on the single mode fiber induces birefringence. About 2 meters of single mode fiber (SMF-28 for 1550 nm) is rolled up inside these pedals, which, depending on their rotation, induce varying birefringence allowing (in principle) general rotations on the Poincaré sphere. In practice, the movement of the (typically three) paddles only approximate the action of lambda/4 and lambda/2 waveplates, and thus the desirable polarisation state can often only be achieved following an iterative procedure.

## 2.3 Microresonators

In the research conducted for this thesis, three different types of microresonators were used: Fused silica microrod resonators, which were used for most of the groundlaying experiments, fused silica microspheres, and barium fluoride microrod resonators. Some experimental aspects of these resonators will be discussed here.

### 2.3.1 Silica microrod resonators

Fused silica microrod resonators, with diameters ranging from 500 µm to 1.3 mm were fabricated in collaboration with the Del'Haye group, at the National Physical Laboratory (NPL) in Teddington, London, using a laser lathe, which was already set up at the NPL. To fabricate these resonators, a fused silica workpiece, in the shape of a rod, would be placed on a motorised spindle, while a focused $CO_2$ laser beam is moved across the spinning surface. After a first stage, where the end part of the spinning workpiece would be reduced in diameter to the nominal design diameter of the resonator by laser ablation, in a second step, the laser focus would be moved between two closely adjacent sites on the surface. The result of this procedure is two ring-shaped troughs, with the remainder between them forming a bulge around the perimeter, which can guide the light around by total internal reflection. The manufacturing procedure is described in detail in [DDP13]. These resonators were used for the experiments presented in chapters 3 and 5, and for the setup discussed in section 6.3.

The initial design choice in the diameter of 660 µm was oriented towards the photonics line of research, to achieve a free spectral range of 100 GHz, which is a common channel spacing in wavelength division multiplexing in telecommunication fiber networks. Resonator diameters in the range of 300 µm to 1.5 mm turned out to work well for Brillouin optomechanics experiments. There exists a trade-off between spatial confinement for high coupling rates, compare equation 1.52 (small resonators, strong lateral confinement, sparse mode forests), and the probability to find a mode trio in a resonator within the laser's tuning range. The radii of curvature of the resonator side wall via this fabrication method can be changed between 15 µm and 125 µm. For the Brillouin optomechanics experiments, a radius of curvature of approximately 40 µm was deemed to be desirable, and aimed for in the fabrication process. Fused silica microrod resonators are shown in figure 2.5, and a plot of a typical piezo laser frequency scan showing parts of the optical "mode forest" are shown in figure 2.6.

The optical resonance linewidths achieved with these resonators were mostly found to lie in the sub-MHz regime. The quality factors would then typically degrade on a time scale

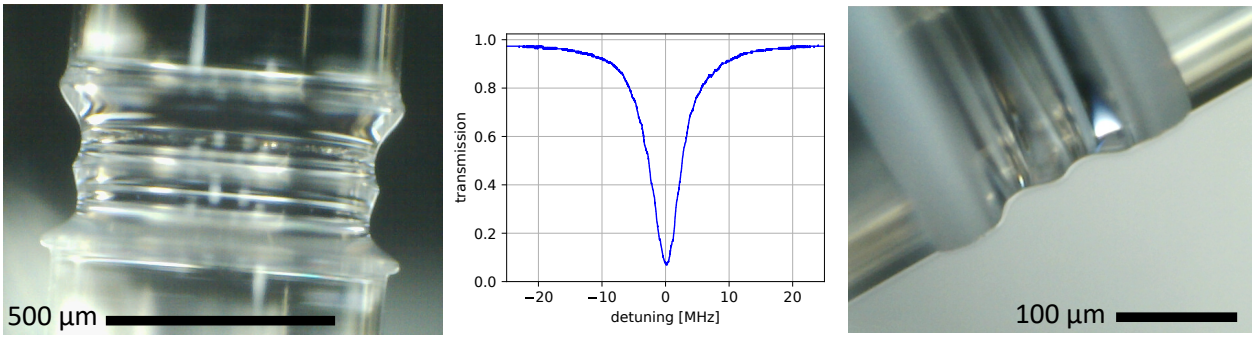


Figure 2.5: Left: Optical microscope image of a fused silica microrod resonator. The transverse confinement (radius of curvature) can be varied between 15 µm and 125 µm [DDP13]. Middle: Optical resonance close to critical coupling (the resonator's quality factor had already degraded at this stage due to dust). Right: Border of 1.3 mm diameter rod resonator with visible diffraction fringe. Next to the two troughs there is a matte finish to the surface due to deposited material.

of days to weeks (in ambient conditions). While the fast time scale can be attributed to adhesion of atmospheric water to the resonator surface [GSI96], the slower degradation time scale is connected to microscopic dust in the laboratory.

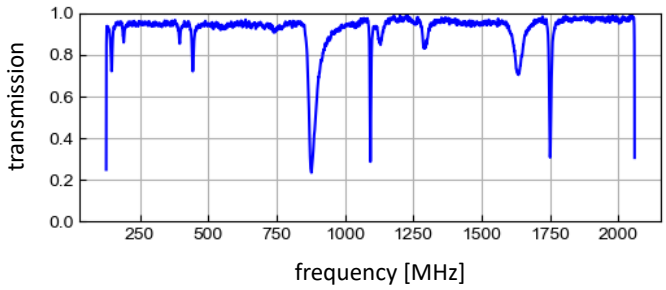


Figure 2.6: Example of an optical spectrum of a microresonator, showing part of the "mode forest". If the tapered fiber is in close proximity of the resonator surface it can induce substantial coupling between otherwise orthogonal whispering-gallery modes and lead to asymmetric and Fano lineshapes [Li+11] based on interference in the evanescent coupling region.

### 2.3.2 Silica microspheres

Some experiments were performed with fused silica microsphere whispering-gallery resonators. Predominantly they were used at the explorative stages of the work presented in chapters 3, 5, and section 6.3, as well as for the measurements presented in section 6.2

where freshly made resonators were benefitial in order to reach low (40 µW) Brillouin lasing thresholds. These resonators are relatively easy to make and have been used in many studies of nonlinear optical phenomena [Chi+10], [TC09]. In our case the manufacturing was done using a fiber splicing machine (Fujikura FSM100). The splicer allows for a mode of operation where a ball lens is formed at the stripped and cleaved end of a single-mode optical fiber. To do this, the fiber glass is melted by an electric arc discharge which is maintained for several seconds while the optical fiber is moved into the plasma. The surface tension leads to glass spheres with very low surface roughness. In this way optical whispering-gallery modes with quality factors in the $Q \approx 10^8$ range (i.e. sub-MHz optical linewidths) were obtained. The stalk is provided by the optical fiber which smoothly transitions into the sphere. The diameter range accessible using this manufacturing technique is approximately $200 - 500$ $\mu$m. A microscope image of such a resonator is shown in figure 2.7.

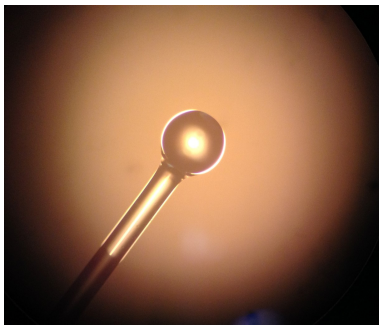

Figure 2.7: Fused silica microsphere resonator, as seen through a microscope. The sphere diameter is 300 µm. The resonator is produced by melting the tip of a single mode optical fiber with an electric arc discharge in a fiber splicer. The surface tension during the cool down phase of the melted glass leads to very smooth surfaces resulting in optical quality factors of $Q \approx 10^8$.

### 2.3.3 Barium fluoride crystalline microresonators

Due to their expected lower acoustic attenuation, microrod resonators of crystalline material were also developed during this thesis, with the main objective to facilitate the observation of true quantum behaviour in this Brillouin cavity optomechanical platform. As explained in the theory section, one particular point of attention here, apart from the desirable low optical loss, is the anisotropy of a given crystalline material. Barium fluoride was identified, and

confirmed, to have a unique combination of very low optical loss, and high elastic isotropy (see outlook), making it a strong contender for the material of choice, for this roadmap. The barium fluoride resonators described here were used for the experiments in chapter 4.

The procedure for making fused silica microrod resonators could not be applied to barium fluoride crystalline samples, as the process is based on melting and would have transformed the barium fluoride at the sample surface to an amorphous structure, which would not have the desirable low acoustic attenuation rates. Therefore a mechanical procedure involving a nano-lathe is required. Such a nano-lathe, employing a diamond cutting tool, was available at Australian National University, Canberra, where collaborators (J. Janousek, B. Buchler, and Ping Koy Lam) were able to cut and polish microrod resonators from commercially available crystalline barium flouride samples, which were sent to Australia. The radius of curvature for the initial barium fluoride resonators was chosen to be 40 µm, to match the geometry, and successful lateral confinement previously demonstrated, in the fused silica microresonators. Figure 2.8 shows the first barium fluoride rod containing three bulge shaped whispering-gallery resonators.

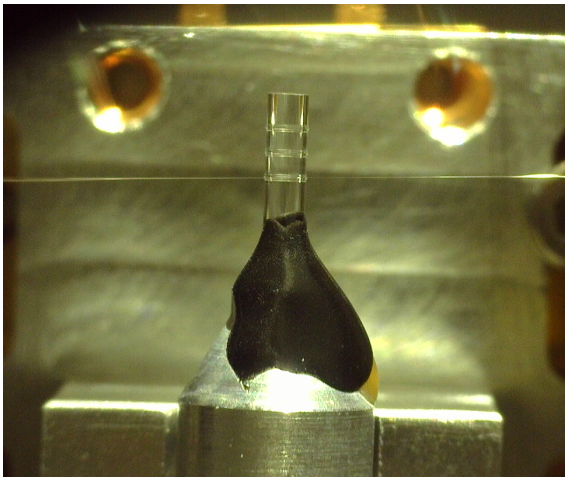

Figure 2.8: Barium fluoride microrod resonators. Shown is a rod of 1.5 mm diameter containing three bulge-shaped whispering-gallery resonators.

The diameter for the initial generation of barium fluoride resonators was 1.5 mm, due to limitations of the diamond nano-lathe manufacturing. These are more of practical than of fundamental nature, and future re-runs of the process should, according to our collaborators,

be able to achieve lower resonator diameters.

## 2.4 Lasers, modulation, locking

The light sources used were two erbium doped continuous-wave fiber lasers operating at 1550 nm, which have a maximum optical output power of 200 mW, each. Their output is linearly polarised along the slow axis of polarisation maintaining panda-style fiber, and the polarisation is maintained throughout the setup by the use of polarisation maintaining fiber. As discussed in chapter 3, section 6.2, and seen in figure 1.14, optical input powers in the range of a few tens of µW to a few tens of mW are sufficient to observe all nonlinear optical phenomena studied in this work. Typical circulating intracavity powers are then in the range of one to tens of W, corresponding to typical intensities of $\sim 10^{12}\,\mathrm{W/m^2}$.

### 2.4.1 Laser locking

It is desirable to be able to keep the laser light driving the cavity resonant with a particular optical eigenmode. To do this, two approaches were followed, which will now be briefly discussed here.

#### Passive/thermal locking

A simple way to keep a laser close to resonant with a resonance of a fused silica microresonator is to rely on the thermal self-stability of the system. Here, instead of the laser being stabilised with respect to a cavity resonance like in conventional feedback locking, the microresonator reaches a dynamic equilibrium, and follows the laser frequency. For this purpose, the laser is adjusted to a frequency slightly blue detuned from a resonance of interest. As a certain optical power building up in the mode volume heats the resonator, its resonances will have the tendency to shift to the red, as $\partial n/\partial T > 0$. As the resonance shifts to the red, the detuning grows and leads to less optical power in the mode volume, and thus less heat being

deposited. Depending on the particular laser wavelength, there can be a variety of dynamical equilibria reached on the blue flank of a cavity resonance. The technique is described in detail in [CYV04]. The authors point out that there is two different thermal time scales involved in this equilibration dynamics, namely the mode volume equilibrating to the resonator volume (fast time scale), and the resonator volume equilibrating to the environment/support (slower time scale). Depending on the particular geometry, this separation of time scales, and relative magnitude of the contributions, should continuously transform, e.g. an infinite rod resonator with a bulge will show quite different behaviour than in the reference.

Figure 2.9 shows a "thermal triangle" as frequently found in experiments with optical whispering-gallery resonators, which is mostly a consequence of the temperature dependence of the refractive index of the resonator material.

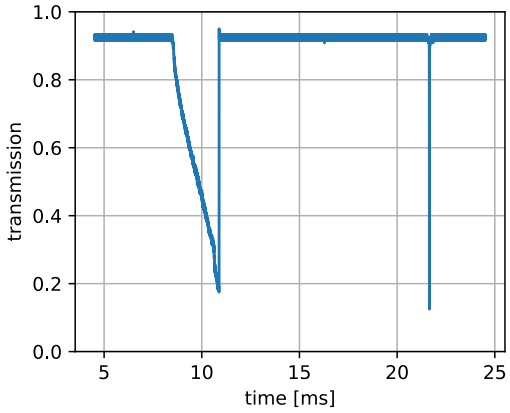


Figure 2.9: "Thermal triangle" with crossing of Brillouin lasing threshold in a fused silica microrod resonator. Shown is a laser frequency scan from blue to red (left), resulting in a triangular shaped resonance dip by virtue of the cavity thermally following the light source's frequency shift, and back from red to blue (right). The two dips correspond to the same cavity resonance. In this particular case the Brillouin lasing power threshold is crossed at some point along the flank, resulting in a kink, and the slope changes above the threshold as the thermal response is altered. The asymmetry between scanning directions vanishes in the limit of low probe light power.

It was experimentally observed that the slow time scale of the equilibration of the thermal lock was of the order of tens of seconds for a fused silica rod resonator diameter of 660 µm. While the technique is very simple and robust (no laser feedback is required), it has the limitation that one can neither drive exactly on resonance (zero detuning) nor red detuned.

It has also been observed that the stability of this locking technique does not only depend on the thermo-optic response, but also seems to depend on the interplay between Kerr and thermal nonlinearities. In the barium fluoride resonator, where $\partial n/\partial T$ has a different sign than silica at room temperature, the thermal lock is not stable, while one could assume that stable operation should be possible on the red flank of the resonance instead. It has also been shown [Gru+11] that the thermal bistability on the red slope of resonances in fused silica resonators can be compensated and made accessible by use of an additional laser field.

**Pound-Drever-Hall laser stabilisation**

An alternative to the thermal locking scheme is the Pound-Drever-Hall (PDH) locking scheme [Dre+83; Bla01]. Here the laser light impinging on the cavity is phase modulated using an electro-optic phase modulator, and the light from the cavity is subsequently detected and this signal mixed down with the original modulation signal. The light signal coming back from the cavity contains information about the phase response of the resonance, and it can be shown that the mixed down signal has a detuning dependence allowing it to be used as an error signal for feedback locking.

In practice choosing a modulation (sideband) frequency of 5-10 times the resonance linewidth has proven as a robust rule of thumb. The phase of the mixed down signal can be fine adjusted by changing the modulation frequency. It is desirable to chose the phase such that a long flank, with a zero crossing at zero detuning is achieved. The error signal is then fed into a PI (proportional+integrator) feedback controller, the output of which, is connected via a high voltage amplifier to the piezo tuning input of the laser. With the sign and PI gain adjusted correctly, it is then possible to keep the laser locked on a resonance of the cavity. An example of an error signal is shown in figure 2.10. Optimal choices of the phase modulation depth for PDH locking is e.g. also discussed in [Bla01].

It should be noted here, that while in Fabry-Perot cavities the phase response for PDH locking is usually derived from the reflection, in our single coupler ring resonator system, the signal is derived from the transmission.

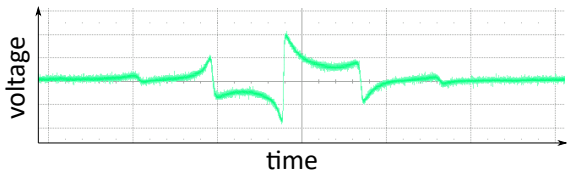


Figure 2.10: Pound-Drever-Hall error signal obtained with a whispering-gallery resonance of a microrod resonator. Phase modulated light that has probed the cavity is mixed down with the carrier to obtain a signal which has a linear flank around zero detuning, which can be employed as an error signal for feedback laser stabilisation.

## 2.5 Optical measurement devices

There were several optical measurement devices used for the experiments presented in this work, which will now be described here.

### 2.5.1 Photodetectors

Typically, the first measurement carried out with a microresonator is the exploration of its optical spectrum, including the determination of typical, and narrowest resonance linewidths. For this purpose, a triangle voltage signal is applied to the piezo tuning port of the laser, linearly ramping up and down between 0 and 200 V, at relatively low frequency of 10-100 Hz. This results in the laser wavelength being scanned linearly over a range of approximately 20 pm (2.5 GHz). With the laser frequency scanning, the transmission of light through the tapered fiber is monitored with a photodetector while the microresonator-taper distance is carefully reduced. Once evanescent coupling is achieved, the transmission through the taper will be affected, see e.g. figures 2.5, 2.6, or 2.9. The photodetector used for this purpose was a standard reverse biased InGaAs photodiode (Thorlabs DET01CFC).

### 2.5.2 Optical spectrum analyser

In order to confirm the occurrence of nonlinear optical phenomena like Brillouin lasing or stimulated four-wave-mixing (FWM) and Kerr frequency comb generation, commercial optical spectrum analysers were used (Yokogawa AQ6370D and Anritsu MS9740A). These

analysers require a certain light power level in order to overcome their electronic noise floor, thus precluding spectrally resolved measurements at the single/few photon level.

The minimum resolution of ≈ 3 GHz of the device allows the detection of stimulated Brillouin scattering/Brillouin lasing which occurs at a frequency separation between pump and Stokes light of ≈ 11 GHz in fused silica (≈ 8 GHz in barium fluoride). An example of a spectrum of Brillouin lasing in a fused silica microsphere is shown in figure 2.11.

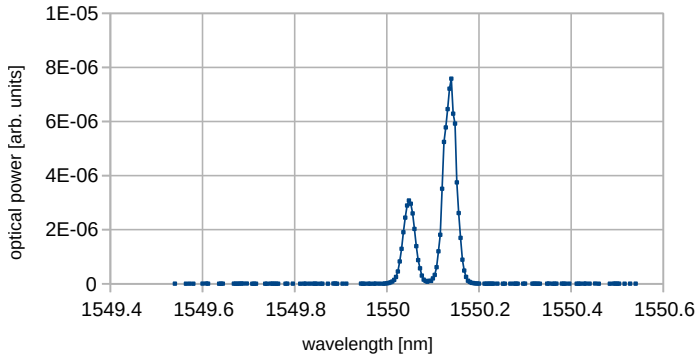


Figure 2.11: Optical spectrum analyser recording of Brillouin lasing. The spectral width is due to the minimum resolution bandwidth of the optical spectrum analyser.

### 2.5.3 Optical balanced homodyne and heterodyne detection

Whenever we want to measure a weak optical signal, for which the photocurrent would be smaller than the electronic noise floor in a conventional photodetector, balanced dyne detection can help, as it provides a purely optical linear amplification of the light field to be measured before the electronic noise of the photodetectors is added. This type of linear photodetection is used extensively in this work, e.g. in chapters 3, 4, and 5.

In optical balanced homodyne detection two photodiodes are arranged at the output ports of a 50:50 beam splitter and their photocurrents are subtracted One input arm receives a strong coherent state input referred to as the local oscillator, while the other input receives the optical field of interest. For homodyne detection, this field of interest is typically derived from a pump field with a rigid phase relationship with the local oscillator field (often from the same source, therefore the nomenclature greek ὁμός (homos) = same, common).

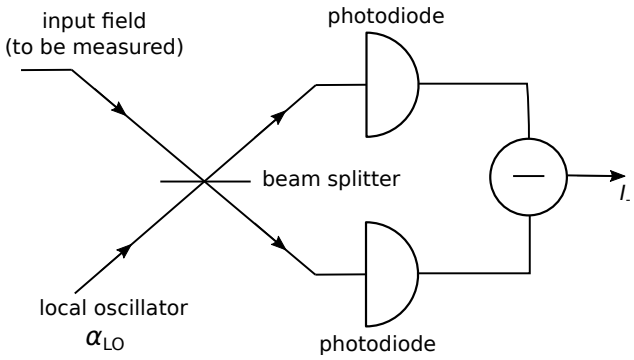


Figure 2.12: Optical balanced homodyne detection.

It can be shown then [Leo97] that the photocurrent difference is proportional to an optical field quadrature of the input state of interest, where the phase angle is defined by the local oscillator phase. The photocurrent difference is proportional to the difference of the photon numbers impinging on the photodiodes in the two arms, that is

$$I_- = I_2 - I_1 \propto \hat{n}_2 - \hat{n}_1 \approx \sqrt{2}|\alpha_{\mathrm{LO}}|\hat{X}_\theta \ , \tag{2.1}$$

where $I$ is intensity, $\hat{n}$ photon number, $\alpha_{\mathrm{LO}}$ coherent amplitude of the local oscillator field, and $\hat{X}_\theta$ a quadrature operator of the input field, and the quality of the approximation grows with the ratio of the amplitudes of the coherent state acting as the local oscillator, and the signal light field to be measured.

In our experiments, the beam splitter is a 50:50 fiber coupler, and the photodiodes and photocurrent subtraction are included in a high bandwidth (400 MHz cut-off) balanced photodetector (Insight Photonics model BPD-1). As the scattered light of interest in the experiment lies 11 GHz (8 GHz) away from the pump laser frequency, which exceeds the bandwidth of the balanced photodetector, a second laser is used for the local oscillator input. This laser is not phase locked to the pump laser and was for most experiments operated at a frequency displaced from the Brillouin scattered light frequency (anti-Stokes or Stokes frequency) by tens to a few hundred MHz.

This configuration can be called rotating homodyne detection, as the reference phase $\theta$ is rotating with respect to the signal field. In the limit of fast rotation, which is chosen for

the experiments in chapter 5, it is equivalent to optical heterodyne detection, in which two orthogonal quadratures of the light field are measured simultaneously, such that a complex amplitude is determined. Such a measurement corresponds to a projection onto a coherent state.

### 2.5.4 Single photon avalanche diode (SPAD) photodetectors

For the detection of single quanta of light (as used for the experiments in chapter 4 and section 6.2), avalanche photodiodes (APDs) were used. They have a similar principle of operation to that of the classic photomultipliers. The APDs are operated in Geiger mode, where a single excitation in the depletion zone of the diode causes an electrical avalanche which completely discharges the reverse bias of the diode (saturated regime of the gain-voltage characteristic). Together with control electronics which allow gate times, dead times and other parameters to be set, the APDs are housed in self-contained single-photon avalanche diode (SPAD) detector modules.

An important figure of merit of such a detector is its quantum efficiency in relation to its dark count rate. In the spectral range of 1550 nm, most photodiodes, as also the one in use here, are based on indium gallium arsenide (InGaAs). The quantum efficiency of the module can be adjusted, and for the experiments performed in this work, a quantum efficiency of 12.5 % was used. Characterisation of the device (IDquantique ID210), showed this efficiency to provide the best quantum efficiency to dark counts ratio.

## 2.6 Optical filtering

Spectral filtering of light in our experiments is required if we want to do single photon counting, as the photon counters cannot discriminate the colour of pump and signal photons, and the optical power of scattered light, which carries the information about the mechanical degrees of freedom, is much lower than the power of the unwanted elastically scattered

light at the pump laser's wavelength (mainly by Rayleigh scattering and elastic scattering off static surface/dielectric inhomogeneities). Similarly, also in four-wave mixing via the Kerr nonlinearity, filtering is required, where here the pump power which must be rejected is many orders of magnitude higher, as both, signal and pump fields, propagate in the forward direction. High frequency Brillouin optomechanics has the advantage over many other optomechanical platforms that signal light is backscattered, thus not ending up in the same spatial mode as the pump laser light (assuming appropriate separation using an optical circulator).

For the specification of the filtering performance, the following parameters can be identified: Reflected pump power, expected signal power, pump-signal frequency separation, signal bandwidth, insertion loss, and frequency tunability.

Amongst the options considered were fiber Bragg gratings and tunable fiber Fabry-Perot etalons. Fiber Bragg gratings have the advantage to be able to filter out a single frequency that satisfies the Bragg condition, and they can be made tunable, e.g. through the application of variable mechanical stress. For filtering Brillouin scattered light, the filter bandwidth is an important parameter. It needs to be substantially lower than the Brillouin shift in order to provide effective filtering (pump suppression). Commercial fiber Bragg gratings available at the time were unfortunately just shy of the required narrow bandwidths ($\ll$10 GHz). Mechanically tunable fiber Bragg grating filters were, however, in the end chosen for a project aiming at implementing a heralded single photon source (see section 6.3).

For the filtering in the Brillouin scattering experiments, two temperature tunable fiber Fabry-Perot filters were acquired. The free spectral range was chosen to be 25 GHz, such that with fused silica the pump light would be almost anti-resonant (11 GHz away), but also the filter frequency would not be twice the Brillouin shift, such that spurious Stokes (anti-Stokes) processes would be suppressed by the filter, too, when measuring anti-Stokes (Stokes) scattering.

The filter bandwidth (i.e. FWHM pass-band linewidth) was chosen at 120 MHz. This choice was based on expected signal bandwidths which would typically lie in the range of 1

to 100 MHz, and desired extinction ratio. The filter finesse 25 GHz/120 MHz $\approx$ 208 results in an extinction ratio (anti-resonant transmission) of $-42.4$ dB, as

$$T = \frac{T_{\max}}{1 + \left(\frac{2\mathcal{F}}{\pi}\right)^2 \sin^2(\phi)} \ , \tag{2.2}$$

with transmission $T$, maximum transmission $T_{\max}$, finesse $\mathcal{F}$, and round trip phase $\phi$ [ST07]. At the pump frequency offset (11 GHz), the extinction is still almost maximal at $-42.3$ dB for each filter, while at twice the pump frequency separation (i.e. the Stokes/anti-Stokes frequency) the filter is still suppressing light at $-33.7$ dB.

Two of these filters were used in series to suppress elastically scattered pump light in the single-phonon counting experiments. The filters were separated by an optical circulator in order to avoid undesired double-cavity effects (i.e. reflections). In combination, they suppress anti-resonant light by $2 \times 42.3$ dB $= 84.6$ dB. This attenuation factor was shown to be sufficient to reduce pump light on the photocounters to a negligible level (see chapter 4). The filters have an insertion loss of 1.0 dB and 1.3 dB, respectively.

# Chapter 3

# Brillouin optomechanical strong coupling

Here we are going to describe the experimental arrangement and theoretical considerations associated with the first observation of cavity optomechanical strong coupling via Brillouin scattering. Reaching the strong coupling regime with high-frequency acoustic waves is desirable for quantum technology development, including quantum memory, transduction and state-transfer, as well as fundamental studies of quantum behaviour of mechanical degrees of freedom. Achieving such coupling rates with GHz-range frequency phonons has proved challenging however, with a prominent hindrance being material- and surface-induced optical absorption in many materials.

Optomechanical strong coupling was observed between a pair of optical and an acoustic whispering-gallery mode of a fused silica microrod resonator via Brillouin scattering. An optical heterodyne detection scheme was used to measure anti-Stokes light backscattered from the microresonator and normal-mode splitting and an avoided crossing were observed in the recorded spectra, giving unambiguous evidence of strong coupling. A model was set up in order to theoretically understand the measurements. The optomechanical coupling rate reaches values as high as $G/2\pi = 39$ MHz by use of an auxiliary pump resonance, dominating both the optical ($\kappa/2\pi = 3$ MHz) and mechanical ($\gamma/2\pi = 21$ MHz) amplitude

decay rates of the cavity.

This chapter describes one of the main results of this thesis, and the author played a leading role in all aspects of this project apart from device fabrication, which was performed with collaborators at the NPL. The chapter is based on the supplementary information and main text of [Enz+19], first-authored by the author.

## 3.1 Introduction

Since its discovery in the 1920s [Bri22; Man26; RK28] Brillouin scattering has been a field of intense and diverse study. Brillouin scattering is a three-wave mixing process where an optical field interacts with a mechanical travelling wave and generates a frequency shifted optical signal. There are two sides to this light-matter interaction: electrostriction, where the electric field of light influences the mechanical wave, and photoelasticity, where the mechanical wave modifies the light field. Momentum and energy conservation allow two types of scattering processes: Stokes scattering, where the frequency of the light is downshifted giving rise to optical gain and is commonly observed in the form of stimulated Brillouin scattering or Brillouin lasing; and anti-Stokes scattering, where the light is upshifted giving rise to a mechanical damping mechanism. The phase-matching conditions for the anti-Stokes process utilized in this work are shown pictorially in figure 3.1, or see figure 1.11. Here, an optical pump field interacts with a counter-propagating mechanical wave generating a back-scattered optical anti-Stokes field. Since the pump and anti-Stokes fields are of a similar frequency, the wavevectors in this back-scatter process are related via $|k_{\mathrm{m}}| \approx 2|k_{\mathrm{p}}| \approx 2|k_{\mathrm{aS}}|$, where the subscripts m, p, and aS refer to the mechanical, optical pump, and anti-Stokes modes, respectively.

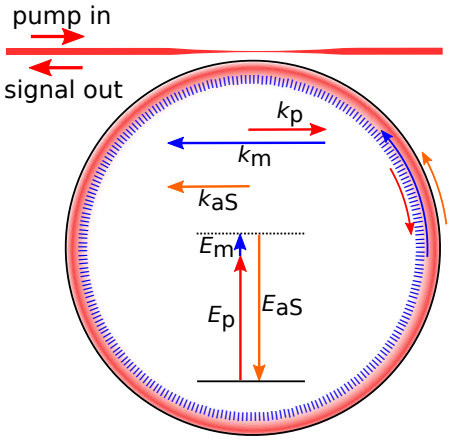


Figure 3.1: Optical and acoustic wave vectors and energy in microresonator Brillouin scattering.

## 3.2 Experimental setup

We used an optical microresonator that supports two optical whispering-gallery modes spaced by approximately the mechanical frequency, see figure 1.12. A pump laser drives the lower frequency auxiliary cavity mode (with small detuning $\delta_p$) to generate a large intracavity optical field. This field interacts with the mechanical mode and anti-Stokes light is resonantly scattered into the higher frequency optical mode. As there are only two optical modes that participate, the symmetry between Stokes and anti-Stokes scattering is broken and the Stokes scattering is strongly suppressed. We label the angular frequency mismatch between the mechanical frequency $\omega_m$ and the difference between the anti-Stokes resonance frequency $\omega_{aS}$ and the pump laser frequency $\omega_L$ by $\Delta = \omega_{aS} - \omega_L - \omega_m$. Note that the Brillouin frequency does not correspond to the free-spectral-range of the microresonator. Rather, the two optical modes with the desired frequency spacing are achieved by using different spatial modes that provide significant overlap with the mechanical traveling wave.

The Brillouin frequency shift in bulk silica at 1550 nm is 10.7 GHz, which is obtained from the simple relation $\omega_m \approx 2\omega v/(c/n)$. Here, $\omega_m$ is the Brillouin angular frequency shift, $v$ is the speed of sound in silica, $c$ is the speed of light in vacuum, $n$ is the refractive index, and $\omega$ is the optical angular frequency. To measure the Brillouin frequency shift we pumped the higher frequency mode of the optical mode pair and observed Brillouin lasing [TC09;

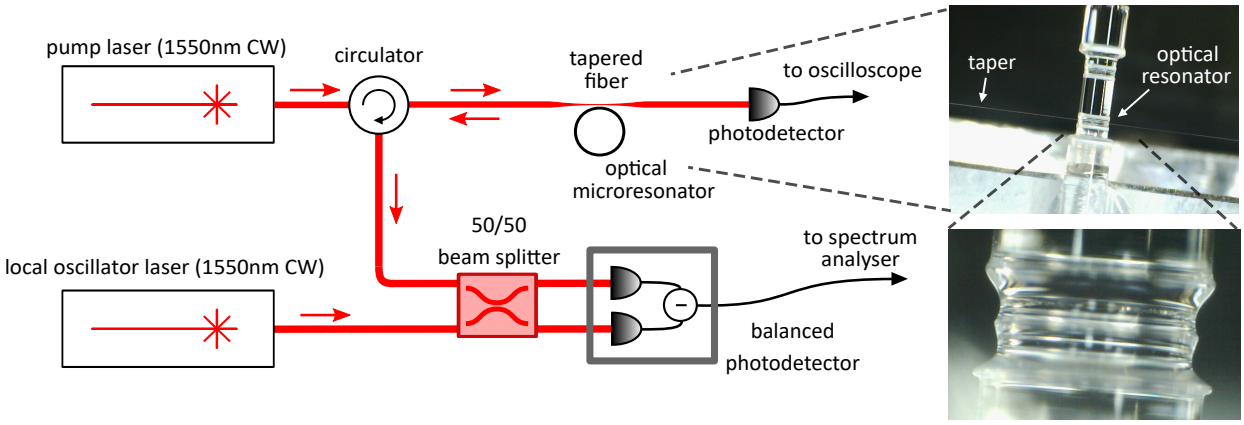


Figure 3.2: Experimental setup for observation of strong optomechanical coupling via Brillouin scattering.

GMM09; SB15a] using an optical spectrum analyzer. We observed $\omega_m/(2\pi) = (11.01 \pm 0.09)$ GHz, which is consistent with previous stimulated Brillouin scattering measurements in silica microresonators [TC09] and indicates that electrostriction is the dominant coupling mechanism. The mechanical frequency in the anti-Stokes experiments discussed below must lie very close to this value. We would also like to note here that, unlike in conventional optomechanics, the Brillouin frequency shift has very little dependence on both the optical power and temperature thus providing a robust and convenient platform.

A schematic of our telecom-fiber-based experimental setup is shown in figure 3.2. We utilize a fused silica micro-rod-resonator [DDP13] (diameter: 700 $\mu$m, lateral radius of curvature: $\sim 40$ $\mu$m, free-spectral-range: 90 GHz) evanescently coupled to a tapered optical fiber. The lower frequency cavity resonance of the pair is driven by a continuous-wave pump laser and a thermal lock [CYV04] is used, which stabilizes the resonance to the pump laser. The frequency upshifted light backscattered in the resonator is coupled out via the tapered fiber, separated from the pump light by an optical circulator, and mixed with a local oscillator on a 50:50 fiber-beam splitter. We then observe this signal with a balanced detector, implementing optical heterodyne detection with a local oscillator frequency offset of approximately 200 MHz. Heterodyne detection provides a large signal-to-electronic noise ratio and with the frequency offset allows the shape of the spectra to be easily observed. The heterodyne spectra are recorded using an electrical spectrum analyzer and the pump power is varied to

characterize the Brillouin optomechanical strong coupling features.

The optical damping rates are obtained from separate transmission spectra measurements. Figure 2.5 shows the cavity mode that enhances the anti-Stokes signal, which has an amplitude decay rate of $\kappa_{\mathrm{aS}}/2\pi = 3.0$ MHz. Similarly, the pump mode was measured to have an amplitude decay rate of 3.5 MHz. As the mechanical frequency is orders of magnitude larger than the damping rate of the anti-Stokes optical mode, the experiment lies deeply within the resolved sideband regime, i.e. $\omega_{\mathrm{m}} \gg \kappa_{\mathrm{aS}}$, which strongly suppresses the Stokes scattering. These optical damping rates have an intrinsic contribution for which the major loss mechanisms have been identified [GSI96] and an external contribution due to the tapered optical fiber coupling.

By fitting to our heterodyne spectra, the mechanical amplitude decay rate was estimated to be $\gamma/2\pi = (20.9 \pm 1.6)$ MHz. This value is similar to previous room-temperature in-fiber and bulk silica measurements at 1550 nm [Boy08; NTR97]. We would like to highlight that it has been previously observed that the mechanical damping in such materials is significantly reduced when operating at low temperature, reducing by an order of magnitude at approximately 4 K [VSH80; LC03]. In our experiment, we observe that the detuning $\Delta$

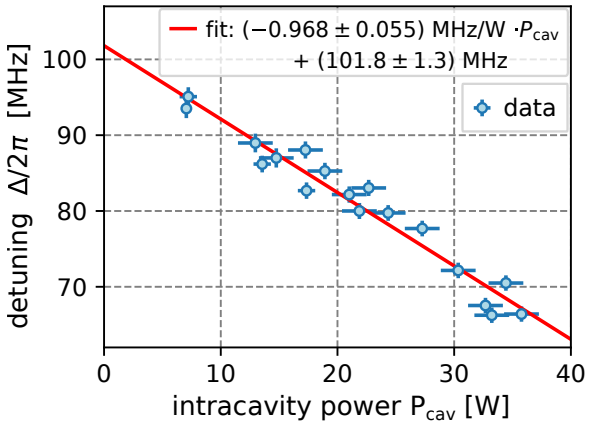


Figure 3.3: Optical power dependence of the detuning. The effect can be attributed to a combination of thermorefractive nonlinearity and the optical Kerr effect.

decreases linearly with increasing intracavity pump power, see figure 3.3. We attribute this detuning change to the optical Kerr effect and a possible contribution from the cavity-mode-

dependent thermo-refractive effect, which can both cause pump-power-dependent relative frequency shifts between the two optical cavity modes. Further details are discussed in section 3.5 on practical aspects.

## 3.3 Model

The Brillouin interaction may be described by a simplified Hamiltonian that couples the two optical modes via the high-frequency mechanical oscillation. Since we are coherently driving the optical pump mode, we approximate its associated field operator by a classical amplitude, which acts to enhance the optomechanical coupling strength. In a frame rotating with the two optical frequencies, we model our system with the Hamiltonian

$$\frac{H}{\hbar} = G\left(a_{\mathrm{aS}}^{\dagger} b + a_{\mathrm{aS}} b^{\dagger}\right) - \Delta b^{\dagger} b\,.$$

Here, $a_{\mathrm{aS}}$ and $b$ are the optical anti-Stokes mode and mechanical field operators, respectively, and $G = g_0|\alpha| \propto \sqrt{P_{\mathrm{cav}}}$ is the intracavity-pump-enhanced optomechanical coupling strength. Starting from this Hamiltonian, we compute the system dynamics using quantum Langevin equations. We then utilize optical input-output theory and compute the noise power spectral density of a rotating quadrature of the anti-Stokes field to describe the spectra observed with our heterodyne detection measurements (see section 3.3.3).

It is important to note here that the present experiment operates in a regime where the acoustic density of states is a quasi-continuum, as the damping rate of each mechanical eigenfrequency component is larger than the mechanical free-spectral range. Even in this regime, considering only one mode family, the optomechanical coupling can be regarded to be to a single mechanical mode, which is represented in our model by the field operator $b$, by virtue of the conservation of wave-vector which results in the azimuthal mode number conservation criterion implied by the choice of a pair of optical whispering-gallery resonances of the cavity (labelled "pump" and "anti-Stokes") with azimuthal mode numbers $M_{\mathrm{p}}$ and $M_{\mathrm{aS}}$, compare section 1.5.1.

While the azimuthal mode number is conserved, there will generally be coupling to multiple other transverse modes at smaller optomechanical coupling rates $g_0^i$, where $i$ is an index labelling the transverse mode, according to smaller values of the triple mode overlap discussed at equation 1.52 and 1.56, which we neglect here, for simplicity.

Consistent with our experimental observations detailed in the following section, our model indicates that, for zero detuning, the system undergoes normal-mode-splitting when $G > |\kappa_{\mathrm{aS}} - \gamma|/2$. We would like to clarify that satisfying this condition does not necessarily demonstrate that strong coupling has been achieved as the two peaks in the spectra may not be clearly resolved. The conditions of strong coupling are met, when the coupling strength $G$ becomes larger than the effective damping rates of the hybrid optical-mechanical modes, i.e. $G > (\kappa_{\mathrm{aS}} + \gamma)/2$ (see section 3.4.1). Under these conditions, a clearly separated avoided crossing may be observed in the spectra, which is an unambiguous signature of strong coupling.

### 3.3.1 System Hamiltonian

In this section we will derive in some more detail how the simplified Hamiltonian is obtained. The resonance frequencies of the two optical modes are separated by approximately the frequency of the mechanical resonance (see figure 1.12), and the system is coherently driven at a frequency close to the lower frequency (pump) optical resonance. The main dynamics then take place between the higher frequency optical (anti-Stokes) mode and the mechanical resonance, while the pump mode field is approximated as a complex-number, which acts to enhance the interaction strength. Additionally, we account for the optical Kerr effect in silica, which leads to pump-power dependent resonance frequency shifts of the pump and anti-Stokes modes. More details of the mechanical eigenmode structure and the Brillouin phase-matching conditions are given in section 1.5.1.

The Hamiltonian of this interacting three-mode system is then

$$\begin{aligned}\hat{H} =&\hbar g_0 \left(\hat{a}_{\mathrm{p}}\hat{a}_{\mathrm{aS}}^{\dagger}\hat{b} + \hat{a}_{\mathrm{p}}^{\dagger}\hat{a}_{\mathrm{aS}}\hat{b}^{\dagger}\right) + \hbar\omega_{\mathrm{p}}\hat{a}_{\mathrm{p}}^{\dagger}\hat{a}_{\mathrm{p}} + \hbar\omega_{\mathrm{aS}}\hat{a}_{\mathrm{aS}}^{\dagger}\hat{a}_{\mathrm{aS}} \\ &+ \hbar\omega_m\hat{b}^{\dagger}\hat{b} \quad + \hat{H}_{\mathrm{drive}} + \hat{H}_{\mathrm{SPM}} + \hat{H}_{\mathrm{XPM}} \,.\end{aligned} \tag{3.1}$$

Here $\omega_{\mathrm{p}}$, $\omega_{\mathrm{aS}}$, and $\omega_{\mathrm{m}}$ denote the angular frequencies of the pump, anti-Stokes, and mechanical modes; $\hat{a}_{\mathrm{p}}$, $\hat{a}_{\mathrm{aS}}$, and $\hat{b}$ are their field operators, respectively, and $g_0$ is the Brillouin optomechanical coupling strength. Throughout this chapter, hats denote operators, and tildes denote their Fourier transforms. The additional terms are given by [MW95]:

$$\begin{aligned}\hat{H}_{\mathrm{drive}} &= \hbar\Omega^* e^{i\omega_{\mathrm{L}}t}\hat{a}_{\mathrm{p}} + \hbar\Omega e^{-i\omega_{\mathrm{L}}t}\hat{a}_{\mathrm{p}}^{\dagger} \\ &\text{with} \quad \Omega = \sqrt{\kappa_{\mathrm{e}}P_{\mathrm{in}}/(\hbar\omega_{\mathrm{p}})},\end{aligned} \tag{3.2}$$

which models the coherent drive. The remaining terms are the all-optical self phase modulation (SPM) and cross phase modulation (XPM):

$$\hat{H}_{\mathrm{SPM}} = \frac{1}{2}\hbar\chi_{\mathrm{s}}(\hat{a}_{\mathrm{p}}^{\dagger}\hat{a}_{\mathrm{p}})^2 \,, \tag{3.3}$$

$$\hat{H}_{\mathrm{XPM}} = 2\hbar\chi_{\mathrm{x}}(\hat{a}_{\mathrm{p}}^{\dagger}\hat{a}_{\mathrm{p}})(\hat{a}_{\mathrm{aS}}^{\dagger}\hat{a}_{\mathrm{aS}}) \,. \tag{3.4}$$

Here, $\chi_{\mathrm{s}}$ and $\chi_{\mathrm{x}}$ are each linearly related to the $\chi^{(3)}$ third order susceptibility tensor.

### Optical Kerr effect

The third order nonlinearity present in silica leads to the optical Kerr effect, which is usually described in terms of a refractive index shift that linearly depends on the light intensity. The self- and cross-phase modulation terms lead to a frequency shift of the pump and anti-Stokes resonances depending on the circulating intensity in the pump mode. We can neglect self-phase modulation of the anti-Stokes mode since the power circulating in this mode is many orders of magnitude lower than the power in the coherently driven pump mode.

The pump-power dependent frequency shifts of the resonances are given by:

$$\omega_{\mathrm{p}} = \omega_{\mathrm{p},0} - \chi \hat{n}_{\mathrm{p}} \tag{3.5}$$

$$\omega_{\mathrm{aS}} = \omega_{\mathrm{aS},0} - 2\chi \hat{n}_{\mathrm{p}} \tag{3.6}$$

where the zero-subscripts indicate the initial frequencies, and we use the fact that in isotropic media (like fused silica) we have $\chi_{\mathrm{s}} = \chi_{\mathrm{x}} = \chi$, which assumes the pump and anti-Stokes modes have unity spatial overlap.

Equivalently, the resonance frequency shift can be expressed as due to an intensity dependent change in the refractive index:

$$n(I_{\mathrm{p}}) = n_0 + n_2 I_{\mathrm{p}} \quad \text{self phase modulation} \tag{3.7}$$

$$n(I_{\mathrm{p}}) = n_0 + 2n_2 I_{\mathrm{p}} \quad \text{cross phase modulation} \tag{3.8}$$

where $I_{\mathrm{p}}$ denotes the pump intensity, and $n_2$ is the nonlinear refractive index, which is proportional to $\chi^{(3)}$.

The factor of 2 in equations 3.6 and 3.8 is present if the modes have a perfect intensity overlap. The overlap is not unity in our experiment as the pump and anti-Stokes modes are not part of the same mode family and the precise value of the overlap is not known. Nevertheless, the mode overlap may be estimated from our experimental data, which is used to check the agreement between our model and the experiment. A more general treatment is given in the next section.

For the case where the optical modes overlap well, the refractive index change described by equations 3.7 and 3.8 leads to the detuning $\Delta = \omega_{\mathrm{aS}} - \omega_{\mathrm{L}} - \omega_{\mathrm{m}} = \omega_{\mathrm{aS}} - \omega_{\mathrm{p}} - \omega_{\mathrm{m}} - \delta_{\mathrm{p}}$ changing with the pump power circulating in the cavity $P_{\mathrm{cav}}$ in the following way:

$$\Delta - \Delta_0 = -\frac{\omega_p}{n}\left(2n_2\frac{P_{\mathrm{cav}}}{A_{\mathrm{eff}}} - n_2\frac{P_{\mathrm{cav}}}{A_{\mathrm{eff}}}\right) \quad , \tag{3.9}$$

where we used $\omega_{\mathrm{aS}} \approx \omega_{\mathrm{p}}$, and, $A_{\mathrm{eff}}$ is the effective mode area of the pump mode. Thus, including the initial (low pump-power limit) detuning $\Delta_0$, the detuning then depends on the pump power as

$$\Delta \approx \Delta_0 - \frac{\omega_0 n_2}{n A_{\mathrm{eff}}} \cdot P_{\mathrm{cav}} \quad . \tag{3.10}$$

It should be noted here that this expression is valid only when the pump and anti-Stokes modes overlap well. For smaller intensity overlaps and different mode shapes of the anti-Stokes mode, the slope of the linear relationship of equation 3.10 can change and even change sign.

The thermal effect that is used to lock the pump optical resonance to the pump laser [CYV04] is considered to have only a small effect on the detuning as the refractive index change due to temperature affects both the pump and anti-Stokes modes in the same way. Since the anti-Stokes mode is not perfectly overlapping with the pump mode whose absorption acts as the heat source, a significant difference of the thermo-optic responses of the two modes may also contribute to the power-dependent detuning observed in our experiment.

**Intensity overlap in the optical Kerr effect**

The refractive index change via the optical Kerr effect that an optical mode A experiences under the presence of optical power in a (partly) overlapping mode B (cross phase modulation) is given via

$$\Delta n_A = 2 n_2 \frac{\int I_B(\vec{x}) |u_A(\vec{x})|^2 d^3x}{\int |u_A(\vec{x})|^2 d^3x} \quad , \tag{3.11}$$

where $u_A(\vec{x})$ is the mode field function of mode A, defined via $\vec{E}(\vec{x},t) = \vec{E}_0 e^{-i\omega t} u(\vec{x})$, and $I_B(\vec{x})$ is the intensity distribution of mode B, given by

$$I_B(\vec{x}) = E_B \frac{c}{n} \frac{|u_B(\vec{x})|^2}{\int |u_B(\vec{x})|^2 d^3x} \quad , \tag{3.12}$$

where $E_B$ is the energy stored in mode B. Putting this together, we obtain the expression containing the intensity overlap integral:

$$\Delta n_A = 2n_2 E_B \frac{c}{n} \frac{\int |u_A(\vec{x})|^2 |u_B(\vec{x})|^2 d^3x}{\int |u_A(\vec{x})|^2 d^3x \int |u_B(\vec{x}')|^2 d^3x'} \tag{3.13}$$

The frequency shift of the resonance frequency $\nu_A = N\Delta\nu_{\mathrm{FSR}} = Nc/(n_A L)$ is then simply $\Delta\nu_A/\nu_A = -\Delta n_A/n_A$. Here $N$ denotes the longitudinal mode number, and $L$ the round trip length.

Similarly the expression for self phase modulation is

$$\Delta n = n_2 E \frac{c}{n} \frac{\int |u(\vec{x})|^4 d^3x}{(\int |u(\vec{x})|^2 d^3x)^2} \quad . \tag{3.14}$$

With $E = P \cdot t_{\mathrm{rt}}$, with $t_{\mathrm{rt}}$ the round trip time, and the effective mode area being defined as

$$A_{\mathrm{eff}} = \frac{(\int |u(\vec{x})|^2 d^2x)^2}{\int |u(\vec{x})|^4 d^2x} \tag{3.15}$$

we see that equation 3.14 applied to the pump mode is equivalent to the expression $\Delta n = n_2 I_{\mathrm{p}} = n_2 \cdot P_{\mathrm{cav}}/A_{\mathrm{eff}}$ used in the previous section.

Thus we obtain a more general expression for the contribution of the optical Kerr effect

on the detuning

$$\begin{aligned}
\Delta &= \Delta_0 - \frac{\omega_\mathrm{p}}{n}(\Delta n_\mathrm{aS} - \Delta n_\mathrm{p}) \\
&= \Delta_0 - \frac{\omega_\mathrm{p}}{n}\left(2n_2 E_\mathrm{cav}\frac{c}{n}\frac{\int |u_\mathrm{aS}|^2|u_\mathrm{p}|^2 d^3x}{\int |u_\mathrm{aS}|^2 d^3x \int |u_\mathrm{p}|^2 d^3x}\right. \\
&\qquad\qquad \left. -n_2 E_\mathrm{cav}\frac{c}{n}\frac{\int |u_\mathrm{p}|^4 d^3x}{(\int |u_\mathrm{p}|^2 d^3x)^2}\right) \\
&= \Delta_0 - \frac{\omega_\mathrm{p} n_2 L P_\mathrm{cav}}{n}\left(\frac{2L\int |u_\mathrm{aS}|^2|u_\mathrm{p}|^2 r dr d\theta}{L^2\int |u_\mathrm{aS}|^2 r dr d\theta \cdot \int |u_\mathrm{p}|^2 r dr d\theta}\right. \\
&\qquad\qquad \left. -\frac{L\int |u_\mathrm{p}|^4 r dr d\theta}{L^2(\int |u_\mathrm{p}|^2 r dr d\theta)^2}\right) \\
&= \Delta_0 - \frac{\omega_\mathrm{p} n_2}{n\int |u_\mathrm{p}|^2 r dr d\theta}\cdot P_\mathrm{cav}\cdot\left(2\frac{\int |u_\mathrm{aS}|^2|u_\mathrm{p}|^2 r dr d\theta}{\int |u_\mathrm{aS}|^2 r dr d\theta}\right. \\
&\qquad\qquad \left. -\frac{\int |u_\mathrm{p}|^4 r dr d\theta}{\int |u_\mathrm{p}|^2 r dr d\theta}\right),
\end{aligned} \tag{3.16}$$

where we changed to polar coordinates, carried out the $\phi$-integration, and are left with an expression containing the difference of an overlap and an inverse effective mode area in the azimuthal plane of the cylindrically symmetric microresonator.

This can be written as

$$\Delta = \Delta_0 - \frac{\omega_\mathrm{p} n_2}{n A'}\cdot P_\mathrm{cav} \quad , \tag{3.17}$$

where $A'$ relates to the mode overlap, has dimensions of an area, and is used in the main text. From the slope of the dependence of the detuning on the intracavity pump power (see figure 3.3), we experimentally determine $A' = 3.9\ \mu\mathrm{m}^2$, based on the assumption that only the optical Kerr effect affects the detuning.

For comparison, the mode overlap integral associated with the Brillouin optomechanical coupling is given by

$$I_\mathrm{om} = \int u_\mathrm{m} u_\mathrm{aS} u_\mathrm{p} r dr d\theta \quad , \tag{3.18}$$

where $u_\mathrm{m}$ is the mechanical mode field function, compare [Bah+12] or equation 1.56.

**Simplifying the Hamiltonian**

In order to simplify the Hamiltonian, we perform a change of basis in Hilbert space, transforming to rotating frames with respect to the pump and anti-Stokes modes, and to a detuned frame with respect to the mechanical mode. The self- and cross-phase modulation we treat as a detuning that depends on the intracavity pump power, as described in the previous section. We also linearize the cubic Brillouin interaction treating the pump-mode field operator as a complex number. Starting from the Hamiltonian

$$\begin{aligned}\frac{\hat{H}}{\hbar} =& g_0\left(\hat{a}_{\mathrm{p}}\hat{a}_{\mathrm{aS}}^{\dagger}\hat{b} + \hat{a}_{\mathrm{p}}^{\dagger}\hat{a}_{\mathrm{aS}}\hat{b}^{\dagger}\right) + \omega_{\mathrm{p}}\hat{a}_{\mathrm{p}}^{\dagger}\hat{a}_{\mathrm{p}} \\ &+ \omega_{\mathrm{aS}}\hat{a}_{\mathrm{aS}}^{\dagger}\hat{a}_{\mathrm{aS}} + \omega_m\hat{b}^{\dagger}\hat{b}\ ,\end{aligned} \tag{3.19}$$

we enter the rotating frame

$$\frac{\hat{H}}{\hbar} = g_0(\hat{a}_{\mathrm{p}}\hat{a}_{\mathrm{aS}}^{\dagger}\hat{b} + \hat{a}_{\mathrm{p}}^{\dagger}\hat{a}_{\mathrm{aS}}\hat{b}^{\dagger}) - \Delta\hat{b}^{\dagger}\hat{b}\ \ , \tag{3.20}$$

and then make the approximation

$$\hat{a}_{\mathrm{p}} \to \alpha = |\alpha|e^{i\phi} \qquad \hat{a}_{\mathrm{p}}^{\dagger} \to \alpha^* = |\alpha|e^{-i\phi}\ \ . \tag{3.21}$$

Picking $\phi = 0$, the Hamiltonian further simplifies to

$$\frac{\hat{H}}{\hbar} = G(\hat{a}_{\mathrm{aS}}^{\dagger}\hat{b} + \hat{a}_{\mathrm{aS}}\hat{b}^{\dagger}) - \Delta\hat{b}^{\dagger}\hat{b}\ , \tag{3.22}$$

where $G = g_0|\alpha|$ is the intracavity-pump-power enhanced optomechanical coupling strength. At this point we put in the intracavity power dependence for $G$ and $\Delta$ and we arrive at the Hamiltonian used to model our experiment.

It is useful to relate the intracavity pump amplitude $\alpha$ to the intracavity power via

$$|\alpha|^2 = \langle\hat{n}\rangle = \frac{P_{\mathrm{cav}}}{\hbar\omega_{\mathrm{p}}}t_{\mathrm{rt}} \tag{3.23}$$

where $P_{\mathrm{cav}}/\hbar\omega_{\mathrm{p}}$ is the mean circulating pump photon rate and $t_{\mathrm{rt}}$ the round trip time. We then have

$$G = g_0|\alpha| = g_0\sqrt{\frac{\pi n d}{\hbar\omega_{\mathrm{p}} c}P_{\mathrm{cav}}}\ . \tag{3.24}$$

Here, we inserted $t_{\mathrm{rt}} = \pi n d/c$, where $d$ is the resonator diameter.

### 3.3.2 Quantum Langevin equations of motion

The open quantum system dynamics of the mode operators can be computed using the quantum Langevin equations

$$\dot{\hat{a}}_{\mathrm{aS}} = -i\left[\hat{a}_{\mathrm{aS}}, \frac{\hat{H}}{\hbar}\right] - \kappa\hat{a}_{\mathrm{aS}} + \sqrt{2\kappa_i}\hat{a}_{\mathrm{in}}^{(i)} + \sqrt{2\kappa_e}\hat{a}_{\mathrm{in}}^{(e)}\ , \tag{3.25}$$

$$\dot{\hat{b}} = -i\left[\hat{b}, \frac{\hat{H}}{\hbar}\right] - \gamma\hat{b} + \sqrt{2\gamma}\hat{b}_{\mathrm{in}}\ . \tag{3.26}$$

Here, $\gamma$ is the mechanical (amplitude) damping rate, and $\kappa$ is the total optical (amplitude) decay rate, which consists of intrinsic $\kappa_i$ and extrinsic $\kappa_e$ contributions, where $\kappa = \kappa_i + \kappa_e$. The two optical vacuum inputs and the mechanical thermal input noise terms are described by $\hat{a}_{\mathrm{in}}^{(i)}$, $\hat{a}_{\mathrm{in}}^{(e)}$, and $\hat{b}_{\mathrm{in}}$, respectively. Substituting, $\hat{H}/\hbar = G(\hat{a}_{\mathrm{aS}}^{\dagger}\hat{b} + \hat{a}_{\mathrm{aS}}\hat{b}^{\dagger}) - \Delta\hat{b}^{\dagger}\hat{b}$, we solve these coupled differential equations using the Fourier transform to obtain

$$-i\omega\tilde{a}_{\mathrm{aS}} = -iG\tilde{b} - \kappa\tilde{a}_{\mathrm{aS}} + \sqrt{2\kappa_i}\tilde{a}_{\mathrm{in}}^{(i)} + \sqrt{2\kappa_e}\tilde{a}_{\mathrm{in}}^{(e)} \tag{3.27}$$

$$-i\omega\tilde{b} = -i(G\tilde{a}_{\mathrm{aS}} - \Delta\tilde{b}) - \gamma\tilde{b} + \sqrt{2\gamma}\tilde{b}_{\mathrm{in}}\ \ . \tag{3.28}$$

Writing this as a matrix equation

$$\begin{aligned}\begin{pmatrix} \kappa - i\omega & iG \\ iG & \gamma - i(\omega+\Delta) \end{pmatrix}\begin{pmatrix} \tilde{a}_{\mathrm{aS}} \\ \tilde{b} \end{pmatrix} \\ = \begin{pmatrix} \sqrt{2\kappa_i}\tilde{a}_{\mathrm{in}}^{(i)} + \sqrt{2\kappa_e}\tilde{a}_{\mathrm{in}}^{(e)} \\ \sqrt{2\gamma}\tilde{b}_{\mathrm{in}} \end{pmatrix}\ ,\end{aligned} \tag{3.29}$$

and solving for $\tilde{a}_{\mathrm{aS}}$ and $\tilde{b}$, we obtain

$$\begin{pmatrix} \tilde{a}_{\mathrm{aS}} \\ \tilde{b} \end{pmatrix} = D \cdot \begin{pmatrix} -i(\omega+\Delta)+\gamma & -iG \\ -iG & -i\omega+\kappa \end{pmatrix} \times ... \tag{3.30}$$

$$\times \begin{pmatrix} \sqrt{2\kappa_i}\tilde{a}_{\mathrm{in}}^{(i)} + \sqrt{2\kappa_e}\tilde{a}_{\mathrm{in}}^{(e)} \\ \sqrt{2\gamma}\tilde{b}_{\mathrm{in}} \end{pmatrix} \tag{3.31}$$

where

$$D = \frac{1}{(-i\omega+\kappa)(-i(\omega+\Delta)+\gamma)+G^2} \ . \tag{3.32}$$

**Cavity input-output theory**

The field operator that describes the output of the cavity via the external decay channel introduced by the taper is obtained via

$$\tilde{a}_{\mathrm{out}} = \tilde{a}_{\mathrm{in}}^{(e)} - \sqrt{2\kappa_e}\tilde{a}_{\mathrm{aS}} \ . \tag{3.33}$$

We can account for extra loss in the detection system by applying a beam splitter transformation with transmissivity $t = \sqrt{\eta_{\mathrm{det}}}$ and reflectivity $r = \sqrt{1-\eta_{\mathrm{det}}}$ to this output mode. Here, $\eta_{\mathrm{det}}$ is the total detection efficiency after the out-coupling from the cavity into the tapered fiber, and we obtain

$$\tilde{a} = \sqrt{\eta_{\mathrm{det}}}(\tilde{a}_{\mathrm{in}}^{(e)} - \sqrt{2\kappa_e}\tilde{a}_{\mathrm{aS}}) + \sqrt{1-\eta_{\mathrm{det}}}\tilde{a}_{\mathrm{in}}^{(bs)} \ , \tag{3.34}$$

where $\tilde{a}_{\mathrm{in}}^{(bs)}$ represents the vacuum noise introduced by the open port of the beam splitter, which models the loss associated with the finite detection efficiency. Putting in the first line

of equation 4.16 we obtain

$$\begin{aligned}\tilde{a}(\omega) &= 2\sqrt{\eta_{\rm det}}(iG)D\sqrt{\kappa_e\gamma}\ \cdot\ \tilde{b}_{\rm in} \\ &\quad - 2\sqrt{\eta_{\rm det}}\sqrt{\kappa_e\kappa_i}D(-i(\omega+\Delta)+\gamma)\ \cdot\ \tilde{a}_{\rm in}^{(i)} \\ &\quad + \sqrt{\eta_{\rm det}}(1-2\kappa_e D(-i(\omega+\Delta)+\gamma))\ \cdot\ \tilde{a}_{\rm in}^{(e)} \\ &\quad + \sqrt{1-\eta_{\rm det}}\ \cdot\ \tilde{a}_{\rm in}^{(bs)} \\ &= \quad A_1(\omega)\tilde{b}_{\rm in}(\omega) + A_2(\omega)\tilde{a}_{\rm in}^{(i)}(\omega) \\ &\quad + A_3(\omega)\tilde{a}_{\rm in}^{(e)}(\omega) + A_4(\omega)\tilde{a}_{\rm in}^{(bs)}(\omega)\end{aligned} \tag{3.35}$$

where in the last row we abbreviated the coefficients in front of the noise operators.

### 3.3.3 Heterodyne power spectrum

In our experiment we measure the light backscattered from the cavity using heterodyne (more precisely: rotating homodyne) detection. Given the mode $\hat{a}(t)$ impinging on the detector, this rotating field quadrature is described by

$$\hat{X}_\theta(t) = \frac{1}{\sqrt{2}}\left(\hat{a}^\dagger(t)e^{i\omega_{\rm het}t} + \hat{a}(t)e^{-i\omega_{\rm het}t}\right) \tag{3.36}$$

where the heterodyne frequency is given by the difference between the frequency of the anti-Stokes cavity resonance and the freely chosen local oscillator frequency $\omega_{\rm het} = \omega_{\rm aS} - \omega_{\rm LO}$.

We write the power spectral density in terms of the Fourier transformed quadrature operators

$$S_{XX}(\omega) = \int_{-\infty}^{\infty} d\omega' \langle \tilde{X}^\dagger(\omega)\tilde{X}(\omega')\rangle\ . \tag{3.37}$$

Firstly,

$$\tilde{X}(\omega) = \frac{1}{\sqrt{2}}\int dt e^{i\omega t}(\hat{a}^\dagger(t)e^{i\omega_{\rm het}t} + \hat{a}(t)e^{-i\omega_{\rm het}t}) \tag{3.38}$$

$$= \frac{1}{\sqrt{2}}(\tilde{a}^\dagger(\omega+\omega_{\rm het}) + \tilde{a}(\omega-\omega_{\rm het}))\ . \tag{3.39}$$

Re-inserting this expression, we obtain for the power spectrum

$$\begin{aligned} S_{XX}(\omega) = \frac{1}{2}\int d\omega' (\langle (\tilde{a}(-\omega-\omega_{\rm het}))^\dagger \tilde{a}(\omega'-\omega_{\rm het})\rangle \\ + \langle \tilde{a}(\omega-\omega_{\rm het})(\tilde{a}(-\omega'-\omega_{\rm het}))^\dagger\rangle) \ , \end{aligned} \tag{3.40}$$

where the two other cross terms are zero for a mechanical thermal state. In order to compute $S_{XX}(\omega)$, we take the expression for $\tilde{a}(\omega)$ from equation 3.35 and compute its adjoint

$$\begin{aligned} (\tilde{a}(\omega))^\dagger &= A_1^*(\omega)(\tilde{b}_{\rm in}(\omega))^\dagger + A_2^*(\omega)(\tilde{a}_{\rm in}^{(i)}(\omega))^\dagger \\ &\quad + A_3^*(\omega)(\tilde{a}_{\rm in}^{(e)}(\omega))^\dagger + A_4^*(\omega)(\tilde{a}_{\rm in}^{(bs)}(\omega))^\dagger \\ &= A_1^*(\omega)\tilde{b}_{\rm in}(-\omega) + A_2^*(\omega)\tilde{a}_{\rm in}^{(i)}(-\omega) \\ &\quad + A_3^*(\omega)\tilde{a}_{\rm in}^{(e)}(-\omega) + A_4^*(\omega)\tilde{a}_{\rm in}^{(bs)}(-\omega) \end{aligned} \tag{3.41}$$

Inserting this into equation 3.40 and assuming the noise terms are delta correlated we obtain

$$\begin{aligned} S_{XX}(\omega) = \frac{1}{2}\big[ &|A_1(-\omega-\omega_{\rm het})|^2 n_b \\ &+ |A_1(\omega-\omega_{\rm het})|^2(n_b+1) + |A_2(\omega-\omega_{\rm het})|^2 \\ &+ |A_3(\omega-\omega_{\rm het})|^2 + |A_4(\omega-\omega_{\rm het})|^2\big] \ . \end{aligned} \tag{3.42}$$

Then, inserting the $A$-terms from Eqs (3.35 & 3.41) gives

$$S_{XX}(\omega) = \frac{1}{2} \ + \ 2\eta_{\rm det}\kappa_e\gamma G^2 n_b \cdot \left(|D(-\omega-\omega_{\rm het})|^2 + |D(\omega-\omega_{\rm het})|^2\right) \ . \tag{3.43}$$

Lastly, putting in the expression for $D(\omega)$ from equation 3.32 we find the power spectrum given by Eq (3.44).

$$\begin{aligned} S_{XX}(\omega) &= \frac{1}{2} \ + \ 2\eta_{\rm det}\kappa_e\gamma G^2 n_b \times \\ &\times \left( \frac{1}{(G^2 - (\omega+\omega_{\rm het})(\omega+\omega_{\rm het}-\Delta) + \kappa\gamma)^2 + ((\omega+\omega_{\rm het})\gamma + (\omega+\omega_{\rm het}-\Delta)\kappa)^2} \right. \\ &+ \left. \frac{1}{(G^2 - (\omega-\omega_{\rm het})(\omega-\omega_{\rm het}+\Delta) + \kappa\gamma)^2 + ((\omega-\omega_{\rm het})\gamma + (\omega-\omega_{\rm het}+\Delta)\kappa)^2} \right) \ . \end{aligned} \tag{3.44}$$

## 3.4 Observation of normal-mode splitting and avoided crossing

To characterize our Brillouin optomechanical system, we record the heterodyne spectra for a wide range of intracavity pump powers. As $P_{\mathrm{cav}}$ increases, the optomechanical coupling rate increases in proportion to $\sqrt{P_{\mathrm{cav}}}$, and simultaneously, the detuning $\Delta$ changes linearly with $P_{\mathrm{cav}}$. We then record and fit the heterodyne spectra to obtain estimates of the experimental parameters, aside from the two optical decay rates measured previously, and excellent agreement between our model and the data is found. We would also like to highlight here that the optical resonator does not exhibit optical mode splitting through backscattering from imperfections of the material [KSV02], which enabled us to more easily confirm that the signals observed originate from the Brillouin optomechanical interaction. We plot and analyze the results of this work in terms of the intracavity pump power instead of the input pump power, so that the dependence on the pump detuning $\delta_{\mathrm{p}}$ and taper coupling conditions is removed. This way also provides greater convenience, as the optomechanical coupling rate $G$ and detuning $\Delta$ directly depend on $P_{\mathrm{cav}}$. At close to critical coupling, the intracavity power is approximately the input power multiplied by $\mathcal{F}/\pi \approx 4000$, where $\mathcal{F}$ is the cavity finesse.

In figure 3.4 a subset of the observed heterodyne spectra with theoretical fits is plotted. These plots show typical observed spectra, where the detuning varies from large and positive, through zero, to negative, whilst the opto-mechanical coupling rate increases. The spectra comprise a double peak structure on top of a flat optical vacuum background, where both the widths and center frequencies of the peaks change as the intracavity power changes. For low pump power and large positive detuning, the spectrum contains mainly a single narrow peak (figure 3.4 A). As the pump power is increased the strength of the signal grows and a second side peak becomes more pronounced (figure 3.4 B). As the power is further increased (figure 3.4 C), two well separated approximately symmetric peaks are observed. At this power, the coupling rate dominates over all damping rates and the detuning in the system. For our

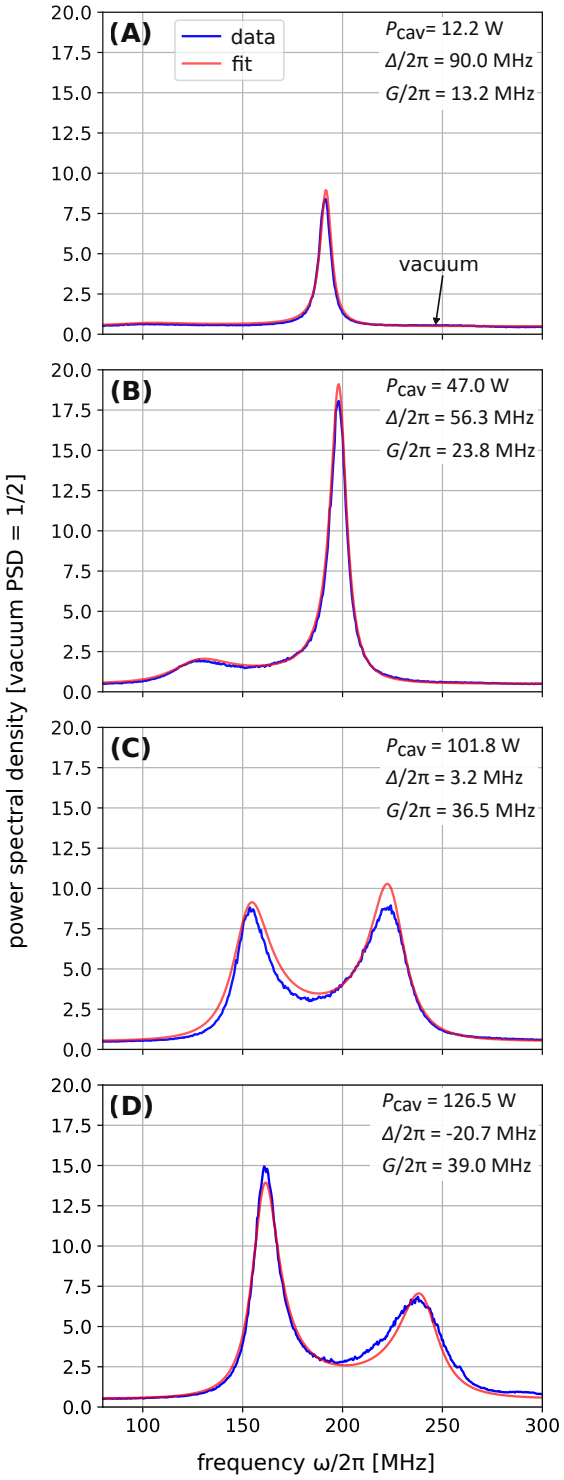


Figure 3.4: Observed Brillouin optomechanical anti-Stokes spectra. Power spectral densities of the Brillouin anti-Stokes heterodyne signal (blue) with theoretical fits (red). The spectra are normalized such that a vacuum input corresponds to a value of 1/2. The heterodyne frequency is 190 MHz. As the intracavity pump power is increased from (A) through to (D), the detuning decreases, and the coupling rate increases. As the detuning goes through zero, an avoided crossing and normal mode splitting are observed, see plot (C).

particular physical implementation, the detuning passes through zero at this point and the heights and widths of the two peaks observed are approximately equal. The two peaks in the spectrum correspond to the in-phase and out-of-phase hybrid optical-mechanical modes, being the eigenstates of the system in the strong coupling regime. The peaks are spaced by $2G$, and their widths are given by the hybrid optical-mechanical damping rates. As the pump power is yet further increased, the peak to the left now becomes stronger and narrower compared to the peak on the right (figure 3.4 D), and the separation between the two peaks further increases.

Figure 3.5 plots the observed coupling rate with intracavity pump power for our complete set of measurements. The data fits very well to the model and the predicted scaling $G = g_0|\alpha| \propto \sqrt{P_{\mathrm{cav}}}$ is observed. From a fit to this data we observe that the coupling rate increases by (3.605±0.016) MHz $\mathrm{W}^{-1/2}$ of intracavity pump power. To aid comparison we have overlaid the mechanical amplitude decay rate, the optical amplitude decay rate, and the hybrid-mode damping rate $(\kappa_{\mathrm{aS}}+\gamma)/2$, on this plot. It is seen that the coupling rate surpasses the hybrid-mode damping rate at an intracavity power of less than 10 W, corresponding to a very low input-pump power for these silica systems of only 2.5 mW. With increasing pump power, we can go deeply into the strong coupling regime, achieving a very high coupling rate of approximately 40 MHz, which exceeds the mean of the decay rates by a factor of more than 3.25. Using this fit result for $G$ and knowledge of the resonator geometry, we estimate the underlying Brillouin optomechanical coupling rate to be $g_0/2\pi = (396.5 \pm 1.8)$ Hz, which is consistent with previous theoretical related work on Brillouin Stokes scattering [Wol+15; SS16; VBV16; ZH16; Huy+16].

In figure 3.6 the observed evolution of the heterodyne spectrum with varying intracavity power is shown. As the intracavity power increases, a second lower frequency peak appears and grows, comes closer in frequency to the first peak and then the separation increases as the optomechanical coupling rate further increases. This is an avoided crossing, which is an unambiguous signature of strong coupling. In contrast to the more common avoided crossing plots, where the system eigenfrequencies are plotted against the detuning, here, we plot

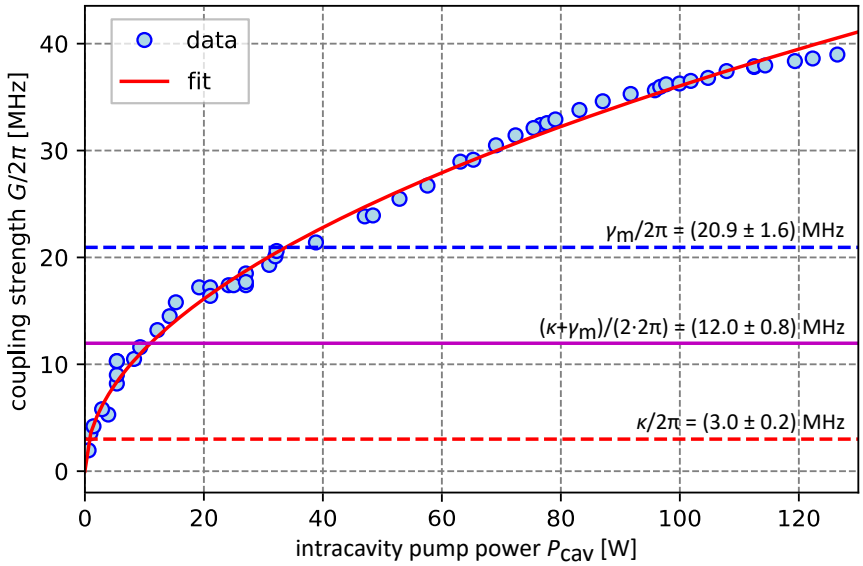


Figure 3.5: Brillouin optomechanical coupling rate vs damping rates. Observed coupling strength, as determined from the measured spectra, plotted with the intracavity pump power. The expected square-root scaling with the intracavity power is observed and the input-pump powers used were up to 30 mW. The coupling rate achieved far exceeds the damping rates of the system allowing us to go deeply into the strong coupling regime (above the purple line).

against the intracavity power, which acts as a proxy for the detuning because the detuning changes linearly with the intracavity power. Our theoretical model for the heterodyne spectrum with intracavity power is plotted in figure 3.7 (A) for our experimental parameters. This model accounts for both the intracavity power dependent coupling and detuning, and we find excellent agreement with our observations plotted in figure 3.6 (B) for comparison. An avoided crossing can be confirmed from our data (figure 3.4, figure 3.6) by noting that at the point where $\Delta \approx 0$ is reached ($G/2\pi \approx 36$ MHz , $P_{\mathrm{cav}} \approx 100$ W) a splitting is observed in the spectrum. Such a splitting would not be present at $\Delta \approx 0$ if an avoided crossing were not present. For convenience, a list of the main experimental parameters is given in table 3.1.

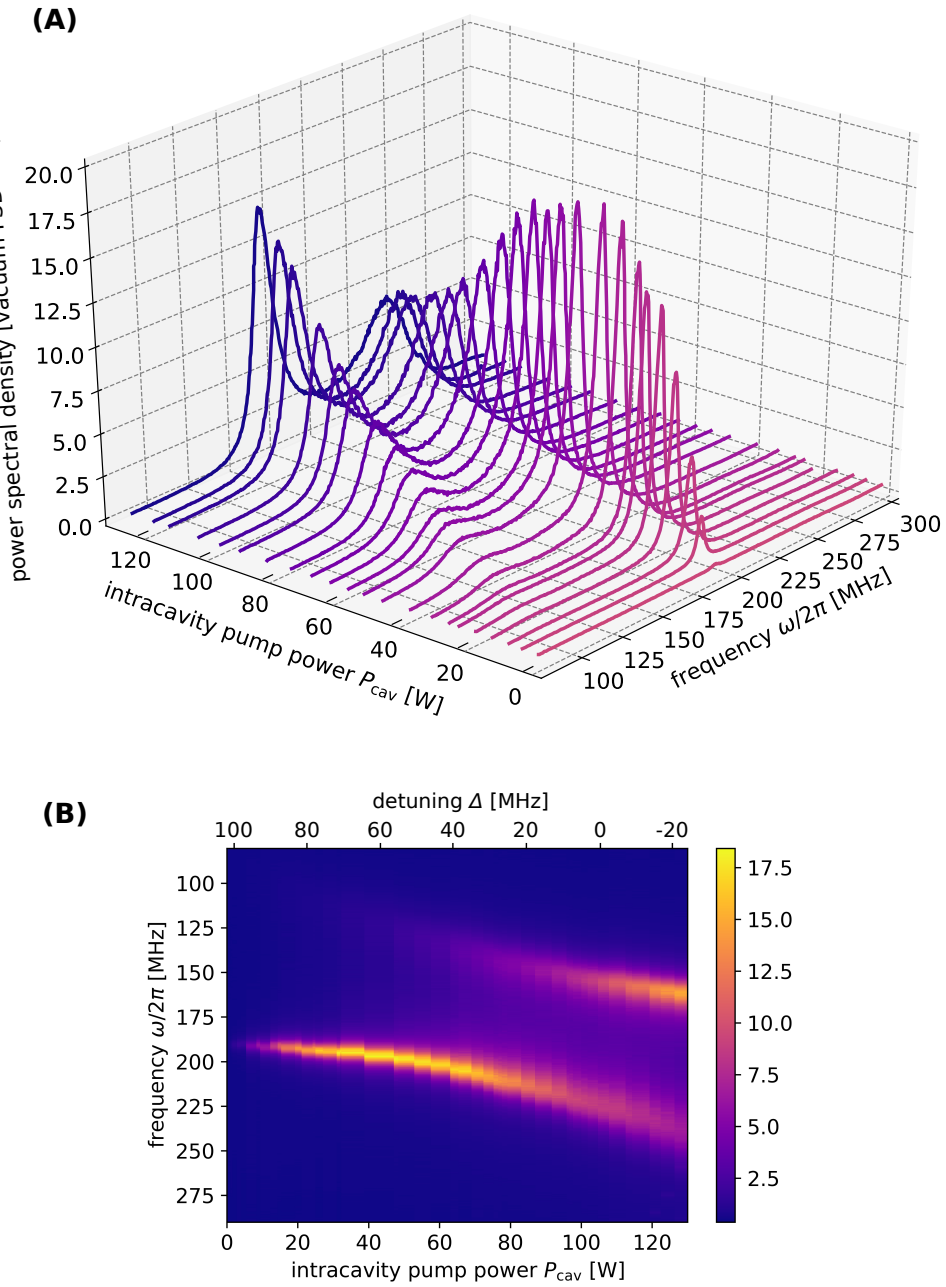


Figure 3.6: (A) Experimentally observed heterodyne spectra of the anti-Stokes scattered light with varying intracavity pump power. As the power increases, the point of zero detuning is crossed, where an avoided crossing is clearly observed. (B) Measured spectra in a colour-coded heatmap 2D plot with intracavity pump power. Note the excellent agreement between theory (figure 3.7 A), which includes the power dependent detuning, and experiment.

Table 3.1: Microresonator parameters achieving Brillouin optomechanical strong coupling.

| **Parameter** | **Value** |
|---|---|
| Microresonator diameter | 700 $\mu$m |
| $\omega_{\mathrm{aS}}/2\pi \approx \omega_{\mathrm{p}}/2\pi$ | 193 THz ($\lambda \sim 1550$ nm) |
| $\kappa/2\pi$ | 3.0 MHz |
| $\omega_{\mathrm{m}}/2\pi$ | 11.0 GHz |
| $\gamma/2\pi$ | 20.9 MHz |
| Anti-Stokes quality factor $Q_{\mathrm{aS}}$ | $3.2 \times 10^7$ |
| Pump quality factor $Q_{\mathrm{p}}$ | $< 2.8 \times 10^7$ |
| $\Delta/2\pi$ | -20 ... +102 MHz |
| $g_0/2\pi$ | $(396.5 \pm 1.8)$ Hz |
| Input pump power $P_{\mathrm{in}}$ | 0 ... 30 mW |
| Intracavity pump power $P_{\mathrm{cav}}$ | 0 ... 126 W |
| $G/2\pi$ | 0 ... 39 MHz |

### 3.4.1 Normal mode splitting and strong coupling condition in the model

If the Brillouin optomechanical coupling between the anti-Stokes and mechanical modes is sufficiently strong then normal-mode splitting and an avoided crossing will be observed in the spectra. This phenomenon is associated with the emergence of hybrid optical-mechanical modes.

In order to find the eigenfrequencies and damping rates of the system we diagonalize a non-Hermitian Hamiltonian that includes the damping terms. These terms are chosen such that in the Heisenberg equation of motion they explicitly produce the same damping terms as found in the Langevin equations of motion.

The non-Hermitian Hamiltonian for our system in the rotating frame reads

$$\frac{\hat{H}}{\hbar} = G(\hat{a}_{\mathrm{aS}}^{\dagger}\hat{b} + \hat{a}_{\mathrm{aS}}\hat{b}^{\dagger}) - (\Delta + i\gamma)\hat{b}^{\dagger}\hat{b} \; - \; i\kappa\hat{a}_{\mathrm{aS}}^{\dagger}\hat{a}_{\mathrm{aS}} \quad . \tag{3.45}$$

We can write this expression as a matrix equation

$$\frac{\hat{H}}{\hbar} = \begin{pmatrix} \hat{a}_{\mathrm{aS}}^{\dagger} \; , & \hat{b}^{\dagger} \end{pmatrix} \cdot \begin{pmatrix} -i\kappa & G \\ G & -(\Delta + i\gamma) \end{pmatrix} \begin{pmatrix} \hat{a}_{\mathrm{aS}} \\ \hat{b} \end{pmatrix} \quad . \tag{3.46}$$

Eigenfrequencies and effective damping rates of the system follow from this matrix. We write down the characteristic polynomial and find its roots:

$$\lambda^2 + (\Delta + i(\kappa+\gamma))\,\lambda + i\kappa\Delta - \kappa\gamma - G^2 = 0 \tag{3.47}$$

The two roots, and thus the complex eigenvalues of the matrix, are

$$\begin{aligned}\lambda_\pm = &-\frac{\Delta}{2} - i\frac{\kappa+\gamma}{2} \\ &\pm \sqrt{G^2 + \left(\frac{\Delta}{2}\right)^2 - \left(\frac{\kappa-\gamma}{2}\right)^2 - i\Delta\frac{\kappa-\gamma}{2}}\quad .\end{aligned} \tag{3.48}$$

We know that the complex square root of $z = x + iy$ is given by

$$\sqrt{z} = \sqrt{\frac{|z|+x}{2}} + i\ \mathrm{sgn}^+(y)\cdot\sqrt{\frac{|z|-x}{2}} \tag{3.49}$$

with $x = G^2 + \left(\frac{\Delta}{2}\right)^2 - \left(\frac{\gamma-\kappa}{2}\right)^2$ and $y = \frac{\gamma-\kappa}{2}\Delta$.

From the negative of the real parts of this pair of eigenvalues we obtain the eigenfrequencies, and from the negative of the imaginary parts we obtain the damping rates associated with the modes. The general case of $\Delta \neq 0$ can not be brought into a simpler form. To discuss the transition from weak to strong coupling we discuss the case of zero detuning, which contains the essential features.

For $\Delta = 0$ the complex eigenvalues are:

$$\lambda_{\pm,\Delta=0} = -\frac{\kappa+\gamma}{2}i \pm \sqrt{G^2 - \left(\frac{\kappa-\gamma}{2}\right)^2} \tag{3.50}$$

We see that the real part of this equation is 0 as long as $G < |\kappa-\gamma|/2$, corresponding to the case of degenerate eigenfrequencies of optical and mechanical modes in the rotating frame. In the case of vanishing coupling $G \to 0$, we observe that the imaginary parts approach the uncoupled damping rates of the modes, i.e. $-\mathrm{Im}(\lambda_{\pm,\Delta=0})|_{G\to 0} = \kappa, \gamma$.

As the coupling between the modes increases, the damping is redistributed among the

new eigenstates up until the point where $G$ becomes larger than $|(\kappa - \gamma)/2|$, at which point the term under the square root becomes positive and the damping rates of both eigenmodes are equal, given by $(\kappa + \gamma)/2$. It is also here that normal mode splitting occurs, as the real part of equation 3.50 divides into the branches of the square root. In this parameter regime we have hybrid optical-mechanical modes with equal contributions from both of the oscillators.

We observe that normal-mode splitting formally occurs as soon as $G > |(\kappa - \gamma)/2|$, but that this normal mode splitting is not resolved until the coupling strength $G$ also overcomes the effective damping rate of the hybrid optical-mechanical modes $(\kappa + \gamma)/2$.

The criterion of strong coupling is fulfilled if the coupling is strong enough so that the normal mode splitting at $\Delta = 0$ can actually be resolved. This occurs if

$$G > \frac{\kappa + \gamma}{2} \tag{3.51}$$

i.e. when G becomes larger than the damping rate of the hybrid optical-mechanical modes.

Figure 3.7 plots the predicted heterodyne spectra as a function of the intracavity power to highlight different physical scenarios of variable detuning and coupling strength.

## 3.5 Practical aspects

For lack of funding there were no frequency offset locking electronics in place and the pump and local oscillator lasers were free running, slowly drifting with respect to each other around their individual thermally stabilised operating points. The fact that the heterodyne frequency could not be fixed or made a simple function of the pump power complicated the data acquisition and analysis.

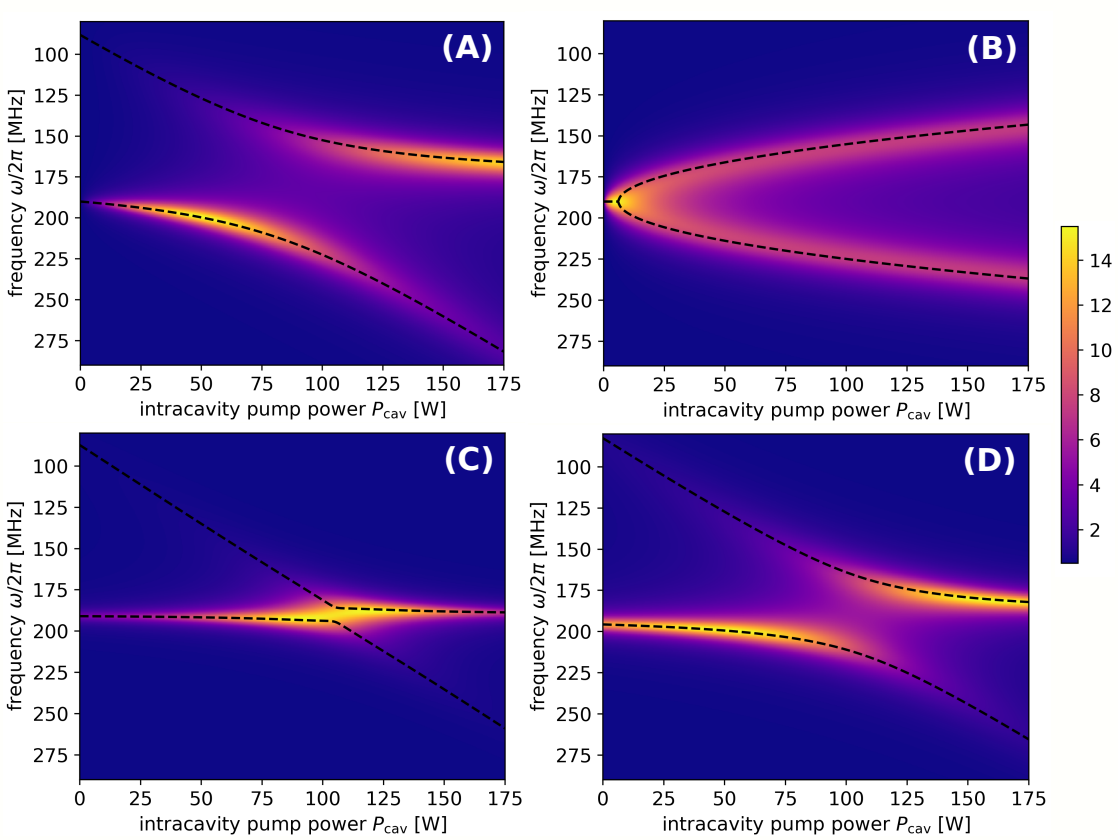


Figure 3.7: Contour plots of optical spectra and superimposed eigenfrequencies (black dashed line) for different forms of the power dependence of the detuning $\Delta$ and optomechanical coupling strength $G$. A value of 1/2 on the colour scale corresponds to optical vacuum. (A) Spectrum and eigenvalues for the parameters implemented in the experiment. (B) Hypothetical situation with the same parameters however the detuning is constant at 0 (optical Kerr/thermal effect switched off). Plot shows the well-known bifurcation. (C) and (D) Hypothetical scenarios where the Kerr effect is switched on, but the optomechanical coupling strength $G$ is assumed constant, at 10 MHz (C), and 25 MHz (D). Here we see that the spectra and eigenvalues are symmetric around the zero detuning point found just above 100 W. Plots (C) and (D) represent classic avoided crossing plots.

### 3.5.1 Identifying cavity-mode pairs

A first exploration of the system would include measuring cavity transmission and determining optical line widths. After finding a suitable relative taper-resonator positioning for coupling, a step pursued to find optical mode pairs resulting in significant optomechanical coupling would be to look for low-threshold Brillouin lasing ([TC09; GMM09]) via Stokes scattering where the higher frequency cavity mode is driven. (For the present silica microresonator, this corresponded to $\sim$ 1 mW input power.) The roles of the modes would then be swapped around and the pump laser would be tuned to "candidate Stokes modes" in order to drive the anti-Stokes (up-conversion) process. Frequently there would be a couple of optical resonances in the relevant range (i.e. 10.7 GHz red detuned with respect to the pump laser in the Brillouin lasing search). The pump laser would then be tuned to each of these optical resonances and scattered anti-Stokes light spectra would be measured via heterodyne detection in order to evaluate the coupling strength.

It should be noted here that depending on the taper position relative to the microresonator (especially the transverse positioning with respect to the bulge) the coupling to optical modes of the cavity can hugely vary. In practice the approach was taken to operate slightly undercoupled with respect to most optical modes, with the taper not sticking to the resonator surface in order to provide a good trade-off between narrow optical linewidth and pump-power build-up, in order to obtain low Brillouin lasing thresholds. Also, the taper would typically be positioned around the center of the bulge, thought being that here the coupling to the most fundamental modes with the smallest mode volumes would be found. Clearly it can't be excluded the case that the experimenter is missing mode trios where coupling to the pump mode is very weak at the explored taper position.

### 3.5.2 Detuning dependence

The previously mentioned observed linear dependence of the optomechanical detuning $\Delta$ on the intracavity pump power can be attributed to thermal and Kerr effects. Focusing our

discussion on the Kerr effect first, self- and cross-phase modulation cause power-dependent shifts to the cavity resonances depending on the mode overlap and we can model the dependence of the detuning on the intracavity power by $\Delta \simeq \Delta_0 - P_{\mathrm{cav}}\omega n_2/(nA')$ . Here, $\Delta$ is the detuning, $\Delta_0$ is the initial (low power) detuning, $\omega$ is the laser angular frequency, $n_2$ is the nonlinear refractive index, $n$ is the refractive index, $A'$ depends on the difference between the self- and cross-phase modulation terms and has dimensions of an area (see section 3.3.1), and $P_{\mathrm{cav}}$ is the intracavity pump power. This purely optical mode overlap is different from the Brillouin optomechanical mode overlap, in that it involves only two (optical) modes, whereas the latter involves a triple overlap integral of one acoustic and two optical modes (see section 1.5.2). From the fit shown in figure 3.3 we observe a linear shift of approximately 1 MHz $\mathrm{W}^{-1}$ of intracavity power. The measurements in 3.3 were performed at low power in order to avoid nonlinear loss mechanisms, such as four-wave mixing parametric oscillation. This detuning measurement was also used as a calibration to determine the intracavity pump power in addition to the transmission measurement described in section sec:intracavpower. We would like to remark that it may be practically possible to engineer a cavity that eliminates the pump-power dependence of the detuning. This could be achieved by exploiting both the self- and cross-phase modulation and using an optical mode structure with an overlap such that the two modes have the same frequency shift as the pump power changes.

In the measurements presented in figure 3.6 the thermal locking technique was used to stabilize the cavity pump resonance with respect to the laser wavelength. In this locking scheme, as the input pump power is increased the cavity becomes warmer and the thermal locking point is shifted increasingly towards the red. In order to maintain a low pump detuning $\delta_{\mathrm{p}}$ the wavelength of the pump laser is adjusted in order to follow the red-shifting resonance, such that a stable equilibrium is reached. In this way, for these measurement runs, a typical thermal tuning range would reach $\Delta\lambda \approx 100$ pm. This corresponds to a frequency shift of the pump resonance of $\approx 13$ GHz. At the same time the optomechanical detuning $\Delta$ changes by $\approx 120$ MHz (compare figure 3.3, and table 3.1). The optomechanical detuning shift is thus only 1 % of the absolute frequency shift to the pump resonance. It

is imaginable that the equilibrium temperature distribution in the mode volumes of the two optical resonances would affect the detuning in this way. As the temperature changes are small, the linear correspondence between heating power and detuning change are in accordance with Newton's law of cooling.

### 3.5.3 Kerr frequency comb as nonlinear loss channel

It was observed that when pushing up the input pump powers to reach the strong coupling regime of cavity optomechanics, at a threshold intracavity power of approximately 45 W the intrinsic damping rate of the pump optical resonance seemed to increase, manifesting in a change in the cavity transmission levels when thermally locked. After further investigation it showed that the system would here start to parametrically oscillate via stimulated four-wave mixing induced by the Kerr nonlinearity of fused silica, and in fact generate a frequency comb [Del+07]. This would appear to increase the internal loss contribution to the damping. While initially operating the experiments close to critical coupling to achieve the highest intracavity pump powers, the kicking-in of the four-wave mixing parametric oscillation would make the system become increasingly undercoupled as the internal loss of pump power into the frequency comb increased, while the coupling to the taper remained constant at constant taper-resonator distance (initially I thought that here some process, e.g. thermal expansion, affected the distance between resonator and tapered fiber, thus shifting the coupling condition from critical to undercoupled).

It was experimentally found that after crossing the frequency comb threshold, the intracavity pump power would continue to grow with increasing the input pump power, despite at a lower rate, as a substantial fraction of the added input power would be "pushed out" into the frequency comb (see figure 1.14). Thus, the relationship between input pump power and optomechanical coupling rate is a non-trivial function of both the pump laser detuning and the power with respect to the parametric oscillation threshold, which could only be extracted by using the linear detuning (figure 3.3) as a calibration and proxy of the intracavity pump power in an iterative fitting procedure, which could not be fully automated, but required

manual adjustments to the parameters.

To reach the high intracavity powers and cross the zero detuning point presented in figure 3.6 the taper-resonator distance was reduced, such that one would start with a substantially overcoupled situation at low input powers. During the experiments the taper was hovering over the resonator surface at a distance of the order of 1 $\mu$m, in order to maintain narrow optical linewidths. The distance would be close to the distance where environmental vibrations would cause the taper to get stuck on the resonator surface through the strong surface force.

### 3.5.4 Determining the intracavity power

We determine the intracavity pump power via transmission measurements using the following procedure. For low to moderate intracavity pump powers ($<$ 40W), the pump-mode linewidth (damping rate) is power independent as there are no significant optical nonlinearities present, such as four-wave mixing. We then use our knowledge of the pump linewidth and the dimensions of the cavity to compute the finesse of the pump resonance $F_{\mathrm{p}} = \Delta\nu_{\mathrm{FSR}}/\Delta\nu_{\mathrm{p}} = c/(\pi n d \Delta\nu_{\mathrm{p}})$. Here, $\Delta\nu_{\mathrm{FSR}}$ is the cavity's free spectral range, $\Delta\nu_{\mathrm{p}}$ is the pump-mode linewidth, and $d$ is the microresonator diameter. We then compare the observed transmission when thermally locked $T$ to the minimum transmission when on-resonance $T_0$ to determine the detuning $\delta_{\mathrm{p}}$ of the pump laser from resonance. This requires knowledge of the linewidth and cavity coupling conditions, i.e. being under- or over-coupled. Knowing the detuning, total linewidth, finesse, and external cavity coupling rate, we determine the intracavity power via $P_{\mathrm{cav}} = F_{\mathrm{p}}/\pi \cdot P_{\mathrm{in}} \cdot (1-T)/(1-\sqrt{T_0})$. Note that this expression is valid for the over-coupled condition and the sign in the denominator flips for the under-coupled condition (compare appendix).

For higher powers ($>$ 40W), the above procedure cannot be used due to optical nonlinearities becoming significant and increasing the pump-mode loss. (Note that the signal-mode loss is not increased by these nonlinear effects.) In this regime, we determine the intracavity power via the linear relationship between the detuning, as obtained from a fit to the het-

erodyne spectra, and the pump-mode intracavity power (cf. figure 3.3). This method gives consistent results with the above method for the low power regime.

## 3.6 Conclusions

Using an optically doubly-resonant silica micro-rod-resonator, we have experimentally demonstrated optomechanical strong coupling via Brillouin scattering for high-frequency phonons (11 GHz) in the back-scattering regime. We observe normal-mode splitting and an avoided crossing in the optical emission spectrum, which give unambiguous signatures of the system operating in the strong coupling regime. This large optomechanical coupling rate was achieved by utilizing silica's electrostriction and very low optical loss. We would like to highlight that our silica system does not suffer from two-photon absorption and strong surface-induced optical losses, which currently preclude many other micro-scale devices, primarily those fabricated from silicon, from entering the strong coupling regime. The Brillouin interaction utilized here additionally provides the advantage that the signal (anti-Stokes) photons are well separated from the pump field due the high mechanical frequency and being back-scattered from the pump field. To the best of our knowledge, this platform demonstrates optomechanical strong coupling with the highest mechanical frequency reported thus far.

The strong coupling performance achieved here can be even further improved via several near-, mid-, and longer-term routes. These include: (i) optimizing the choice of cavity mode pairs to simultaneously increase $g_0$ and reduce the power-dependent detuning; (ii) using higher optical quality factor resonances (quality factors of $10^9$ can be routinely fabricated that have an amplitude decay rate $\kappa/2\pi = 100$ kHz), which will allow lower input pump powers to be employed; (iii) using crystalline materials to reduce the mechanical damping rate [Gal+13; Ren+18; HSK10]; (iv) performing the experiments at cryogenic temperatures to reduce the thermal occupation and decoherence rate, which also provides the further advantage of reducing the mechanical damping rate [VSH80; LC03]; and (v) exploring the use of resonators fabricated from other materials with a larger photoelastic coupling such

as $As_2S_3$. We would also like to highlight at this point, that the heating due to intrinsic material absorption in silica for 10 W of intracavity power is expected to be $< 100$ mK when operating at a base temperature of 4 K.

The united favorable properties of this Brillouin optomechanical system provide a rich avenue to develop a suite of new technologies including classical and quantum information-processing applications, sensors, and even provide a path for coherent X-band microwave-to-optical conversion. As highlighted above, operating at cryogenic temperatures and using crystalline materials will dramatically reduce the mechanical damping rate. At 4 K, the 11 GHz mechanical mode will have a mean thermal occupation of $\bar{n} \simeq 7.6$, and making the conservative assumption that the mechanical (material) damping rate reduces to $\gamma \simeq 2$ MHz (assuming there is no geometrical contribution to the damping), the ratio of the mechanical decoherence rate to the mechanical frequency is $\bar{n}\gamma/\omega_{\mathrm{m}} = \bar{n}/Q \simeq 10^{-3}$, which means there are approximately $10^3$ oscillations before decoherence becomes significant. With such reductions to the mechanical damping rate, the mechanical coherence length can exceed the resonator circumference, or equivalently, the mechanical free-spectral range can exceed the mechanical decay rate, i.e. $v/\pi D > \gamma/2\pi$, where $D$ is the resonator diameter. This parameter regime will be easily entered for resonators of similar size at cryogenic temperatures and the system will become resonant also for the elastic waves. Of the numerous applications and further studies that can be performed in this regime, we would like to highlight that this system can readily enter and explore the quantum-coherent-coupling regime where $G > \bar{n}\gamma$. The coupling rates achieved so far ($G/2\pi \sim 40$ MHz), should be compared with our conservative estimate for the decoherence ($\bar{n}\gamma/2\pi \sim 15$ MHz). Operating in the quantum-coherent-coupling regime allows optomechanical state-swap to be performed. Moreover, the regime allows Rabi-like oscillations with non-classical optical input states, such as single-photon Fock states [Akr+10; Kha+10; Ver+12], to be observed, which is a key outstanding goal in the field. Achieving the strong coupling regime for this system paves the way to pursue this outlook and perform Brillouin-based quantum control of light and sound.

# Chapter 4

# Single-phonon addition and subtraction to a mechanical thermal state

In this chapter we describe experiments implementing the addition and subtraction of a single phonon to a mechanical thermal state via Brillouin scattering and single-photon detection. These operations applied to a thermal state have the counter-intuitive effect of approximately doubling the mean thermal occupation. This doubling signature is observed with an optical probe field and a heterodyne detection scheme.

We model the return of the system to equilibrium and deduce that the optomechanical coupling is consistent with being predominantly to a single mode. The application of joint quadratic (click) and linear (dyne) measurements opens an avenue for quantum state engineering and fundamental studies with macroscopic mechanical degrees of freedom.

The author spearheaded this project and took a leading role in the experimental setup design, implementation, recording and analysing the data, as well as theoretical modelling. The chapter is partly based on a manuscript which is about to be submitted for peer-reviewed publication, with the author as first author.

## 4.1 Introduction

Performing single-quanta-level operations to bosonic quantum systems provides a rich avenue for quantum-state engineering, quantum-information and communication applications, as well as exploring the foundations of physics. Prominent examples of quantum-state engineering at this level include the generation of non-classical states of microwave fields inside a cavity [Del+08] or a superconducting circuit [Hof+09], and the motion of trapped ions [Lei+96]. Single-quanta level operations are also a key component in many quantum technologies such as long-distance quantum communications with quantum repeaters [Dua+01; San+11], on-demand single-photon preparation [Lau+06; Spe+11], and continuous-variable entanglement distillation [Our+07]. Moreover, these operations allow for studies of non-classicality [ZVB04], and the exploration of the interface between quantum information and quantum thermodynamics [Vid+16].

A practical and powerful way to achieve these operations without having a significant nonlinearity in the system of interest is to use an interaction with light followed by single-photon detection on the scattered signal. These operations have been used to great success in optics to create 'kitten' states by single-photon subtraction from squeezed vacuum [Our+06; Nee+06], and to explore the properties of single-photon-added coherent states [ZVB04]. Single-quanta addition via single-photon detection has also been recently applied to atomic-spin ensembles to create non-Gaussian spin states [Chr+14] that exhibit significant non-classicality [McC+15]. These non-Gaussian operations can be used to create highly non-classical states and it has been theoretically shown that the addition operation creates non-classicality for any initial mean thermal occupation [Man86; AT92].

Curiously, when single-quanta addition or subtraction is applied to a thermal state, the mean number of quanta actually increases in both cases. Indeed, for a thermal state of mean occupation $\bar{n}$, when applying a subtraction (addition) operation, the mean occupation changes to $\bar{n} \to 2\bar{n}$ ($\bar{n} \to 2\bar{n} + 1$). Though this transformation appears counterintuitive, a qualitative understanding of this effect can be obtained by considering the Bayesian inference with the information gained by the measurement that heralds this non-unitary operation.

This behaviour has been observed for thermal optical fields by performing heralded single photon addition/subtraction followed by homodyne detection [ZPB07; Par+07], and the approximate doubling of the mean occupation was utilized for work extraction in reference[Vid+16]. Though these operations are now well studied for optical fields, they remain far less explored for other bosonic systems. In particular, the approximate doubling of the thermal occupation by these operations to a thermal state is yet to be demonstrated for any system other than traveling light fields.

Quantum optomechanics now provides a means to explore heralded single-phonon addition and subtraction to macroscopic mechanical resonators [VAK13; Gal+14]. These operations were first demonstrated experimentally using optical phonon modes in bulk diamond to create non-classical light-matter correlations [Lee+12] and entangled states of motion of two diamond crystals [Lee+11]. Then, extending these techniques to silicon photonic-crystal structures, second-order correlation function measurements [Coh+15] and Hanbury Brown–Twiss-type interferometry [Hon+17] have been performed, and entanglement between two of these structures [Rie+18] has also been demonstrated. Quantum optomechanics provides significant scope for further exploration of single-phonon addition and subtraction, which can be used for macroscopic quantum state engineering, studies of open-system dynamics, and determining the mechanical mode-contributions.

In this chapter heralded single-phonon addition and subtraction to a mechanical thermal state in a Brillouin optomechanical system is reported. We measure the temporal dynamics of the resulting increase in the mechanical variance via a heterodyne detection scheme and observe the aforementioned increase in the mean occupation to a high precision. This observation indicates that the operation is performed with very low noise and is also used to verify that the optomechanical coupling is predominantly to a single mechanical mode. This work combines both photon counting and optical dyne detection in a single experiment thus taking a step towards future hybrid quantum protocols that exploit both discrete and continuous variables [MKV16]. Moreover, multiple applications of phonon addition or subtraction can be used for optics-based mechanical quantum state synthesis [VAK13], and the

strong coupling [Enz+19] and ultra-long mechanical coherence times [Ren+18] achievable in these systems provide a promising experimental path for the development of mechanical quantum memories and repeaters.

## 4.2 Experimental scheme

In our optomechanical system we employ two-mode squeezer and beam-splitter-type optomechanical interaction in the weak coupling regime, by driving on the bluer and on the redder mode of an optical mode pair, respectively, see figure 4.1. A part of the Stokes or anti-Stokes light backscattered from the cavity is separated by a beam splitter, and is filtered by tunable fiber-Fabry-Perot cavities in order to suppress elastically scattered light, and subsequently sent to a single photon avalanche diode (SPAD) detector, to herald addition or subtraction events, respectively. The other output of the beam splitter is directed towards a heterodyne detection scheme, which is then used to verify a characteristic (doubling) feature of the quadrature variances upon addition or subtraction of a single quantum to the thermal state (compare figure 2.1).

The detection of a photocount by the SPAD, originating from the parametrically converted mechanical excitation, is represented by the action of the phonon annihilation operator $b$, and the phonon creation operator $b^\dagger$, when implementing the beam splitter, and two-mode squeezer schemes, respectively. The scattered light field is continuously monitored by a heterodyne detection scheme (rotating homodyne), where the local oscillator is not phase locked to the pump laser. Thus, the scheme measures a quadrature $X_\theta$ of the output light mode, with a random reference phase angle $\theta$. Since the thermal state does not carry phase information and its Wigner function has polar symmetry in phase space, in the following we will just write $X$ for $X_\theta$ and refer to it as a generic quadrature of the output light field.

After state preparation by projection through the SPAD, the mean phonon number decays back to its equilibrium value via interaction with the thermal reservoir. We calculate the time dependence of the doubling feature by solving quantum Langevin equations for the

mechanical and optical degrees of freedom of the cavity and computing the expectation value of the mechanical quadrature variance conditioned on the detection of a photocount (see section 4.5.2).

## 4.3 Setup

For the experiment, a setup as depicted in figure 4.1 (B) is used, where compared to the strong-coupling and measurement-cooling experiments, Fabry-Perot filters and an SPAD detector are used to herald the addition/subtraction operation.

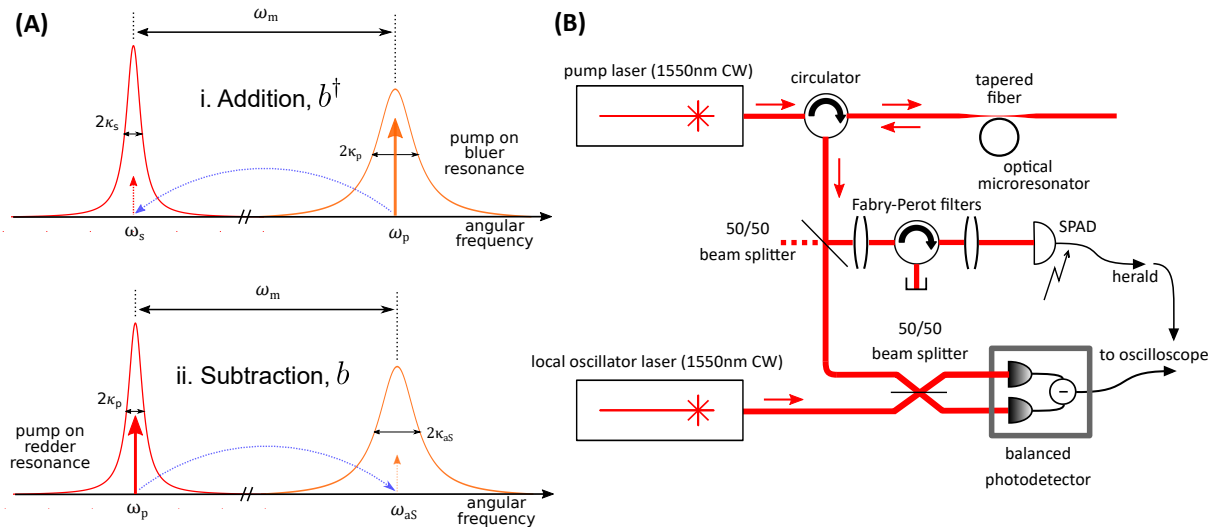


Figure 4.1: Scheme (A) and setup (B) used in the single-phonon-addition/subtraction experiment. A barium fluoride whispering-gallery microresonator, as shown in figure 2.8, was used for the measurements.

As the pump wave is in a large amplitude coherent state with photon numbers of $\approx 10^8$, we can approximate it as a $c$-number, and are (in a rotating frame) left with a beam-splitter-type Hamiltonian $\hbar G(a^\dagger b + a b^\dagger)$ when driving on the red resonance of the pair, while switching on a two-mode-squeezing-type Hamiltonian $\hbar G(a^\dagger b^\dagger + a b)$ when driving on the bluer resonance of the pair. It might be noted here that while in our experiment we are always pumping in the forward direction, and observing scattered light in the backward direction, owing to the system's symmetry under simultaneous inversion of propagation directions of all three waves, applying the pump light in backwards direction allows to perform addition and subtraction

operations on the same mechanical mode, should it be desired.

In the all-in-fiber optical experiment, a barium fluoride whispering-gallery microresonator with geometry similar to the one reported in reference [DDP13] is excited by a continuous-wave pump laser running at a wavelength of 1550 nm via evanescent coupling from a tapered optical fiber. A pair of optical whispering-gallery resonances of different transverse structure is identified, which by virtue of its frequency separation being approximately equal to the Brillouin shift and a significant value of the triple spatial overlap of equation 1.56 features a significant optomechanical coupling [Enz+19]. Other than in the strong-coupling and measurement-cooling experiments, the laser pump power is typically chosen comparably weak at $\approx$ 1 mW, leading to optomechanical coupling strengths of typically 2-3 MHz, in order to operate in a regime, where cooling/heating of the mechanical mode is negligible. The pump laser is locked to either the blue or red resonance of the optical mode pair. In the former case, the optomechanical coupling is predominantly to the forward (co-)propagating acoustic mode (associated with the two-mode-squeezing Hamiltonian, see section 1.5.4) and leads to frequency down-conversion of pump photons, while in the latter case the coupling is to the counter-propagating acoustic mode, associated with a beam-splitter-type Hamiltonian, leading to frequency up-conversion of pump photons.

Brillouin Stokes (anti-Stokes) light backscattered from the cavity is coupled out through the taper and is separated from pump light via an optical circulator, see figure 4.1, before impinging on an optical heterodyne detection scheme. Part of the light stream is picked off at a 50:50 beam splitter and is directed onto a single-photon avalanche diode (SPAD) module, after having passed through a sequence of two fiber Fabry-Perot spectral filters. The temperature-tunable filters are manually tuned to the Stokes (anti-Stokes) resonance frequencies of the cavity, and fulfil the role of suppressing elastically/Rayleigh scattered pump light which is several orders of magnitude brighter than the weak Brillouin signal. The filters possess a bandwidth (FWHM) of 120 MHz and a free spectral range of 25 GHz. They are separated by an optical circulator, in order to suppress unwanted double-cavity effects. Furthermore a second SPAD was used in some experiments for measuring the degree

of second-order coherence of the scattered light. Furthermore an optical circulator was needed to suppress spurious reflection of the strong local oscillator beam in the heterodyne part of the setup from the single-photon counter. The output of the SPAD module is used to trigger a digital storage oscilloscope recording of the balanced photodetector output. For a summary of experimental parameters see table 4.1.

Table 4.1: Overview of parameters of system and experiment for single-phonon addition/subtraction to a mechanical thermal state.

| **Parameter** | **Value** |
|---|---|
| Microresonator diameter | 1.5 mm |
| Microresonator free spectral range (FSR) | 33 GHz |
| Pump power $P_{\mathrm{in}}$ | 1 mW |
| Coupling rate $G/2\pi$ | $\approx$ 2 MHz |
| Mechanical frequency $\omega_{\mathrm{m}}/2\pi$ | 8.21 GHz |
| Optical linewidths $2\kappa_1/2\pi, 2\kappa_2/2\pi$ | 13.5 , 15.5 MHz |
| Mechanical linewidth $2\gamma/2\pi$ | $(34.0 \pm 6.4)$ MHz |
| SPAD count rate | $\approx 500\ \mathrm{s}^{-1}$ |
| Total SPAD detection efficiency $\eta_{\mathrm{det}}$ | $\approx 0.005$ |
| Mean phonon number $\bar{n} \rightarrow 2\bar{n}$ | $760 \rightarrow 1520$ |

## 4.4 Measurement results

For each measurement run, circa twenty thousand oscilloscope traces of the heterodyne detection output are recorded, where each recording is triggered by the SPAD detecting a photocount. For both, the subtraction and addition operations, we observe a doubling signature in the mean (as in ensemble average) of the variance of the mechanical noise contribution to the output optical quadrature, as shown in figure 4.2. The temporal dynamics of the doubling feature follow precisely the shape described by a model, which predicts the mechanical noise contribution on top of the temporally constant vacuum contribution (blue baseline in figure 4.2). This model will be described in detail in the following section. A small reduction of the order of 1 % is introduced by a finite ratio of photocounts to dark-counts of the SPAD (The SPAD was gated at 50 kHz, with gate length set to 10 ns. At these settings, the dark count rate, including spuriously transmitted light, was 3 counts/s, while signal count rates were typically 300 counts/s to 600 counts/s).

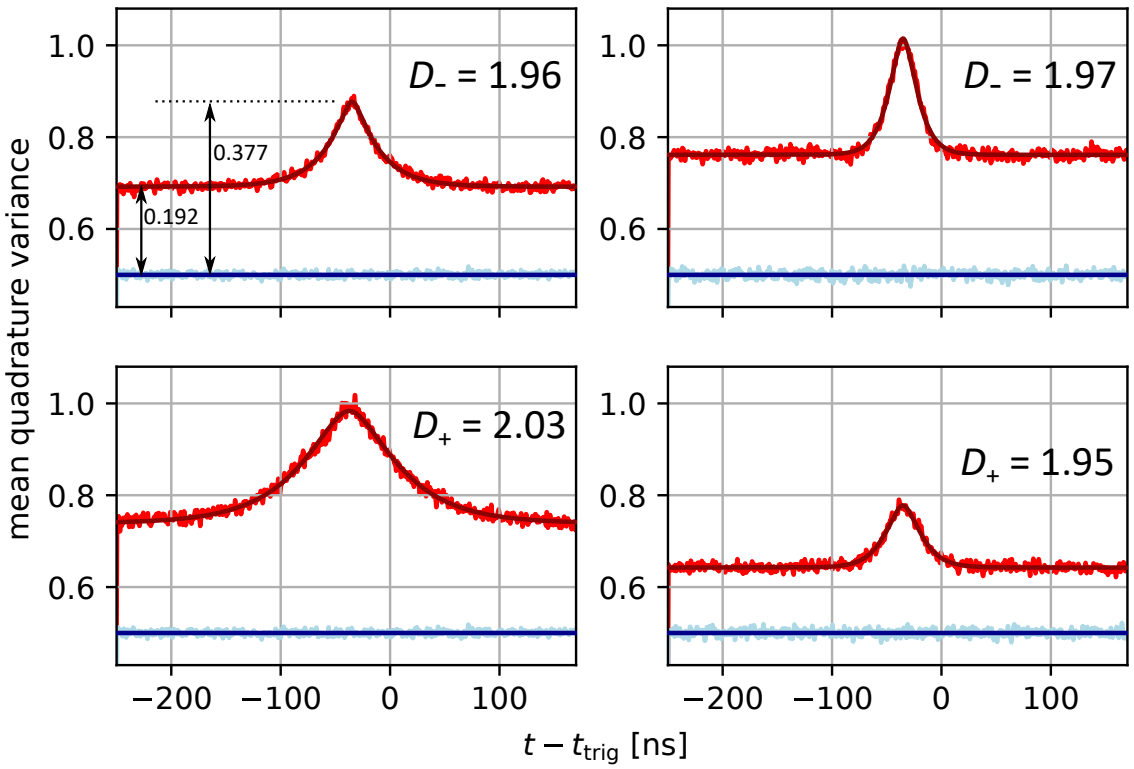


Figure 4.2: Measured mean quadrature variance around the time of single-phonon addition and subtraction to a mechanical thermal state, and fitted model. The red trace shows the total quadrature variance of the optical output signal, with the blue trace showing the variance of optical vacuum, for reference (the signals are normalised such that optical vacuum corresponds to $\langle X^2 \rangle = 1/2$). Top left: Subtraction with narrow optical linewidth $2\kappa/2\pi = 7.6$ MHz, $2\gamma/2\pi = 74.6$ MHz (fit) and doubling factor $D_- = 1.96$. Top right: Subtraction with larger optical linewidth $2\kappa/2\pi = 15$ MHz, $2\gamma/2\pi = 41.8$ MHz (fit), and doubling factor $D_- = 1.97$. Bottom left: Addition with narrow optical linewidth $2\kappa/2\pi = 3.8$ MHz, $2\gamma/2\pi = 18.0$ MHz (fit), doubling factor $D_+ = 2.03$. Bottom right: Addition with broader optical linewidth $2\kappa/2\pi = 13.5$ MHz, $2\gamma/2\pi = 32.6$ MHz (fit) and doubling factor $D_+ = 1.95$. All these measurements were undertaken with the same optical mode pair, at different coupling positions of the tapered fiber with respect to the resonator. For each of the plots circa twenty thousand time traces were recorded. It can be assumed that the coupling in all four measurements is to the same mechanical mode. The spread in the mechanical linewidths obtained from fitting might be attributed to the insensitivity of the fit function to changes in the faster one of the two entering rates ($\kappa$ and $\gamma$), in situations when the two rates are very different. Thus the mechanical linewidths determined from fits of measurements using larger optical linewidths will be more reliable. The temporal offset is due to a propagation delay between the counting, and heterodyne arms. It is consistent with the delay due to filtering and optical and electronic cables, and has no physical significance beyond that. The estimated uncertainty on the doubling factor is 0.02, mainly due to laser power drift.

The time scales of the doubling feature, whose height we denote by $D_+$ and $D_-$ respectively for the addition and subtraction configurations, are governed by an interplay between the optical and mechanical damping rates of the cavity, $\kappa$ and $\gamma$ (see section 4.5.2). Cases of different optical linewidth were experimentally explored by changing the position of the tapered fiber relative to the microresonator. In the case of large optical linewidth (plot figure 4.2, top right), the feature is temporally short ($\approx$ 25 ns), while for narrower optical linewidth the feature is temporally extended ($\approx$ 75 ns, plot figure 4.2, bottom left). This is an indication that the mechanical linewidth in this experiment is larger than the optical linewidths, as the temporal decay of the doubling feature (thermal correlation timescale of the output light) is given by the slower decaying species, according to our model, compare equations 4.34 and 4.35.

In order to compare this finding to measurements of the Brillouin linewidth in a similar material, we can look at the value for calcium fluoride, which was measured by Sonehara et al [Son+07] in a bulk sample, obtaining an acoustic damping equivalent of $2\gamma/2\pi = 5.7$ MHz at 1550 nm. Due to the similar crystal composition and structure of these materials it can be assumed that the bulk acoustic attenuation in barium fluoride will be of the same order, if not lower. From the measurements it can be concluded that there is most likely an additional, substantial dissipation mechanism at play, associated with the proximity of the waves' propagation path to the surface of the structure. This additional damping channel could have to do with diffraction of acoustic waves (getting lost into the support), the nanoscopic structure of the surface leading to scattering, or (less likely) external pollution by dust. It is interesting to note that for both, the fused-silica, and the barium-fluoride resonators, this damping, which arises additionally to the material's intrinsic damping, is of the same order, 20-30 MHz. Taking into consideration that the manufacturing process for the two systems is very different, a melting process in the case of fused silica, and a cut-and-polish-process in the case of barium fluoride, the similarity of the excess damping might hint at a common role of geometry.

The measurements of the variance conditioned on photocounts of the SPAD were supple-

mented by measurements of the second order autocorrelation function of the optical output mode, $g^{(2)}$. These measurements confirmed the thermal nature of the output optical field, with the cavity time scales imprinted.

For the beam-splitter-type interaction, and the weak two-mode-squeezing-type interaction, another point-of-view can be adopted, in that the generated light field possesses thermal statistics and we measure its classical correlation in an unconventional way, namely by employing a linear detector in the dyne scheme, and subsequently squaring its output, and using a quadratic (click) type measurement alongside it, then correlating the two.

In fact, the rapid acquisition of temporal information about the correlation function in our dyne-click combined scheme provides an interesting alternative compared with the conventional approach of measuring $g^{(2)}$ to characterize sources. The approach should be transferable to arbitrary input states.

## 4.5 Theoretical model

In this section we present theoretical considerations supporting the experimental findings. First, we will present a calculation showing the effect of the application of a bosonic creation or annihilation operator to a thermal state. Next, we will solve Langevin equations of motion and find solutions for the system dynamics in the time domain. We then present an argument how the variance of an optical quadrature can be computed around an addition/subtraction operation, in time. Finally, we discuss how the detection by heterodyne measurement can be represented in the model, and which conditions have to be fulfilled by the photon-counting arrangement.

### 4.5.1 Single-phonon addition and subtraction to a thermal state

In this section we show how single-phonon addition and subtraction to a thermal state increases the mean occupation $\bar{n}$ according to:

$$\text{Addition: } \bar{n} \to 2\bar{n}+1 \qquad \text{Subtraction: } \bar{n} \to 2\bar{n}\,. \tag{4.1}$$

In our experiment, we achieve single-phonon addition or subtraction by pumping the higher-frequency or the lower-frequency mode of a pair of cavity resonances, respectively, followed by single photon detection of the scattered signal that heralds the operation (see figure 4.1). For the case of addition, the pump field drives a two-mode-squeezing-type interaction, and the detected signal is red-shifted with respect to the pump. For the case of subtraction, the pump field drives a light-mechanics beam-splitter-type interaction, and the detected signal is blue-shifted with respect to the pump. These heralded processes are then close experimental approximations to the single-phonon creation and (annihilation) operators $b^\dagger$ ($b$).

#### Change in the mean thermal occupation

Let's first compute the effect of the single-phonon subtraction on an initial thermal mechanical state of motion. The density operator of the resulting mechanical state is obtained via

$$\rho_{\text{sub}} = \frac{b\rho_{\text{th}}b^\dagger}{\text{Tr}(\rho_{\text{th}}b^\dagger b)} = \frac{b\rho_{\text{th}}b^\dagger}{\bar{n}}\ , \tag{4.2}$$

where $\rho_{\text{th}} = \sum_n \frac{\bar{n}^n}{(\bar{n}+1)^{n+1}}|n\rangle\langle n|$ is the density operator of a thermal state. (For clarity, we have neglected here the proportionality factors that go into the heralding probability.) The

mean phonon number of the single-phonon-subtracted state is then given by

$$\langle b^\dagger b\rangle_- = \mathrm{Tr}(\rho_{\mathrm{sub}} b^\dagger b) \tag{4.3}$$
$$= \frac{1}{\bar{n}}\,\mathrm{Tr}(b\rho_{\mathrm{th}} b^\dagger b^\dagger b) \tag{4.4}$$
$$= \frac{1}{\bar{n}}\sum_n \frac{\bar{n}^n}{(\bar{n}+1)^{n+1}}\langle n|b^\dagger b^\dagger bb|n\rangle \tag{4.5}$$
$$= \frac{1}{\bar{n}}\sum_n \frac{\bar{n}^n}{(\bar{n}+1)^{n+1}} n(n-1) \tag{4.6}$$
$$= \frac{1}{\bar{n}(\bar{n}+1)}\sum_n q^n n(n-1)\ , \tag{4.7}$$

where in the last line we introduced $q = \bar{n}/(\bar{n}+1)$. We can now use $\frac{d^2}{dq^2}q^n = (n-1)nq^{n-2}$, and the sum of a geometric series, to write

$$\langle b^\dagger b\rangle_- = \frac{\bar{n}}{(\bar{n}+1)^3}\frac{d^2}{dq^2}\sum_n q^n \tag{4.8}$$
$$= \frac{\bar{n}}{(\bar{n}+1)^3}\frac{d^2}{dq^2}\frac{1}{1-q} \tag{4.9}$$
$$= \frac{\bar{n}}{(\bar{n}+1)^3}\frac{2}{(1-q)^3} \tag{4.10}$$
$$= \frac{\bar{n}}{(\bar{n}+1)^3}2(\bar{n}+1)^3 \tag{4.11}$$
$$= 2\bar{n}\ . \tag{4.12}$$

The calculation for phonon addition, achieved using the two-mode-squeezing-type Hamiltonian, proceeds in a similar manner and results in $\langle b^\dagger b\rangle_+ = 2\bar{n}+1$.

### 4.5.2 Dynamics

In this section we derive the temporal evolution of the mean quadrature variance observed in the optical heterodyne detection around the single-phonon addition/subtraction event. For this purpose, we first solve quantum Langevin equations for the coupled optical and mechanical modes, and compute the correlation between the single-phonon detection events that herald the addition/subtraction operations and the heterodyne signal.

### 4.5.3 Quantum Langevin equations

The time evolution of the optical and mechanical modes, $a$ and $b$, respectively, including open-system dynamics, is modelled using quantum Langevin equations. These equations read

$$\dot{a} = -i\,[a, H/\hbar] - \kappa\, a + \sqrt{2\kappa}\, a_{\rm in}\ , \tag{4.13}$$

$$\dot{b} = -i\,[b, H/\hbar] - \gamma\, b + \sqrt{2\gamma}\, b_{\rm in}\ , \tag{4.14}$$

where $H$ is the light-mechanics Hamiltonian driven, $\kappa$ and$\gamma$ are the optical and mechanical amplitude decay rate, respectively, and $a_{\rm in}$, and $b_{\rm in}$ represent the optical and mechanical environments, respectively. These latter noise operators have the following correlations:

$$\begin{aligned}
\langle a_{\rm in}^\dagger(t) a_{\rm in}(t')\rangle &= 0\ , \\
\langle a_{\rm in}(t) a_{\rm in}^\dagger(t')\rangle &= \delta(t-t')\ , \\
\langle b_{\rm in}^\dagger(t) b_{\rm in}(t')\rangle &= \bar{n}_{\rm th}\delta(t-t')\ , \\
\langle b_{\rm in}(t) b_{\rm in}^\dagger(t')\rangle &= (\bar{n}_{\rm th}+1)\delta(t-t')\ ,
\end{aligned} \tag{4.15}$$

where $\bar{n}_{\rm th}$ is the mean occupation of the mechanical bath, the optical bath is at zero temperature, and correlations of any other combinations of the two operators is equal to zero.

We will now solve the dynamics for single-phonon subtraction, which uses the beam-splitter Hamiltonian. The calculation for single-phonon addition, which uses the two-mode-squeezing interaction, proceeds in a similar manner. Working in a frame co-rotating with the optical and mechanical fields, we linearise the pump-field such that the Hamiltonian for the interaction takes the form of beam-splitter-type Hamiltonian $H = \hbar G(ab^\dagger + a^\dagger b)$. After inserting this Hamiltonian into equations 4.13 and 4.14, we write the equations in matrix form in the frequency-domain, to get

$$\begin{pmatrix} \widetilde{A}(\omega) \\ \widetilde{B}(\omega) \end{pmatrix} = \frac{1}{(i\omega+\gamma)(i\omega+\kappa)+G^2} \begin{pmatrix} i\omega+\gamma & -iG \\ -iG & i\omega+\kappa \end{pmatrix} \begin{pmatrix} \sqrt{2\kappa}\,\widetilde{A}_{\rm in}(\omega) \\ \sqrt{2\gamma}\,\widetilde{B}_{\rm in}(\omega) \end{pmatrix}\ , \tag{4.16}$$

where $\widetilde{A}$, $\widetilde{A}_{\rm in}$, $\widetilde{B}$ and $\widetilde{B}_{\rm in}$, are the Fourier transforms of the operators $a$, $a_{\rm in}$, $b$ and $b_{\rm in}$, respectively.

Making the approximation that the coupling is weak, i.e. $G \ll \kappa, \gamma$, the frequency-domain solution for the intra-cavity optical field simplifies to

$$\widetilde{A}(\omega) = \frac{\sqrt{2\kappa}}{i\omega + \kappa}\, \widetilde{A}_{\rm in}(\omega) - \frac{iG\sqrt{2\gamma}}{(i\omega + \gamma)(i\omega + \kappa)}\, \widetilde{B}_{\rm in}(\omega)\ . \tag{4.17}$$

Returning to the time-domain by applying the inverse Fourier transform, and using the convolution theorem, we arrive at

$$a(t) = \sqrt{2\kappa}\left(e^{-\kappa t}\,\Theta(t)\right) * a_{\rm in}(t) - \frac{iG\sqrt{2\gamma}}{\kappa - \gamma}\left(\left(e^{-\gamma t} - e^{-\kappa t}\right)\Theta(t)\right) * b_{\rm in}(t)\ , \tag{4.18}$$

where $\Theta(t)$ is the Heaviside-Lorentz step function.

Similarly, for the two-mode-squeezing-type Hamiltonian $H = \hbar G(a^\dagger b^\dagger + ab)$, one obtains

$$a(t) = \sqrt{2\kappa}\left(e^{-\kappa t}\,\Theta(t)\right) * a_{\rm in}(t) + \frac{iG\sqrt{2\gamma}}{\kappa - \gamma}\left(\left(e^{-\gamma t} - e^{-\kappa t}\right)\,\Theta(t)\right) * b_{\rm in}^\dagger(t)\ . \tag{4.19}$$

Comparing equations 4.18 and 4.19, we see that they have a very similar form, where the optical field operator $a$ is correlated to the mechanical noise operator $b_{\rm in}$ for the beam-splitter interaction, and $a$ is correlated to $b_{\rm in}^\dagger$ for the two-mode-squeezing interaction.

### Intra-cavity dynamics

Using the solutions to the Langevin equations, we now compute the temporal evolution of the quadrature variance of the intra-cavity optical field, around the single-phonon addition/subtraction events. This quantity provides a proxy for the mechanics, and is used to verify the effect of the operation on the mechanical oscillator.

It is important to note at this stage that although it is insightful to consider the intra-cavity field, it is not experimentally accessible, and that cavity input-output relations, and

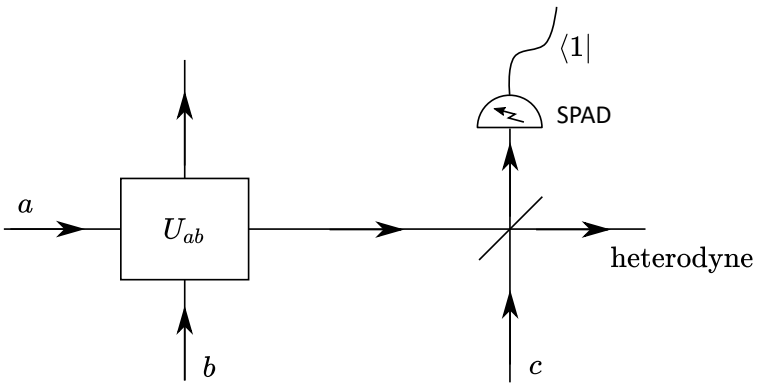


Figure 4.3: Simplified schematic of our experimental setup to implement and characterize single-phonon addition and subtraction to a mechanical thermal state. Here, $a$ represents the optical cavity mode of the scattered signal, $b$ is the mechanical mode, and $U_{\rm ab}$ describes the (weak) light-matter beam splitter/two-mode-squeezing-type interaction.

an appropriate detector model, must be accounted for when considering the actual measurements. We omit this additional level of complexity for now, returning to it in section 4.5.4.

In figure 4.3, a simplified toy-model for our joint click-dyne detection scheme is shown, where we have introduced an additional optical mode $c$, which participates in the optical beam-splitter between the single-photon counter and the heterodyne detector. The quadrature variance of the optical cavity mode $X^2_{\rm cav}$, for a general light-mechanics interaction, is then determined by computing

$$\langle X^2_{\rm cav}\rangle = \frac{1}{\mathcal{P}}\,\mathrm{Tr}\left({}_{\rm c}\langle 1|\, B_{\rm ac}U_{\rm ab}\;\rho_{\rm m}\otimes|0\rangle_{\rm a}\langle 0|\otimes|0\rangle_{\rm c}\langle 0|\;U^\dagger_{\rm ab}B^\dagger_{\rm ac}\,|1\rangle_{\rm c}\,X^2_{\rm cav}\right)\;, \tag{4.20}$$

where $U_{\rm ab}$ represents the light-matter interaction, $B_{ac}$ the beam-splitter dividing the signal between the single-photon and heterodyne detectors, and $\mathcal{P}$ is the heralding probability.

Also note that the states produced here are phase invariant in phase space, meaning that the statistics of the measurement are independent of the time-varying local-oscillator phase. Thus, we can ignore the time-varying phase in the rotating quadrature operator and, in practice, we do not need to lock the phase of our local oscillator.

For a weak signal field $a$, and having negligible probability of two or more photons at the single-photon counter, we may write ${}_{\rm c}\langle 1|B_{\rm ac}|0\rangle_{\rm c} = r\,a$, where $r$ is the reflectivity parameter

of the beam splitter. This regime is relevant to our experiment and the heterodyne signal variance thus becomes

$$\left\langle \left(X_{\mathrm{cav}}(\tau)\right)^2 \right\rangle = \frac{r^2}{\mathcal{P}} \,\mathrm{Tr}\left(\rho_{\mathrm{m}} \otimes |0\rangle_{\mathrm{a}}\langle 0|\; U_{\mathrm{ab}}^{\dagger}\, a^{\dagger}(0) \left(X_{\mathrm{cav}}(\tau)\right)^2 a(0)\, U_{\mathrm{ab}}\right) \ . \tag{4.21}$$

At this point we substitute the solutions to the Langevin equations, given by equations 4.18 and 4.19 respectively, to determine $X_{\mathrm{cav}}^2(\tau)$, so as to take into account the full cavity dynamics. Note also that here we have used the time-stamp $t = 0$ to indicate when the heralding event occurred and $\tau = t - t_0$ is the time after the heralding operation. The mean heterodyne variance is then given by

$$\left\langle \left(X_{\mathrm{cav}}(\tau)\right)^2 \right\rangle = \frac{r^2}{\mathcal{P}} \left\langle a^{\dagger}(0) \left(X_{\mathrm{cav}}(\tau)\right)^2 a(0) \right\rangle = \frac{\left\langle a^{\dagger}(0) \left(X_{\mathrm{cav}}(\tau)\right)^2 a(0) \right\rangle}{\left\langle a^{\dagger}(0) a(0) \right\rangle} \ , \tag{4.22}$$

where we have used $\mathcal{P} = r^2 \langle a^{\dagger}(0) a(0) \rangle$.

Inserting $\left(X_{\mathrm{cav}}(\tau)\right)^2 = 1/2 \left(a^{\dagger}(\tau) + a(\tau)\right)^2$ into equation 4.22 we obtain

$$\left\langle \left(X_{\mathrm{cav}}(\tau)\right)^2 \right\rangle = \frac{\left\langle a^{\dagger}(0) a^{\dagger}(\tau) a(\tau) a(0) \right\rangle + \left\langle a^{\dagger}(0) a(\tau) a^{\dagger}(\tau) a(0) \right\rangle}{2 \left\langle a^{\dagger}(0) a(0) \right\rangle} \ . \tag{4.23}$$

To proceed, we apply the Isserlis-Wick theorem [Iss18; BR97], which states that for Gaussian systems, the following is true:

$$\langle ABCD \rangle = \langle AB \rangle \langle CD \rangle + \langle AC \rangle \langle BD \rangle + \langle AD \rangle \langle BC \rangle \ , \tag{4.24}$$

where $A, B, C$ and $D$ correspond to (bosonic) operators. Using this, we arrive at

$$\left\langle \left(X_{\mathrm{cav}}(\tau)\right)^2 \right\rangle = \frac{\langle a^{\dagger}(0) a(\tau) \rangle \langle a^{\dagger}(\tau) a(0) \rangle}{\langle a^{\dagger}(\tau) a(\tau) \rangle} + \frac{\langle a^{\dagger}(0) a(0) \rangle}{2 \langle a^{\dagger}(\tau) a(\tau) \rangle} \left( \langle a(\tau) a^{\dagger}(\tau) \rangle + \langle a^{\dagger}(\tau) a(\tau) \rangle \right) \ , \tag{4.25}$$

which, using the fact that the field leaving the cavity is stationary $\langle a^{\dagger}(t_1) a(t_1) \rangle = \langle a^{\dagger}(t_2) a(t_2) \rangle$, and that the two-time correlator has the symmetry $\langle a^{\dagger}(0) a(t_1) \rangle = \langle a^{\dagger}(t_1) a(0) \rangle^*$, we can fur-

ther simplify to get

$$\left\langle \left(X_{\mathrm{cav}}(\tau)\right)^2 \right\rangle = \frac{|\langle a^\dagger(0)a(\tau)\rangle|^2}{\langle a^\dagger(0)a(0)\rangle} + \langle a^\dagger(0)a(0)\rangle + \frac{1}{2} \ . \tag{4.26}$$

At this point, we have an expression that allows us to conveniently compute the quadrature variance for both single-phonon addition and subtraction operations (substituting in equation 4.18 for the subtraction, and equation 4.19 for the addition). We also note that since $\langle a^\dagger(0)a(0)\rangle$ is included in $\langle a^\dagger(0)a(\tau)\rangle$, we only need to evaluate the latter.

Let's first compute the case of single-phonon subtraction. As the optical vacuum noise has a mean photon number of zero (see equation 4.15), and cross terms between the optical and mechanical noise operators vanish, only the thermal mechanical noise terms contribute, and we obtain:

$$\begin{aligned}
&\langle a^\dagger(0)a(\tau)\rangle = ... \\
&= \frac{2\gamma\, G^2}{(\kappa-\gamma)^2} \left\langle \int dt' \int dt'' \left( \left(e^{\gamma t'} - e^{\kappa t'}\right) \Theta(-t') \right) \left( \left(e^{-\gamma(\tau - t'')} - e^{-\kappa(\tau - t'')}\right) \Theta(\tau - t'') \right) b_{\mathrm{in}}^\dagger(t')\, b_{\mathrm{in}}(t'') \right\rangle \\
&= \frac{2\gamma\, G^2}{(\kappa-\gamma)^2} \left\langle \int_{-\infty}^{0} dt' \int_{-\infty}^{\tau} dt'' \left(e^{\gamma t'} - e^{\kappa t'}\right) \left(e^{-\gamma(\tau - t'')} - e^{-\kappa(\tau - t'')}\right) b_{\mathrm{in}}^\dagger(t')\, b_{\mathrm{in}}(t'') \right\rangle \ .
\end{aligned} \tag{4.27}$$

We then make a case distinction, assuming first $\tau > 0$ :

$$\begin{aligned}
\langle a^\dagger(0)a(\tau)\rangle_{\tau>0} &= \bar{n}_{\mathrm{th}} \frac{2\gamma\, G^2}{(\kappa-\gamma)^2} \int_{-\infty}^{0} dt' \left(e^{\gamma t'} - e^{\kappa t'}\right) \left(e^{-\gamma(\tau - t')} - e^{-\kappa(\tau - t')}\right) \\
&= \bar{n}_{\mathrm{th}} \frac{2\gamma\, G^2}{(\kappa-\gamma)^2} \left[ e^{-\gamma\tau} \int_{-\infty}^{0} dt' \left(e^{2\gamma t'} - e^{(\kappa+\gamma)t'}\right) - e^{-\kappa\tau} \int_{-\infty}^{0} dt' \left(e^{(\kappa+\gamma)t'} - e^{2\kappa t'}\right) \right] \\
&= \bar{n}_{\mathrm{th}} \frac{2\gamma\, G^2}{(\kappa-\gamma)^2} \left[ e^{-\gamma\tau} \left(\frac{1}{2\gamma} - \frac{1}{\kappa+\gamma}\right) - e^{-\kappa\tau} \left(\frac{1}{\kappa+\gamma} - \frac{1}{2\kappa}\right) \right] \\
&= \bar{n}_{\mathrm{th}} \frac{\gamma\, G^2}{(\kappa+\gamma)(\kappa-\gamma)} \left(\frac{e^{-\gamma\tau}}{\gamma} - \frac{e^{-\kappa\tau}}{\kappa}\right) \ ,
\end{aligned} \tag{4.28}$$

and now $\tau < 0$ :

$$\begin{aligned}
\langle a^\dagger(0)a(\tau)\rangle_{\tau<0} &= \bar{n}_{\rm th}\,\frac{2\gamma\,G^2}{(\kappa-\gamma)^2}\int_{-\infty}^{\tau}dt''\left(e^{\gamma t''}-e^{\kappa t''}\right)\left(e^{-\gamma\tau+\gamma t''}-e^{-\kappa\tau+\kappa t''}\right)\\
&= \bar{n}_{\rm th}\,\frac{2\gamma\,G^2}{(\kappa-\gamma)^2}\left[e^{\gamma|\tau|}\int_{-\infty}^{-|\tau|}dt''\left(e^{2\gamma t''}-e^{(\kappa+\gamma)t''}\right)-e^{\kappa|\tau|}\int_{-\infty}^{-|\tau|}dt''\left(e^{(\kappa+\gamma)t''}-e^{2\kappa t''}\right)\right]\\
&= \bar{n}_{\rm th}\,\frac{2\gamma\,G^2}{(\kappa-\gamma)^2}\left[e^{\gamma|\tau|}\left(\frac{e^{-2\gamma|\tau|}}{2\gamma}-\frac{e^{-(\kappa+\gamma)|\tau|}}{\kappa+\gamma}\right)-e^{\kappa|\tau|}\left(\frac{e^{-(\kappa+\gamma)|\tau|}}{\kappa+\gamma}-\frac{e^{-2\kappa|\tau|}}{2\kappa}\right)\right]\\
&= \bar{n}_{\rm th}\,\frac{\gamma\,G^2}{(\kappa-\gamma)(\kappa+\gamma)}\left(\frac{e^{-\gamma|\tau|}}{\gamma}-\frac{e^{-\kappa|\tau|}}{\kappa}\right)\,.
\end{aligned} \tag{4.29}$$

Thus, we can summarize the result for general $\tau$:

$$\langle a^\dagger(0)a(\tau)\rangle_- = \bar{n}_{\rm th}\,\frac{\gamma\,G^2}{(\kappa-\gamma)(\kappa+\gamma)}\left(\frac{e^{-\gamma|\tau|}}{\gamma}-\frac{e^{-\kappa|\tau|}}{\kappa}\right)\,, \tag{4.30}$$

giving

$$\langle a^\dagger(0)a(0)\rangle_- = \bar{n}_{\rm th}\,\frac{G^2}{\kappa\,(\kappa+\gamma)}\,. \tag{4.31}$$

For the case of single-phonon addition, the calculation proceeds in a similar manner, but using the result in equation 4.19, and we obtain

$$\langle a^\dagger(0)a(\tau)\rangle_+ = (\bar{n}_{\rm th}+1)\,\frac{\gamma\,G^2}{(\kappa-\gamma)(\kappa+\gamma)}\left(\frac{e^{-\gamma|\tau|}}{\gamma}-\frac{e^{-\kappa|\tau|}}{\kappa}\right)\,, \tag{4.32}$$

and

$$\langle a^\dagger(0)a(0)\rangle_+ = \big(\bar{n}_{\rm th}+1\big)\frac{G^2}{\kappa\,(\kappa+\gamma)}\,. \tag{4.33}$$

Inserting these terms back into equation 4.26, we obtain the expected quadrature variance in the optical cavity mode for a single-phonon-subtracted thermal state

$$\left\langle\big(X_{\rm cav}(\tau)\big)^2\right\rangle_- = \frac{1}{2}\;+\;\frac{G^2}{\kappa(\kappa+\gamma)}\left(\bar{n}_{\rm th}\;+\;\bar{n}_{\rm th}\left(\frac{\kappa\,e^{-\gamma|\tau|}-\gamma\,e^{-\kappa|\tau|}}{\kappa-\gamma}\right)^2\right)\,, \tag{4.34}$$

and for a single-phonon-added thermal state

$$\left\langle \left(X_{\rm cav}(\tau)\right)^2 \right\rangle_+ = \frac{1}{2} \; + \; \frac{G^2}{\kappa(\kappa+\gamma)} \left( \bar{n}_{\rm th} \; + \; (\bar{n}_{\rm th}+1) \left( \frac{\kappa\, e^{-\gamma|\tau|} - \gamma\, e^{-\kappa|\tau|}}{\kappa-\gamma} \right)^2 \right) . \tag{4.35}$$

In equations 4.34 and 4.35 we can identify three terms: the vacuum noise in the optical cavity mode, the equilibrium value of the transduced mechanical thermal noise, and a time-dependent non-equilibrium term corresponding to the effect of the single-phonon addition/subtraction operation. We see that at the time the operation is heralded ($\tau = 0$), the characteristic doubling of the mechanical quadrature variance is mapped onto these expressions.

### 4.5.4 Detection

As can be seen from equations 4.34) and 4.35, the doubling of the mechanical quadrature variance is mirrored in the intra-cavity field, but it is only the field outside of the cavity that is accessible to our measurement. We now discuss how this output field is used to herald the operation (via single-photon detection), and to also observe and verify the charactersitic doubling in the quadrature variance (via heterodyne detection). A toy model of this joint click-dyne detection scheme is depicted in figure 4.7.

#### Heterodyne detection

We first demonstrate how heterodyne detection of the output signal field is intimately linked to the intra-cavity dynamics described in Section 4.5.3. Applying cavity input-output theory, the optical field emerging from the cavity is given by

$$a_{\rm out}(t) = a_{\rm in}(t) - \sqrt{2\kappa}\, a(t) \; , \tag{4.36}$$

where it is important to note that $a_{\rm in}$ and $a_{\rm out}$ have units of $\mathrm{s}^{-1/2}$, as opposed to intra-cavity mode operator $a$, which is dimensionless. This field then passes through a filtering setup,

and is picked off by a 50:50 beam-splitter, before arriving at the heterodyne detection setup, as shown in figure 4.7.

### Output-voltage signal of the balanced detector

The output voltage signal of the balanced detector used for (finite-bandwidth) heterodyne detection in our experiment, can be modelled as

$$U_{\text{out}}(t) = \eta_{\text{bd}}\, e\, R_{\text{fb}}\, |\alpha_{\text{LO}}| \left(\mathcal{F}^{-1}\left\{H(\omega)\right\}\right) * \left(\hat{a}_{\text{out}}(t)\, e^{-i\omega_{\text{het}}t} + \hat{a}^{\dagger}_{\text{out}}(t)\, e^{i\omega_{\text{het}}t}\right), \tag{4.37}$$

where $\eta_{\text{bd}}$ is the quantum efficiency of the photodiodes of the balanced photodetector, $e$ is the elementary charge, $R_{\text{fb}}$ is the feedback resistance and $H(\omega)$ the transfer function of the transimpedance amplifier, $|\alpha_{\text{LO}}|$ is the coherent amplitude of the local osccilator, and $\omega_{\text{het}}$ is the heterodyne frequency. The low-pass behaviour of the balanced photodetector used in this experiment can be approximated by the transfer function $H(\omega) = 1/(1 + i\omega/\omega_{\text{c}})^2$, i.e. a second-order Butterworth filter, where $\omega_{\text{c}}$ is a characteristic frequency, related to the cut-off frequency via $\omega_{\text{co}} = \sqrt{\sqrt{2}-1}\omega_{\text{c}}$. This has been examined for example in [MKL17].

For an arbitrary filter function, written in the time domain, $h(t) = \mathcal{F}^{-1}\{H(\omega)\}$, we can write the mean variance of the output-voltage signal of the balanced detector (for our phase-insensitive state) as

$$\left\langle (U_{\text{out}}(t))^2 \right\rangle = \eta_{\text{bd}}^2\, e^2\, R_{\text{fb}}^2\, |\alpha_{\text{LO}}|^2 \left\langle \int_{-\infty}^{\infty} dt'\, h(t-t') \left(\hat{a}_{\text{out}}(t') + \hat{a}^{\dagger}_{\text{out}}(t')\right) \times \int_{-\infty}^{\infty} dt''\, h(t-t'') \left(\hat{a}_{\text{out}}(t'') + \hat{a}^{\dagger}_{\text{out}}(t'')\right) \right\rangle . \tag{4.38}$$

In our experiment, as the spectral width of the measured signal ($\approx 30$ MHz) is much less than the bandwidth of the balanced detector ($\approx 400$ MHz), and the heterodyne frequency is much less than the cut-off frequency ($\omega_{\text{het}} \approx 100$ MHz) such that the signal lies in a flat part of the detectors response, we are able to neglect any filtering effects that the finite-bandwidth

response of the detector may have on the signal.

### Vacuum noise

The total vacuum noise contribution to the measured quadrature variance is given by

$$\begin{aligned}\left\langle (U_{\rm out}(t))^2 \right\rangle_{\rm vac} &= \eta_{\rm bd}^2\, e^2\, R_{\rm fb}^2\, |\alpha_{\rm LO}|^2 \int_{-\infty}^{\infty} dt'\, h^2(t-t') \\ &= \eta_{\rm bd}^2\, e^2\, R_{\rm fb}^2\, |\alpha_{\rm LO}|^2 \int_{0}^{\infty} d\omega\, |H(\omega)|^2 \ ,\end{aligned} \tag{4.39}$$

where we have used Plancherel's theorem to go from the first to the second line.

It is important to note that as we are using a continuous-wave local oscillator, and are performing the measurement outside of the cavity, extra vacuum noise is introduced into the measurement, compared to what would be the case, if the intra-cavity field was otherwise accessible, or a bandwidth-matched (pulsed) local oscillator was used.

The ratio of signal (or thermal noise) to vacuum noise is therefore reduced at the detector. A consequence of this is that additional statistics are required, in order to verify the doubling of the mechanical quadrature variance. We stress again here that the operation is indeed applied to the mechanical mode, and that the effect of this operation is manifested in all of the output fields that the mechanical mode is parametrically coupled to.

### Doubling factor

We now look to find an expression that contains the dynamics and characteristic doubling of the quadrature variance, that is similar to equations 4.34 and 4.34, but is experimentally measurable. Considering the case of subtraction, we substitute equation 4.18 into equation 4.36, to obtain

$$a_{\rm out}(t) \ = \ a_{\rm in}(t) + iG\frac{\sqrt{2\kappa}\sqrt{2\gamma}}{\kappa-\gamma}\left(\left(e^{-\gamma t}-e^{-\kappa t}\right)\Theta(t)\right) \ * \ b_{\rm in}(t) \ , \tag{4.40}$$

for the field emerging from the cavity.

If we now consider the heralded mean quadrature variance, and neglect any filtering effect of the finite-bandwidth balanced detector on the thermal contribution to the signal ($H(\omega) \approx 1$ for this term), and once again make use of the fact that cross terms between the optical and mechanical noise operators vanish, proceeding in a similar manner to equations 4.27 to 4.30, we arrive at

$$\frac{\left\langle (U_{\mathrm{out}}(\tau))^2 \right\rangle_-}{\eta_{\mathrm{bd}}^2 e^2 R^2 |\alpha_{\mathrm{LO}}|^2} = \int_0^\infty d\omega \, |H(\omega)|^2 + \eta_{\mathrm{out}} \frac{2G^2}{\kappa+\gamma} \left( \bar{n}_{\mathrm{th}} + \bar{n}_{\mathrm{th}} \left( \frac{\kappa \, e^{-\gamma|\tau|} - \gamma \, e^{-\kappa|\tau|}}{\kappa - \gamma} \right)^2 \right), \quad (4.41)$$

where $\eta_{\mathrm{out}} = \kappa_{\mathrm{e}}/\kappa \cdot \eta_{\mathrm{BS}}$ is a coupling efficiency, multiplied with efficiency describing beam splitter loss and additional insertion losses between the optical cavity mode and the balanced photodetector (compare figures 4.1 and 4.7).

The equivalent expression for addition is found accordingly, and is given by

$$\frac{\left\langle (U_{\mathrm{out}}(\tau))^2 \right\rangle_-}{\eta_{\mathrm{bd}}^2 e^2 R^2 |\alpha_{\mathrm{LO}}|^2} = \int_0^\infty d\omega \, |H(\omega)|^2 + \eta_{\mathrm{out}} \frac{2G^2}{\kappa+\gamma} \left( \bar{n}_{\mathrm{th}} + (\bar{n}_{\mathrm{th}} + 1) \left( \frac{\kappa \, e^{-\gamma|\tau|} - \gamma \, e^{-\kappa|\tau|}}{\kappa - \gamma} \right)^2 \right). \quad (4.42)$$

Once again, we can identify three terms in these expressions, corresponding to the optical vacuum noise, the steady-state mechanical noise contribution, and the dynamical term describing the action of the single-phonon addition/subtraction.

Due to the large ratio of the bandwidth of the fiber-Fabry-Perot filters, which implement an optical bandpass, to the typical signal bandwidths, we have neglected the filtering effect in our modelling. It would become important for the doubling factor once the signal bandwidth would become comparable to the filter bandwidth.

It is important to note that, in contrast to equations 4.34 and 4.34, the optical vacuum noise in this case is, naturally, not equal to 1/2, as discussed in the previous section. However, it is convenient to normalize equations 4.41 and 4.42, such that the shot-noise level in the experiment does indeed correspond to 1/2, and we denote this normalized quantity as $X$, so as to indicate that the heterodyne measurement corresponds to the measurement of a field-quadrature (or more specifically, a field quadrature variance in this work). The normalised

expression for subtraction is given by

$$\langle X^2(\tau)\rangle_- = \frac{1}{2} \; + \; \eta\left(\bar{n}_{\rm th} \; + \; \bar{n}_{\rm th}\left(\frac{\kappa\, e^{-\gamma|\tau|} - \gamma\, e^{-\kappa|\tau|}}{\kappa-\gamma}\right)^2\right) , \tag{4.43}$$

and for addition

$$\langle X^2(\tau)\rangle_+ = \frac{1}{2} \; + \; \eta\left(\bar{n}_{\rm th} \; + \; (\bar{n}_{\rm th}+1)\left(\frac{\kappa\, e^{-\gamma|\tau|} - \gamma\, e^{-\kappa|\tau|}}{\kappa-\gamma}\right)^2\right) , \tag{4.44}$$

where we have introduced the dimensionless parameter $\eta = \eta_{\rm mm}\,\eta_{\rm het}$, which takes into account both the total efficiency of the heterodyne detection $\eta_{\rm het}$ (starting from the mechanical mode), and a mode mismatch parameter $\eta_{\rm mm}$, which quantifies the "excess" shot noise due to the cw nature of the experiment. It is important to note that $\eta_{\rm het}$ captures the efficiency of the effective light-mechanics beam-splitter, $G^2/(\kappa(\kappa+\gamma))$, and the tapered fiber output-coupler efficiency, as well as all other relevant detection efficiencies.

Using equations 4.43 and 4.44, we can define a (doubling) factor $D_\pm$, which represents the increase in the mechanical contribution to the measured quadrature variance, relative to its thermal equilibrium value, upon heralded single-phonon addition or subtraction. For subtraction, we have

$$D_- = \frac{\langle X^2(\tau=0)\rangle_- - \frac{1}{2}}{\lim_{\tau\to\infty}\langle X^2(\tau)\rangle_- - \frac{1}{2}} = \frac{2\bar{n}}{\bar{n}} = 2 \; , \tag{4.45}$$

and for addition,

$$D_+ = \frac{\langle X^2(\tau=0)\rangle_+ - \frac{1}{2}}{\lim_{\tau\to\infty}\langle X^2(\tau)\rangle_+ - \frac{1}{2}} = \frac{2\bar{n}+1}{\bar{n}} \; . \tag{4.46}$$

The calculation presented here was for the case of zero optomechanical detuning ($\Delta = 0$). It was checked that the characteristic doubling of the quadrature variance is unaffected by a finite optomechanical detuning, though these calculations are not presented here. The presence of a finite detuning, which is generally expected experimentally (if no further measures are taken), merely acts to reduce the effective interaction strength $G$.

**Single-photon detection events heralding the addition/subtraction operations**

We now consider the detection of the single photons which herald the addition/subtraction operation on the thermal mechanical state. It is important to note that the fidelity of the operation is only affected by the ratio of photo-counts and dark-counts, however, as the single-photon detectors employed in this experiment are unable to resolve photon number, it is essential that the detection mode has a low mean photon number. This ensures that the probability of multi-photon events is low, and thus detection of photon numbers greater than one can be neglected, making certain that we are indeed performing single-phonon addition and subtraction operations.

Using our detection model, as shown in figure 4.7, we will now demonstrate that a detection event at the SPAD can be confidently taken to correspond to a single-photon event, for the case of single-phonon subtraction (noting that the calculation for addition follows along similarly).

The rate of photons $R$ impinging on the detector from the cavity is computed using equation 4.31 along with the cavity input-output relations, and is given by

$$R = \eta_{\text{out}}\eta_{\text{filter}} \left\langle a^{\dagger}_{\text{out}}(t) a_{\text{out}}(t) \right\rangle = \eta_{\text{out}}\eta_{\text{filter}} \frac{2G^2}{\kappa + \gamma} \, , \bar{n}_{\text{th}} \tag{4.47}$$

where $\eta_{\text{out}}$ is an output effiency from the cavity, and $\eta_{\text{filter}}$ is the combined efficiency of the fiber Fabry-Perot filters.

The total efficiency of the single-photon detection in our experiment is explicitly

$$\eta_{\text{det}} = \eta_{\text{spad}}\, \eta_{\text{filter}}\, \eta_{\text{out}} \tag{4.48}$$

where $\eta_{\text{spad}}$ is the quantum efficiency of the detector, $\eta_{\text{filter}}$ is the filtering efficiency, $\eta_{\text{out}}$ is an output effiency, which includes the efficiency of taper coupling, taper loss, and $\eta_{\text{bs}}$, the efficiency of the beam splitter used for tapping off the light into two arms for single-photon and heterodyne detection. The mean number of photo-counts at the detector (per gate) is

then

$$\bar{n}_{\mathrm{det}} = \eta_{\mathrm{spad}}\, R\, t_{\mathrm{gate}} = \eta_{\mathrm{det}}\, \bar{n}_{\mathrm{th}}\, \frac{2G^2}{\kappa+\gamma}\, t_{\mathrm{gate}}\ , \tag{4.49}$$

where $t_{\mathrm{gate}}$ is the effective gate length of the detector.

For our experimental parameters (see table 4.1), the overall detection efficiency is $\eta \approx 0.005$, and the number of photo-counts per gate is calculated to be of the order of $\bar{n}_{\mathrm{det}} \approx 0.01$ for both addition and subtraction (noting that $\bar{n}_{\mathrm{th}} \approx \bar{n}_{\mathrm{th}} + 1$ for our system at room temperature). As $\bar{n}_{\mathrm{det}} \ll 1$, the assumption of single-photon events at the detector is safely valid.

### 4.5.5 Effect of multi-modeness

In this section we discuss how the doubling signature of the quadrature variance under single-phonon addition/subtraction is changed in the scenario that the optomechanical coupling embraces multiple mechanical modes, as schematically depicted in figure 4.4. In our whispering-gallery Brillouin-optomechanical system, the coupling rate is proportional to a triple overlap integral of the two optical and the mechanical mode field functions (compare section 1.5.2). Due to the axial symmetry of the system, the azimuthal integral corresponds to a sharp condition that the azimuthal mode indices of the interacting waves are connected via $M_{\mathrm{m}} = |M|_{\mathrm{p}} + |M|_{\mathrm{S}}$ for the coupling rate not to vanish, where $M$ is the azimuthal mode number, and m, p, and S stand for mechanical, pump and Stokes modes, respectively, and the absolute value was used to avoid definition ambiguity with respect to the propagation direction (we are considering counter-propagating optical waves in this work). The frequencies of the three involved fields, on the other hand, correspond to an individual value of the optomechanical detuning $\Delta = \omega_{\mathrm{p}} - \omega_{\mathrm{S}} - \omega_{\mathrm{m}}$ for each combination of three modes. Due to finite damping of both species, even in the presence of detuning, effective optomechanical coupling is achieved.

Now, for a given pair of optical resonances, a finite optomechanical coupling is obtained

for a multitude of mechanical modes all sharing the same azimuthal mode index, but differing in their transverse (polar, radial) structure. Both the transverse overlap integral with the optics and the individual detunings due to waveguide dispersion lead to different effective coupling rates to these modes. In our system, a situation with predominantly single-mode coupling can be achieved by careful selection of the optical mode pair.

Our correlator has a very similar form to the well-known degree of second order coherence $g^{(2)}$, and it is known that for chaotic light fields the degree of second-order coherence at zero time offset is $g^{(2)}(0) = 2$ [GK04], which is generally true, also if the thermal field is multi-mode. As we shall see the calculation of the dyne-correlator for a multi-mode thermal state involves the same calculation as the $g^{(2)}(\tau)$ for such a state, with the important difference being in the vacuum noise floor of the dyne correlator, and that for a two-mode squeezing Hamiltonian spontaneous parametric scattering leads to an additional $+1$ on the mechanical noise, as above.

The optical and mechanical resonant structure can also be understood as a filter on an (assumed) approximately spectrally flat white-noise heat bath, and thus it is clear that a non-Lorentzian optical density of states, e.g. through the presence of more than one optical cavity mode (compare figure 4.4), would result in a similar argument to what follows. However, the optical mode structure of the cavity can be directly accessed by transmission measurements with a scanning laser source, and it was in this way confirmed that the optical density of states was well described by a single mode.

In order to demonstrate the effect on the doubling signature, we now consider two mechanical modes with damping rates $\gamma_1$ and $\gamma_2$, and detunings $\Delta_1$ and $\Delta_2$. As we shall see, while the doubling feature persists also in the multi-mode case, the temporal evolution of the mean quadrature variance shows an interference effect due to the spectral composition of the field.

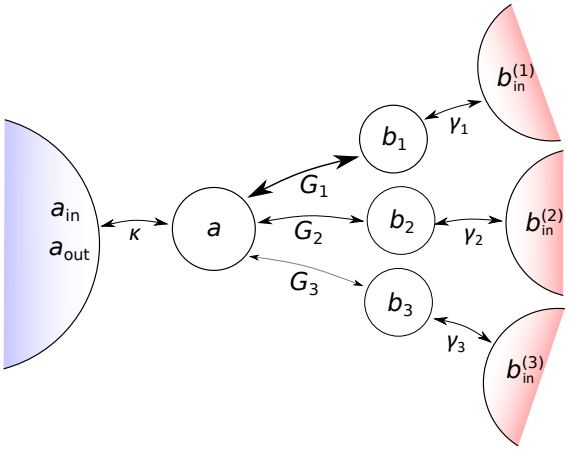


Figure 4.4: Thermodynamic picture of multiple mechanical modes and reservoirs. Once a photocount is detected in the optical output mode, it can be thought of as having originated in one of multiple independent sources of thermal noise. The weighting of contributions is according to the scattering rate (mean photon number) in the output mode from each of the thermal reservoirs. Here only three out of a large number of mechanical modes, most of which are only very weakly coupled, are depicted. The optomechanical coupling is weak, i.e. $G_i \ll \kappa, \gamma_i$.

**Multi-mode doubling feature calculation**

From a two mechanical mode beam-splitter-type Hamiltonian in a rotating frame

$$\frac{H}{\hbar} = G_1(ab_1^\dagger + a^\dagger b_1) + G_2(ab_2^\dagger + a^\dagger b_2) - \Delta_1 b_1^\dagger b_1 - \Delta_2 b_2^\dagger b_2 \tag{4.50}$$

we can derive the quantum Langevin equations of motion for the optical and mechanical degrees of freedom

$$\begin{aligned}
\dot{a} &= -iG_1 b_1 - iG_2 b_2 - \kappa a + \sqrt{2\kappa} a_{\text{in}} \\
\dot{b}_1 &= -iG_1 a - (\gamma_1 + i\Delta_1) b_1 + \sqrt{2\gamma_1} b_{\text{in}}^{(1)} \\
\dot{b}_2 &= -iG_2 a - (\gamma_2 + i\Delta_2) b_2 + \sqrt{2\gamma_2} b_{\text{in}}^{(2)} \ .
\end{aligned} \tag{4.51}$$

After the application of the Fourier transform we obtain the equations in the frequency

domain for the Fourier transforms of the mode operators

$$\begin{pmatrix} i\omega+\kappa & iG_1 & iG_2 \\ iG_1 & i\omega+\gamma_1+i\Delta_1 & 0 \\ iG_2 & 0 & i\omega+\gamma_2+i\Delta_2 \end{pmatrix} \begin{pmatrix} \tilde{A}(\omega) \\ \tilde{B}_1(\omega) \\ \tilde{B}_2(\omega) \end{pmatrix} = \begin{pmatrix} \sqrt{2\kappa}\tilde{A}_{\rm in}(\omega) \\ \sqrt{2\gamma_1}\tilde{B}^{(1)}_{\rm in}(\omega) \\ \sqrt{2\gamma_2}\tilde{B}^{(2)}_{\rm in}(\omega) \end{pmatrix} . \tag{4.52}$$

Inversion of the matrix leads to a general expression for the mode operator spectral densities in terms of the noise operators. After some massaging we obtain for the optical mode operator's spectral density (focusing again on the mechanical noise contribution)

$$\begin{aligned} \tilde{A}(\omega) = ... \times \tilde{A}_{\rm in}(\omega) \; &- \; \frac{i\sqrt{2\gamma_1}G_1(\omega-i\Gamma_2)}{G_1^2(\omega-i\Gamma_2)+G_2^2(\omega-i\Gamma_1)-(\omega-i\kappa)(\omega-i\Gamma_1)(\omega-i\Gamma_2)}\tilde{B}^{(1)}_{\rm in}(\omega) \\ &- \; \frac{i\sqrt{2\gamma_2}G_2(\omega-i\Gamma_1)}{G_1^2(\omega-i\Gamma_2)+G_2^2(\omega-i\Gamma_1)-(\omega-i\kappa)(\omega-i\Gamma_1)(\omega-i\Gamma_2)}\tilde{B}^{(2)}_{\rm in}(\omega) \; , \end{aligned} \tag{4.53}$$

where we wrote the short-hand $\Gamma_i = \gamma_i + i\Delta_i$.

In order to obtain the time domain solution we perform the inverse Fourier transform. The integration is non-trivial for the general case, but becomes easy if we make the weak coupling approximation (as above in the single-mode scenario), i.e. assuming that $G_1, G_2 \ll \kappa, \gamma_1, \gamma_2$, in which case we neglect the corresponding terms in the denominator. Then the time domain solution reads

$$\begin{aligned} a(t) = ... * a_{\rm in}(t) \; &+ \; iG_1\sqrt{2\gamma_1}\frac{1}{\kappa-\gamma_1-i\Delta_1}\left(\left(e^{-(\gamma_1+i\Delta_1)t}-e^{-\kappa t}\right)\cdot H(t)\right) * b^{(1)}_{\rm in}(t) \\ &+ iG_2\sqrt{2\gamma_2}\frac{1}{\kappa-\gamma_2-i\Delta_2}\left(\left(e^{-(\gamma_2+i\Delta_2)t}-e^{-\kappa t}\right)\cdot H(t)\right) * b^{(2)}_{\rm in}(t) \end{aligned} \tag{4.54}$$

Thus the optical and mechanical cavities act like filters on the (assumed) spectrally flat thermal bath sources (presence of multiple optical frequency eigenmodes should have a similar filtering effect).

Then we can write down the correlator (assuming that the Isserlis-Wick theorem still

applies) associated with single-phonon subtraction:

$$\langle X^2(\tau)\rangle = \frac{|\langle a^\dagger(0)a(\tau)\rangle|^2}{\langle a^\dagger a\rangle} + \langle a^\dagger a\rangle + \frac{1}{2} \tag{4.55}$$

In comparison, for the $g^{(2)}(\tau)$ we obtain

$$g^{(2)}(\tau) = \frac{\langle a^\dagger(t)a^\dagger(t+\tau)a(t+\tau)a(t)\rangle}{\langle a^\dagger(t)a(t)\rangle^2} \ , \tag{4.56}$$

applying the Isserlis-Wick theorem

$$g^{(2)}(\tau) = \frac{\langle a^\dagger(t)a(t+\tau)\rangle\langle a^\dagger(t+\tau)a(t)\rangle + \langle a^\dagger(t)a(t)\rangle\langle a^\dagger(t+\tau)a(t+\tau)\rangle}{\langle a^\dagger(t)a(t)\rangle^2} \ . \tag{4.57}$$

This already implies that $g^{(2)}(0) = 2$ if the Isserlis-Wick theorem is applicable, which is the case for a multimode thermal field.

Then we can write

$$g^{(2)}(\tau) = 1 + \frac{\langle a^\dagger(t)a(t+\tau)\rangle\langle a^\dagger(t+\tau)a(t)\rangle}{\langle a^\dagger(t)a(t)\rangle^2} = 1 + \frac{|\langle a^\dagger(0)a(\tau)\rangle|^2}{\langle a^\dagger a\rangle^2} \ , \tag{4.58}$$

where in the weak coupling approximation we can write short for equation 4.54

$$a(t) = ... * a_{\text{in}}(t) + F_1(t;\kappa,\gamma_1,\Delta_1,G_1) * b_{\text{in}}^{(1)}(t) + F_2(t;\kappa,\gamma_2,\Delta_2,G_2) * b_{\text{in}}^{(2)}(t) \ . \tag{4.59}$$

Thus, the only required term for us to compute in order to determine the heterodyne variance excursion, and the $g^{(2)}$ is

$$\langle a^\dagger(0)a(\tau)\rangle = \bar{n}_{\text{th}} \int dt' \left(F_1^*(-t')F_1(\tau - t') + F_2^*(-t')F_2(\tau - t')\right) \ . \tag{4.60}$$

In figure 4.5 there is shown a plot of the degree of second order coherence according to equation 4.58 for the multimode thermal state, where we considered two mechanical modes with linewidths of 6 and 8 MHz respectively, an optical linewidth of 50 MHz and detunings

of -15 and +10 MHz. The relative rates $\propto G_i^2$ have a ratio of 4 to 1.

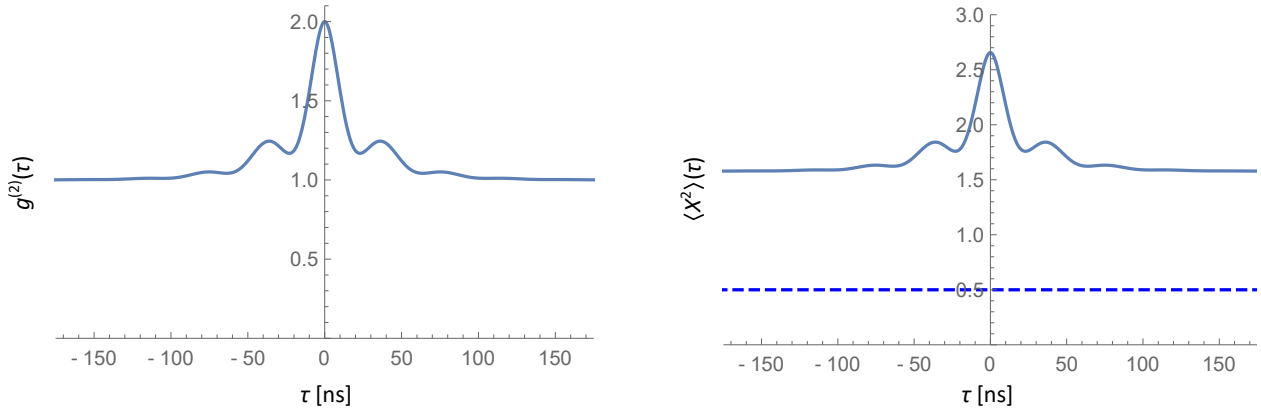


Figure 4.5: Degree of second order coherence $g^{(2)}(\tau)$ of a multi-mode thermal field (left), and the doubling feature for single-phonon subtraction ("click-dyne correlator") with the same system parameters (right), where the dashed line represents vacuum noise. The parameters are given by the linewidths of $2\gamma_1/(2\pi) = 6$MHz, $2\gamma_2/(2\pi) = 8$MHz, an optical linewidth of $2\kappa/(2\pi) = 50$ MHz and detunings of $\Delta_1/(2\pi) =$ -15 MHz and $\Delta_2/(2\pi) = +10$ MHz. The coupling rates are $G_1/(2\pi) = 1$MHz and $G_2/(2\pi) = 0.5$MHz.

## 4.6 Non-Gaussian nature of the prepared state

For thermal excitation $\bar{n} \gg 1$ the prepared single quantum added/subtracted states are very non-Gaussian, with their Wigner functions showing a "hole" in the middle of phase space. As the states are symmetric in phase space, a marginal quadrature distribution of the mechanical oscillator at any phase angle will be a non-Gaussian function.

In order to measure this non-Gaussian character of the prepared mechanical state, it is necessary to read-out the state and overcome a certain minimum efficiency when doing so, such that the non-Gaussian quadrature distribution is not covered by optical vacuum noise.

The beam-splitter drive, used for phonon subtraction, is implementing a continuous partial light-matter state swap. Thus, it should be possible to see the non-Gaussianity of the quadrature distribution when looking at the output of the continuously driven beam splitter, as long as a minimum total efficiency of the read-out is fulfilled. This efficiency requirement becomes easier to fulfil the more classical the thermal state is, i.e. $\bar{n}_{\mathrm{th}} \gg 1$. In our case we have $\bar{n}_{\mathrm{th}} \approx 760$ at room temperature. When approaching the ground state and $\bar{n}_{\mathrm{th}} \sim 1$,

the single-quantum-subtracted thermal state qualitatively changes, and its Wigner function becomes more Gaussian, as the quantum noise contribution becomes more dominant. The two-mode squeezing operation, however, does only implement a similar operation like a beam splitter in the limit of weak optomechanical coupling (small squeezing parameter):

For a two-mode squeezing operator $S = e^{ir(ab+a^\dagger b^\dagger)}$, for small squeezing parameter $r$ one has

$$S^\dagger a S \approx a + irb^\dagger \ , \tag{4.61}$$

while the beam splitter operation for small reflectivity $r$ gives

$$B^\dagger a B \approx a + irb \ . \tag{4.62}$$

As this approximation fails for higher squeezing parameters, the two-mode-squeezer continuous drive is not as predestined as the beam splitter drive to reveal the non-Gaussianity of the prepared mechanical state. In the high-temperature limit the states prepared by single-phonon addition and subtraction are indeed identical, while towards the quantum regime they are fundamentally different. While single-phonon subtraction on a thermal state close to the ground state ($\bar{n} \ll 1$) leaves the state almost unaltered, the single-phonon-addition operation applied to the same state makes it highly non-classical, showing significant Wigner negativity. The non-classicality of the single-phonon-added thermal state is also present for arbitrarily high initial occupation.

A separation between state preparation and state read-out phases of the experiment, which would naturally be tried to achieve, is not possible here at this stage, as the mechanical damping rate, being of the same order of magnitude as typical optical linewidths, only permit experiments on the nanoseconds timescale.

### 4.6.1 Toy model and lossy read-out of non-Gaussian quadrature distribution

Here we will present a toy model of the continuous optomechanical state read-out for the beam splitter Hamiltonian case, revealing requirements for both state preparation and read-out efficiency.

#### Quadrature distribution of the single-quantum-subtracted thermal state

Upon single-phonon subtraction the initial thermal state of the mechanical mode $\rho_{\mathrm{th}}$ changes to

$$\rho_{-} = \frac{b\rho_{\mathrm{th}}b^{\dagger}}{\mathcal{P}} \ , \tag{4.63}$$

where the normalisation is given through $\mathcal{P} = \mathrm{Tr}(b\rho_{\mathrm{th}}b^{\dagger}) = \mathrm{Tr}(\rho_{\mathrm{th}}b^{\dagger}b) = \bar{n}$, where $\bar{n}$ is the mean phonon number of the (initial) thermal state.

We can then write down the probability distribution for the position quadrature

$$\begin{aligned}
\mathrm{Pr}(X) &= \langle X|b\rho b^{\dagger}|X\rangle/\mathcal{P} \\
&= \langle X|b\frac{1}{\pi\bar{n}}\int d^2\beta e^{-|\beta|^2/\bar{n}}|\beta\rangle\langle\beta|b^{\dagger}|X\rangle/\mathcal{P} \\
&= \frac{1}{\pi\bar{n}}\int d^2\beta e^{-|\beta|^2/\bar{n}}|\beta|^2|\langle X|\beta\rangle|^2/\mathcal{P} \\
&\quad \text{with } |\beta|^2 = 1/2(X_{\beta}^2 + P_{\beta}^2) \text{ and } |\langle x|\beta\rangle|^2 = \frac{1}{\sqrt{\pi}}e^{-(X-X_{\beta})^2} \\
&= \frac{1}{4\bar{n}\pi^{3/2}}\int\int dX_{\beta}dP_{\beta}e^{-X_{\beta}^2/2\bar{n}}e^{-P_{\beta}^2/2\bar{n}}(X_{\beta}^2 + P_{\beta}^2)e^{-(X-X_{\beta})^2} \ .
\end{aligned} \tag{4.64}$$

The probability distribution of the position quadrature $\mathrm{Pr}(X)$ for the single-quantum-subtracted thermal state is plotted in figure 4.6 for an initial thermal occupation of $\bar{n} = 760$, as found in the experiment. The distribution can be thought of, in the classical limit $\bar{n} \gg 1$, as a result of the exponential phonon number distribution, combined with the scattering probability being proportional to the phonon number $\bar{n}$. Thus, after the acquisition of the information that a photocount embodies, the probability that the instantaneous displacement

of the oscillator is in the center of phase space is very low. This is apparent in the Wigner function having a "hole" in the center, and the marginal distribution in the plot of figure 4.6 reflects this.

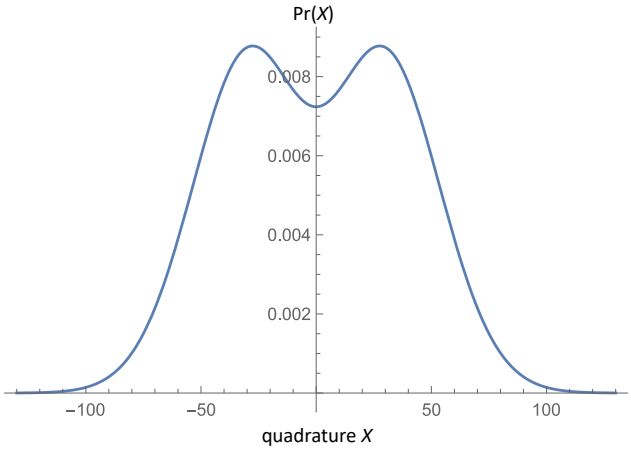


Figure 4.6: Theory plot of quadrature distribution of phonon subtracted thermal state.

### Toy model and mean phonon/photon number $\bar{n}$

In order to better understand the experimental results, a toy model was set up and investigated. It considers the mechanical mode of the cavity in a thermal state as the source of excitation, then follows the excitation to the detector through multiple beam splitters, where the thermal nature of the fields is preserved by the beam splitters. A scheme of the toy model is shown in figure 4.7.

In the weak coupling case (where $G$ is small) the first light-matter beam splitter can be also implemented by the two-mode squeezing Hamiltonian, as for small squeezing parameters the interaction approximates a beam-splitter-type interaction.

The toy model does not consider cavity effects (as have been considered in the correlation function calculation) or the cooling of the original mechanical mode, but offers appreciable insight into the physics of the experiment.

When looking at figure 4.7, we can see how the mean phonon number in the respective modes changes from initially $\bar{n} \approx 760$ for the mechanical mode, to a mean photon number

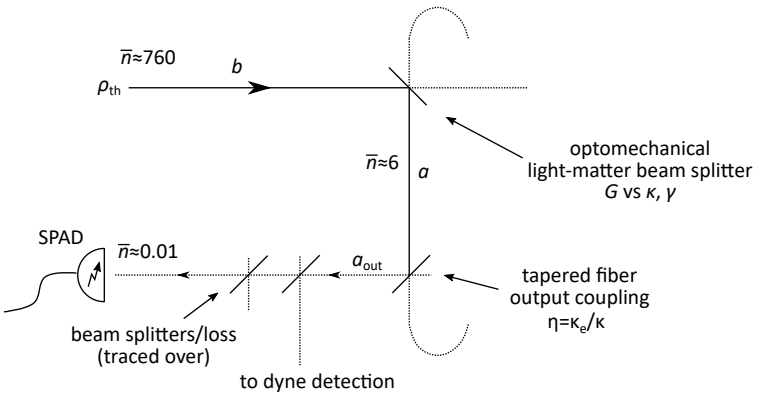


Figure 4.7: Toy model showing the detection scheme used to herald, observe and verify single-phonon subtraction and addition to a mechanical thermal state. The mean number of phonons in the equilibrium thermal state (identical to the reservoir occupation), photons in the cavity mode, and photons per gate at the SPAD detector, are highlighted. Importantly, multi-photon detection events at the SPAD are negligible, as the mean photon number per gate is much less than one.

of $\bar{n} \approx 6$ in the optical cavity mode, to $\bar{n} \approx 0.01$ on the single photon avalanche diode (SPAD) photodetector. This change in the mean phonon/photon number reflects all the effective efficiencies in the path of the excitation, and also includes the effective efficiency of the detector itself, which is given by a product of the detector's quantum efficiency and its gating duty cycle $\eta_{\mathrm{det}} = \eta_{\mathrm{qe}} \cdot f_{\mathrm{gate}} \cdot t_{\mathrm{gate}} = 0.125 \cdot 50 \times 10^3\ \mathrm{s}^{-1} \cdot 10\ \mathrm{ns}$.

The low value of $\bar{n} \ll 1$ in a detector gate is a requirement for the probabilistic preparation to correspond to a single-phonon operation. In this case the probability of photon numbers higher than 1 on the detector is negligible, and the SPAD, which is not photon number resolving, operates as such when distinguishing photon numbers $n = 0$ and $n > 0$, thus projecting onto the single photon Fock state $\langle 1|$.

### Read-out of quadrature distribution including loss

The following calculation will detail, how in the toy model the quadrature distribution of the mechanical oscillator will be degraded by optical vacuum noise. A scheme of the calculation is shown in figure 4.8.

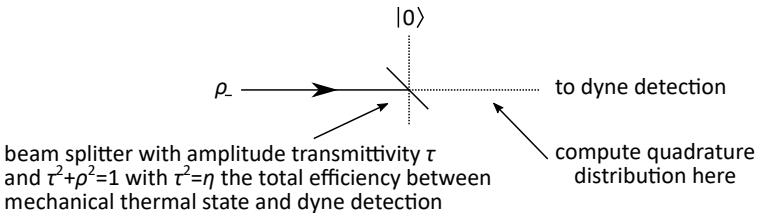


Figure 4.8: Toy model of quadrature distribution measurement including optical loss. The phonon subtracted thermal state $\rho_-$ undergoes a beam splitter operation, related to the overall efficiency/loss, and the quadrature distribution of the beam splitter output is then to be measured using an optical homodyne/heterodyne setup. The other output mode is traced over to model the loss.

As the action of a beam splitter operation is well known in the coherent state basis

$$|\alpha\rangle_{\mathrm{A}} \otimes |\beta\rangle_{\mathrm{B}} = |t\alpha - r\beta\rangle_{\mathrm{C}} \otimes |r\alpha + t\beta\rangle_{\mathrm{D}} \ , \tag{4.65}$$

with $t^2 + r^2 = 1$, see e.g. [BR97], we first express the density operator in a coherent state basis $|\{\alpha\}\rangle$ (Glauber-Sudarshan or $P$-representation), which reads

$$\rho = \int P(\alpha, \alpha^*) |\alpha\rangle\langle\alpha| d^2\alpha \ , \tag{4.66}$$

with the $P$-representation of a thermal state being a gaussian

$$P(\alpha) = \frac{1}{\pi\bar{n}} e^{-|\alpha|^2/\bar{n}} \ . \tag{4.67}$$

The position quadrature distribution (identical for all quadrature angles, as the state is symmetric in phase space) of the single-phonon subtracted thermal state undergone loss,

then reads

$$
\begin{aligned}
\Pr(X) &= \mathrm{Tr}_{\mathrm{v}}\left(\langle X|U_{\mathrm{BS}}\left(\frac{1}{\bar{n}}b\int d^2\beta P(\beta)|\beta\rangle_{\mathrm{m}}\langle\beta|b^\dagger\right)\otimes|0\rangle_{\mathrm{v}}\langle 0|U_{\mathrm{BS}}^\dagger|X\rangle\right)\\
&= \frac{1}{\pi\bar{n}^2}\mathrm{Tr}_{\mathrm{v}}\left(\langle X|\int d^2\beta e^{-|\beta|^2/\bar{n}}|\beta|^2|\sqrt{\eta}\beta\rangle_{\mathrm{m}}\langle\sqrt{\eta}\beta|\otimes|\sqrt{1-\eta}\beta\rangle_{\mathrm{v}}\langle\sqrt{1-\eta}\beta||X\rangle\right)\\
&= \frac{1}{\pi^2\bar{n}^2}\int d^2\gamma\int d^2\beta e^{-|\beta|^2/\bar{n}}|\beta|^2|\langle X|\sqrt{\eta}\beta\rangle|^2|\langle\gamma|\sqrt{1-\eta}\beta\rangle|^2\\
&\quad \text{with}\quad |\langle X|\sqrt{\eta}\beta\rangle|^2 = \frac{1}{\sqrt{\pi}}e^{-(X-\sqrt{\eta}X_\beta)^2}\quad\text{and}\quad |\langle\gamma|\sqrt{1-\eta}\beta\rangle|^2 = e^{-|\gamma-\sqrt{1-\eta}\beta|^2}\\
&= \frac{1}{4\pi^{5/2}\bar{n}^2}\int dX_\gamma\int dP_\gamma\int dX_\beta\int dP_\beta e^{-\frac{X_\beta^2+P_\beta^2}{2\bar{n}}}(X_\beta^2+P_\beta^2)e^{-(X-\sqrt{\eta}X_\beta)^2}\ \times ...\\
&\qquad ...\times\ e^{-\frac{X_\gamma^2+P_\gamma^2}{2}-\frac{1-\eta}{2}(X_\beta^2+P_\beta^2)+\sqrt{1-\eta}(X_\gamma X_\beta+P_\gamma P_\beta)}\\
&= \frac{(1+\eta\bar{n}(3+2\eta\bar{n}+2X^2))e^{-\frac{X^2}{1+2\eta\bar{n}}}}{(1+2\eta\bar{n})^{5/2}}\ ,
\end{aligned}
\tag{4.68}
$$

where the last step was obtained using the symbolic computation software Wolfram Mathematica.

We see that the quadrature distribution of equation 4.68, which we obtained from our toy model, only depends on one parameter, namely $\eta\bar{n}$. As long as this "transmitted thermal variance" is significantly larger than the quadrature variance of the vacuum noise (1/2), the non-Gaussian character of the distribution function can be observed.

### 4.6.2 Experimental results

In order to observe the non-Gaussian character of the state, as discussed in the previous section, the overall efficiency of the dyne measurement had to be substantially increased. Also the vacuum noise needed to be limited to the bandwidth of the signal, in order to maximize signal-to-noise ratio. To achieve this, the heterodyne frequency was moved to DC, and a low-pass filter (consisting of a combination of low-pass filters 23 MHz slow cut-off (minicircuits SBLP-39) and 48 MHz steep cut-off (minicircuits SLP-50)) was used, in order to limit the effective detector bandwidth to approximately the signal bandwidth of

the Brillouin scattered light. The optical pump power was increased compared to previous measurements, from $\approx$ 1 mW to 9 mW. Additionally the 50:50 beam splitter was replaced with a 90:10 beam splitter, which was affordable, as the light-matter beam splitter was now much stronger with 9 mW pump power. While a flat-top distribution was relatively quickly observed, it required an optimisation of all of these measures to observe the predicted dip in the quadrature distribution.

Figure 4.9 shows a measurement of the non-Gaussian quadrature distribution.

Shown in figure 4.10 is the measured quadrature distribution around the time of the subtraction event (click), at time $\tau = 0$. It can be seen how the mode relaxes back to thermal equilibrium. Also, as is already apparent in the doubling signature, the time symmetry of the feature is clearly visible.

The single parameter quadrature probability distribution of the single-phonon subtracted thermal state undergone loss, is fitted to the measured histogram data, and is shown in figure 4.11.

## 4.7 Outlook

Brillouin optomechanics with high frequency phonons [Chu+17; Kha+19; Enz+19], is emerging as a powerful new platform for quantum and classical optomechanics applications. Owing to the favourable bulk properties of crystalline materials, such systems now set the state-of-the-art for mechanical $Qf$ products [Gal+13; Ren+18], where $Qf > 10^{17}$, and provide ultra-low mechanical decoherence rates even for modest cryogenic temperatures. At 4 K we expect that the $BaF_2$ crystalline resonators used here should also have such ultra-low mechanical decoherence rates and operate deeply within the 'coherent phonon limit' where the mechanical coherence length is much greater than the resonator circumference. Moreover, $BaF_2$ is an ultra-low-loss optical material, which enables optically-induced heating to be minimized and Brillouin optomechanical strong-coupling to be readily achieved [Enz+19]. These advantages, combined with the techniques demonstrated here, open a rich avenue for further

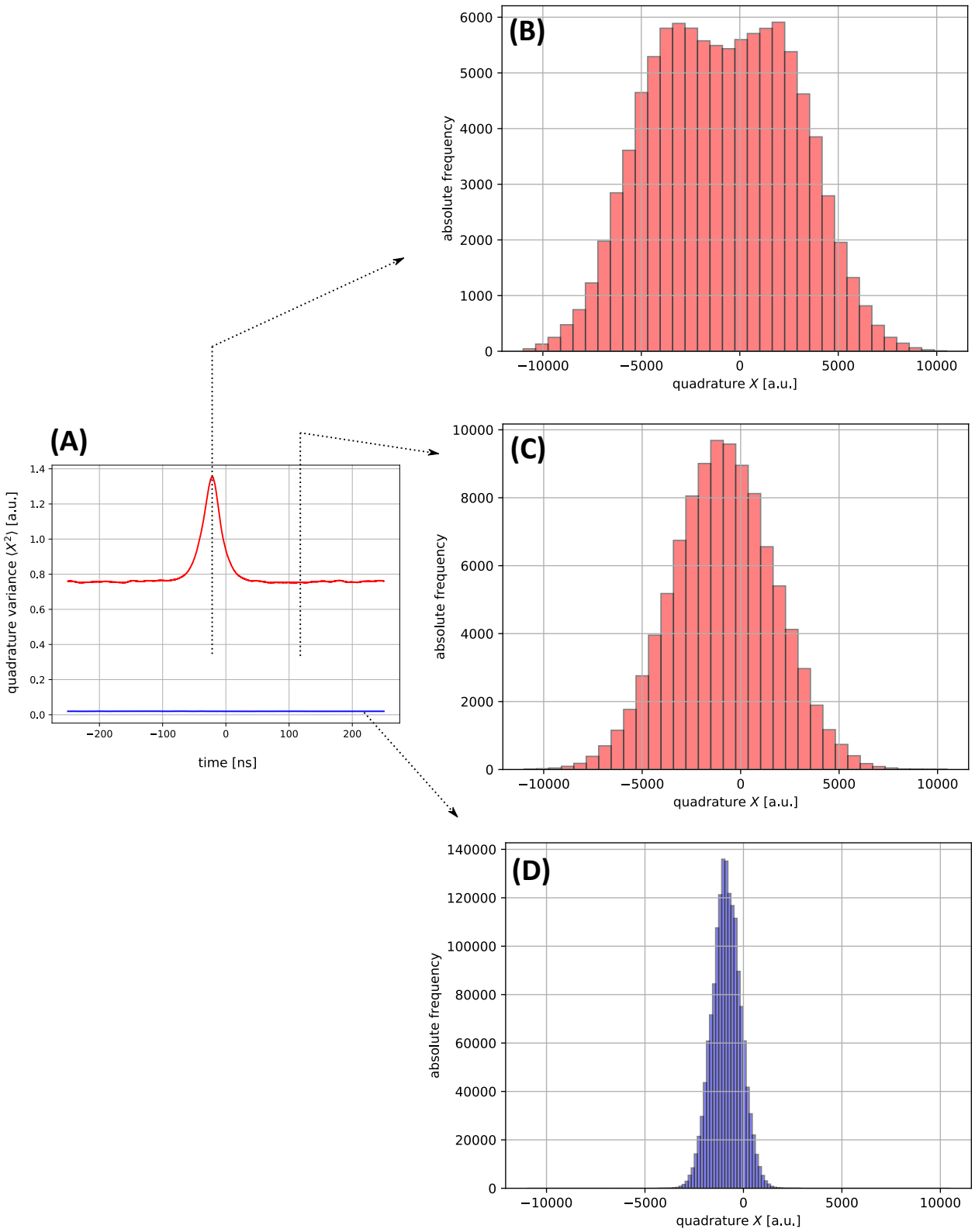


Figure 4.9: Non-Gaussian quadrature distribution of phonon subtracted thermal state. (B) shows a quadrature distribution of the output light mode at time of subtraction (centre of the doubling feature in (A)). (C) shows the quadrature distribution 100 ns later. (D) shows optical vacuum noise for comparison. For this experiment the coupling rate was high (non-negligible cooling) through 8 mW optical pump power, and a 90:10 beam splitter was used instead of a 50:50 beam splitter to minimise loss on the homodyne measurement. Also a low-pass filter was used to suppress vacuum noise beyond the signal bandwidth. The x-axis offset is due to an offset in the fast preamp of the oscilloscope used for the acquisition.

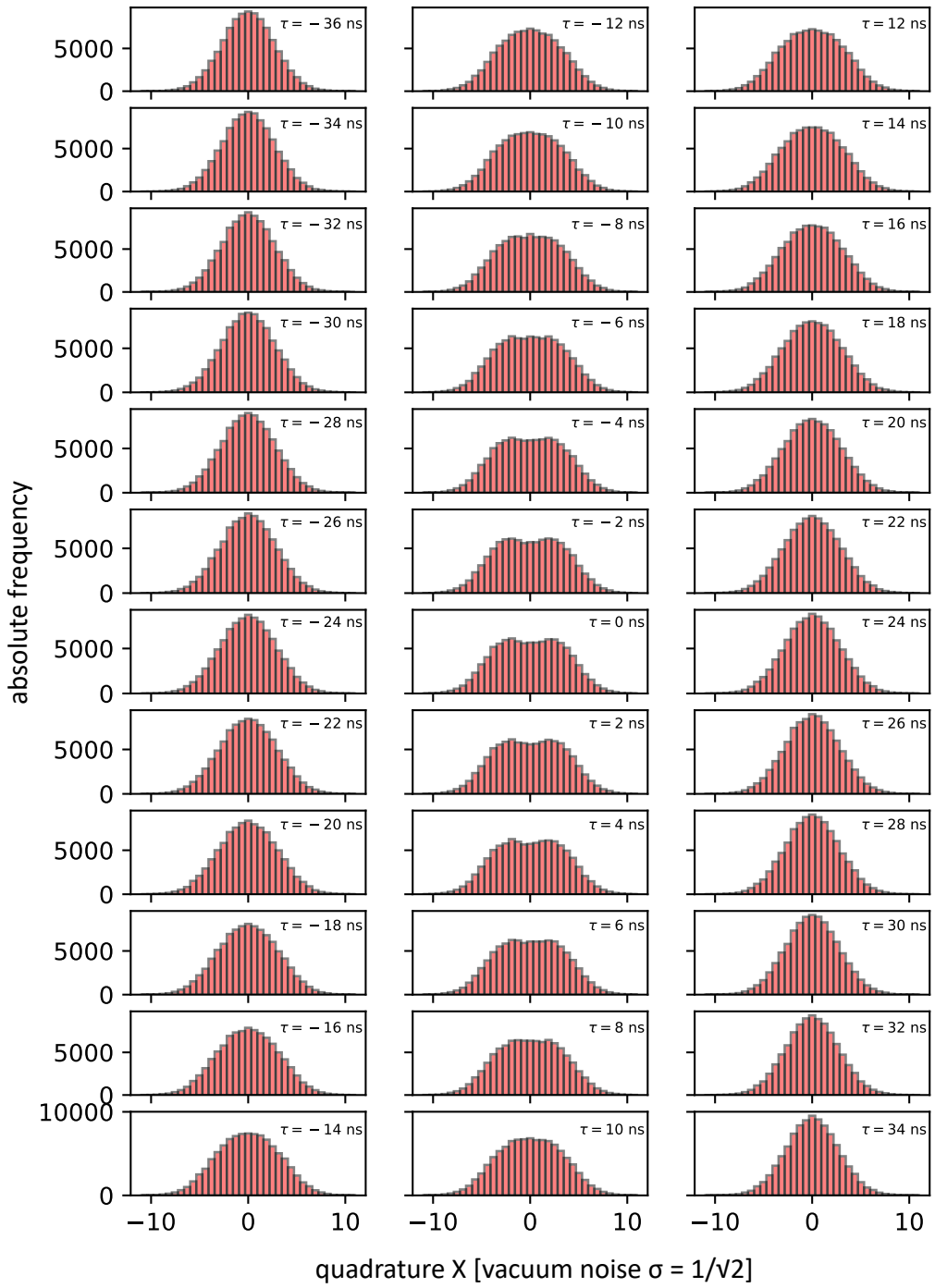


Figure 4.10: Time evolution of non-Gaussian quadrature distribution. Plotted are histograms of the output mode quadrature, in time steps of 2 ns, centered around the time of single-phonon subtraction at $\tau = 0$. Observable is the relaxation of the mode to thermal equilibrium. This occurs both in forward, and in backward running time.

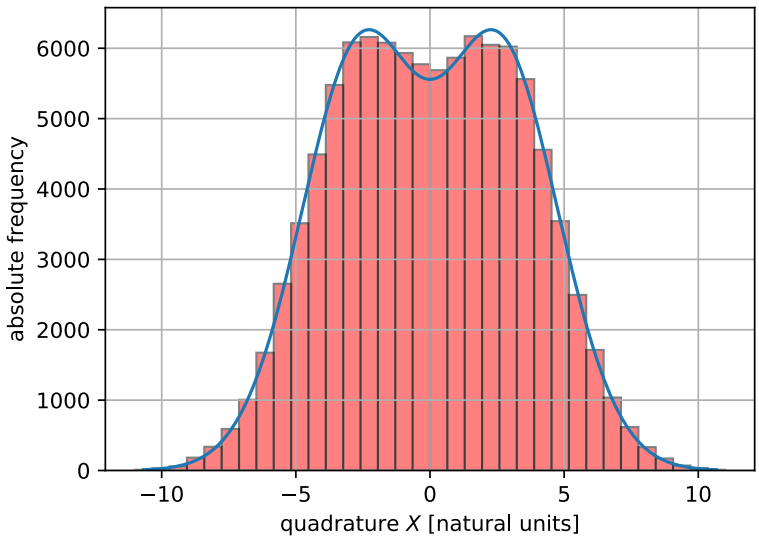


Figure 4.11: Toy model fit to measured non-Gaussian quadrature distribution of a single-phonon subtracted thermal state. The single fit parameter (except scaling the height) is $\eta\bar{n}_{\mathrm{th}} = 5.8$.

studies. For example, the ultra-long coherence times attainable with these mechanical modes [Gal+13; Ren+18] make these systems an interesting candidate for quantum memories and repeaters [Dua+01; San+11]. Additionally, these properties are also well suited for mechanical quantum state engineering, for example mechanical superposition-state preparation via mechanical squeezing and then single-phonon addition/subtraction [MKV16]. Following a state preparation protocol, one can then utilize the strong coupling achievable with these systems [Enz+19] for mechanical state reconstruction [VPK15]. Further exciting lines of study opened by this direction include developing more advanced protocols in time involving multiple single-phonon addition/subtraction operations [VAK13], and exploiting the non-reciprocity of the Brillouin scattering interaction for quantum networking/routing applications.

# Chapter 5

# Heterodyne-measurement-enhanced optomechanical sideband cooling

In this chapter we introduce a scheme that enhances optomechanical sideband cooling by use of the measurement record of a continuously monitored dissipation channel of the mechanical mode. Heterodyne measurement is performed on the light scattered by the mechanical mode of interest into an optical cavity mode of the whispering-gallery resonator, which couples out of the cavity via a tapered optical fiber. The Gaussian state of the two-mode system is preserved under time evolution, given by the light-matter beam-splitter-type Hamiltonian and a coupling to the environment, as well as measurement, only linear in the field operators. Thus, the time evolution can be reduced to an evolution problem for the means and variances of the two modes. The continuous measurement record is used to obtain a quantum trajectory of the mechanical mode in phase space with reduced variance compared to the unmonitored state, thus achieving an enhancement of sideband cooling by heterodyne measurement.

We experimentally demonstrate this protocol in a Brillouin optomechanical platform, modelled as one acoustic mode and two optical whispering-gallery modes of a fused-silica whispering-gallery resonator, operating at room temperature, by conditioning the state of the system on past measurement outcomes.

An extension of the protocol allows the application of a retrodiction formalism by propa-

gating the quantum state backwards in time [ZM17], which can only be done "offline" after a time series of the continuous measurement record has been obtained. The protocol estimates the mechanical state optimally which offers a rich avenue for sensing applications.

This project was led jointly with Magdalena Szczykulska on the experimental side, and obtained valuable theoretical support from Jinglei Zhang and Klaus Mølmer, at the university of Aarhus. I took a leading role in building the setup for this experiment, modelling of the optomechanical system, finding favourable experimental conditions in terms of system parameters, data taking and analysis, and interpretation of the findings. Jinglei Zhang and Klaus Molmer developped the Gaussian state evolution model which is described in [ZM17] and helped in applying it to our platform, with code written for solving the Gaussian state evolution for a given measurement record by Jinglei Zhang, as well as obtaining analytical results.

## 5.1 Introduction

Quantum control of mechanical systems lies at the heart of optomechanics. It is of major interest in fundamental physics [Bre+08; AKM14; Nie+17; Rin+18] and applied sciences such as precision metrology [Met14; Qva+18; Doo+14] and quantum information processing [ZGB07; Fio+11; Wie+11; Bak+16]. Cooling of mechanical motion is an important step for these areas and different cooling techniques have been considered. They include sideband cooling (passive back-action cooling) [Teu+11; Cha+11; Pet+16; Bah+12; Kar+12; Sch+11], conditional state preparation and cooling by measurement [Wie+15; Van+13], feedback cooling [KB06; Ros+18], cooling a hybrid system [Vog+13], and enhancing sideband cooling by feedback [Ros+17].

Sideband cooling was first studied in atomic physics, where it allowed trapping of ions and atoms [Die+89; Rei+13], and preparation of exotic atomic states [And+95; Hu+17]. With the development of gravitational wave detectors, this cooling technique gained an interest in the field of optomechanics to cool the mechanical motion of macroscopic objects [BM67;

Bra68]. The principle here is to red-detune a pump laser with respect to an optical cavity mode so that it results in damping of a mechanical mode of interest and the creation of frequency upconverted photons in the respective optical cavity mode. This effectively leads to a beam-splitter interaction Hamiltonian between these modes [AKM14]. Further advances and miniaturisation of optomechanical systems enabled remarkable sideband cooling of mechanical modes in micro- and nano-scale resonators [Gig+06; Arc+06; Bah+12; Kar+12] with mechanical ground states reported in [Cha+11; Teu+11; Pet+16] starting from cryogenic temperatures. Sideband cooling was also applied to cool the collective mode of an atomic ensemble inside an optical cavity [Sch+11].

While sideband cooling reduces the thermal fluctuations of the mechanical state by removing phonons from it, more information about the system can be inferred if the upconverted light is continuously monitored. The state can then be conditioned on the measurement record by invoking a suitable stochastic master equation model. Such conditional state preparation is optimal in terms of minimising the mean-squared error of the associated phase space trajectories [WM09] and effectively purifies the state [Van+11; Van+13]. Conditioning on the past measurements allows real-time state estimation [Wie+15] and can be incorporated into feedback protocols to prepare a thermal mechanical state of reduced fluctuations [Ros+17; Ros+18; KB06; Pog+07; LKR11]. In particular, reference [Ros+17] uses a (non-homodyne/heterodyne) feedback loop to enhance sideband cooling, and [Ros+18] reports reaching the ground state of a mechanical mode of a nanomechanical membrane resonator from cryogenic temperatures.

If real-time state estimation is not of importance, the corresponding uncertainty and therefore our knowledge of the system can be further improved by employing both past and future events from the measurement record. Such offline protocol can give rise to the so-called past quantum state formalism [GJM13; ZM17] which shares similarities with quantum state smoothing [GW15] in that both can be used to optimally extract information about the system state given a complete measurement record.

The optimal choice of a measurement depends on the type of interaction Hamiltonian.

While phase sensitive detection, such as homodyne, is a common measurement scheme in optomechanics, it is not always the optimal one.

Here we present an experimental protocol for heterodyne-measurement-enhanced cooling of an acoustic mode inside a Brillouin optomechanical system at room temperature. Here, the third-order coupling Hamiltonian between the mechanical and optical modes associated with Brillouin scattering, can be approximated under strong pumping as a light-matter beam-splitter-type Hamiltonian. We show the advantage of heterodyne over the commonly used homodyne detection for such interactions. We use the past quantum state formalism for Gaussian systems [ZM17] to optimally estimate the phase space trajectories of the mechanical state and the associated uncertainties. We consider the finite bandwidth of the detector and verify that our conditional state assignment is correct. The protocol effectively purifies the mechanical state which provides a rich avenue for sensing applications.

## 5.2 Theory

Figure 5.1 illustrates the principle of the purification protocol. The first aspect is sideband cooling of the mechanical mode. For our platform, this is achieved by selecting two optical whispering-gallery modes (WGMs) of different transverse profiles which are separated by the frequency of an acoustic WGM of a microresonator, and which fulfil the phase matching conditions as described in section 1.5.1. Pump laser light, resonant with lower frequency resonance, scatters photoelastically off the thermally excited acoustic mode (subscript m) into the higher frequency anti-Stokes mode (subscript aS). This is shown schematically in figure 5.1 (A). Stokes scattering is suppressed by the cavity mode structure, as there is no optical resonance of the cavity with a red-detuning from the pump corresponding to the Brillouin shift. The amplitude decay rates of the optical and mechanical modes are denoted by $\kappa$ and $\gamma$ respectively. The Hamiltonian of this interaction in an appropriate rotating

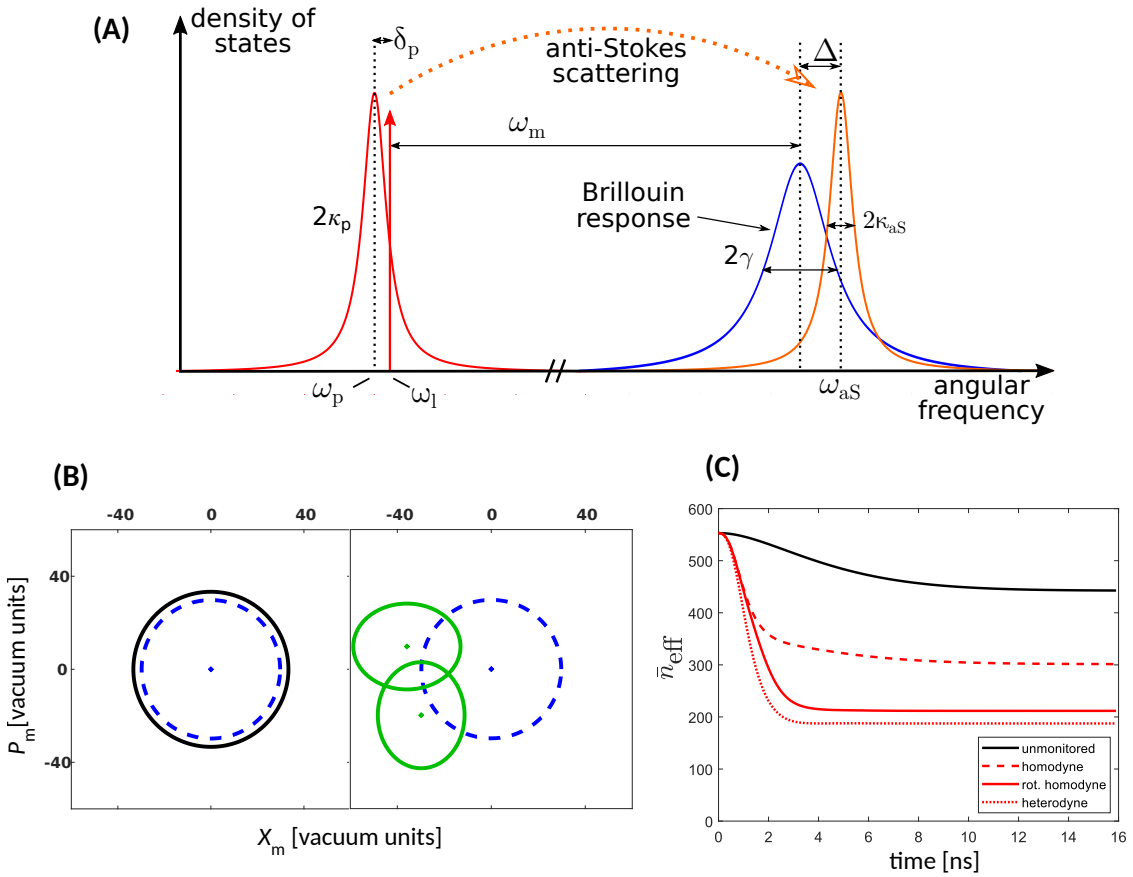


Figure 5.1: Illustration of the heterodyne measurement cooling protocol. (A) Three-mode Brillouin system with a beam-splitter interaction between the anti-Stokes and mechanical modes with the pump laser acting as an auxiliary field. This interaction is associated with sideband cooling of the mechanical mode. Here, $\Delta_p$ is the detuning of the pump laser from resonance and $\Delta$ is the optical-mechanical detuning. (B) Heterodyne-measurement-enhanced cooling in phase space. The left plot shows sideband cooling (dashed blue line) of the mechanical mode from the initial thermal state at room temperature(continuous black line). The right plot shows the reduced uncertainty of the state by using the past measurement record only (green line). Points and contours represent mean values and standard deviations of $\hat{X}_m$ and $\hat{P}_m$, respectively. (C) Effective phonon number as a function of time for different detection schemes. Figures (B) and (C) are theoretical plots for the following system parameters: $G/2\pi = 20\,\mathrm{MHz}$, $2\kappa_{aS}/2\pi = 90\,\mathrm{MHz}$, $2\gamma_m/2\pi = 42\,\mathrm{MHz}$, $\eta = 0.5$, $\Delta/2\pi = 0$, $\bar{n} = 555$, $\omega_{het}/2\pi = 150\,\mathrm{MHz}$.

frame is [Enz+19] (compare section 1.5.4)

$$\frac{\hat{H}_{\mathrm{BS}}}{\hbar} = G\left(\hat{a}_{\mathrm{aS}}^{\dagger}\hat{b} + \hat{a}_{\mathrm{aS}}\hat{b}^{\dagger}\right) - \Delta\hat{b}^{\dagger}\hat{b}, \tag{5.1}$$

where $\hat{a}_{\mathrm{aS}}$ and $\hat{b}$ are the annihilation operators corresponding to the anti-Stokes and mechanical modes respectively. $G$ is the optomechanical coupling strength and $\Delta = \omega_{\mathrm{aS}} - \omega_{\mathrm{L}} - \omega_{\mathrm{m}}$ is the optomechanical detuning, where $\omega_{\mathrm{L}}$ is the pump laser frequency.

The anti-Stokes light, produced as a result of this beam-splitter-type interaction, is coupled out of the cavity and is continuously monitored by an optical heterodyne detector. This is the second aspect of the protocol, where the full measurement record is incorporated into the formalism. Here, the optomechanical state is evolved forward in time by inputting the time-domain data into a stochastic master equation. It describes the evolution of the density matrix $\rho$ conditioned on the past measurements and this is the forward evolution of the state.

This forward evolution can be complemented by a second equation which describes the evolution of the effect matrix $E$ conditioned on the future measurements and this the backward evolution of the state. This backward quantum state formalism approach has not yet been implemented on the experimental data, but is described in [ZM17].

The stochastic master equation of the general form of equation 1.13 here takes the form

$$d\hat{\rho} = -\frac{i}{\hbar}\left[\hat{H}, \hat{\rho}\right] dt \; + \; \sum_{h} D[\hat{c}_h]\{\hat{\rho}\}dt \; + \; \sum_{h} \sqrt{\eta_h}\mathcal{H}[\hat{c}_h]\{\rho\}dW_h(t) \; , \tag{5.2}$$

where $\{\hat{c}_h\}$ are the participating dissipation operators, $D$ is the Lindblad superoperator, and $\mathcal{H}$ is the measurement superoperator, which are defined through

$$D[\hat{c}]\{\rho\} = \hat{c}\rho\hat{c}^{\dagger} - \frac{1}{2}\left(\hat{c}^{\dagger}\hat{c}\rho + \rho\hat{c}^{\dagger}\hat{c}\right) \tag{5.3}$$

and

$$\mathcal{H}[\hat{c}]\{\rho\} = \hat{c}\rho + \rho\hat{c}^{\dagger} - \langle\hat{c} + \hat{c}^{\dagger}\rangle\rho \; . \tag{5.4}$$

$dW_h(t)$ is the Wiener increment. It satisfies the following relations: It has mean zero $\langle dW_h(t)\rangle = 0$. There is no correlation of its values at different times $\langle dW_h(t)dW_h(t')\rangle = 0$ for $t' \neq t$. And finally $(dW_h(t))^2 = dt$.

The first term in equation 5.2 describes the unitary dynamics governed by the Hamiltonian, the second term describes the dissipation through the system-environment interaction, and the third term describes the information gain and resulting quantum measurement back-action through the monitoring (measurement) of dissipation channels with efficiency $\eta_h$.

For the system presented here, the dissipation operators take the form:

$$\begin{aligned} \hat{c}_1 &= \sqrt{2\gamma(\bar{n}_{\mathrm{th}}+1)}\hat{b} \\ \hat{c}_2 &= \sqrt{2\gamma\bar{n}_{\mathrm{th}}}\hat{b}^\dagger \\ \hat{c}_3 &= \sqrt{2\kappa}\hat{a}_{\mathrm{aS}}e^{-i\omega_{\mathrm{het}}t} \end{aligned} \tag{5.5}$$

Here, $\omega_{\mathrm{het}} = \omega_{\mathrm{LO}} - \omega_{\mathrm{aS}}$ is the heterodyne frequency. These dissipation operators correspond to the annihilation of a quantum of mechanical excitation through coupling to the thermal reservoir ($c_1$), the creation of a quantum of mechanical excitation received from the thermal reservoir ($c_2$), and the removal of quanta of optical excitation at a damping rate of $\kappa$ ($c_3$). Here, the expectation value of the photon number of the optical environment at room temperature is negligible and was set to zero. Also, an effective finite temperature corresponding to the phase noise of the pump laser [Saf+13] at 11 GHz was neglected.

We then find the stochastic master equation describing the dynamics of the monitored system:

$$\begin{aligned} d\rho = &-\frac{i}{\hbar}[H,\rho] + 2\gamma(\bar{n}_{\mathrm{th}}+1)D[b]\rho dt + 2\gamma\bar{n}_{\mathrm{th}}D[b^\dagger]\rho dt + 2\kappa D[ae^{-i\omega_{\mathrm{het}}t}]\rho dt + ... \\ &... + \sqrt{2\kappa\eta}\mathcal{H}[ae^{-i\omega_{\mathrm{het}}t}]\rho dW(t) \end{aligned} \tag{5.6}$$

At the start of the measurement-enhanced cooling scheme, the mechanical mode can be considered to be in a thermal state at the sideband-cooled equilibrium temperature. This

initial state is, naturally, Gaussian[1]. Since the Hamiltonian in equation 5.1 is only quadratic in the field operators, the couplings to the thermal environment are considered only linear in the quadratures [GZ04] and a dyne measurement preserves the Gaussianity of the state [Ser17], the state of the system will remain Gaussian throughout its time evolution. It can therefore be fully specified by the means and variances (first and second moments) at all times. Equations of motion for the first and second moments replace the more general equation 5.6 for the density operator $\rho$ forwards in time (and the effect matrix $E$ for backwards time evolution).

We can introduce a vector $\hat{\vec{r}}$ containing the mechanical position and momentum operators $X_{\mathrm{m}}$, and $P_{\mathrm{m}}$, and the optical position and momentum quadratures $X_{\mathrm{aS}}$, and $P_{\mathrm{aS}}$ (labelled aS to refer to the optical mode which resonantly enhances the anti-Stokes Brillouin scattering process) and its mean:

$$\hat{\vec{r}} = \begin{pmatrix} \hat{r}_1 \\ \hat{r}_2 \\ \hat{r}_3 \\ \hat{r}_4 \end{pmatrix} = \begin{pmatrix} \hat{X}_{\mathrm{m}} \\ \hat{P}_{\mathrm{m}} \\ \hat{X}_{\mathrm{aS}} \\ \hat{P}_{\mathrm{aS}} \end{pmatrix} \quad \text{and} \quad \langle \hat{\vec{r}} \rangle = \begin{pmatrix} \langle \hat{X}_{\mathrm{m}} \rangle \\ \langle \hat{P}_{\mathrm{m}} \rangle \\ \langle \hat{X}_{\mathrm{aS}} \rangle \\ \langle \hat{P}_{\mathrm{aS}} \rangle \end{pmatrix} \tag{5.7}$$

Here $\hat{X}_{\mathrm{m}} = \left(\hat{b}^\dagger + \hat{b}\right)/\sqrt{2}$ and $\hat{P}_{\mathrm{m}} = i\left(\hat{b}^\dagger - \hat{b}\right)/\sqrt{2}$, and $\hat{X}_{\mathrm{aS}}$ and $\hat{P}_{\mathrm{aS}}$ are defined analogously, with the mode operator $\hat{b}$ replaced with $\hat{a}_{\mathrm{aS}}$.

We describe the second moments by the covariance matrix $\sigma$ with elements $\sigma_{jk} = \langle \{r_j, r_k\} \rangle - 2 \langle r_j \rangle \langle r_k \rangle$ such that the diagonal elements are twice the variances of the position and momentum operators of the optical and mechanical degrees of freedom.

The evolution of these quantities was calculated in [ZM17], for a general scenario, where the condition for this approach to be applicable is that the Hamiltonian is at most quadratic and the dissipation operators at most linear in the system's quadrature/mode operators. These conditions are fulfilled here. Then the equations of motion for the forward (regular)

[1] As in: it possesses a Gaussian Wigner distribution.

time evolution read

$$d\left\langle \hat{\vec{r}}^{(\mathrm{f})} \right\rangle = A \left\langle \hat{\vec{r}}^{(\mathrm{f})} \right\rangle dt + C^{(\mathrm{f})} \sqrt{\eta} dW, \tag{5.8}$$

$$\frac{d\sigma^{(\mathrm{f})}}{dt} = A\sigma^{(\mathrm{f})} + \sigma^{(\mathrm{f})} A^{\mathrm{T}} + D - 2C^{(\mathrm{f})} \eta \left(C^{(\mathrm{f})}\right)^{\mathrm{T}} \ . \tag{5.9}$$

In [ZM17] it was shown that analogously one can define a backward time evolution which can be performed offline, after a measurement record has been obtained. Here the conditional quantum state at a time depends on future measurement records. For the backward time evolution the equations of motion read

$$d\left\langle \hat{\vec{r}}^{(\mathrm{b})} \right\rangle = -A \left\langle \hat{\vec{r}}^{(\mathrm{b})} \right\rangle dt - C^{(\mathrm{b})} \sqrt{\eta} dW, \tag{5.10}$$

$$\frac{d\sigma^{(\mathrm{b})}}{dt} = -A\sigma^{(\mathrm{b})} - \sigma^{(\mathrm{b})} A^{\mathrm{T}} + D - 2C^{(\mathrm{b})} \eta \left(C^{(\mathrm{b})}\right)^{\mathrm{T}} \ , \tag{5.11}$$

where superscripts (f) and (b) denote the forward and backward evolution, and T denotes the transpose.

Here the matrices $A$, $C$, $D$ and $\eta$ are defined through

$$A = \begin{pmatrix} -\gamma & -\Delta & 0 & G \\ \Delta & -\gamma & -G & 0 \\ 0 & G & -\kappa & 0 \\ -G & 0 & 0 & -\kappa \end{pmatrix} \ , \tag{5.12}$$

$$C = \sigma B^{\mathrm{T}} - N^{\mathrm{T}} \ , \tag{5.13}$$

where

$$B = \begin{pmatrix} \sqrt{(\bar{n}_{\mathrm{th}} + 1)\gamma} & 0 & 0 & 0 \\ \sqrt{\bar{n}_{\mathrm{th}}\gamma} & 0 & 0 & 0 \\ 0 & 0 & \sqrt{\kappa}\cos(\omega_{\mathrm{het}} t) & \sqrt{\kappa}\sin(\omega_{\mathrm{het}} t) \end{pmatrix} \ , \tag{5.14}$$

and

$$N = \begin{pmatrix} \sqrt{(\bar{n}_{\mathrm{th}}+1)\gamma} & 0 & 0 & 0 \\ -\sqrt{\bar{n}_{\mathrm{th}}\gamma} & 0 & 0 & 0 \\ 0 & 0 & \sqrt{\kappa}\cos(\omega_{\mathrm{het}}t) & \sqrt{\kappa}\sin(\omega_{\mathrm{het}}t) \end{pmatrix}, \tag{5.15}$$

$$D = \begin{pmatrix} 4\left(\bar{n}_{\mathrm{th}}+\frac{1}{2}\right)\gamma & 0 & 0 & 0 \\ 0 & 4\left(\bar{n}_{\mathrm{th}}+\frac{1}{2}\right)\gamma & 0 & 0 \\ 0 & 0 & 2\kappa & 0 \\ 0 & 0 & 0 & 2\kappa \end{pmatrix}, \tag{5.16}$$

and

$$\eta = \begin{pmatrix} 0 & 0 & 0 \\ 0 & 0 & 0 \\ 0 & 0 & \eta \end{pmatrix}. \tag{5.17}$$

$\eta$ is the total efficiency with which the light in the anti-Stokes optical mode is detected and $dW$ is a stochastic Wiener increment.

While the evolution equation for the first moments is non-deterministic and contains the stochastic term $dW$, which represents the measurement back-action, the second moment evolution is deterministic and depends only on the system parameters.

For a general quadrature of a Gaussian state, $\hat{X}_\theta = \hat{X}\cos(\theta) + \hat{P}\sin(\theta)$, the combined effect of the forward and backward evolutions on that state results in the following mean quadrature value

$$\left\langle \hat{X}_\theta \right\rangle = \frac{\left\langle \hat{X}_\theta^{(\mathrm{f})} \right\rangle \mathrm{Var}\left(\hat{X}_\theta^{(\mathrm{f})}\right) + \left\langle \hat{X}_\theta^{(\mathrm{b})} \right\rangle \mathrm{Var}\left(\hat{X}_\theta^{(\mathrm{b})}\right)}{\mathrm{Var}\left(\hat{X}_\theta^{(\mathrm{f})}\right) + \mathrm{Var}\left(\hat{X}_\theta^{(\mathrm{b})}\right)} \tag{5.18}$$

and its associated variance satisfies [ZM17]

$$\frac{1}{\mathrm{Var}\left(\hat{X}_\theta\right)} = \frac{1}{\mathrm{Var}\left(\hat{X}_\theta^{(\mathrm{f})}\right)} + \frac{1}{\mathrm{Var}\left(\hat{X}_\theta^{(\mathrm{b})}\right)}. \tag{5.19}$$

A pictorial example of how the measurement cooling protocol affects the mechanical mode is shown in the phase space plots in figure 5.1 (B). Here, dots and contours represent mean values and standard deviations of the mechanical quadratures respectively. The plot on the left illustrates sideband cooling of the mechanical mode (dashed blue line) from the initial thermal state at room temperature (continuous black line). The plot on the right shows the conditional state after the (forward evolution only) measurement cooling protocol has been applied to the measurement record (green line). The decreased standard deviations of the mechanical quadratures are indicators of the increased purity of the conditioned state. The ellipsoidal shapes of the green contours arise due to the finite heterodyne frequency $\omega_{\mathrm{het}}/2\pi$ as a result of which the measured quadrature rotates at this frequency. However, if the system's evolution timescale (the inverse damping rate) is appreciably longer than $2\pi/\omega_{\mathrm{het}}$ then information about two orthogonal quadratures can be obtained. This is saying that in the limit of the heterodyne frequency being much larger than the mechanical linewidth, the rotating homodyne is equivalent to a true heterodyne setup, where the two orthogonal quadratures are simultaneously measured. This is further captured in figure 5.2, where the variances of the mechanical quadratures vary periodically at twice the heterodyne frequency.

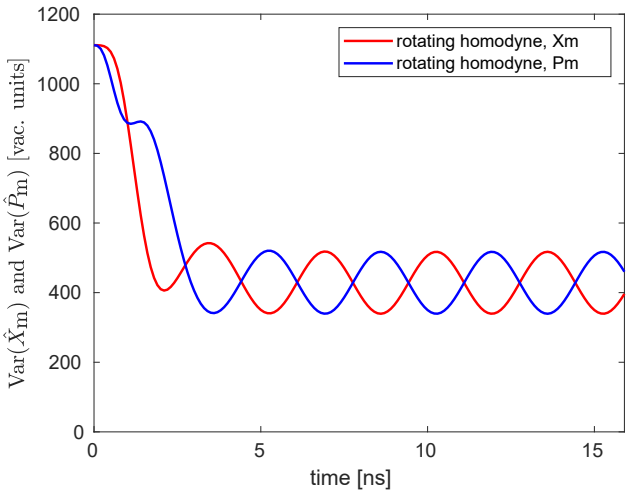


Figure 5.2: Oscillating variance of the position and momentum quadratures of the mechanical mode, due to a finite heterodyne frequency, corresponding to continuous measurement of a rotating quadrature, instead of simultaneous measurement of the $X$ and $P$ quadratures of the light field, as in (true) heterodyne detection.

The figure of merit describing the purity of the state of the mechanical mode is the

effective phonon number defined as $\bar{n}_{\text{eff}} = 1/2(\text{Var}_{\text{max}} + \text{Var}_{\text{min}}) - 1/2$, where $\text{Var}_{\text{max}}$ and $\text{Var}_{\text{min}}$ are the maximum and minimum variances of the state quadratures at a given time [Van+11]. The effective phonon number of a state describes the thermal occupation of the state after undergoing the inverse of unitary displacement and squeeze operations. It therefore quantifies the mixedness of the state.

The optimal choice of a measurement depends on the optomechanical interaction Hamiltonian. The beam-splitter-type Hamiltonian in equation 5.1 is proportional to $\hat{X}_{\text{aS}}\hat{X}_{\text{m}} + \hat{P}_{\text{aS}}\hat{P}_{\text{m}}$, and from this we can see that both optical quadratures are affected by the mechanical motion ($\hat{P}_{\text{aS}}$ by $\hat{X}_{\text{m}}$ and $\hat{X}_{\text{aS}}$ by $\hat{P}_{\text{m}}$), thus motivating the simultaneous acquisition of information about two orthogonal quadratures of light and use of heterodyne as opposed to homodyne detection, which is commonly used in optomechanics. Figure 5.1 (C) shows the advantage of the heterodyne detection over the homodyne detection in terms of the effective phonon number for a realistic set of system parameters for our Brillouin system. It also shows the effect of finite heterodyne frequency which is a good approximation to the ideal heterodyne scheme, where information about the two quadratures of light is acquired simultaneously.

## 5.3 Experimental setup

As described in chapter 3, an optical whispering-gallery mode of a fused silica microresonator of $\approx 700\,\mu\text{m}$ diameter is excited via evanescent coupling to a tapered optical fibre by a pump laser operating at 1550 nm. Anti-Stokes light backscattered from the cavity is observed with an optical heterodyne detection scheme shown in figure 5.3. As described above, the mechanical wave has a frequency of $\omega_{\text{m}}/2\pi = 11$ GHz, and an amplitude decay rate of $\gamma/2\pi \sim 21\,\text{MHz}$, which is determined by fitting a theoretical model for the power spectrum of the detected light (compare equation 3.44) to the observed spectra. The experimental setup is thus almost the same as the one used in the observation of strong coupling of chapter 3, with the important difference of a fast digital storage oscilloscope being used to

sample the output of the balanced photodetector, in order to record time traces. Another key difference is the taper coupling position, which was carefully optimised for best cooling performance, as we will discuss in the next paragraph. On a practical note, the correlator-technique discussed in section 4.5.5 of the previous chapter can be used here in order to confirm that the optomechanical coupling is predominantly to a single mechanical mode.

Since the strong continuous wave pump field can be well approximated by a classical coherent amplitude, the three-wave mixing interaction Hamiltonian associated with the anti-Stokes scattering turns into a beam-splitter Hamiltonian, shown in equation 5.1, between the mechanical and optical anti-Stokes modes. Optical linewidths are typically $10 - 100$ MHz, placing the system deep in the resolved sideband regime. In particular, the anti-Stokes amplitude decay rate is $\kappa_{\mathrm{aS}}/2\pi = 45$ MHz. The conversion of phonons into anti-Stokes photons via optomechanical coupling and subsequent removal from the system via internal loss or outcoupling via the tapered fiber represents a damping channel for the mechanical mode, attenuating its thermal fluctuations and thus cooling it. The coupled optical and mechanical modes can be considered as each coupled to a reservoir (compare figure 1.3), thus implying a desirable hierarchy of the rates $\kappa_{\mathrm{aS}} > G > \gamma_{\mathrm{m}}$, in order to obtain the lowest temperature of the mechanical mode. In practice, a trade-off between a broad anti-Stokes linewidth $\kappa_{\mathrm{aS}}$ and a large coupling rate $G$ needs to be made. The maximally available pump power is limited, and the optomechanical coupling rate $G = g_0|\alpha|$, at a given pump power, is proportional to the inverse linewidth of the pump resonance (compare appendix A). The anti-Stokes and pump linewidths are both intimately linked to the position of the tapered fiber relative to the surface of the bulge of the resonator. It is thus desirable to achieve narrow linewidth of the pump mode, while at the same time obtaining a broad linewidth (and ideally high efficiency) of the anti-Stokes resonance. Here, with the taper stuck on the resonator's surface by surface forces, sub-wavelength-scale positioning was aimed for, navigating the nodes, and anti-nodes of pump and anti-Stokes resonances, while moving the probing laser back and forth between them.

The collected time-domain data of heterodyne measurement on the anti-Stokes light are

further input into the past quantum state formalism [ZM17], given in equation 5.18 and equation 5.19, to reduce the uncertainty of the mechanical phase space trajectories. This effectively purifies the mechanical mode and can be quantified via the effective phonon number. The heterodyne detector has a bandwidth of $\sim 350$ MHz and data is acquired at a sampling rate of 10 GSa/s. Ten time traces, each of length 100 µs, are recorded corresponding to different coupling rates $G$ and therefore different detunings $\Delta$, due to the power dependent detuning present in the fused silica whispering-gallery resonator (compare section 3.3.1).

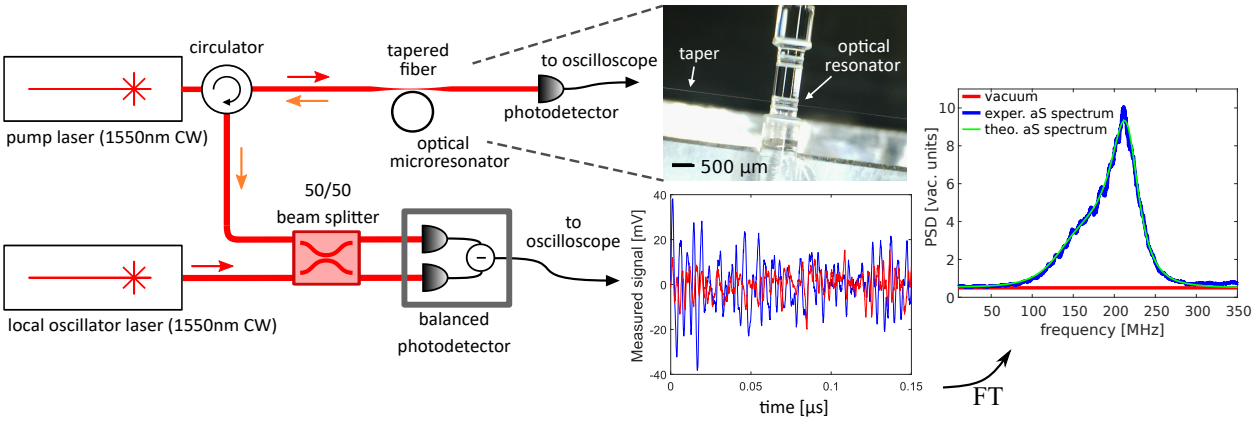


Figure 5.3: Experimental setup: pump light (red) is evanescently coupled into the microrod resonator and backscatters off fluctuations of one of the resonator's acoustic modes. The resulting anti-Stokes light (orange arrows) is heterodyned and further analysed to reveal phase space trajectories of the mechanical mode with reduced uncertainties. The red curve in the time trace represents a vacuum signal while the blue curve an anti-Stokes signal. PSD stands for power spectral density and FT for Fourier transform.

### 5.3.1 Measured heterodyne current and its appropriate normalisation

The measured heterodyne current increments $dy(t)$ are related to the monitored dissipation operator $c_3$ via

$$dy(t) = \langle c_3 + c_3^\dagger \rangle dt + dW(t) \ , \tag{5.20}$$

and after inserting $c_3 = \sqrt{2\kappa\eta}\, a e^{-i\omega_{\mathrm{het}} t}$ with $a = (X_{\mathrm{aS}} + iP_{\mathrm{aS}})/\sqrt{2}$ we obtain

$$dy(t) = 2\sqrt{\kappa\eta}\, \langle X_{\mathrm{aS}} \cos(\omega_{\mathrm{het}} t) + P_{\mathrm{aS}} \sin(\omega_{\mathrm{het}} t) \rangle \, dt + dW(t) \ . \tag{5.21}$$

Once a particular measurement current has been measured, we would like to apply the formalism in order to compute a quantum trajectory of the mechanical and optical quadratures (first moments, as the time evolution of the second moments is deterministic).

Equation 5.21 provides us with a connection between the measured current, the current estimates of $\langle X_{\mathrm{aS}} \rangle$ and $\langle P_{\mathrm{aS}} \rangle$ and the Wiener increment, so we can use it to determine the Wiener increments from the experimental record and use it in the (stochastic) equation of motion for the means, equation 5.8.

$$dW(t) = dy(t) - 2\sqrt{\kappa\eta}\,\langle X_{\mathrm{aS}} \cos(\omega_{\mathrm{het}} t) + P_{\mathrm{aS}} \sin(\omega_{\mathrm{het}} t)\rangle\, dt \ . \tag{5.22}$$

This equation is central to our protocol, as it combines the experimentally observed current increment $dy(t)$ with the current estimates of the optical quadratures according to our model, to obtain $dW(t)$ to be fed back into the time evolution equation 5.8.

Now, $dy(t)$ is the measurement outcome in the natural units of the model, and a technical detail is how to relate it to the measured difference photocurrent into $50\,\Omega$, measured in volts. So we need to appropriately calibrate our heterodyne current measurement. The calibration will be determined by three main parameters which only have to do with the particular experimental implementation of the heterodyne measurement, and that are the local oscillator's optical power, the bandwidth and gain of the balanced photodetector, and the sampling rate. Correctly applying this calibration is a necessity for the protocol, but following the derivation is not essential to understand the main message and results.

In order to apply the calibration, we notice that once the measurement efficiency is turned to 0 in equation 5.21, it just reads $dy(t) = dW(t)$. This situation corresponds to only observing the vacuum noise on the now open port of the beam splitter, or equivalently the shot noise of the local oscillator laser. If now our balanced detector had infinite bandwidth (or at least a bandwidth beyond the sampling rate $1/\Delta t = 10$ GSa/s) we would just have to make sure that the standard deviation of the vacuum noise measured with our detector corresponds to $\sqrt{\Delta t}$, as then in the continuum limit it fulfils the Ito rule $(dW(t))^2 = dt$

(compare e.g. [JS06; Zha18]). This practically means that the normalisation/calibration condition is

$$\mathrm{stddev}(y_{\mathrm{vac}}(t)) = \sqrt{\mathrm{Var}(y_{\mathrm{vac}}(t))} = \sqrt{\Delta t}\ . \tag{5.23}$$

In this scenario the experimentally measured currents $y_{\mathrm{meas}}(t)$ would correspond to the currents in the model $y(t)$ via

$$y(t) = \alpha \cdot y_{\mathrm{meas}}(t) \quad \text{with} \quad \alpha = \sqrt{\frac{\Delta t}{\mathrm{Var}(y_{\mathrm{vac}})}}\ , \tag{5.24}$$

and thus similarly for the current increments $dy(t) = \alpha \cdot dy_{\mathrm{meas}}(t)$, where $\Delta t$ is the inverse of the sampling rate and $\mathrm{Var}(y_{\mathrm{vac}})$ the variance of the measured vacuum noise.

If the sampling rate is higher than the balanced detector's bandwidth, as was the case in our experiment, we are sampling fast enough to resolve the low passing property of the balanced detector on the white shot noise, which naturally comes with a constant power spectral density up to arbitrarily high frequency and contains infinite power if unfiltered. Therefore we chose the normalisation such that the measured power spectral density of the vacuum noise is mapped onto the level of the power spectral density of a simulated white noise signal which has a flat spectrum up to the sampling rate and a standard deviation of $\sqrt{\Delta t}$.

The numerical value of $\alpha$ can then be obtained by dividing the power spectral density of this simulated signal by the reading of the electrical power spectral density in the flat part of the spectrum (detector bandwidth used here was 300 MHz) and performing the square root (as it's an amplitude normalisation). In order to partially account for residual non-flatness of the detector response, a fit to the cumulated spectral power of the experimental vacuum noise can be performed (up to the cut-off frequency of the balanced photodetector), and $\alpha$ extracted from the ratio of square roots of the slopes of this fit and the simulated signal of variance $\Delta t$.

It was confirmed in a simulation [Zha18] that the low-passing of the shot noise has no significant effect on the informational cooling performance, since the signal and the dynam-

ical timescale of the system under study lie within the detector bandwidth. An example of trajectories obtained with simulated data of unfiltered Wiener noise and such noise filtered by the detector response are shown in figure 5.4, where it can be seen that there is no significant change to the reconstructed trajectories whether the bandwidth of the detector extends to the sampling rate or has low-passing characteristic with a lower cut-off frequency.

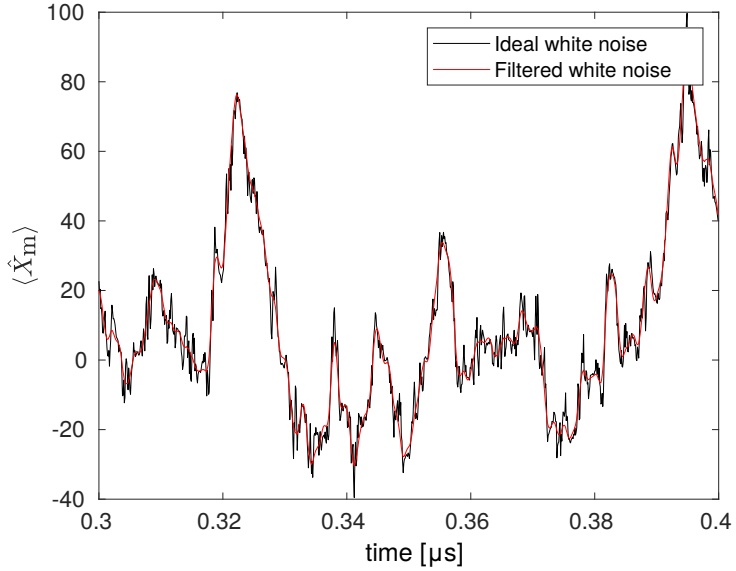


Figure 5.4: Quantum trajectory of the mechanical mode obtained with simulated data for unfiltered and filtered shot noise at the detector. The low-pass filtering property of the balanced detector has no significant influence on the reconstructed trajectories.

## 5.4 Experimental results

The outcomes of applying the past quantum state protocol (forward evolution only) to the time-domain data, acquired by heterodyning the anti-Stokes light from the Brillouin optomechanical system, are shown in figure 5.5. Figure 5.5 (A) shows the estimated quadrature trajectories of the mechanical mode with standard deviations of the position and momentum quadratures denoted by shaded areas. The plots are for the dataset with the highest coupling rate $G/2\pi = 9.6$ MHz and the corresponding detuning $\Delta/2\pi = -74$ MHz. The mean trajectories are obtained using equation 5.18 and require solving equation 5.8 and equation 5.10, where the measurement current is input via the Wiener noise term $dW$. The standard deviations are obtained through equation 5.19, which is fully deterministic, and require

knowledge of system parameters only. The uncertainties associated with the mechanical quadratures are reduced and the amount of cooling depends on two competing processes: the decoherence rates and the rate at which information is acquired during the measurement. Eventually, steady state is reached as shown in figure 5.1 (C).

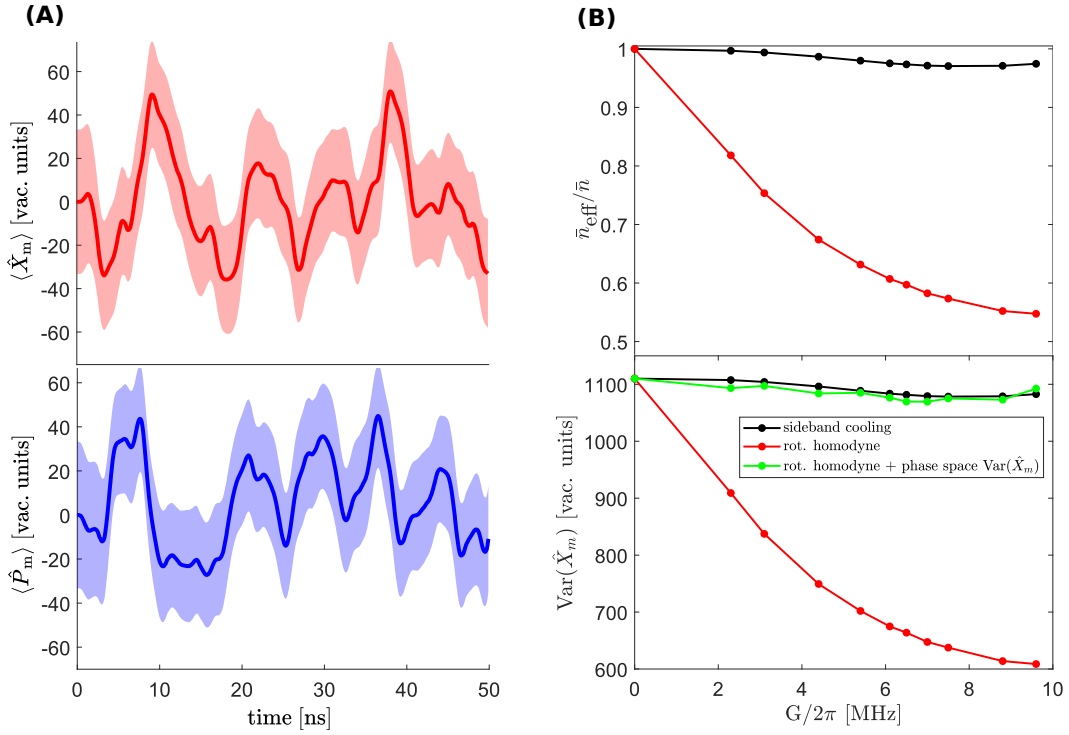


Figure 5.5: Heterodyne-measurement-enhanced cooling results. (A) Quantum trajectories for the mechanical position (top) and momentum (bottom), with the continuous line representing the mean and the shaded area the standard deviation. The informational cooling has reached base temperature after approximately 3 ns, compare figure 5.2, which corresponds approximately to half a heterodyne period in phase space. (B) plain sideband cooling (black) versus informationally enhanced cooling (red) and cross-check (green).

The cooling factor, defined as the ratio of the effective phonon number $\bar{n}_{\rm eff}$ and the thermal phonon number $\bar{n}$, for this room temperature experiment is shown in figure 5.5 (B) (top) for the ten recorded datasets. The mean phonon number in the relevant degrees of freedom of the environment is $\bar{n}_{\rm th} = 555$ and $\bar{n}_{\rm eff}$ is related to the minimum and maximum variances of the mechanical quadratures. The cooling factor therefore depends on the system parameters only. The black points quantify the amount of sideband cooling while the red points include the information gain due to the rotating homodyne measurement. Figure 5.5 (B) (bottom) presents the information budget for the mechanical mode before and after the measurement. It is expected that the unmonitored mechanical quadrature variance (black

points) is the same as the sum of the variance after the measurement (red points) and the variance of the recorded mechanical phase space trajectories. The sum is given by the green points and requires an input of the measured current. The close overlap between green and black points suggests that the formalism is self-consistent.

A nice side-result of the theoretical analysis is a general expression for the amount of plain sideband cooling and the amount of extra informational cooling obtainable in our Brillouin optomechanical platform when a single mechanical mode coupling to a pair of optical resonances, as described in section 1.5.2, is considered. The general expression for plain sideband cooling is

$$\bar{n} = \bar{n}_{\mathrm{th}} \cdot \frac{G^2(\kappa+\gamma)\gamma + \kappa\gamma((\kappa+\gamma)^2+\Delta^2)}{G^2(\kappa+\gamma)^2 + \kappa\gamma((\kappa+\gamma)^2+\Delta^2)} \ , \tag{5.25}$$

which for zero detuning, in the regime of strong optomechanical coupling $G \gg \kappa, \gamma$ takes the simple form $\bar{n} = \bar{n}_{\mathrm{th}} \frac{\gamma}{\kappa+\gamma}$, which corresponds to a balance of rates, the rate at which mechanical quanta are flowing in from the thermal bath (the simplest approximate form of a "decoherence rate") $\bar{n}_{\mathrm{th}}\gamma$, and the rate at which mechanical quanta flow out of the mechanical mode $\bar{n}\kappa + \bar{n}\gamma$, either parametrically upconverted by omnipresent pump-photons, leaving into the optical environment, or flowing back into the thermal bath (compare figure 1.3).

A closed-form expression for the degree of informational cooling was obtained using Wolfram mathematica, but a sufficient simplification to make the expression useful for physical insight was not achieved, therefore the multi-page expression will not be given here. The advantage of heterodyne-measurement-enhanced cooling with respect to plain sideband cooling can be examined though using this expression, and a contour plot of $\bar{n}_{\mathrm{eff}}/\bar{n}_{\mathrm{sb}}$ is shown in figure 5.6, where it is seen that the advantage of the measurement-enhancement of the cooling vanishes as the mean thermal phonon number in the environment approaches 0. This is intuitively clear when considering that the performance of the protocol is fundamentally linked to the ratio of thermal noise to local oscillator shot noise, or measurement back-action noise.

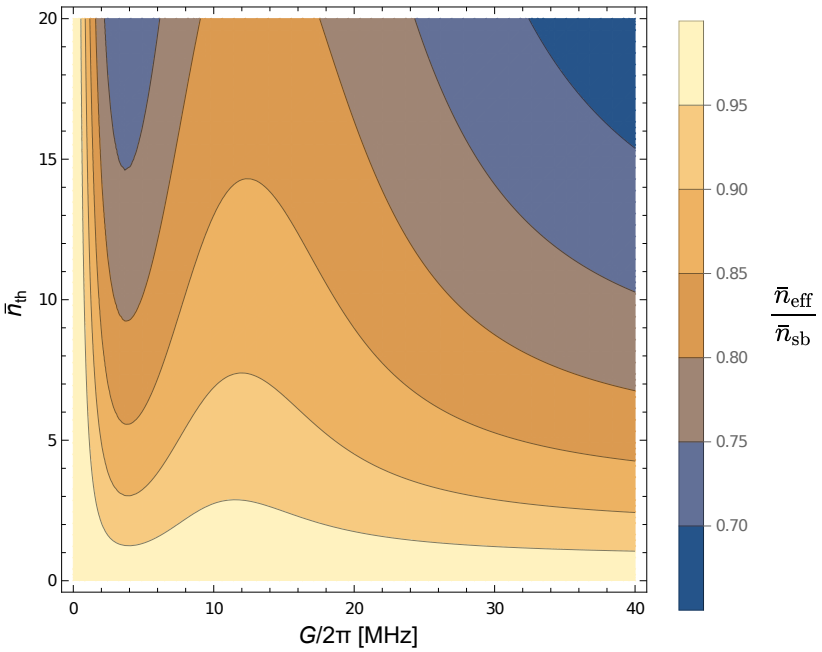


Figure 5.6: Heterodyne-measurement-enhanced optomechanical cooling advantage compared to plain sideband cooling. Plotted is the ratio of the effective phonon number with measurement-enhanced cooling to the equilibrium phonon number for plain sideband cooling (not using the measurement record) $\bar{n}_{\rm eff}/\bar{n}_{\rm sb}$ for realistic system parameters of $\eta = 0.4$, $2\kappa/2\pi = 20$ MHz, $2\gamma/2\pi = 5$ MHz, $\Delta = 0$, as a function of the mean thermal phonon number in the environment $\bar{n}_{\rm th}$ and the optomechanical coupling rate $G/2\pi$.

## 5.5 Summary

We have demonstrated a scheme that enhances optomechanical sideband (dynamical back-action) cooling in a Brillouin cavity optomechanical platform at room temperature. In the experiments a fused silica optical whispering-gallery resonator of rod-with-bulge geometry, which also supports elastic whispering-gallery type waves, was used at an optical wavelength of 1550 nm, and careful selection of a pair of optical resonances with different transverse spatial character, separated approximately by the Brillouin shift (11 GHz), allowed a strong parametric interaction via the photoelastic/electrostriction effect. Resonantly enhancing the anti-Stokes and suppressing the Stokes process by the optical cavity's density of states implemented a beam-splitter-type interaction between the light and the elastic waves.

We then performed a continuous heterodyne measurement on the frequency up-converted light that the optomechanical cavity scatters. This way we were able reconstruct a quantum trajectory with reduced uncertainty compared to the plain sideband-cooled state via a

Gaussian state evolution model derived from a stochastic master equation approach. The effective cooling is quantified through an effective phonon number. Instead of simultaneously measuring the $X$ and $P$ quadratures of the anti-Stokes light field we employ a single balanced photodetector with a fast rotating reference phase (rotating homodyne), at 150 MHz, which well approximates heterodyne measurement. We show that heterodyne measurement outperforms homodyne measurement with respect to measurement cooling for the beam-splitter-type Hamiltonian associated with Brillouin anti-Stokes scattering.

While the root-mean-square displacement of the mechanical mode is not reduced (cooling in the classical, energetic sense), its phase space uncertainty is reduced (cooling in the informational sense), motivating the introduction of an effective phonon number, quantifying the informational degree of cooling additional to the sideband cooling. Extending the approach to include feedback would allow the means of the mechanical mode to be stabilized at zero, which is useful for some optomechanical protocols. This type of feedback would be required to be implemented within the lifetime of the mechanical oscillator, which for our room temperature setup is given by $\tau = 1/(2\pi\Delta\nu_{\mathrm{FWHM}}) \approx 4\,\mathrm{ns}$.

# Chapter 6

# Outlook

In this chapter further lines of investigation in the microresonator platform are discussed. The sections represent areas that I worked on during my doctorate, but are not yet finished research projects, but rather can lay the foundation for further work.

## 6.1 Crystalline Brillouin cavity optomechanics with barium fluoride whispering-gallery microresonators

As it became clear during the research that the limiting factor to observe true quantum behaviour in this platform is the acoustic damping rate, my attention was drawn onto crystalline materials which, as opposed to amorphous materials like fused silica, suffer less from two-level system damping [Phi72; AHV72; Esq98], and are expected to have lower elastic wave attenuation at cryogenic temperatures. It has been discussed in the literature how the two-level system damping model can explain several low temperature properties of amorphous and crystalline solids like specific heat and thermal conductivity [HR86].

While there are crystalline materials which are optically isotropic, it turns out that an elastically isotropic crystalline material does not exist. Due to phase matching considerations, it is desirable in a whispering-gallery geometry to have a high degree of isotropy in

the resonator plane, such that the phase velocity changes only by small amounts around the perimeter of the cavity.

### 6.1.1 Material choice and elastic isotropy

We are looking for a material, transparent at 1550 nm and optically isotropic, which possesses low loss for acoustic phonons, while at the same time having a small or ideally vanishing dependence of the speed of sound on the propagation direction through the material. This independence of the speed of sound on the propagation direction allows the Brillouin shift to not depend on the azimuthal angle in a microresonator made from the material, which is highly desirable.

For amorphous materials like silica or chalcogenide glasses (like $As_2S_3$), the second criterion is fulfilled as they are isotropic with respect to their elastic properties, but it is an empirical fact that phononic dissipation is typically significantly higher in amorphous materials compared to crystalline materials. Therefore the question arises which crystalline materials should be tried.

The elastic properties are quantified in the most general case through the elastic (or stiffness) tensor (see equation 1.23), a fourth rank tensor completely characterising the elastic response of the material in the linear small displacement limit.

Taking Newton's axiom in a continuum mechanical context and looking for plane elastic wave solutions of the equation of motion (sometimes called Cauchy's equation) leads to the Christoffel equation 1.21, which constitutes an eigenvalue problem for plane wave solutions to the elastic wave equation. Essentially for a given propagation direction in a material (with respect to certain axes) solving Christoffel's equation corresponds to finding three polarizations and three sound velocities, which always include a quasi-longitudinal wave, as well as a slow transversal and fast transversal wave. We are here only interested in the quasi-longitudinal waves for Brillouin coupling.

Out of all the crystal classes, the cubic crystals come closest to elastic isotropy. When

looking for crystalline materials transparent at 1550 nm, possessing a cubic crystal structure (which naturally comes with optical isotropy) and ideally being non- or weakly hygroscopic and commercially available, not many materials remain; the fluorides, possessing similar properties as fluorite, seem most interesting.

To see how large the variation of the speed of sound for a circular round trip in the material is, one can numerically solve Christoffel's equation (if the elastic tensor is known) using a python program which was provided by Jaeken and Cottenier [JC16].

The relative variation of the speed of sound is then the same as the relative variation of the Brillouin shift as they are linearly related, see equation 1.31. Figure 6.1 shows a colour coded representation of the dependence of the acoustic phase velocity on the propagation direction in a barium fluoride crystal. Then a next question arises, that is which plane cutting through this sphere will minimise the root-mean square or peak-to-peak variation of the speed of sound? Aligning the resonator's symmetry axis with a [111] crystal axis can then be seen as a good strategy to minimise the variation. Acoustic velocities for a circular round trip in a plane perpendicular to certain symmetry axes (eventually to be aligned with the symmetry axis of a cavity cut from the material) are plotted in figure 6.2.

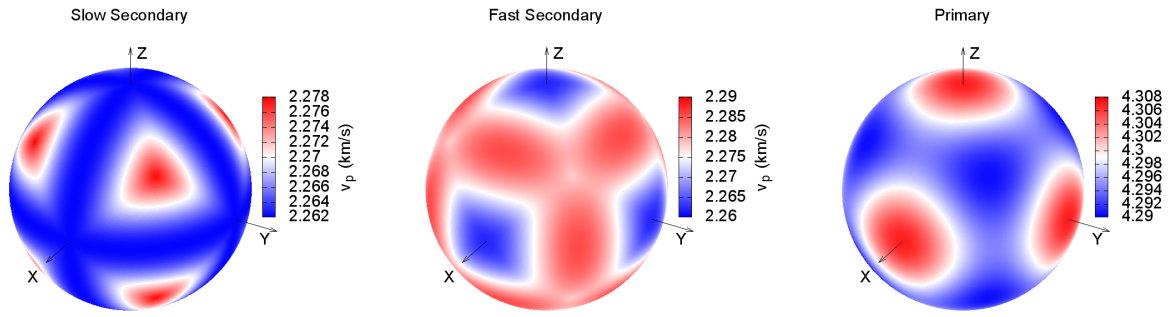


Figure 6.1: Dependence of the acoustic phase velocity on the propagation direction in a (infinitely extended) barium fluoride crystal. Colour coded according to scale (km/s), slow transverse, fast transverse and quasi-longitudinal (primary) sound waves. Calculated numerically using the Christoffel package [JC16].

**Degree of isotropy required**

But how isotropic does it need to be? One can think of the following argument: If the relative variation is much smaller than the inverse of the acoustic azimuthal mode index $1/M_\mathrm{a}$, the acoustic wave will never run out-of-phase with the travelling optical beat note. While the observation that the Brillouin shift depends on the azimuth angle [DAC17] suggests the existence of a kind of inhomogeneous broadening, which would be observable in OMIT, clearly what changes with azimuth angle is not the frequency of an acoustic wave, but its phase velocity (wavelength). Thus it is anticipated that the sound wave will dephase and rephase w.r.t. the optical beat note and no inhomogeneous broadening will be observed. The amount of this dephasing and whether or not partial cancellation of scattering contributions from different sectors of the resonator is significant will therefore depend on the absolute size of the resonator compared to the wavelength $D/\lambda$, and can be calculated from

$$\frac{\partial}{\partial\phi}\left(\Phi_\mathrm{m}-\Phi_\mathrm{beat}\right)=\pi D\left(\frac{\nu_\mathrm{m}}{v_\mathrm{ph,m}(\phi)}-\frac{\nu_\mathrm{beat}}{v_\mathrm{ph,beat}}\right)\ , \tag{6.1}$$

where $\phi$ is the azimuthal angle, $\Phi_\mathrm{m}$ and $\Phi_\mathrm{beat}$ are the phases of mechanical wave and optical beat note, $D$ is the resonator diameter, $\nu_\mathrm{m}$ and $\nu_\mathrm{beat}$ are the frequencies of mechanical and optical waves, and $v_\mathrm{ph,m}(\phi)$ and $v_\mathrm{ph,beat}$ their phase velocities, which for the mechanics is expected to depend on the azimuthal angle due to crystalline anisotropy, as depicted in figure 6.2. Assuming a mean optomechanical detuning of $\Delta=0\Leftrightarrow\nu_\mathrm{m}=\nu_\mathrm{beat}$, the local phase difference between mechanics and optical beat note then takes the form

$$\Delta\Phi(\phi)=\pi D\nu_\mathrm{m}\int_{\phi_0}^{\phi_1}\left(\frac{1}{v_\mathrm{ph,m}(\phi)}-\frac{1}{v_\mathrm{ph,beat}}\right)d\phi\ , \tag{6.2}$$

which can be integrated over the azimuthal angle to obtain a "gain dilution" due to dephasing.

Many cubic materials that seemed attractive (i.e. are non-hygroscopic, and optically transparent at 1550 nm) were investigated. From these, barium fluoride, [111] cut, turned out to have the smallest relative peak-to-peak variation of the acoustic phase velocity. During the

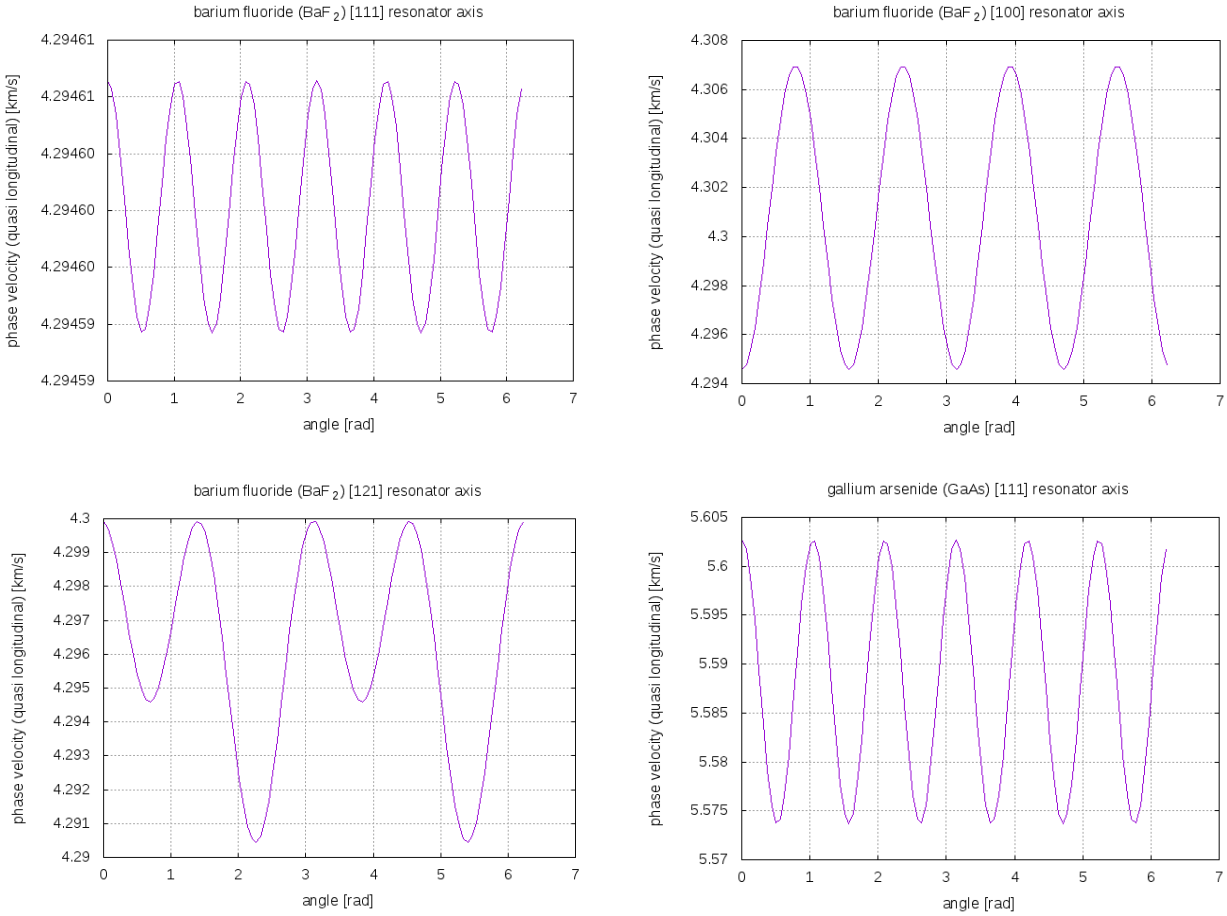


Figure 6.2: Acoustic phase velocity in infinite bulk material over a circle orthogonal to [xxx] crystal axis aligned with the resonator axis, as obtained from solving the Christoffel equation. The spread of phase velocities should approximate that of pseudo-longitudinal whispering-gallery modes on a resonator round-trip (the effect of the surface is not accounted for here). Resonator axis Top-Left: $BaF_2$ [111], $\delta v/v \approx 5 \times 10^{-6}$, Top-Right: $BaF_2$ [100], $\delta v/v \approx 2.5^{-3}$, Bottom-Left: $BaF_2$ [121], $\delta v/v \approx 2.5 \times 10^{-3}$, and Bottom-Right: Gallium arsenide [111], $\delta v/v \approx 5 \times 10^{-3}$, a commonly used material in nonlinear optics which also has cubic crystal structure, for comparison.

investigation the author became aware of a work which investigated the direction dependence of the Brillouin shift for different fluorides [DAC17], which helped to verify some of these ideas.

The fluorides are a material class widely used for optical applications. High optical quality factor whispering-gallery resonators from fluorides have been demonstrated [Lin+14a; Lec+16], and also Brillouin lasing has already been demonstrated in fluoride WGM resonators [GMM09; Lin+14b].

### 6.1.2 Temperature dependence of the Brillouin shift

The Brillouin shift at cryogenic temperatures will be substantially different from the one found at room temperature, as the elastic constants and the refractive index of barium fluoride change. While the bulk Brillouin shift at room temperature is $\Delta\nu_{\mathrm{Br,BaF2}} = 8.12$ GHz, increased to 8.21 GHz due to transverse confinement, at 5 K, we expect a number close to $\Delta\nu_{\mathrm{Br,BaF2}} = 8.44$ GHz, increased to 8.53 GHz due to transverse confinement. These numbers can be obtained by numerically solving the Christoffel equation [JC16] for propagation directions perpendicular to the [111] crystal axis, and extracting the quasi-longitudinal wave phase velocity. The elastic constants of barium fluoride were measured by Gerlich for temperatures between 4.2 K and 300 K [Ger64].

### 6.1.3 Possible diffraction contribution to the acoustic linewidth

An open question is whether there is a geometry-dependent diffraction contribution to the acoustic linewidth. The argument is based on the elementary insight that at a material interface (like the surface of the whispering-gallery resonator) a longitudinal elastic plane wave will, upon reflection, eject part of its energy into a transverse wave component, so as to fulfil the boundary conditions (compare [LL12], section §22, problem 1). One might refer to these modes as "leaky elastic wave modes", as they radiate transverse bulk waves into the support.

In spherical and cylindrical geometries it was shown [SB15b] that hybrid transverse-longitudinal (pseudo-longitudinal) whispering-gallery mode solutions exist. While it can be assumed that in spheroidal geometries the nature of these solutions is preserved, it is not clear if in a tightly laterally confining geometry, like in the rod-with-a-bulge geometry, where transverse wave energy could be lost into the support, the same will be true. It is anticipated that such a loss mechanism will limit the achievable linewidth at cryogenic temperatures. The experimental results obtained in this work (chapters 3 and 4) suggest that there is a loss mechanism additional to the acoustic attenuation of the material. We can compare measurements of sound attenuation for fused silica and calcium fluoride with the measured mechanical linewidths in our microresonator experiments. For fused silica I found a mechanical linewidth of $(41.8 \pm 3.2)$ MHz with a microresonator of 660 µm diameter and a transverse (polar) radius of curvature of $\approx 40$ µm, while the bulk value was reported [NTR97; Boy08] to lie close to 16 MHz (at 1550 nm), thus obtaining an additional linewidth contribution of $\approx 25$ MHz. For barium fluoride an acoustic linewidth of $(34.0 \pm 6.4)$ MHz was measured in a resonator of 1.5 mm diameter, and transverse radius of curvature of $\approx 40$ µm, compared with a bulk value for calcium fluoride equivalent of 5.7 MHz [Son+07]. Although the fluorides might somewhat differ in their attenuation of longitudinal sound waves, we can estimate an additional linewidth contribution of $\approx 28$ MHz.

In the case that the linewidth is indeed limited by such loss mechanism a mitigation of the effect could be delivered by a choice of more spherical or spheroidal whispering-gallery resonators. Staying in the microrod-with-bulge geometry, Brillouin back-scattering from hybrid transverse-longitudinal Rayleigh-type surface acoustic waves, which according to preliminary simulations do not suffer from geometric/radiation damping, will provide an attractive path to GHz crystalline Brillouin quantum optomechanics in whispering-gallery resonators. Modes of similar type were explored in stimulated forward scattering [Bah+11]. Surface acoustic waves in crystalline materials with planar surface were reviewed in [Fav+11], highlighting important physics which is relevant to the Rayleigh-type surface acoustic modes expected in the barium fluoride rod resonators explored in this work. These Rayleigh-type modes are expected to have significant optomechanical coupling in a back-scattering

geometry. Due to their proper surface wave character and lack of radiation loss they are the most promising candidates for reaching the quantum regime in the barium-fluoride rod-resonator platform. In this scenario of back-scattering from Rayleigh-type surface acoustic waves, the acoustic linewidth at cryogenic temperatures would only be limited by surface roughness and the anticipated very low material attenuation, and the system would emerge as a very attractive platform for experimental quantum science, allowing optomechanical ground-state cooling, and the quantum coherent coupling regime to be readily reached at GHz frequencies with single-mode addressing.

### 6.1.4 Optomechanically induced transparency as a tool to measure mechanical detunings and linewidths

At cryogenic temperatures, where the acoustic attenuation of the material substantially decreases, optomechanically induced transparency [Wei+10; Don+15] can serve as a benchmark tool to characterise the coupling to different acoustic eigenmodes.

According to the prediction that only a single azimuthal mode of any acoustic mode family will (effectively) couple to the optical resonance pair, which was discussed in section 1.5.2, optomechanically induced transparency will be a powerful measurement configuration for probing the individual optomechanical coupling strengths and detunings of different acoustic mode families coupling electrostrictively to an optical resonance pair.

In a pump-probe scheme a (weak) probe laser field would scan an optical resonance of the cavity. Once a (strong) pump laser, counter-propagating with respect to the probe field, is then switched on, the lorentzian cavity response will be altered in the presence of optomechanical coupling, and a transmission feature will appear similar to electromagnetically induced transparency (EIT) in atomic systems [BIH91]. As in the EIT case, this can also be viewed as probing a coherence which the system possesses, or a cancellation of excitation pathways [FIM05]. For this measurement it is desirable that the optical linewidth is significantly broader than the mechanical linewidth(s). Then, individual detunings and coupling

strengths of different acoustic mode families can be extracted.

As pointed out in section 1.5.2 a cancellation argument can be made, such that only a single azimuthal mode out of each family will couple to an optical resonance pair, and only one OMIT peak per mode family will be observable. This, together with the directionality of the waves, makes the whispering-gallery platform in some sense cleaner than e.g. the bulk acoustic resonator platform [Ren+18], which has already shown very low mechanical linewidths, but where the coupling is to a whole variety of transverse and longitudinal acoustic modes, and the cancellation of scattering contributions from different sites in the sample is incomplete, such that the OMIT/OMIA spectra obtained in this platform show a complex landscape and depend on the positioning of the bulk resonator inside the light path. Furthermore, OMIT measurement can also serve as a perfect monitor for investigation of tuning techniques discussed in section 6.1.6.

A central question is whether the dissipation channels can be reduced to the bare material loss, in which case the system would develop its full potential for quantum science and technology. In this regard, especially the constant proximity of the elastic wave-field to the surface raises questions about the required surface quality.

### 6.1.5 Use of fused silica microresonators at cryogenic temperatures and saturation of two-level system damping

It is well known from Brillouin scattering experiments with fused silica that the acoustic attenuation when cooling to low temperatures ($\approx$ 4 K) is reduced by at least one order of magnitude compared to room temperature, see e.g. [VSH80; LC03]. Thus acoustic linewidths of the order of 1 MHz can be expected when operating at base temperature (4 K) of a standard helium cryostat.

In order to further reduce acoustic attenuation it might here be a possibility to saturate the absorption due to two-level systems (tunneling systems), by applying a strong phonon flux. This effect was demonstrated in [AMH78; Beh+17]. In the model, the glass behaves

like an ensemble of two-level systems, which correspond to bistable microscopic molecular configurations. These two-level systems have a continuous spectrum of energy splittings and can absorb and emit phonons, and the absorption can be saturated by strongly driving the two-level systems, analogous to the well-known saturation of optical absorption in atomic physics. As the effect is broadband, an acoustic wave could be applied far detuned from the relevant acoustic modes which couple to the optical fields via Brillouin scattering. This can be called acoustic "hole burning". For example, one might consider gluing a piezo transducer to the rod resonator and coherently driving at a frequency detuned from the relevant frequency range.

### 6.1.6 Physics

#### Sideband cooling to the mechanical ground state via Brillouin scattering

With the general cooling expression of equation 5.25, it is clear that with the experimental parameters described here cooling of an acoustic whispering-gallery mode to the quantum ground state (i.e. $\bar{n} \ll 1$) is possible if surface-induced dissipation channels of the acoustic waves beyond the mere material attenuation can be mitigated.

#### Mechanical Fock state preparation by two-mode squeezing and heralding

As discussed for example in [VAK13; Gal+14] the ground state cooling of the previous section will allow the preparation of the single-phonon Fock state by gentle two-mode squeezing and subsequent projection onto the single photon fock state with the use of a click detector (SPAD or superconducting nanowire), in line with the results presented for the single-phonon operations in section 4. A photon number resolving detector like a superconducting transition-edge detector could also be applied to probabilistically prepare higher-order Fock states.

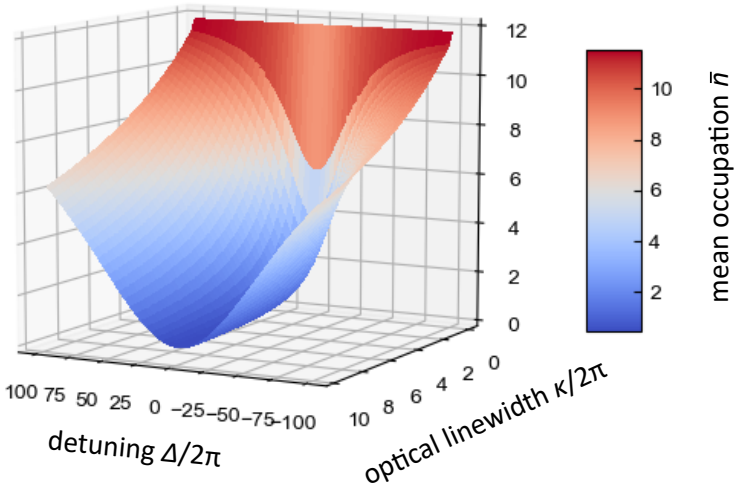


Figure 6.3: Sideband cooling of an acoustic whispering-gallery mode to the quantum ground state via Brillouin scattering. Plotted is the final mean occupation of the mode $\bar{n}$ versus the optical cavity decay rate $\kappa/2\pi$, and the optical-mechanical detuning $\Delta/2\pi$, at an assumed bath temperature of $T = 4$ K, an optomechanical coupling rate of $G/2\pi = 15$ MHz, and an acoustic damping rate of $\gamma/2\pi = 0.25$ MHz.

### Tuning of Brillouin phase matching

As discussed in different parts of the thesis, a point of major interest is the tuning of the Brillouin phase matching condition, namely the matching of the acoustic phase velocity of an acoustic mode with azimuthal mode number $M_\mathrm{a}$ with the speed of the average intensity pattern of two optical modes with azimuthal mode numbers $M_\mathrm{p}$ and $M_\mathrm{s}$, with $|M_\mathrm{a}| = |M_\mathrm{p}| + |M_\mathrm{s}|$. With the dispersion relation $\omega = ck$, this matching of velocities directly corresponds to achieving the condition $\Delta = \omega_\mathrm{blue} - \omega_\mathrm{red} - \omega_\mathrm{m} = 0$.

Thus we have many handles at our disposal to achieve the zero-detuning condition for a particular mode trio (e.g. one with a large bare coupling rate according to 1.56):

We can use the temperature of the bulk resonator (a single mode of interest can still be cooled) primarily via its effect on the refractive index and thus optical resonance frequencies, and its effect on the acoustic phase velocity.

Differential cross Kerr tuning: An additional optical field can be used resonant with a third optical resonance of the resonator, but detuned such that it is not affecting the

Brillouin interaction. By a difference of the optical mode overlap with the pump and Stokes (anti-Stokes) optical resonances a differential refractive index shift experienced by these modes will shift their resonance frequencies and can thus be used to tune the Brillouin phase matching condition. E.g. one might pick a mode from the same mode family (same polar and radial mode indices) as one of the two modes of the optical mode pair, which differ in their azimuthal index by a small integer (one or several free spectral ranges away). Thus the optical mode overlap will be maximal with one of the modes, non-maximal with the other, certifiedly obtaining a finite tuning effect.

These approaches don't require any physical changes to the setup. With making more or less intrusive modifications further tuning approaches can be explored:

One can explore sound velocity engineering in an amorphous material via saturation of TLS damping and exploiting the connection between sound absorption and velocity via the Kramers-Kronig relation [Beh+17]. While in principle the coherent sound drive required for saturation can be obtained by exciting Brillouin lasing at a far detuned colour (e.g. around 1300 nm or 1064 nm), it might be also practical to irradiate it with a piezo transducer.

Other tuning approaches requiring more setup modification are tuning via mechanical stress, which can allow for very wide tuning, as e.g. reported in [Kli+01], and also exploiting the quadratic electro-optic effect (DC Kerr effect), which is available in all materials, in contrast to the linear electro-optic (Pockels) effect, which is only available in materials lacking inversion symmetry, like e.g. lithium niobate crystals. The latter would require the installation of tuning electrodes. The review article by Strekalov presents in section 3 a nice overview of some tuning schemes [Str+16].

## 6.2 Transition from thermal Brillouin scattering to Brillouin lasing and the degree of second-order coherence

Experiments were conducted with spherical fused silica microresonators of 350 $\mu$m diameter with the aim to explore the transition from thermal Brillouin scattering to Brillouin lasing. This was firstly primarily inspired by the frequently found term "spontaneous" Brillouin scattering, as opposed to stimulated Brillouin scattering. While spontaneous parametric scattering is a commonly studied phenomenon in quantum optics, in Brillouin scattering most of the times the source of scattering is predominantly thermal excitation in the mechanical degree of freedom and not the mechanical vacuum fluctuations, which would be associated with the phrase "spontaneous", thus it is encouraged that the term "thermal" Brillouin scattering is preferredly used in this context.

It is well known that thermal states of light show a degree of second order coherence $g^{(2)}(0) = 2$. Indeed, the same property is observed for a single output mode of a parametric down-converter, if the other output mode is ignored (traced over). Thus, thermal/spontaneous Brillouin scattering is expected to show thermal statistics down to arbitrarily low thermal occupation.

The Brillouin lasing transition is a common example of an optomechanical parametric instability. The question arises whether this transition can also be understood in terms of a phase transition between an unordered and an ordered state [Hak83; Fin+18].

Certainly, the Brillouin lasing threshold is associated with a non-equilibrium dissipative phase transition. The phase transition analogy for inversion based lasing has been studied in [GH70; DS70], and Haken has extended these ideas into a much wider context [Hak75].

In the densely populated optical spectrum of the microsphere resonator a low threshold ($P_{\mathrm{in,thr}} \approx 40$ $\mu$W) Brillouin lasing condition was found. A configuration was arranged were the Brillouin back-scattered light was sent to a 50:50 beam splitter and from there to two

SPADs which were synchronously gated, so as to implement a measurement of the degree of second-order coherence $g^{(2)}$. The expectation was that across the lasing transition the $g^{(2)}$ changes from that of thermal statistics with $g^{(2)}(0) = 2$ to that of a coherent state with $g^{(2)}(0) = 1$, and such a measurement has thus far not yet been reported in the literature for Brillouin scattering. In optomechanics, an experiment showing a change in $g^{(2)}$ upon displacement of a thermal state has been reported in [Coh+15].

To complement the $g^{(2)}$ measurements, the back-scattered light was observed with an optical spectrum analyser, and heterodyne time-traces were recorded below, at around, and above the Brillouin lasing threshold. Figure 6.4 shows the measurement of the degree of second-order coherence, plotted against the reconstructed intracavity power $P_{\mathrm{cav}}$. The expected transition is precisely observed in the measurement. At around the threshold power, the system behaves extremely unstably, and is rapidly transitioning from a lasing to a non-lasing state ("flickering"). The excess of $g^{(2)}(0)$ in the threshold region seen in the data (higher value around 7 W) can be interpreted as a manifestation of this flickering, as changing the intensity during a $g^{(2)}$ measurement systematically increases its outcome.

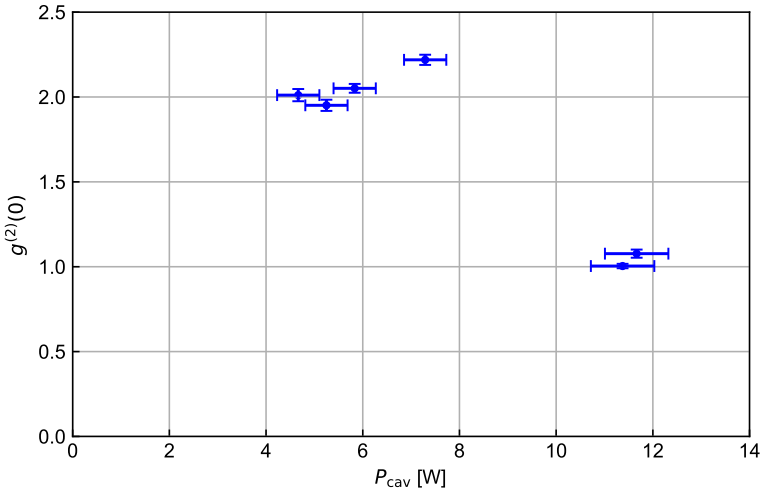


Figure 6.4: Transition from thermal Brillouin scattering ("spontaneous") to Brillouin lasing in a fused silica microsphere resonator in terms of the degree of second order coherence $g^{(2)}(0)$.

In figure 6.5 heterodyne spectra of the backscattered light are shown, corresponding to

measurements below, just below, and above the Brillouin lasing threshold. The phenomenon of linewidth-narrowing can be observed.

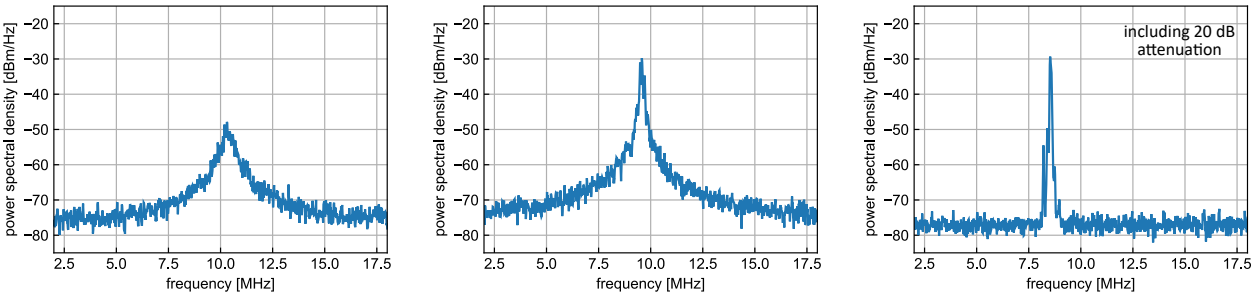


Figure 6.5: Optical heterodyne spectra below, just below, and above the Brillouin lasing threshold. Above threshold optical attenuation of 20 dB was used in order to prevent moving into a nonlinear regime of the balanced photodetector.

While Brillouin lasing is a type of optomechanical parametric instability [BSV01] it is to be distinguished from phonon lasing, which involves the stimulated emission of phonons, while in Brillouin lasing stimulated emission of Stokes photons occurs due to parametric gain associated with the bulk medium [Nun+14]. Phonon lasing has been observed in a couple of systems, e.g. in a trapped ion system [Vah+09] and in an electromechanical platform [Mah+13].

Interestingly, the Landau theory of phase transitions which relies on the thermodynamic potentials, which themselves can only be defined in thermodynamic equilibrium, can be successfully applied to the non-equilibrium system of the laser [GH70]. It has been shown that the lasing threshold is analogous to a continuous second-order phase transition, i.e. one where the second derivatives of thermodynamic potentials show discontinuities. In the case of the laser, a pump parameter takes the role of a temperature in the Landau theory, while the electric field amplitude is the order parameter [GH70; Hak70].

It has also been argued theoretically [YuH+10] that the Brillouin lasing transition can be treated analogously to the inversion based lasing transition, such that it comprises a second-order phase transition with the optical Stokes amplitude playing the role of the order parameter.

Around the Brillouin lasing threshold it is expected that the system will show critical

scaling, according to power laws with critical exponents, which are suspected to be universal [Kad66; Lub72; Lüb04]. One such quantity is the correlation length, which will be accessible via measurements of the optical Stokes field, e.g. via its autocorrelation function.

The preliminary results shown here are complemented by measurements of optical heterodyne time traces of the Stokes scattered light, taken at the threshold, when the system shows a seemingly random flickering, shown in figure 6.6. An analysis of the autocorrelation of such a signal might allow the determination of critical exponents, as in

$$\xi \propto |p - p_\mathrm{c}|^{-\nu} \,, \tag{6.3}$$

with $\xi$ the correlation time, $p$ a pump parameter related to the optical pump power, $p_\mathrm{c}$ the critical pump parameter, and $\nu$ a characteristic critical exponent.

Cryogenic temperatures in combination with the tuning techniques discussed in the previous section will allow the observation of ultralow-threshold Brillouin lasing.

## 6.3 Narrowband heralded single-photon source using spontaneous four-wave mixing in a whispering-gallery microresonator

Heralded single-photon sources based on the inherently probabilistic process of parametric fluorescence (spontaneous parametric down-conversion) and spontaneous four-wave mixing are, next to single-emitter based single-photon sources like quantum dots, cornerstones of modern quantum photonics. The main idea here is that in order to prepare a single-photon state of light one can exploit a process in which photons are naturally only created in pairs, and engineer a system such that detection of one member of the pair heralds the creation of the other. The approaches can mainly be divided into those relying on the second-order nonlinear susceptibility $\chi^{(2)}$, which is only available in non-centrosymmetric materials, and

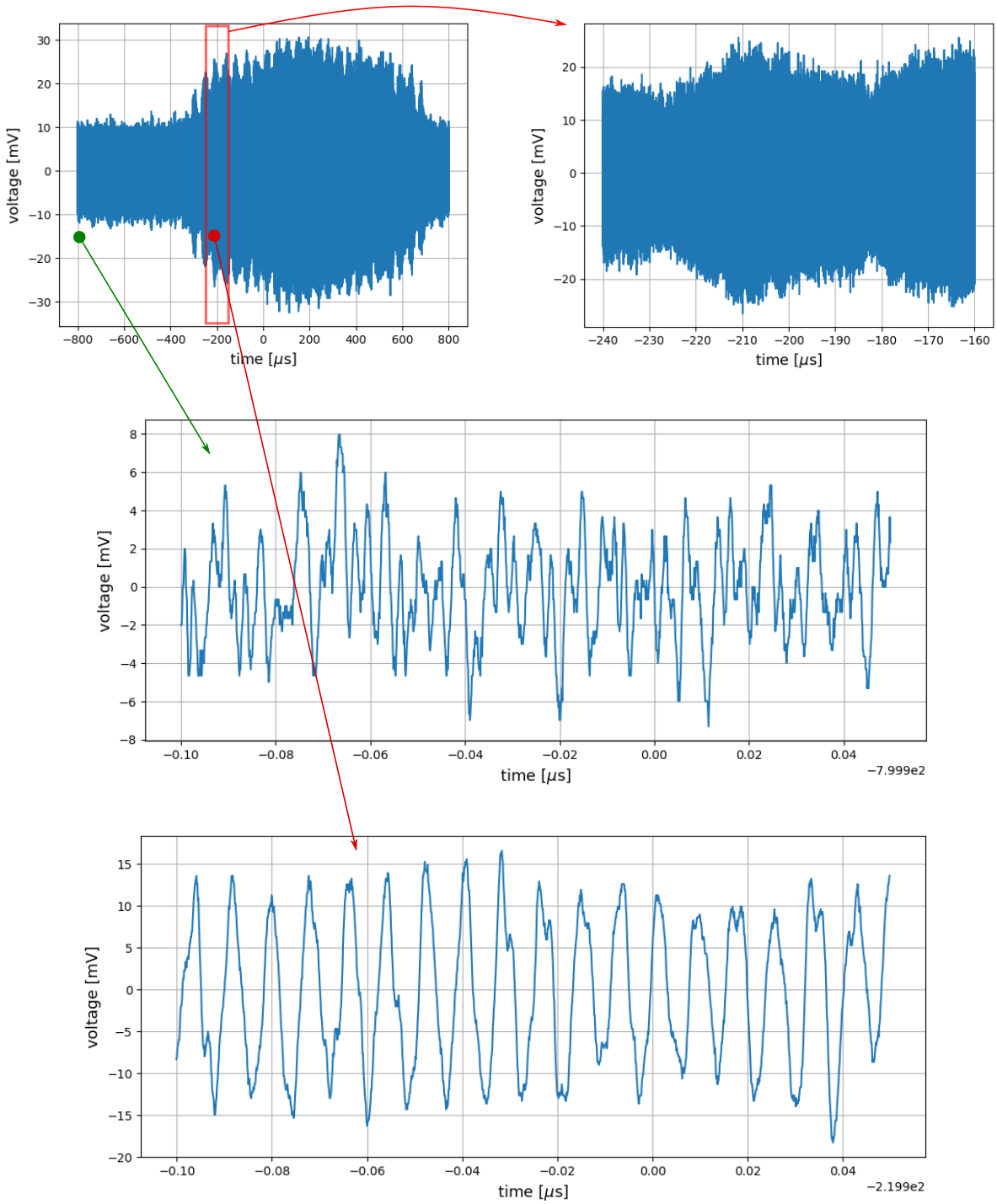


Figure 6.6: Heterodyne time trace of Stokes scattered light at the Brillouin lasing threshold showing the "flickering" of the Stokes field. Within the excursion of the system above the threshold, which here happens at typical timescales of $\approx 1$ ms, there is additional oscillatory behaviour (top right). The zoomed-in time traces (bottom) show the transition from the unordered to the ordered phase, with increasing autocorrelation timescale (not shown).

those relying on the third-order (Kerr) nonlinear susceptibility $\chi^{(3)}$ which is available in all materials. In the former case a pump photon spontaneously decays into two photons of lower energy in a process called parametric fluorescence or spontaneous parametric down-conversion, while in the latter case two pump photons are required to produce a pair of photons at different colours in a process called spontaneous four-wave mixing.

While historically heralded single-photon sources were first implemented in bulk samples and typically short, high-intensity pulses of light were used in order to achieve sufficient rates, in recent years interest has grown into the use of resonant structures which comes with the benefit of reducing the required pump power levels. In our experiment the $\chi^{(3)}$ nonlinearity of fused silica is used to make a single-photon source exploiting the process of spontaneous four-wave mixing in a whispering-gallery microresonator. In this process, two pump photons of the same colour (therefore also called degenerate four-wave mixing) are converted into a pair of photons, one bluer and one redder than the pump colour, called the signal (blue-shifted) and the idler (red-shifted) photons. The two main ingredients required to accomplish this situation besides a pump light source and a nonlinear medium, are firstly a detector able to detect single photons, and secondly some kind of discrimination tool to distinguish pump, signal and idler photons. In bulk sources the latter would often be accomplished by the angle under which the emission is taking place, as certain phase matching requirements have to be met. In our experiments, which are all fiber-based, all fields are guided within the same direction and spatial mode within the fiber, and with the same polarization (type-0), and we therefore need to use narrow spectral filtering to discriminate between the photons.

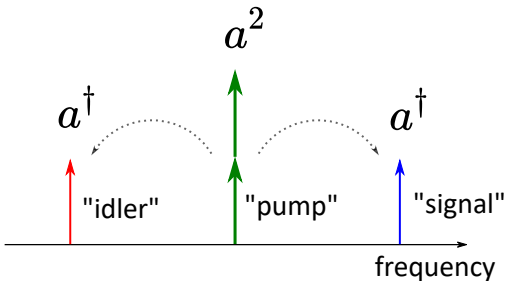


Figure 6.7: Principle of spontaneous four-wave mixing. Two photons from a strong pump field combine and are converted into a pair of photons spaced symmetrically in frequency away from the pump field, via the third-order nonlinearity of the medium.

It can be shown [Boy08] that from the nonlinear polarisation induced due to the $\chi^{(3)}$ nonlinearity of a medium follows an interaction Hamiltonian of the form

$$H_{\mathrm{SFWM}} \propto \chi^{(3)} E^{(+)} E^{(+)} E^{(-)} E^{(-)} \tag{6.4}$$

with $E^{(+)}$ and $E^{(-)}$ the positive and negative frequency parts of the electric field.

The Hamiltonian expressed in terms of mode operators

$$H_{\mathrm{SFWM}} \propto \chi^{(3)} \left( a_{\mathrm{p}}^2 a_{\mathrm{s}}^\dagger a_{\mathrm{i}}^\dagger + \mathrm{h.c.} \right) \ , \tag{6.5}$$

where p, s, and i stand for pump, signal, and idler waves, respectively, under the parametric approximation for a strong pump field ($a_{\mathrm{p}} \to \alpha$) becomes $\propto (|\alpha|^2 a_{\mathrm{s}}^\dagger a_{\mathrm{i}}^\dagger + h.c.)$, and the time evolution operator, written in terms of frequency modes, acting on the vacuum can be written as

$$\left[ \int \int d\omega_1 d\omega_2 f(\omega_1, \omega_2) a^\dagger(\omega_1) a^\dagger(\omega_2) \right] |vac\rangle \ , \tag{6.6}$$

where $f(\omega_1, \omega_2)$ is a function incorporating pump and phase matching conditions. For the simple case of only two modes, where by modes we mean very generally time-frequency modes (the operation in equation 6.6 would generally excite many modes), the time-evolution resembles a two-mode squeezing operator

$$\hat{S}_{\text{two mode}} = \exp\left( r \exp(-i\phi) \hat{a}_s \hat{a}_i - r \exp(i\phi) \hat{a}_s^\dagger \hat{a}_i^\dagger \right) \ , \tag{6.7}$$

with the real squeezing parameter $r$, and the output state is a two-mode-squeezed vacuum.

It can be shown that this operation acted on the vacuum produces a photon number correlated state

$$\hat{S}_{\text{two mode}} |0,0\rangle = \sum_{n=0}^{\infty} c_n |n,n\rangle \ , \tag{6.8}$$

where we used the notation $|n,n\rangle = |n\rangle \otimes |n\rangle$, and the coefficients are given by $c_n = (\tanh(r))^n / \cosh(r)$ [WM08]. The photon number distribution of the two-mode squeezed

vacuum state is shown in figure 6.8 for different squeezing parameters. As figure 6.8 sug-

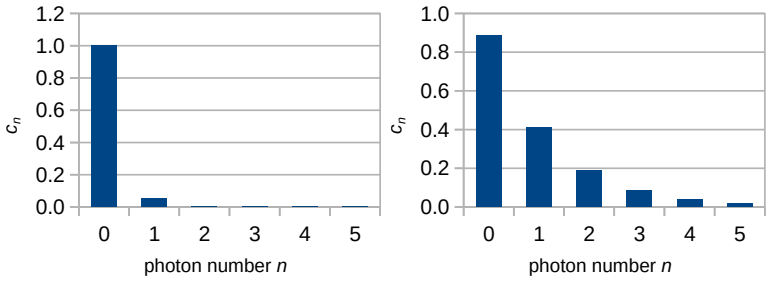


Figure 6.8: Photon number distribution of the two-mode squeezed vacuum state for squeezing parameters $r = 0.05$ and $r = 0.5$.

gests, in order to build a single-photon source we want to operate at low values of the squeezing parameter $r$ to minimize the two- or multi-photon contributions that can lead to "accidentals" in an experiment.

### 6.3.1 Phase matching

As in other nonlinear optical processes, four-wave mixing occurs under the conservation of (quasi-)momentum and energy and applying these conditions leads to phase matching considerations. The photon pairs are generated in pairs of resonances spaced symmetrically around the pump resonance by $\pm 1, \pm 2, \pm 3, ...$ FSRs away, see figure 6.9. The symmetric spacing within the same mode family is demanded by phase matching, and it readily fulfils (quasi-)momentum conservation, i.e.

$$2k_\mathrm{p} = k_\mathrm{s} + k_\mathrm{i} \;\Leftrightarrow\; 2\frac{M_\mathrm{p}}{R} = \frac{M_\mathrm{s}}{R} + \frac{M_\mathrm{i}}{R} \;\Leftrightarrow\; M_\mathrm{s} - M_\mathrm{p} = M_\mathrm{p} - M_\mathrm{i}\ , \tag{6.9}$$

where the subscripts p, s, and i stand for pump, signal and idler modes, respectively, and $M$ is the azimuthal mode number of the respective mode within the mode family.

At the same time energy is conserved in the process.

$$2E_\mathrm{p} = E_\mathrm{s} + E_\mathrm{i} \quad \Leftrightarrow \quad \nu_\mathrm{s} - \nu_\mathrm{p} = \nu_\mathrm{p} - \nu_\mathrm{i} \tag{6.10}$$

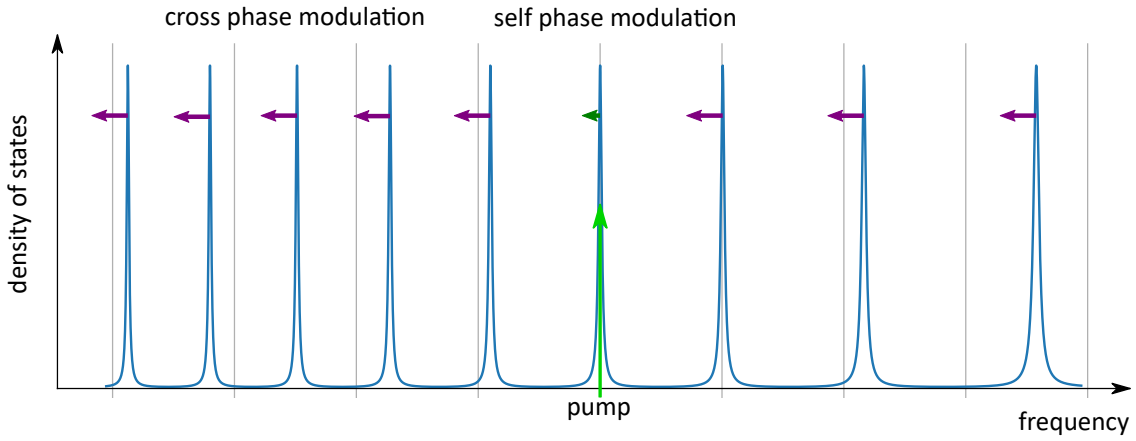


Figure 6.9: Phase matching of four-wave mixing in a resonator. The blue curve shows the optical density of states (power build-up) of modes of a particular mode family of a fused silica whispering-gallery resonator with hugely exaggerated dispersion and a low finesse of $\mathcal{F} = 28$, for better visualisation, corresponding to $a = 0.95$, $|t| = 0.95$ in equation A.4 (in practice the finesse is much higher ($\approx 10^4$)). The non-equidistance of modes relative to the pump resonance due to dispersion can be compensated for by blue detuning the pump laser and the differential effect of self- and cross-phase modulation, resulting in photon pairs being generated $\pm 1, \pm 2, \pm 3, ...$FSRs away.

While a frequency independent refractive index $n$ would lead to perfectly equally spaced modes within a mode family, material and waveguide dispersion correspond to the free spectral range (frequency difference between adjacent members of the same mode family) changing with frequency.

In order to fulfil energy conservation, pump detuning and the self-phase modulation and cross-phase modulation which arises due to the Kerr nonlinearity, too, can be used. As already discussed in section 3.3.1 self-phase and cross-phase modulation lead to a refractive index shift linear in the optical power (see equations 3.7 and 3.8), with cross-phase modulation being an exact factor of 2 larger in magnitude than self-phase modulation for the perfect intensity overlap within a mode family. Thus, the point of best phase-matching will move out from the pump with increasing pump power. Indeed, in the strong-squeezing regime where parametric oscillation sets on, a switching of parametric oscillation between $\pm 3$ and $\pm 4$ FSRs out from the pump under small perturbations of the intracavity power was experimentally observed. Phase matching in fused silica microresonators in the context of frequency-comb generation is discussed in detail in [Del11].

**Continuous-wave and pulsed excitation**

While for the creation of photon pairs via four-wave mixing it is sufficient to use a continuous wave (cw) pump field, for heralded preparation of single photons it is desirable to use a pulsed pump field, such that the perfect frequency anti-correlation of signal and idler photons, which stems from energy conservation, is decreased. By choosing a double-exponential pump pulse shape whose spectral width matches the cavity linewidth, maximal decorrelation of the signal and idler fields can be achieved, so that a high degree of spectral purity/factorability can be achieved. In fact, in [Hel+10] it is stated that the Schmidt number can be as low as 1.09 for pulsed operation, while being substantially larger towards longer pulse length. Techniques how to measure the spectral purity and for characterisation of the joint spectral intensity will be discussed below.

### 6.3.2 Pair generation rate

Following the treatments [Hel+10; HLS12; SKM16] the photon pair generation rate $R_{\mathrm{pair}}$ due to spontaneous four-wave mixing in a microresonator considering a particular phase-matched pair of optical resonances under continuous-wave pumping can be estimated as

$$R_{\mathrm{pair}} = \frac{P_{\mathrm{i}}}{h\nu_{\mathrm{i}}} = \frac{1}{64\pi}\left(\frac{n_2 P_{\mathrm{p}} c\nu}{n^2 L A_{\mathrm{eff}}}\right)^2 \frac{1}{(\Delta\nu_{\mathrm{FWHM}})^3}, \tag{6.11}$$

which assumes perfect phase matching, on-resonance pumping (zero detuning), and $\nu_{\mathrm{p}} \approx \nu_{\mathrm{i}} \approx \nu_{\mathrm{s}}$, as well as the refractive index $n_{\mathrm{p}} = n_{\mathrm{i}} = n_{\mathrm{s}} = n$, for simplicity. It also assumes equal linewidths for the pump, idler and signal modes, which is a reasonable assumtion, as they have identical spatial profiles and closely adjacent wavelength. $P_{\mathrm{i}}$ stands for the idler power, $n_2$ the nonlinear index, which is proportional to $\chi^{(3)}$, $P_{\mathrm{p}}$ the optical input pump power, and $L$ the resonator perimeter.

In this expression, we total over a whole resonance of the whispering-gallery resonator, thus the generation bandwidth is identical with the linewidth (unfiltered case). This is due to the fact that the fiber Bragg grating filters, with typical filter bandwidth of 0.2 nm or

20 GHz, is much larger than the typical cavity linewidth (1-10 MHz). We see that the pair generation rate scales as $(\Delta\nu_{\mathrm{FWHM}})^{-3}$, maybe surprisingly, as the four contributing fields suggest a scaling as $Q^4 \propto (\Delta\nu_{\mathrm{FWHM}})^{-4}$. This is explained by the fact that the linewidth ($Q$ factor) also enters in the generation bandwidth. We also see that the process scales with the square of the energy density of the pump, where $A_{\mathrm{eff}}$ is the effective mode area of the modes, and $L$ the round trip length.

For some typical parameters ($\Delta\nu_{\mathrm{FWHM}} = 4\,\mathrm{MHz}$, $A_{\mathrm{eff}} = 30\,\mu\mathrm{m}^2$, diameter 660 µm, and $n_2 = 2.8 \times 10^{-20}\,\mathrm{m}^2\,\mathrm{W}^{-1}$) the pair generation rate under continuous wave pumping is given by $R_{\mathrm{pair}} = 12 \times 10^3\,\mathrm{s}^{-1} \cdot \left(\frac{P_{\mathrm{p}}}{\mathrm{mW}}\right)^2$.

In pulsed operation, the squeezing parameter is the main quantity of interest (see figure 6.8), which is obtained for a certain peak pump power of the pulse. For strong squeezing, and continuous wave pumping, the system reaches the regime of optical parametric oscillation and soon after Kerr frequency-comb generation, as shown in figure 1.14. The SFWM pair generation process in a high $Q$ whispering-gallery resonator can therefore also be viewed as the sub-threshold low-squeezing regime of a Kerr frequency comb, and this perspective is described in [Che16].

In order to observe the photon pairs generated by the two-mode squeezing operation on the vacuum, firstly the detected rate (accounting for inefficiencies) needs to substantially overcome the dark-count rate of the detector, and secondly the filtering needs to sufficiently suppress both pump light and other unwanted fields, e.g. from other squeezed modes or amplified spontaneous emission in the laser. For these purposes filters were acquired which will be further described in the setup section.

### 6.3.3 Setup and filtering scheme

Figure 6.10 shows the setup for the spontaneous four-wave mixing pair generation and heralded single photon-source experiment.

Pump light is filtered from broadband amplified spontaneous emission (ASE = superlumi-

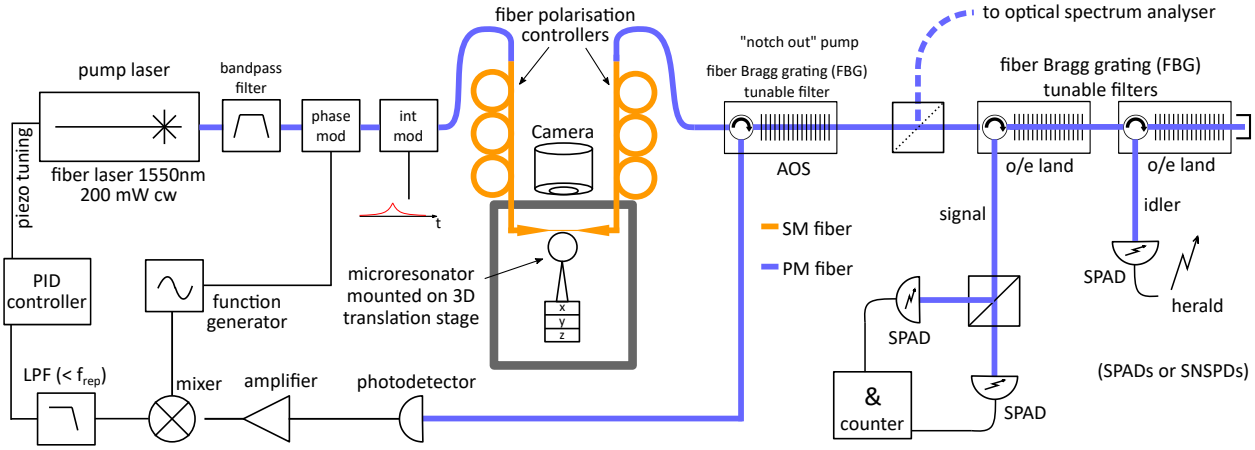


Figure 6.10: Setup for the four-wave-mixing-based single-photon source experiment.

nescence) with a tunable filter (Alnair inc), which limits the ASE to a range of $\pm < 1\Delta\nu_{\mathrm{FSR}}$ around the pump laser frequency, such that it does not contaminate the frequencies of the comb lines one or multiple FSRs away from the pump.

The PDH locking scheme described in section 2.4.1 can be used in continuous-wave operation, but also in pulsed operation, once a low-pass filter with a cut-off below the repetition rate of the pulsing is employed (slow PDH).

After interaction with the resonator the transmitted pump light is notched out by two high-reflectivity tunable fiber Bragg grating filters (AOS photonics), which come with a reflectivity of $>$ 99.999 %, each. Thus the pump photon rate is brought down from $P_{\mathrm{p}}/(\hbar\omega_{\mathrm{p}}) \approx 10^{16}\,\mathrm{s}^{-1}$ to the $10^{6}\,\mathrm{s}^{-1}$ range. The rest of the filtering is accomplished by four tunable fiber Bragg grating filters (o/eland) which can be tuned to reflect the signal and idler fields, respectively.

In free-running mode the InGaAs SPADs have a performance figure of merit (quantum efficiency/dark count rate) of 10 %/4.5 kHz, while available superconducting nanowire single-photon detectors have 80 %/5 Hz, thus achieving an improvement of 38 dB over InGaAs SPADs.

The diameter of the silica microresonator for the experiment was chosen at 660 µm, in order to obtain a FSR of 100 GHz and thus match a typical channel spacing in telecommu-

nications networks using wavelength division multiplexing in the C-band.

### 6.3.4 Measurements

Here we present a list of measurements which are desirable to perform in order to characterise the performance of firstly the photon-pair source, and secondly the heralded single-photon source. A nice review of the basic physics of parametric nonlinear photon pair and single-photon sources is given in [Cas+17].

The first interesting quantity to measure is the singles count rate (in either signal or idler arm). This can be done in a continuous wave or pulsed pumping regime. Measuring a quadratic scaling with input pump power will be a signature of spontaneous four-wave mixing, and will allow to investigate how strongly modification of the phase-matching condition by self- and cross-phase modulation changes this scaling at different linewidths.

Another quantity of interest is the coincidence rate of signal and idler fields. In a lossless system this rate would be identical to the singles rate.

The marginal $g^{(2)}$, i.e. the degree of second-order coherence, in the signal arm, not regarding (tracing over) the idler arm, is another cross-check whether a single mode of a two-mode squeezer is being generated. In the limit of perfect spectral separability [Gra+18], we expect a marginal $g^{(2)}(0) = 2$, since tracing over the other mode in a two-mode squeezed vacuum state leaves the system in a thermal state.

The heralded $g^{(2)}$ behaves in quite the opposite way to the marginal $g^{(2)}$. If the degree of second order coherence $g^{(2)}$ of the signal arm is measured conditioned on a herald click in the idler arm, the signature of single photon state preparation is a $g^{(2)}(0) < 1$, which is a truely non-classical feature. A pure $N = 1$ Fock state has a $g^{(2)}(0) = 0$, i.e. there is never a coincidence in the signal arm (as there is only one photon present). This measurement is most conveniently performed with three single-photon detector modules.

It is interesting to examine the temporal correlations of the photon pairs within their temporal envelope, as these correlations affect the purity of the prepared single photon

states. Similarly to the well-known joint spectral amplitude, whose modulus squared, the joint spectral intensity (JSI), is frequently measured in broadband parametric pair sources to characterise correlations [Zie+18], one can define the joint temporal amplitude, which is the Fourier transform of the joint spectral amplitude.

As the photons produced by this source are spectrally very narrow ($\approx 1 - 10$ MHz), it is going to be difficult to measure a joint spectral intensity. Rather it is conceivable to measure a joint temporal intensity of signal and idler fields, as the photons are temporally longer than the detector's timing resolution. Such a measurement can reveal and quantify residual signal-idler correlation. It has been investigated how self and cross-phase modulation affect the purity in four-wave mixing photon-pair sources [Bel+15; ST16].

The waveguide dispersion in our system was not quantified through a mode-solver calculation, but the onset of parametric oscillation by four-wave mixing at a pump power threshold of as low as 9 mW, and frequency-comb generation by intercombination four-wave mixing at only slightly higher pump power, see figure 1.14, suggest that dispersion is not a problem in our system and phase matching can be achieved by the combined effect of blue-detuning of the pump laser and self- and cross-phase modulation (compare figure 6.9).

With our resonator having an FSR of 100 GHz by design (97.3GHz measured), matching a common telecommunications channel spacing, the wavelength separations are small and chromatic dispersion (which is usually dominating against waveguide dispersion at the size-scale of resonators used here) is $\approx$ 300 kHz/FSR, which was calculated by applying the Sellmeier formula [Sel71] and self-consistently solving for the resonance frequencies of adjacent modes around 1550 nm.

Another interesting possibility for research applications in the platform, which is related to the pair-generation process of degenerate four-wave mixing, is the appearance of squeezing in the amplitude difference which can be observed with a balanced detector above the parametric-oscillation threshold, as has been demonstrated in [Dut+15]. The amplitude (and intensity) difference between the two parametrically oscillating fields is smaller than the shot-noise level, which can be intuitively understood by the fact that photons in the two

modes are always created and destroyed in pairs (compare equation 6.7).

### Outlook

A single-photon source producing spectrally narrow ($\approx$ MHz) photons might prove valuable for certain branches of quantum information science, e.g. narrowband quantum memories, or cases where there is strong dispersion present. The narrowband single-photon source outlined here also has the potential of being itself useful as a tool for optomechanics experiments with whispering-gallery resonators, e.g. as an ancilla, as the bandwidths of the single photons can be precisely matched to the optical cavity linewidths. The whispering-gallery modes of the photon source can in such a scenario be tuned to the required absolute frequency of the optical mode of the optomechanical system using temperature tuning.

# Appendix A

# Optical ring resonator compendium

In this section we are going to go through some basic ring resonator theory and derive some simple, frequently used connections.

In many regards a ring resonator behaves very similarly to the familiar Fabry-Perot type resonator. A ring resonator with only one coupling port, and no add-drop port (as used in this work), behaves analogously to a one-sided Fabry-Perot resonator, with a perfectly reflecting second mirror, where the transmission through the ring resonator coupler corresponds to the Fabry-Perot reflection.

A ring resonator supports travelling optical waves (unidirectional), in contrast to the standing waves obtained in a Fabry-Perot cavity.

## Ring resonator coupling through a beam splitter

The evanescent coupling between a tapered optical fiber (in general a side channel) and a whispering-gallery mode of a microresonator can be modelled by a beam splitter, with one of its input and one of its output ports connected trough a resonator round-trip, as depicted in figure A.1.

The lossless beam splitter having amplitude coupling parameter $r$ (analogously to the reflectivity), and amplitude transmittivity $t$, following Yariv [Yar00] the transformation of

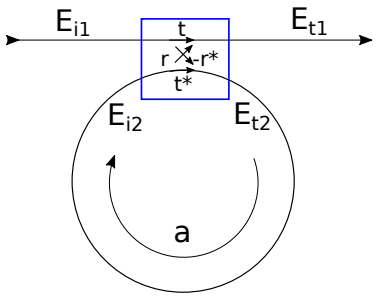


Figure A.1: Scheme of the coupling between a side channel and a microresonator modelled through a lossless beam splitter.

input to output fields can be written as

$$\begin{pmatrix} E_{o1} \\ E_{o2} \end{pmatrix} = \begin{pmatrix} t & r \\ -r^* & t^* \end{pmatrix} \begin{pmatrix} E_{i1} \\ E_{i2} \end{pmatrix} \ . \tag{A.1}$$

Here $E_{ii}$ and $E_{oi}$ stand for the input and output electric field amplitudes.

Modelling internal losses of the resonator by the round-trip attenuation parameter $a$, stemming from the attenuation coefficient $\alpha$ acting over the length of a round trip $L$, and by using the phase propagation constant $\beta$ (i.e. the component of the wave-vector in the propagation direction), the round trip propagation of the field amplitude can be written as

$$\begin{aligned} E_{i2} &= \exp\left((-\frac{\alpha}{2} + i\beta)L\right) E_{o2} \\ &= a \cdot \exp\left(2\pi i \frac{L}{\lambda/n}\right) E_{o2} = a \cdot \exp(i\theta) E_{o2} \ . \end{aligned} \tag{A.2}$$

From these two equations A.1 and A.2 one can solve for all four fields in terms of the input field $E_{i1}$, and after modulus squaring readily find an expression for the transmitted power and the power build-up inside the cavity:

$$P_{o1} = |E_{o1}|^2 = \frac{|t|^2 + a^2 - 2|t|a\cos(\theta - \phi_t)}{1 + |t|^2 a^2 - 2|t|a\cos(\theta - \phi_t)} \cdot P_{i1} \tag{A.3}$$

$$P_{i2} = |E_{i2}|^2 = \frac{a^2(1 - |t|^2)}{1 + a^2|t|^2 - 2a|t|cos(\theta - \phi_t)} \cdot P_{i1} \ , \tag{A.4}$$

where we introduced a coupler phase $t = |t| \exp(i\phi_t)$. We can see that in the limit of low loss ($a \to 1$, $|t| \to 1$), the expressions are symmetric in $a$ and $|t|$.

From equation A.4 we can derive the following expression for the full-width at half maximum (FWHM) linewidth, which is identical with the total energy damping rate (in plain frequency units):

$$\Delta\nu_{\mathrm{FWHM}} = \frac{2c}{\pi n L} \arcsin\left(\frac{1 - a|t|}{2\sqrt{a|t|}}\right) \tag{A.5}$$

In the practically well fulfilled small angle approximation for the sin and $a|t| \approx 1$, we obtain the following connection between $|at|$ and the total damping rate:

$$a|t| = 1 - \frac{\pi\Delta\nu_{\mathrm{FWHM}}}{\Delta\nu_{\mathrm{FSR}}} = 1 - \frac{\kappa}{\Delta\nu_{\mathrm{FSR}}} \quad \Leftrightarrow \quad \frac{1}{1 - a|t|} = \frac{\mathcal{F}}{\pi} \ , \tag{A.6}$$

where $\kappa$ is the amplitude decay rate and $\mathcal{F}$ is the finesse.

Inserting the expressions for $a$ and $|t|$ we obtain

$$\frac{\kappa_{\mathrm{i}}}{\Delta\nu_{\mathrm{FSR}}} = 1 - a \quad \text{and} \quad \frac{\kappa_{\mathrm{e}}}{\Delta\nu_{\mathrm{FSR}}} = 1 - |t| \ , \tag{A.7}$$

where we introduced the intrinsic and external damping rates, which represent the losses and add up to the total damping rate $\kappa = \kappa_{\mathrm{i}} + \kappa_{\mathrm{e}}$.

Depending whether the losses are dominated by intrinsic or external damping, one speaks of under- and overcoupling, and critical coupling if the two damping contributions are equal, in which case the transmitted power on resonance completely vanishes, see figure A.2.

Q factors of up to $10^{11}$ have been experimentally achieved [GSI96], and atmospheric water adsorption has been identified as the fundamental limitation to the Q factor with devices operated under normal atmospheric conditions. Accounting for this effect still Q factors of $10^8$ to $10^9$ can be achieved in practice.

Besides the Q factor, the most important parameter of a resonator is its free spectral range (FSR), which is defined as the frequency difference between two adjacent modes (of

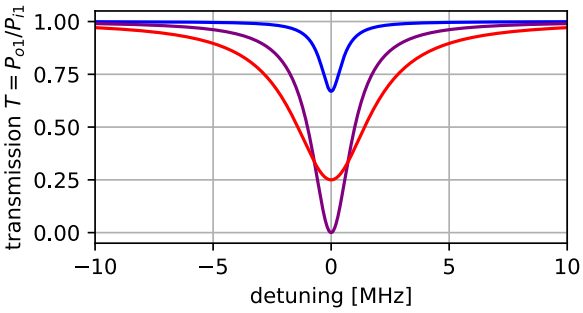


Figure A.2: Taper transmission for undercoupling (blue), critical coupling (purple) and overcoupling (red) to an optical ring resonator. The example is for an FSR of 100 GHz and an intrinsic linewidth of $2\kappa_\mathrm{i}/2\pi = 1\,\mathrm{MHz}$, with external (taper coupling induced) linewidth contribution of $2\kappa_\mathrm{e}/2\pi = 0.1\,\mathrm{MHz}, 1\,\mathrm{MHz}$ and $3\,\mathrm{MHz}$, respectively. The corresponding round-trip amplitude transmittivity is $a = 0.999969$, and at critical coupling the effective beam-splitter reflectivity parameter of the taper-resonator coupling is $r = 0.0079$.

the same mode family). It is given approximately by

$$\Delta\nu_\mathrm{FSR} \approx \frac{c}{n(\nu)\pi d} \tag{A.8}$$

Due to dispersion in silica, $n$ in equation 1.30 cannot be regarded constant with respect to wavelength, the consequence being that the FSR changes with wavelength. Aditionally there is waveguide dispersion (also called geometric dispersion): The light doesn't "perceive" the guiding structure the same for different wavelengths (compare Goos-Hänchen effect).

In order to calculate free spectral ranges (considering only material dispersion) more precisely, one can numerically solve the self-consistent equation 1.30 after inserting the refractive index given by a Sellmeier formula [Sel71], which allows conveniently embodying material dispersion into calculations, as it specifies refractive index changes across a large wavelength range with excellent precision. To correctly include the combined effects of material and waveguide dispersion into calculations, for most geometries there is not known analytical solutions for the mode frequencies, and this can, to date, only be achieved by means of a numerical electromagnetic mode solver, e.g. [Kra11].

## Round-trip time and FSR

Directly related to the absolute size of the microresonator are the round trip time and its inverse, the free spectral range (FSR). The round trip time and FSR are given by

$$t_{\mathrm{rt}} = \frac{\pi D}{c/n} \quad \text{and} \quad \Delta\nu_{\mathrm{FSR}} = \frac{1}{t_{\mathrm{rt}}} = \frac{c}{n\pi D} \ , \tag{A.9}$$

where $D$ is the diameter of the axially symmetric resonator, and $n$ the refractive index. Its inverse is the FSR, and it is also the frequency spacing of adjacent azimuthal modes. As the refractive index is generally frequency dependent, the FSR depends on the frequency (other than vacuum-filled Fabry-Perot resonators). Also different transverse modes of the whispering-gallery type will possess slightly different FSRs. Thus, at optical frequencies and azimuthal mode numbers in the thousands, azimuthal modes with different azimuthal mode numbers will spectrally intermix and produce an apparent "mode forest", where spectral grouping of transverse modes is stretched beyond typical scan ranges.

All modes which have the same polar and radial mode numbers, but only differ in their azimuthal mode number (compare section 1.3.2) we call members of a "mode family" or "azimuthal mode family".

## Attenuation and linewidth

Just as in any other electromagnetic cavity the light trapped in the cavity is attenuated, i.e. photons are lost through different damping mechanisms. In the first section of the appendix we distinguished between a round-trip attenuation and attenuation induced by the beam-splitter coupler (external damping; tapered fiber coupling).

For whispering-gallery resonators of the type and sizes used in this work, major intrinsic damping mechanisms have been identified [GSI96]. Without surface contamination and adhesion of atmospheric water record Q-values of $1.5 \cdot 10^{11}$ were reported in fused silica at a wavelength of 1.55 µm. Under normal atmospheric conditions this record value then quickly

(timescale of hours) decays to values in the regime $\approx 10^9$ which could be maintained for many months [GSI96]. In descending order of significance, the damping mechanisms include i) absorption by atmospheric water microdroplets adsorbed to the surface, ii) scattering off surface inhomogeneities, iii) Rayleigh scattering (i.e. elastic scattering off thermally induced density fluctuations), iv) material absorption, v) bending losses (a non-planar dielectric interface radiates). As mentioned before, additionally to these intrinsic losses the coupling to the tapered fiber which is used to couple light into the cavity, also acts as a loss channel.

At resonator sizes of 300 µm to 2000 µm the radius of curvature is much larger than the wavelength of light and bending/radiation losses are negligible [BGI89].

Practically, contamination of the resonator surface with scatterers/absorbers (dust) was a significant experimental challenge. The use of a sealed vacuum environment will mitigate this and also reduce the infrared attenuation from the OH-bonds in atmospheric water adsorbed to the resonator surface.

Light is attenuated per unit length while travelling through the resonator, which we denote $\alpha$, and is coupled out to a side channel (e.g. tapered optical fiber) when traversing the coupling region. As intensity is proportional to amplitude squared $I \propto A^2$ it will decay at double the rate of the amplitude of the field. By dividing the intensity loss per round trip by the time per roundtrip $t_{\mathrm{rt}}$ we obtain the intensity loss per time, which is the linewidth $\Delta\nu_{\mathrm{FWHM}}$. The exponential decay in time of electromagnetic energy in a cavity mode due to attenuation is associated with a Lorentzian line-shape function in frequency space, which can be simply obtained by Fourier transform. The full-width at half-maximum linewidth in plain frequency units, as determined in the experiment, is related to the frequently used (angular frequency) amplitude decay rate $\kappa$ via

$$\Delta\nu_{\mathrm{FWHM}} = \frac{2\kappa}{2\pi} \,. \tag{A.10}$$

The linewidth is a very important quantity and one of the most frequently referred-to quantities of a particular eigenmode of an optical whispering-gallery resonator. It can be directly

measured in the experiment by frequency sweeping a narrow-band laser across the spectral region of interest while monitoring the transmission through the tapered fiber coupled to the resonator. In the case of narrow linewidths it can also be practical to do a ring-down measurement, where the light intensity is abruptly changed and the information about the cavity lifetime is inferred from the transient temporal response.

As different damping mechanisms typically don't interfere, and cause individual exponential damping factors, the observed linewidth is just a result of individual linewidth contributions from different mechanisms:

$$\kappa = \kappa_{\text{dust}} + \kappa_{\text{Rayleigh}} + \kappa_{\text{taper}} + \kappa_{\text{taper scattering}} + \kappa_{\text{abs}} + ... \tag{A.11}$$

Often, not bothering about factors of 2 or $2\pi$, $\kappa$ is losely referred to as the linewidth.

## Finesse and quality factor

From the linewidth we can define two other important quantities, the finesse $\mathcal{F}$ and the (angular) quality factor (or Q factor) $Q$. The finesse

$$\mathcal{F} = \frac{\Delta\nu_{\text{FSR}}}{\Delta\nu_{\text{FWHM}}} = 2\pi \cdot \frac{t_{1/\text{e}}}{t_{\text{rt}}} \tag{A.12}$$

is the ratio of free spectral range and linewidth, or also the ratio of the resonance lifetime to the round-trip time. At a given surface-finishing capability of the manufacturing (given linewidth) the finesse scales inversely with the absolute resonator dimension $\mathcal{F} \propto 1/D$. It can be seen roughly as the quantity which tells how well the cavity resonance does its job of recycling the light.

The quality factor

$$Q = \frac{\nu}{\Delta\nu_{\text{FWHM}}} \tag{A.13}$$

is the ratio of the optical frequency to the linewidth. It is rather a quantity specifying the

quality of an oscillator (with only one degree of freedom), thus interpreting one particular resonance of a device supporting waves as an oscillator (which we of course implicitly do all the time here). For optical whispering-gallery resonators with given linewidth it does NOT scale with size. This quantity is directly sensitive to the loss mechanisms and not directly to size.

As mentioned in the previous section, in the regime of weak damping (which is practically always well fulfilled), damping mechanisms just add up, as in their damping rates, i.e. their linewidths, add up: $\kappa_{\mathrm{tot}} = \kappa_1 + \kappa_2 + ... + \kappa_N$. With $\Delta\nu_{\mathrm{FWHM}} = 2\kappa/(2\pi)$ and deviding through the optical frequency $\nu$, it's clear that the quality factors add up reciprocally:

$$\frac{1}{Q} = \frac{1}{Q_1} + \frac{1}{Q_2} + ... + \frac{1}{Q_N} \tag{A.14}$$

Above we summarized the intrinsic loss mechanisms in one number, the propagation loss $\alpha$.

In practice one often considers the "intrinsic linewidth", which sums up all loss mechanisms except those induced by the tapered fiber coupling, and it can be obtained by extrapolating the linewidth to zero coupling. The ratio of "intrinsic" loss to external coupling (to guided modes of the tapered optical fiber) determines whether the resonator mode is under-, over- or critically coupled, compare figure A.2. The taper, besides useful coupling, can also induce scattering loss, and the ideality of the coupling can be defined as the ratio of these [Spi+03].

## Intracavity power build-up and photon number

The intracavity photon number can be obtained from the built-up intracavity power, the energy per photon, and the cavity round trip time as

$$\bar{n} = \frac{P_{\mathrm{cav}}}{\hbar\omega} t_{\mathrm{rt}} = \frac{P_{\mathrm{cav}}}{\hbar\omega \cdot \Delta\nu_{\mathrm{FSR}}} \ . \tag{A.15}$$

From input-output theory [AKM14] we know $a = \frac{\sqrt{2\kappa_e}}{\kappa - i\Delta} a_{in}$, where the input power is connected to the input operator $P_{in}/(\hbar\omega) = a_{in}^2$ and the intracavity power to the cavity mode operator via $P_{cav}/(\hbar\omega) = a^2/t_{rt} = a^2 \cdot \Delta\nu_{FSR}$ . Then for the build-up factor (ratio of intracavity power to input power) we obtain for general coupling condition and detuning

$$\frac{P_{cav}}{P_{in}} = \frac{2\kappa_e}{\kappa} \cdot \frac{\kappa^2}{\kappa^2 + \Delta^2} \cdot \frac{\mathcal{F}}{\pi} \ , \tag{A.16}$$

which in the special case of critical coupling, where $\kappa_e = \frac{\kappa}{2}$, and on-resonance pumping, $\Delta = 0$, takes the form of the useful rule-of-thumb

$$P_{cav} = \frac{\mathcal{F}}{\pi} \cdot P_{in} \ . \tag{A.17}$$

The on-resonance transmission $T_0$ of a ring resonator coupled to a side-channel (tapered optical fiber) is related to the intrinsic and external damping rates via

$$T_0 = \frac{(\kappa_i - \kappa_e)^2}{(\kappa_i + \kappa_e)^2} \ , \tag{A.18}$$

such that in the undercoupled case ($\kappa_e < \kappa_i$), we have $\kappa_i = \frac{\kappa}{2}\left(1 + \sqrt{T_0}\right)$, and $\kappa_e = \frac{\kappa}{2}\left(1 - \sqrt{T_0}\right)$, and flipped $+/-$ signs in the overcoupled case.

In order to determine the intracavity pump power and mean photon number in practice it is useful to consider the Lorentzian lineshape function and to obtain the following connection of detuning and transmission, $\left(\frac{\Delta}{\kappa}\right)^2 = \frac{T - T_0}{1 - T}$.

Combining this relation with equations A.18 and A.16, we obtain an expression for the intracavity power in terms of input power, finesse, transmission and on-resonance transmission

$$P_{cav} = \frac{\mathcal{F}}{\pi} \cdot \frac{1 - T}{1 - \sqrt{T_0}} \cdot P_{in} \tag{A.19}$$

(overcoupled case, sign in the demoninator flipped for the undercoupled case).

Then, substituting for the finesse in equation A.16, we obtain the following relation for

the intracavity photon number and amplitude of a coherently driven cavity mode

$$\bar{n} = |\alpha|^2 = \frac{2\kappa_\mathrm{e}}{\kappa^2 + \Delta^2} \cdot \frac{P_\mathrm{in}}{\hbar\omega} \quad \underbrace{=}_{\substack{\text{crit. coupl.,} \\ \Delta=0}} \quad \frac{P_\mathrm{in}}{\kappa \cdot \hbar\omega} \tag{A.20}$$

# Acknowledgements

I would like to thank my academic advisors Michael Vanner and Ian Walmsley for the opportunity to work on a doctorate in Oxford, and in particular Michael Vanner for his support and encouragements over the course of my doctorate. I also want to thank Peter Norreys for being a supportive point of contact in Oxford after the move of my academic advisors.

Also I am extremely grateful to my friends and family, especially my parents, Angelika and Hansgeorg, who always unconditionally supported me. Magda Szczykulska and Amnu Wiegandt, thank you for having been there with me on this journey.

Special thanks for many valuable discussions, general help, supporting or enabling different parts of the science presented here, or just good company, go to my early and late colleagues Magda Szczykulska, Heng Shen, John Price, Jack Clarke, Lars Freisem, and Andreas Svela, all from the Quantum Measurement Lab (sub)group, which grew from including only Dr. Vanner and myself, when I joined in March 2016, to a respectable number of people by the end of my time, as well as my collaborators at the National Physical Laboratory Jonathan Silver and Pascal Del'Haye, in Aarhus Jinglei Zhang and Klaus Mølmer, in Bath Josh Nunn, and at the Australian National University Jiri Janousek! In particular I also want to thank John Price, Lars Freisem and Andreas Svela for the careful continuation of the experiments after my departure from the lab.

Furthermore I would like to thank all my colleagues from the Ultrafast quantum optics group at Oxford for creating such a friendly work environment throughout the years. My thanks also go to all my physics teachers at school and university, Klaus Beyersdorf, Andreas

Steffens, Klaus Lengsfeld, Norbert Wermes, Dieter Meschede, Martin Weitz and many more who will go unnamed here, for sharing their fascination for the subject with me. Last not least I want to wholeheartedly thank the hard-working people of Europe who pay their taxes and made it possible for me to devote my time to this research.

# Bibliography


AT92 Agarwal, G. S. & Tara, K. Nonclassical character of states exhibiting no squeezing or sub-Poissonian statistics. *Physical Review A* **46,** 485–488 (1992).

Agr13 Agrawal, G. P. *Nonlinear Fiber Optics* (Academic Press, 2013).

Akr+10 Akram, U., Kiesel, N., Aspelmeyer, M. & Milburn, G. J. Single-photon optomechanics in the strong coupling regime. *New Journal of Physics* **12,** 083030 (2010).

And+95 Anderson, M. H., Ensher, J. R., Matthews, M. R., Wieman, C. E. & Cornell, E. A. Observation of Bose-Einstein Condensation in a Dilute Atomic Vapor. *Science* **269,** 198–201 (1995).

AHV72 Anderson, P. w., Halperin, B. I. & Varma, c. M. Anomalous low-temperature thermal properties of glasses and spin glasses. *Philosophical Magazine* **25,** 1–9 (1972).

Arc+06 Arcizet, O., Cohadon, P.-F., Briant, T., Pinard, M. & Heidmann, A. Radiation-pressure cooling and optomechanical instability of a micromirror. *Nature* **444,** 71–74 (2006).

AMH78 Arnold, W., Martinon, C. & Hunklinger, S. Direct experimental observation of spectral diffusion in vitreous silica at low temperatures. *Le Journal de Physique Colloques* **39,** C6–961–C6–962 (C6 1978).

AKM14 Aspelmeyer, M., Kippenberg, T. J. & Marquardt, F. Cavity optomechanics. *Reviews of Modern Physics* **86,** 1391–1452 (2014).

Bah+12 Bahl, G., Tomes, M., Marquardt, F. & Carmon, T. Observation of spontaneous Brillouin cooling. *Nature Physics* **8,** 203–207 (2012).

Bah+11 Bahl, G., Zehnpfennig, J., Tomes, M. & Carmon, T. Stimulated optomechanical excitation of surface acoustic waves in a microdevice. *Nature Communications* **2,** 403 (2011).

Bak+16 Baker, C. G., Bekker, C., McAuslan, D. L., Sheridan, E. & Bowen, W. P. High bandwidth on-chip capacitive tuning of microtoroid resonators. *Optics Express* **24,** 20400–20412 (2016).

BR97 Barnett, S. M. & Radmore, P. M. *Methods in theoretical quantum optics* (Clarendon Press, Oxford, 1997).

Beh+17 Behunin, R. O., Kharel, P., Renninger, W. H. & Rakich, P. T. Engineering dissipation with phononic spectral hole burning. *Nature Materials* **16,** 315–321 (2017).

Bel+15 Bell, B., McMillan, A., McCutcheon, W. & Rarity, J. Effects of self- and cross-phase modulation on photon purity for four-wave-mixing photon pair sources. *Physical Review A* **92,** 053849 (2015).

Bla01 Black, E. D. An introduction to Pound–Drever–Hall laser frequency stabilization. *American Journal of Physics* **69,** 79–87 (2001).

BIH91 Boller, K.-J., Imamoğlu, A. & Harris, S. E. Observation of electromagnetically induced transparency. *Physical Review Letters* **66,** 2593–2596 (1991).

Bor26 Born, M. Quantenmechanik der Stoßvorgänge. *Zeitschrift für Physik* **38,** 803–827 (1926).

Boy08 Boyd, R. *Nonlinear Optics* 3rd ed. (Academic Press, 2008).

BM67 Braginskii, V. B. & Manukin, A. B. Ponderomotive Effects of Electromagnetic Radiation. *Soviet Physics JETP* **25,** 3 (1967).

Bra68 Braginskiĭ, V. B. Classical and Quantum Restrictions on the Detection of Weak Disturbances of a Macroscopic Oscillator. *Soviet Physics JETP* **26,** 831 (1968).

BGI89 Braginsky, V. B., Gorodetsky, M. L. & Ilchenko, V. S. Quality-factor and nonlinear properties of optical whispering-gallery modes. *Physics Letters A* **137,** 393–397 (1989).

BSV01 Braginsky, V., Strigin, S. & Vyatchanin, S. Parametric oscillatory instability in Fabry–Perot interferometer. *Physics Letters A* **287,** 331–338 (2001).

BZB72 Brenig, W., Zeyher, R. & Birman, J. L. Spatial Dispersion Effects in Resonant Polariton Scattering. II. Resonant Brillouin Scattering. *Physical Review B* **6,** 4617–4622 (1972).

Bre+08 Brennecke, F., Ritter, S., Donner, T. & Esslinger, T. Cavity Optomechanics with a Bose-Einstein Condensate. *Science* **322,** 235–238 (2008).

BP02 Breuer, H.-P. & Petruccione, F. *The Theory of Open Quantum Systems* (Oxford University Press, Oxford, 2002).

Bri22 Brillouin, L. Diffusion de la lumière et des rayons X par un corps transparent homogène - Influence de l'agitation thermique. *Annales de Physique* **9,** 88–122 (1922).

CPV00 Cai, M., Painter, O. & Vahala, K. J. Observation of Critical Coupling in a Fiber Taper to a Silica-Microsphere Whispering-Gallery Mode System. *Physical Review Letters* **85,** 74–77 (2000).

CW51 Callen, H. B. & Welton, T. A. Irreversibility and Generalized Noise. *Physical Review* **83,** 34–40 (1951).

Car93 Carmichael, H. *An Open Systems Approach to Quantum Optics* (Springer-Verlag Berlin Heidelberg, 1993).

CYV04 Carmon, T., Yang, L. & Vahala, K. J. Dynamical thermal behavior and thermal self-stability of microcavities. *Optics Express* **12,** 4742–4750 (2004).

Cas+17 Caspani, L. *et al.* Integrated sources of photon quantum states based on nonlinear optics. *Light: Science & Applications* **6,** e17100–e17100 (2017).

Cha+11 Chan, J. *et al.* Laser cooling of a nanomechanical oscillator into its quantum ground state. *Nature* **478,** 89–92 (2011).

Cha65 Chandrasekharan, V. The exact equation for Brillouin shifts. *Journal de Physique* **26,** 655 (1965).

Che16 Chembo, Y. K. Quantum dynamics of Kerr optical frequency combs below and above threshold: Spontaneous four-wave mixing, entanglement, and squeezed states of light. *Physical Review A* **93,** 033820 (2016).

CTS64 Chiao, R. Y., Townes, C. H. & Stoicheff, B. P. Stimulated Brillouin Scattering and Coherent Generation of Intense Hypersonic Waves. *Physical Review Letters* **12,** 592–595 (1964).

Chi+10 Chiasera, A. *et al.* Spherical whispering-gallery-mode microresonators. *Laser & Photonics Reviews* **4,** 457–482 (2010).

Chr+14 Christensen, S. L. *et al.* Quantum interference of a single spin excitation with a macroscopic atomic ensemble. *Physical Review A* **89,** 033801 (2014).

Chu+17 Chu, Y. *et al.* Quantum acoustics with superconducting qubits. *Science* **358,** 199–202 (2017).

Coh+15 Cohen, J. D. *et al.* Phonon counting and intensity interferometry of a nanomechanical resonator. *Nature* **520,** 522–525 (2015).

CL86 Cottam, M. G. & Lockwood, D. J. *Light scattering in magnetic solids* (Wiley, 1986).

Deb09 Debye, P. Der Lichtdruck auf Kugeln von beliebigem Material (Light pressure on spheres of arbitrary material). *Annalen der Physik* **335,** 57–136 (1909).

DS70 DeGiorgio, V. & Scully, M. O. Analogy between the Laser Threshold Region and a Second-Order Phase Transition. *Physical Review A* **2,** 1170–1177 (1970).

Del11 Del'Haye, P. *Optical Frequency Comb Generationin Monolithic Microresonators* Ph.D. Thesis (Ludwigs-Maximilian-Universität München, 2011).

DDP13 Del'Haye, P., Diddams, S. A. & Papp, S. B. Laser-machined ultra-high-Q microrod resonators for nonlinear optics. *Applied Physics Letters* **102,** 221119 (2013).

Del+07 Del'Haye, P. *et al.* Optical frequency comb generation from a monolithic microresonator. *Nature* **450,** 1214–1217 (2007).

Del+08 Deléglise, S. *et al.* Reconstruction of non-classical cavity field states with snapshots of their decoherence. *Nature* **455,** 510–514 (2008).

DAC17 Diallo, S., Aubry, J.-P. & Chembo, Y. K. Effect of crystalline family and orientation on stimulated Brillouin scattering in whispering-gallery mode resonators. *Optics Express* **25.** Publisher: Optical Society of America, 29934–29945 (2017).

Die+89 Diedrich, F., Bergquist, J. C., Itano, W. M. & Wineland, D. J. Laser Cooling to the Zero-Point Energy of Motion. *Physical Review Letters* **62,** 403–406 (4 1989).

Dir30 Dirac, P. *The principles of quantum mechanics* (Oxford University Press, 1930).

DBT03 Donadio, D., Bernasconi, M. & Tassone, F. Photoelasticity of crystalline and amorphous silica from first principles. *Physical Review B* **68,** 134202 (2003).

Don+15 Dong, C.-H. *et al.* Brillouin-scattering-induced transparency and non-reciprocal light storage. *Nature Communications* **6,** 6193 (2015).

Doo+14 Doolin, C., Kim, P. H., Hauer, B. D., MacDonald, A. J. R. & Davis, J. P. Multidimensional optomechanical cantilevers for high-frequency force sensing. *New Journal of Physics* **16,** 035001 (2014).

Dre+83 Drever, R. W. P. *et al.* Laser phase and frequency stabilization using an optical resonator. *Applied Physics B Photophysics and Laser Chemistry* **31,** 97–105 (1983).

DH14 Drummond, P. D. & Hillery, M. S. *The Quantum Theory of Nonlinear Optics* (New York: Cambridge University Press, 2014).

Dua+01 Duan, L.-M., Lukin, M. D., Cirac, J. I. & Zoller, P. Long-distance quantum communication with atomic ensembles and linear optics. *Nature* **414,** 413–418 (2001).

Dut+15 Dutt, A. *et al.* On-Chip Optical Squeezing. *Physical Review Applied* **3,** 044005 (2015).

Eic+09 Eichenfield, M., Camacho, R., Chan, J., Vahala, K. J. & Painter, O. A picogram- and nanometre-scale photonic-crystal optomechanical cavity. *Nature* **459,** 550–555 (2009).

Enz+19 Enzian, G. *et al.* Observation of Brillouin optomechanical strong coupling with an 11 GHz mechanical mode. *Optica* **6,** 7 (2019).

Esq98 *Tunneling Systems in Amorphous and Crystalline Solids* (ed Esquinazi, P.) (Springer-Verlag Berlin Heidelberg, 1998).

Fav+11 Favretto-Cristini, N., Komatitsch, D., Carcione, J. M. & Cavallini, F. Elastic surface waves in crystals. Part 1: Review of the physics. *Ultrasonics* **51,** 653–660 (2011).

Fin+18 Fink, T., Schade, A., Höfling, S., Schneider, C. & Imamoglu, A. Signatures of a dissipative phase transition in photon correlation measurements. *Nature Physics* **14,** 365–369 (2018).

Fio+11 Fiore, V. *et al.* Storing Optical Information as a Mechanical Excitation in a Silica Optomechanical Resonator. *Physical Review Letters* **107,** 133601 (2011).

FIM05 Fleischhauer, M., Imamoglu, A. & Marangos, J. P. Electromagnetically induced transparency: Optics in coherent media. *Reviews of Modern Physics* **77,** 633–673 (2005).

Fom+05 Fomin, A. E., Gorodetsky, M. L., Grudinin, I. S. & Ilchenko, V. S. Nonstationary nonlinear effects in optical microspheres. *JOSA B* **22,** 459–465 (2005).

Fre32 Frenkel, J. I. *Wave Mechanics: Elementary Theory* (Clarendon Press, Oxford, 1932).

Gal+14 Galland, C., Sangouard, N., Piro, N., Gisin, N. & Kippenberg, T. J. Heralded Single-Phonon Preparation, Storage, and Readout in Cavity Optomechanics. *Physical Review Letters* **112,** 143602 (2014).

Gal+13 Galliou, S. *et al.* Extremely Low Loss Phonon-Trapping Cryogenic Acoustic Cavities for Future Physical Experiments. *Scientific Reports* **3,** 2132 (2013).

GJM13 Gammelmark, S., Julsgaard, B. & Mølmer, K. Past Quantum States of a Monitored System. *Physical Review Letters* **111,** 160401 (2013).

GZ04 Gardiner, C. & Zoller, P. *Quantum Noise* (Springer-Verlag Berlin Heidelberg, 2004).

Ger64 Gerlich, D. Elastic Constants of Barium Fluoride Between 4.2 and 300 K. *Physical Review* **135,** A1331–A1333 (1964).

GK04 Gerry, C. & Knight, P. *Introductory Quantum Optics* (Cambridge University Press, 2004).

Gig+06 Gigan, S. *et al.* Self-cooling of a micromirror by radiation pressure. *Nature* **444,** 67–70 (2006).

GL91 Glauber, R. J. & Lewenstein, M. Quantum optics of dielectric media. *Physical Review A* **43,** 467–491 (1991).

GSI96 Gorodetsky, M. L., Savchenkov, A. A. & Ilchenko, V. S. Ultimate Q of optical microsphere resonators. *Optics Letters* **21,** 453–455 (1996).

GF06 Gorodetsky, M. & Fomin, A. Geometrical theory of whispering-gallery modes. *IEEE Journal of Selected Topics in Quantum Electronics* **12,** 33–39 (2006).

Gra+18 Graffitti, F., Kelly-Massicotte, J., Fedrizzi, A. & Brańczyk, A. M. Design considerations for high-purity heralded single-photon sources. *Physical Review A* **98,** 053811 (2018).

GH70 Graham, R. & Haken, H. Laserlight — first example of a second-order phase transition far away from thermal equilibrium. *Zeitschrift für Physik* **237,** 31–46 (1970).

Gro30a Gross, E. Change of Wave-length of Light due to Elastic Heat Waves at Scattering in Liquids. *Nature* **126,** 201–202 (1930).

Gro30b Gross, E. Über Änderung der Wellenlänge bei Lichtzerstreuung in Kristallen. *Zeitschrift für Physik* **63,** 685–687 (1930).

GMM09 Grudinin, I. S., Matsko, A. B. & Maleki, L. Brillouin Lasing with a CaF2 Whispering Gallery Mode Resonator. *Physical Review Letters* **102,** 043902 (2009).

Gru+11 Grudinin, I., Lee, H., Chen, T. & Vahala, K. Compensation of thermal nonlinearity effect in optical resonators. *Optics Express* **19,** 7365 (2011).

GW96 Gruner, T. & Welsch, D.-G. Green-function approach to the radiation-field quantization for homogeneous and inhomogeneous Kramers-Kronig dielectrics. *Physical Review A* **53,** 1818–1829 (1996).

GW15 Guevara, I. & Wiseman, H. Quantum State Smoothing. *Physical Review Letters* **115,** 180407 (2015).

Hak75 Haken, H. Cooperative phenomena in systems far from thermal equilibrium and in nonphysical systems. *Reviews of Modern Physics* **47,** 67–121 (1975).

Hak70 Haken, H. *Laserlicht - ein neues Beispiel für eine Phasenumwandlung? Advances in Solid State Physics* 351–365 (Elsevier, 1970).

Hak83 Haken, H. *Synergetics* (Springer-Verlag Berlin Heidelberg, 1983).

Hei+87 Heidmann, A. *et al.* Observation of Quantum Noise Reduction on Twin Laser Beams. *Physical Review Letters* **59,** 2555–2557 (1987).

Hel+10 Helt, L. G., Yang, Z., Liscidini, M. & Sipe, J. E. Spontaneous four-wave mixing in microring resonators. *Optics Letters* **35,** 3006–3008 (2010).

HLS12 Helt, L. G., Liscidini, M. & Sipe, J. E. How does it scale? Comparing quantum and classical nonlinear optical processes in integrated devices. *JOSA B* **29,** 2199–2212 (2012).

HSK10 Hofer, J., Schliesser, A. & Kippenberg, T. J. Cavity optomechanics with ultrahigh-Q crystalline microresonators. *Physical Review A* **82,** 031804 (2010).

Hof+09 Hofheinz, M. *et al.* Synthesizing arbitrary quantum states in a superconducting resonator. *Nature* **459,** 546–549 (2009).

Hon+17 Hong, S. *et al.* Hanbury Brown and Twiss interferometry of single phonons from an optomechanical resonator. *Science* **358,** 203–206 (2017).

Hu+17 Hu, J. *et al.* Creation of a Bose-condensed gas of 87Rb by laser cooling. *Science* **358,** 1078–1080 (2017).

YuH+10 Yu-Huan, S., Jin-Wei, S., Min, O., Guo-Jian, Y. & Da-He, L. Theoretical Analysis of the Critical Phenomena of a Brillouin Laser. *Chinese Physics Letters* **27,** 074203 (2010).

HR86 Hunklinger, S. & Raychaudhuri, A. *Progress in Low Temperature Physics, Chapter 3: Thermal and Elastic Anomalies in Glasses at Low Temperatures* (ed Brewer, D.) 265–344 (Elsevier, 1986).

Huy+16 Huy, K. P., Beugnot, J.-C., Tchahame, J.-C. & Sylvestre, T. Strong coupling between phonons and optical beating in backward Brillouin scattering. *Physical Review A* **94** (2016).

Iss18 Isserlis, L. On a Formula for the Product-Moment Coefficient of any Order of a Normal Frequency Distribution in any Number of Variables. *Biometrika* **12,** 134–139 (1918).

JS06 Jacobs, K. & Steck, D. A. A straightforward introduction to continuous quantum measurement. *Contemporary Physics* **47,** 279–303 (2006).

JC16 Jaeken, J. W. & Cottenier, S. Solving the Christoffel equation: Phase and group velocities. *Computer Physics Communications* **207,** 445–451 (2016).

Jai+13 Jain, A. *et al.* Commentary: The Materials Project: A materials genome approach to accelerating materials innovation. *APL Materials* **1,** 011002 (2013).

Kad66 Kadanoff, L. P. Scaling laws for ising models near $T_c$. *Physics Physique Fizika* **2,** 263–272 (1966).

Kar+12 Karuza, M. *et al.* Optomechanical sideband cooling of a thin membrane within a cavity. *New Journal of Physics* **14,** 095015 (2012).

Kha+10 Khalili, F. *et al.* Preparing a Mechanical Oscillator in Non-Gaussian Quantum States. *Physical Review Letters* **105,** 070403 (2010).

Kha+19 Kharel, P. *et al.* High-frequency cavity optomechanics using bulk acoustic phonons. *Science Advances* **5,** eaav0582 (2019).

KSV02 Kippenberg, T. J., Spillane, S. M. & Vahala, K. J. Modal coupling in traveling-wave resonators. *Optics Letters* **27,** 1669 (2002).

KB06 Kleckner, D. & Bouwmeester, D. Sub-kelvin optical cooling of a micromechanical resonator. *Nature* **444,** 75–78 (2006).

Kli+01 Klitzing, W. v., Long, R., Ilchenko, V. S., Hare, J. & Lefèvre-Seguin, V. Frequency tuning of the whispering-gallery modes of silica microspheres for cavity quantum electrodynamics and spectroscopy. *Optics Letters* **26,** 166–168 (2001).

Kni+97 Knight, J. C., Cheung, G., Jacques, F. & Birks, T. A. Phase-matched excitation of whispering-gallery-mode resonances by a fiber taper. *Optics Letters* **22,** 1129 (1997).

Kra11 Krause, M. Finite-Difference Mode Solver for Curved Waveguides With Angled and Curved Dielectric Interfaces. *Journal of Lightwave Technology* **29,** 691–699 (2011).

LL12 Landau, L. D. & Lifshitz, E. *Theory of Elasticity* 3rd edition (Butterworth-Heinemann, 2012).

Lau+06 Laurat, J. *et al.* Efficient retrieval of a single excitation stored in an atomic ensemble. *Optics Express* **14,** 6912–6918 (2006).

LC03 Le Floch, S. & Cambon, P. Study of Brillouin gain spectrum in standard single-mode optical fiber at low temperatures (1.4–370 K) and high hydrostatic pressures (1–250 bars). *Optics Communications* **219,** 395–410 (2003).

Lec+16 Lecaplain, C., Javerzac-Galy, C., Gorodetsky, M. L. & Kippenberg, T. J. Mid-infrared ultra-high- Q resonators based on fluoride crystalline materials. *Nature Communications* **7,** 1–8 (2016).

Lee+11 Lee, K. C. *et al.* Entangling Macroscopic Diamonds at Room Temperature. *Science* **334,** 1253–1256 (2011).

Lee+12 Lee, K. C. *et al.* Macroscopic non-classical states and terahertz quantum processing in room-temperature diamond. *Nature Photonics* **6,** 41–44 (2012).

Lei+96 Leibfried, D. *et al.* Experimental Determination of the Motional Quantum State of a Trapped Atom. *Physical Review Letters* **77,** 4281–4285 (1996).

Leo97 Leonhardt, U. *Measuring the Quantum State of Light* (Cambridge University Press, 1997).

LF06 Leviton, D. B. & Frey, B. J. *Temperature-dependent absolute refractive index measurements of synthetic fused silica* SPIE Astronomical Telescopes + Instrumentation (eds Atad-Ettedgui, E., Antebi, J. & Lemke, D.) (Orlando, Florida , USA, 2006), 62732K.

LFK05 Leviton, D. B., Frey, B. J. & Kvamme, T. *High accuracy, absolute, cryogenic, refractive index measurements of infrared lens materials for JWST NIRCam using CHARMS Cryogenic Optical Systems and Instruments XI* Cryogenic Optical Systems and Instruments XI. **5904** (International Society for Optics and Photonics, 2005), 59040O.

Li+11 Li, B.-B. *et al.* Experimental observation of Fano resonance in a single whispering-gallery microresonator. *Applied Physics Letters* **98,** 021116 (2011).

LKR11 Li, T., Kheifets, S. & Raizen, M. G. Millikelvin cooling of an optically trapped microsphere in vacuum. *Nature Physics* **7,** 527–530 (2011).

Lin+14a Lin, G., Diallo, S., Henriet, R., Jacquot, M. & Chembo, Y. K. Barium fluoride whispering-gallery-mode disk-resonator with one billion quality-factor. *Optics Letters* **39,** 6009–6012 (2014).

Lin+14b Lin, G. *et al.* Cascaded Brillouin lasing in monolithic barium fluoride whispering gallery mode resonators. *Applied Physics Letters* **105,** 231103 (2014).

Lou00 Loudon, R. *The Quantum Theory of Light* 3rd ed. (Oxford University Press, 2000).

Lüb04 Lübeck, S. Universal scaling behavior of non-equilibrium phase transitions. *International Journal of Modern Physics B* **18,** 3977–4118 (2004).

Lub72 Lubkin, G. B. Universality and scaling in critical behavior. *Physics Today* **25,** 17–20 (1972).

Mah+13 Mahboob, I., Nishiguchi, K., Fujiwara, A. & Yamaguchi, H. Phonon Lasing in an Electromechanical Resonator. *Physical Review Letters* **110,** 127202 (2013).

Man86 Mandel, L. Non-Classical States of the Electromagnetic Field. *Physica Scripta* **T12,** 34–42 (1986).

MW95 Mandel, L. & Wolf, E. *Optical coherence and quantum optics* (Cambridge University Press, 1995).

Man26 Mandelstam, L. I. Light scattering by inhomogeneous media. *Zhurnal Russkogo fiziko-khimicheskogo obshchestva* **58,** 381 (1926).

Mar+07 Marquardt, F., Chen, J. P., Clerk, A. A. & Girvin, S. M. Quantum Theory of Cavity-Assisted Sideband Cooling of Mechanical Motion. *Physical Review Letters* **99,** 093902 (2007).

MKL17 Masalov, A. V., Kuzhamuratov, A. & Lvovsky, A. I. Noise spectra in balanced optical detectors based on transimpedance amplifiers. *Review of Scientific Instruments* **88,** 113109 (2017).

McC+15 McConnell, R., Zhang, H., Hu, J., Ćuk, S. & Vuletić, V. Entanglement with negative Wigner function of almost 3,000 atoms heralded by one photon. *Nature* **519,** 439–442 (2015).

Met14 Metcalfe, M. Applications of cavity optomechanics. *Applied Physics Reviews* **1,** 031105 (2014).

MW11 Milburn, G. & Woolley, M. An Introduction to Quantum Optomechanics. *Acta Physica Slovaca. Reviews and Tutorials* **61** (2011).

MKV16 Milburn, T. J., Kim, M. S. & Vanner, M. R. Nonclassical-state generation in macroscopic systems via hybrid discrete-continuous quantum measurements. *Physical Review A* **93,** 053818 (2016).

Nee+06 Neergaard-Nielsen, J. S., Nielsen, B. M., Hettich, C., Mølmer, K. & Polzik, E. S. Generation of a Superposition of Odd Photon Number States for Quantum Information Networks. *Physical Review Letters* **97,** 083604 (2006).

Nie+17 Nielsen, W. H. P., Tsaturyan, Y., Møller, C. B., Polzik, E. S. & Schliesser, A. Multimode optomechanical system in the quantum regime. *Proceedings of the National Academy of Sciences* **114,** 62–66 (2017).

NTR97 Nikles, M., Thevenaz, L. & Robert, P. Brillouin gain spectrum characterization in single-mode optical fibers. *Journal of Lightwave Technology* **15,** 1842–1851 (1997).

NMG16 Norte, R. A., Moura, J. P. & Gröblacher, S. Mechanical Resonators for Quantum Optomechanics Experiments at Room Temperature. *Physical Review Letters* **116,** 147202 (2016).

Nun+08 Nunn, J. *et al.* Multimode Memories in Atomic Ensembles. *Physical Review Letters* **101,** 260502 (2008).

Nun+14 Nunnenkamp, A., Sudhir, V., Feofanov, A. K., Roulet, A. & Kippenberg, T. J. Quantum-Limited Amplification and Parametric Instability in the Reversed Dissipation Regime of Cavity Optomechanics. *Physical Review Letters* **113,** 023604 (2014).

Ora02 Oraevsky, A. N. Whispering-gallery waves. *Quantum Electronics* **32,** 377–400 (2002).

Our+07 Ourjoumtsev, A., Jeong, H., Tualle-Brouri, R. & Grangier, P. Generation of optical 'Schrödinger cats' from photon number states. *Nature* **448,** 784–786 (2007).

Our+06 Ourjoumtsev, A., Tualle-Brouri, R., Laurat, J. & Grangier, P. Generating Optical Schrödinger Kittens for Quantum Information Processing. *Science* **312,** 83–86 (2006).

Pal+13 Palomaki, T. A., Harlow, J. W., Teufel, J. D., Simmonds, R. W. & Lehnert, K. W. Coherent state transfer between itinerant microwave fields and a mechanical oscillator. *Nature* **495,** 210–214 (2013).

Par+07 Parigi, V., Zavatta, A., Kim, M. & Bellini, M. Probing Quantum Commutation Rules by Addition and Subtraction of Single Photons to/from a Light Field. *Science* **317,** 1890–1893 (2007).

PK99 Parkins, A. S. & Kimble, H. J. Quantum state transfer between motion and light. *Journal of Optics B: Quantum and Semiclassical Optics* **1,** 496–504 (1999).

Pet+16 Peterson, R. W. *et al.* Laser Cooling of a Micromechanical Membrane to the Quantum Backaction Limit. *Physical Review Letters* **116,** 063601 (2016).

Phi81 *Amorphous Solids - Low-Temperature Properties* (ed Philipps, W. A.) (Springer-Verlag Berlin Heidelberg, 1981).

Phi72 Phillips, W. A. Tunneling states in amorphous solids. *Journal of Low Temperature Physics* **7,** 351–360 (1972).

Pog+07 Poggio, M., Degen, C. L., Mamin, H. J. & Rugar, D. Feedback Cooling of a Cantilever's Fundamental Mode below 5 mK. *Physical Review Letters* **99,** 017201 (2007).

Qva+18 Qvarfort, S., Serafini, A., Barker, P. F. & Bose, S. Gravimetry through non-linear optomechanics. *Nature Communications* **9,** 1–11 (2018).

Rak+12 Rakich, P. T., Reinke, C., Camacho, R., Davids, P. & Wang, Z. Giant Enhancement of Stimulated Brillouin Scattering in the Subwavelength Limit. *Physical Review X* **2,** 011008 (2012).

RK28 Raman, C. V. & Krishnan, K. S. A New Type of Secondary Radiation. *Nature* **121,** 501 (1928).

RN70 Rao, K. & Narasimhamurty, T. Photoelastic constants of CaF2 and BaF2. *Journal of Physics and Chemistry of Solids* **31,** 876–878 (1970).

Rei+13 Reiserer, A., Nölleke, C., Ritter, S. & Rempe, G. Ground-State Cooling of a Single Atom at the Center of an Optical Cavity. *Physical Review Letters* **110,** 223003 (2013).

Ren+18 Renninger, W. H., Kharel, P., Behunin, R. O. & Rakich, P. T. Bulk crystalline optomechanics. *Nature Physics* **14,** 601–607 (2018).

Ric39 Richtmyer, R. D. Dielectric Resonators. *Journal of Applied Physics* **10** (1939).

Rie+18 Riedinger, R. *et al.* Remote quantum entanglement between two micromechanical oscillators. *Nature* **556,** 473–477 (2018).

Rin+18 Ringbauer, M., Weinhold, T. J., Howard, L. A., White, A. G. & Vanner, M. R. Generation of mechanical interference fringes by multi-photon counting. *New Journal of Physics* **20,** 053042 (2018).

Riv+11 Rivière, R. *et al.* Optomechanical sideband cooling of a micromechanical oscillator close to the quantum ground state. *Physical Review A* **83,** 063835 (2011).

Ros+17 Rossi, M. *et al.* Enhancing Sideband Cooling by Feedback-Controlled Light. *Physical Review Letters* **119,** 123603 (2017).

Ros+18 Rossi, M., Mason, D., Chen, J., Tsaturyan, Y. & Schliesser, A. Measurement-based quantum control of mechanical motion. *Nature* **563,** 53–58 (2018).

Saf+13 Safavi-Naeini, A. H. *et al.* Laser noise in cavity-optomechanical cooling and thermometry. *New Journal of Physics* **15,** 035007 (2013).

ST07 Saleh, B. E. A. & Teich, M. C. *Fundamentals of photonics* 2nd ed. eng (Wiley-Interscience, Hoboken, N.J., 2007).

San+11 Sangouard, N., Simon, C., de Riedmatten, H. & Gisin, N. Quantum repeaters based on atomic ensembles and linear optics. *Reviews of Modern Physics* **83,** 33–80 (2011).

SKM16 Savanier, M., Kumar, R. & Mookherjea, S. Photon pair generation from compact silicon microring resonators using microwatt-level pump powers. *Optics Express* **24,** 3313 (2016).

SB91 Schiller, S. & Byer, R. L. High-resolution spectroscopy of whispering gallery modes inlarge dielectric spheres. *Optics Letters* **16,** 1138–1140 (1991).

Sch+11 Schleier-Smith, M. H., Leroux, I. D., Zhang, H., Van Camp, M. A. & Vuletić, V. Optomechanical Cavity Cooling of an Atomic Ensemble. *Physical Review Letters* **107,** 143005 (2011).

SKZ13 Schlosshauer, M., Kofler, J. & Zeilinger, A. A snapshot of foundational attitudes toward quantum mechanics. *Studies in History and Philosophy of Science Part B: Studies in History and Philosophy of Modern Physics* **44,** 222–230 (2013).

Sch+08 Schmidt, C. *et al.* Nonlinear thermal effects in optical microspheres at different wavelength sweeping speeds. *Optics Express* **16,** 6285 (2008).

Sch80 Schroeder, J. Brillouin scattering and pockels coefficients in silicate glasses. *Journal of Non-Crystalline Solids* **40,** 549–566 (1980).

Sch+14 Schunk, G. *et al.* Identifying modes of large whispering-gallery mode resonators from the spectrum and emission pattern. *Optics Express* **22,** 30795 (2014).

Sel71 Sellmeier. Zur Erklärung der abnormen Farbenfolge im Spectrum einiger Substanzen. *Annalen der Physik* **219,** 272–282 (1871).

Ser17 Serafini, A. *Quantum Continuous Variables: A Primer of Theoretical Methods* (Taylor & Francis Group, 2017).

SLB85 Shelby, R. M., Levenson, M. D. & Bayer, P. W. Guided acoustic-wave Brillouin scattering. *Physical Review B* **31,** 5244–5252 (1985).

ST16 Sinclair, G. F. & Thompson, M. G. Effect of self- and cross-phase modulation on photon pairs generated by spontaneous four-wave mixing in integrated optical waveguides. *Physical Review A* **94,** 063855 (2016).

SS16 Sipe, J. E. & Steel, M. J. A Hamiltonian treatment of stimulated Brillouin scattering in nanoscale integrated waveguides. *New Journal of Physics* **18,** 045004 (2016).

Son+07 Sonehara, T., Konno, Y., Kaminaga, H., Saikan, S. & Ohno, S. Frequency-modulated stimulated Brillouin spectroscopy in crystals. *Journal of the Optical Society of America B* **24,** 1193 (2007).

Spe+11 Specht, H. P. *et al.* A single-atom quantum memory. *Nature* **473,** 190–193 (2011).

Spi+03 Spillane, S. M., Kippenberg, T. J., Painter, O. J. & Vahala, K. J. Ideality in a Fiber-Taper-Coupled Microresonator System for Application to Cavity Quantum Electrodynamics. *Physical Review Letters* **91,** 043902 (2003).

Str+16 Strekalov, D. V., Marquardt, C., Matsko, A. B., Schwefel, H. G. L. & Leuchs, G. Nonlinear and quantum optics with whispering gallery resonators. *Journal of Optics* **18,** 123002 (2016).

Str78 Strutt, J. W. *The Theory of Sound* 1st ed. (Dover, 1878).

SB15a Sturman, B. & Breunig, I. Brillouin lasing in whispering gallery micro-resonators. *New Journal of Physics* **17,** 125006 (2015).

SB15b Sturman, B. & Breunig, I. Acoustic whispering gallery modes within the theory of elasticity. *Journal of Applied Physics* **118,** 013102 (2015).

TE97 Taraskin, S. N. & Elliott, S. R. Phonons in vitreous silica: Dispersion and localization. *Europhysics Letters (EPL)* **39,** 37–42 (1997).

Teu+11 Teufel, J. D. *et al.* Sideband cooling of micromechanical motion to the quantum ground state. *Nature* **475,** 359–363 (2011).

TC09 Tomes, M. & Carmon, T. Photonic Micro-Electromechanical Systems Vibrating at X -band (11-GHz) Rates. *Physical Review Letters* **102** (2009).

Tom+11 Tomes, M., Marquardt, F., Bahl, G. & Carmon, T. Quantum-mechanical theory of optomechanical Brillouin cooling. *Physical Review A* **84,** 063806 (2011).

VSH80 Vacher, R., Sussner, H. & Hunklinger, S. Brillouin scattering in vitreous silica below 1 K. *Physical Review B* **21,** 5850–5853 (1980).

Vah+09 Vahala, K. *et al.* A phonon laser. *Nature Physics* **5,** 682–686 (2009).

VBV16 Van Laer, R., Baets, R. & Van Thourhout, D. Unifying Brillouin scattering and cavity optomechanics. *Physical Review A* **93,** 053828 (2016).

VAK13 Vanner, M. R., Aspelmeyer, M. & Kim, M. S. Quantum State Orthogonalization and a Toolset for Quantum Optomechanical Phonon Control. *Physical Review Letters* **110,** 010504 (2013).

Van+13 Vanner, M. R., Hofer, J., Cole, G. D. & Aspelmeyer, M. Cooling-by-measurement and mechanical state tomography via pulsed optomechanics. *Nature Communications* **4,** 2295 (2013).

Van+11 Vanner, M. R. *et al.* Pulsed quantum optomechanics. *Proceedings of the National Academy of Sciences* **108,** 16182–16187 (2011).

VPK15 Vanner, M. R., Pikovski, I. & Kim, M. S. Towards optomechanical quantum state reconstruction of mechanical motion. *Annalen der Physik* **527,** 15–26 (2015).

Ved50 Vedam, K. The Elastic and Photoelastic Constants of Fused Quartz. *Physical Review* **78,** 472–473 (1950).

Ver+12 Verhagen, E., Deléglise, S., Weis, S., Schliesser, A. & Kippenberg, T. J. Quantum-coherent coupling of a mechanical oscillator to an optical cavity mode. *Nature* **482,** 63–67 (2012).

Vid+16 Vidrighin, M. D. *et al.* Photonic Maxwell's Demon. *Physical Review Letters* **116,** 050401 (2016).

Vog+13 Vogell, B. *et al.* Cavity-enhanced long-distance coupling of an atomic ensemble to a micromechanical membrane. *Physical Review A* **87,** 023816 (2013).

vNeu32 Von Neumann, J. *Mathematical Foundations of Quantum Mechanics* (Springer, Berlin, 1932).

WM08 Walls, D. F. & Milburn, G. J. *Quantum Optics* 2nd ed. (Springer-Verlag Berlin Heidelberg, 2008).

Web02 *Handbook of Optical Materials* 1st edition (ed Weber, M. J.) (CRC Press, 2002).

Wei+10 Weis, S. *et al.* Optomechanically Induced Transparency. *Science* **330,** 1520–1523 (2010).

WU82 Weisbuch, C. & Ulbrich, R. G. *Resonant light scattering mediated by excitonic polaritons in semiconductors Light Scattering in Solids III. Topics in Applied Physics* (eds Cardona, M. & Güntherodt, G.) (Springer, 1982).

Wie+15 Wieczorek, W. *et al.* Optimal State Estimation for Cavity Optomechanical Systems. *Physical Review Letters* **114,** 223601 (2015).

WDM19 Wiederhecker, G. S., Dainese, P. & Mayer Alegre, T. P. Brillouin optomechanics in nanophotonic structures. *APL Photonics* **4,** 071101 (2019).

Wie+11 Wiederhecker, G. S., Manipatruni, S., Lee, S. & Lipson, M. Broadband tuning of optomechanical cavities. *Optics Express* **19,** 2782–2790 (2011).

Wil+07 Wilson-Rae, I., Nooshi, N., Zwerger, W. & Kippenberg, T. J. Theory of Ground State Cooling of a Mechanical Oscillator Using Dynamical Backaction. *Physical Review Letters* **99,** 093901 (2007).

WM09 Wiseman, H. M. & Milburn, G. J. *Quantum Measurement and Control* (Cambridge University Press, 2009).

Wol+15 Wolff, C., Steel, M. J., Eggleton, B. J. & Poulton, C. G. Stimulated Brillouin scattering in integrated photonic waveguides: Forces, scattering mechanisms, and coupled-mode analysis. *Physical Review A* **92** (2015).

Yar65 Yariv, A. Quantum theory for parametric interactions of light and hypersound. *Journal of Quantum Electronics* **1,** 28–36 (1965).

Yar00 Yariv, A. Universal relations for coupling of optical power between microresonators and dielectric waveguides. *Electronics Letters* **36,** 321–322 (2000).

YDT02 Yeniay, A., Delavaux, J.-M. & Toulouse, J. Spontaneous and stimulated Brillouin scattering gain spectra in optical fibers. *Journal of Lightwave Technology* **20,** 1425–1432 (2002).

ZPB07 Zavatta, A., Parigi, V. & Bellini, M. Experimental nonclassicality of single-photon-added thermal light states. *Physical Review A* **75,** 052106 (2007).

ZVB04 Zavatta, A., Viciani, S. & Bellini, M. Quantum-to-Classical Transition with Single-Photon-Added Coherent States of Light. *Science* **306,** 660–662 (2004).

Zeh+11 Zehnpfennig, J., Bahl, G., Tomes, M. & Carmon, T. Surface optomechanics: calculating optically excited acoustical whispering gallery modes in microspheres. *Optics Express* **19.** Publisher: Optical Society of America, 14240–14248 (2011).

ZPB03 Zhang, J., Peng, K. & Braunstein, S. L. Quantum-state transfer from light to macroscopic oscillators. *Physical Review A* **68,** 013808 (2003).

Zha18 Zhang, J. *Quantum measurement and preparation of Gaussian states* Ph.D. Thesis (University of Aarhus, 2018).

ZM17 Zhang, J. & Mølmer, K. Prediction and retrodiction with continuously monitored Gaussian states. *Physical Review A* **96,** 062131 (2017).

ZGB07 Zhu, Z., Gauthier, D. J. & Boyd, R. W. Stored Light in an Optical Fiber via Stimulated Brillouin Scattering. *Science* **318,** 1748–1750 (2007).

Zie+18 Zielnicki, K. *et al.* Joint spectral characterization of photon-pair sources. *Journal of Modern Optics* **65,** 1141–1160 (2018).

ZH16 Zoubi, H. & Hammerer, K. Optomechanical multimode Hamiltonian for nanophotonic waveguides. *Physical Review A* **94,** 053827 (2016).